

ACTIVITY CHARACTERISATION
OF
POTENTIAL PLANET HOSTS

Dissertation
zur Erlangung des Doktorgrades
des Fachbereichs Physik
der Universität Hamburg

vorgelegt von

Lalitha Sairam
aus Chennai, India

Hamburg
2013

Gutachter der Dissertation:

Prof. Jürgen Schmitt
Prof. Manuel Güdel

Gutachter der Disputation:

Prof. Peter Hauschildt
Prof. Marcus Brüggem

Datum der Disputation

10.05.2013

Vorsitzender des Prüfungsausschusses

Dr. Robert Baade

Vorsitzender des Promotionsausschusses

Prof. Peter Hauschildt

Dekan der Physik Fakultät

Prof. Heinrich Graener

Abstract

Low mass stars make up $\sim 75\%$ of the stellar population in our galaxy, making them the most common potential planetary hosts. An ultimate goal of the exo-planetary science is discovering terrestrial-type planets inside the habitable zone. M dwarfs are in the focus of ongoing and planned surveys for habitable planet since the distance of the habitable zone to the star decreases with decreasing stellar temperature and therefore the stellar mass. Further, M dwarfs are also excellent targets for high precision radial velocity searches of low mass planets, since, the amplitude of the radial velocity signal is inversely proportional to the mass of the star. However, due to extremely low luminosities the habitable zones around low mass stars lie very close to the hosts, making the orbiting world extremely vulnerable to the effects of magnetic activity and the high energy emission from its host. In addition to the hazardous environment around the M hosts, an important obstacle in low mass planet finding survey is the magnetic/stellar activity. An active region on the surface of the star can influence the spectra as well as precise measurement of radial velocity.

CARMENES is a radial velocity survey to be conducted on a sample of moderately active M stars with the goal to detect low mass planets. To optimise the scientific return from CARMENES, a careful analysis of the sample stars prior to the selection has to be carried. In this thesis, I characterise the activity properties of CARMENES sample targets with an emphasis on the stellar coronae in the X-rays. Nearly 40% of the stars from the CARMENES targets was detected as X-ray sources and for $\sim 60\%$ of the stars an upper-limit coronal fluxes was estimated. Further, most of the detected X-ray sources are intrinsically active and therefore excluded from the CARMENES sample lists since they are not suitable for the survey.

Active low mass stars are capable of producing flares of short as well as longer durations. As the most common potential planetary hosts, it is essential to understand the properties of flaring plasma, how frequently and powerful these flares, etc.. The flare studies in this thesis is based on two active flaring potential planets hosts within 15 pc in the solar neighbourhood.

Flares affect all layers of the stellar atmosphere from the photosphere over the chromosphere and the transition region up to the corona. Hence simultaneous multi-wavelength observations allow us to obtain a comprehensive picture of the different layers of stellar atmosphere and the physical processes going on during different phases of the flares. I investigate the properties of the coronal plasma during flares on Proxima Centauri and AB Dor A observed simultaneously with UVES spectrograph at the VLT and *XMM-Newton*. From the X-ray data, I analysed the temporal evolution of the coronal temperature and the emission measure, and investigate the variation of the electron density and the abundances during the flare. I also derive the size of the flaring structures from the evolution of emitting plasma during the flare rise, the peak and the decay.

The Sun is usually considered as a prototype of low mass stars, hence we often extrapolate the knowledge we have on the Sun to the other stars. AB Dor A being a calibration target for the reflection grating spectrometer (RGS) on board *XMM-Newton*, has been repeatedly observed over last decade. This gives us an ideal opportunity to perform detailed analysis of the coronal emission, and to compare the flare characteristics with the Sun. My studies suggest that the larger flares are hotter and in addition the flares observed on AB Dor A and other stars follow the same slope as the solar flares. To understand the frequency and energetics of the flaring plasma, I also perform a homogeneous study of flare properties and its occurrence in AB Dor A. Furthermore, I show a possible long-term cycle in a very active star both from a photospheric and coronal point of view. My analysis suggests a clear evidence of a long-term variations of the X-ray luminosity in an active K-dwarf AB Dor A correlated with photospheric brightness variability.

Zusammenfassung

Massearme Sterne machen $\sim 75\%$ der gesamten Sternpopulation unserer Milchstraße aus, was sie auch zu den häufigsten Kandidaten macht, die potentiell Planeten beherbergen können. Das höhere Ziel der Suche nach extrasolaren Planeten ist die Entdeckung eines erdähnlichen Planeten in der habitablen Zone. M-Zwerges stehen im Fokus von andauernden und geplanten Durchmusterungen von Sternen um habitable Planeten zu finden, weil die Entfernung der habitablen Zone zum Zentralstern mit sinkender Effektivtemperatur und damit auch mit sinkender stellarer Masse abnimmt. Des Weiteren sind M-Zwerges exzellente Ziele für die Durchmusterung nach gering-massigen Planeten auf der Basis von hochpräzisen Radialgeschwindigkeitsmessungen, weil die Amplitude des Signals invers proportional zur Masse des Sternes ist. Aufgrund der extrem geringen Helligkeit von massearmen Sternen liegt deren habitable Zone sehr nah am Zentralstern, was den Planeten anfällig für magnetische Aktivität und hochenergetische Strahlung macht. Zusätzlich zu der möglicherweise lebensfeindlichen Umgebung von M-Zwerges ist die magnetische/stellare Aktivität ein Hindernis für Durchmusterungen nach gering-massigen Planeten, da aktive Regionen auf der Sternoberfläche sowohl das Spektrum als auch die Radialgeschwindigkeitsmessungen beeinträchtigen.

CARMENES ist eine Radialgeschwindigkeitsdurchmusterung von einer Auswahl von mäßig aktiven M-Sternen mit dem Ziel massearme Planeten zu entdecken. Zur Maximierung der wissenschaftlichen Ergebnisse ist eine gründliche Analyse der zur Auswahl stehenden Sterne nötig. In dieser Arbeit habe ich die Aktivitätseigenschaften potentieller CARMENES Ziele insbesondere in Hinsicht auf die stellare Korona mittels Röntgenstrahlung charakterisiert. Fast 40% dieser Sterne wurden als Röntgenquellen detektiert und für $\sim 60\%$ konnte eine Obergrenze für den koronalen Röntgenfluss bestimmt werden. Die Mehrzahl der detektierten Röntgenquellen ist intrinsisch aktiv und wurde daher von der CARMENES Auswahl ausgeschlossen, weil sie sich nicht für die Durchmusterung eignet.

Aktive massearme Sterne zeigen sowohl kurz als auch lang andauernde Flares. Da sie die zahlreichsten, potentiell Planeten beherbergende Sterne sind, ist es notwendig die Häufigkeit und die Energie der Flares zu bestimmen, sowie die Eigenschaften des Flareplasmas zu verstehen. Die Studien in dieser Arbeit basieren auf zwei aktiven Sternen mit häufigen Flares, die mit einem Abstand von weniger als 15 pc in der Nachbarschaft der Sonne liegen und Planeten beherbergen könnten.

Stellare Flares betreffen alle Atmosphärenschichten von der Photosphäre über die Chromosphäre und die Übergangsregion bis hin zu der Korona. Daher erlauben simultane Beobachtungen in verschiedenen Spektralbereichen ein umfassendes Bild der atmosphärischen Schichten und der physikalischen Prozesse während der unterschiedlichen Phasen eines Flare zu erhalten. Ich untersuche die Eigenschaften des koronalen Flareplasmas auf Proxima Centauri und AB Dor A, welche simultan mit dem UVES Spektrographen am VLT und mit XMM-Newton beobachtet wurden. Mit Hilfe der Röntgendaten habe ich die zeitliche Entwicklung der koronalen Temperatur und des Emissionsmaßes analysiert. Zusätzlich wurde die Variation der Elektronendichte und der Elementhäufigkeiten während der Flares studiert. Es wurde außerdem die Größe der betroffenen Strukturen durch die Entwicklung des strahlenden Plasmas während der Anfangs-, der Haupt- sowie der Endphase der Flares bestimmt.

Die Sonne wird häufig als Standardstern für massearme Sterne angesehen, weshalb unser Wissen über die Sonne auch zu anderen Sternen hin extrapoliert wird. Da AB Dor A ein Kalibrationsziel des Reflection Grating Spectrometer (RGS) an Bord von XMM Newton ist, wurde er über die letzte Dekade hinweg mehrfach beobachtet. Dies gibt uns die ideale Möglichkeit eine detaillierte Analyse der koronalen Emission durchzuführen und diese mit den Flarecharakteristika der Sonne zu vergleichen. Meine Analyse deutet darauf hin, dass starke

Flares heißer sind als auf der Sonne. Die Flares auf AB Dor A und anderen Sternen folgen jedoch dem gleichen Trend wie jene auf der Sonne. Um die Häufigkeit und Energetik der Flares zu verstehen, habe ich eine homogene Studie der Flareeigenschaften und ihres Auftretens auf AB Dor A durchgeführt. Zusätzlich demonstriere ich die Möglichkeit eines Langzeitzyklus auf einem sehr aktiven Stern aus photosphärischer und koronaler Sichtweise. Meine Analyse ergibt Hinweise auf eine Langzeitvariation der Röntgenhelligkeit auf dem aktiven K-Zwerg AB Dor A, die mit der photosphärischen Helligkeitsvariabilität korreliert ist.

Contents

I	Introduction	1
1	Solar-stellar connection	3
1.1	Photosphere	3
1.1.1	Photospheric variability	4
1.1.2	Spots in other stars	5
1.2	The magnetic cycle	5
1.3	Chromosphere	6
1.3.1	Chromospheric activity	6
1.3.2	Mt.Wilson program	7
1.4	Coronae	8
1.4.1	Coronal activity	9
1.4.2	Stellar flares	10
1.5	X-ray instrumentation for coronal observations	10
2	Extra solar planets and habitability	13
2.1	Habitable zone and its description	13
2.2	Exoplanet detection methods	14
2.3	Searches for habitable worlds	16
2.3.1	Space-based survey	16
2.3.2	Ground-based surveys	16
3	Aim and outline of the thesis	19
II	Scientific Contributions	21
4	CARMENES	23
4.1	The instrument	23
4.2	How is CARMENES different from other survey?	23
4.3	M dwarfs as host stars	24
4.3.1	Hazardous M dwarfs	24
4.3.2	Observational difficulties	25
4.4	Survey strategy & sample selection	26
4.5	Activity characterisation	26
4.5.1	H α activity	26
4.5.2	X-ray activity	26
4.6	X-ray activity characterisation of the pre-CARMENES targets	27
4.7	Results	27
4.7.1	X-ray luminosities	27

4.7.2	Coronal activity distribution	28
4.7.3	Chromospheric-coronal activity indicators	29
4.8	Discussion of preliminary results	29
5	Flares in low mass stars	31
5.1	My contribution	31
5.2	Multi-wavelength observations of Proxima Centauri	33
5.3	A multi-wavelength view of AB Dor's outer atmosphere	50
6	Characteristics of flares on AB Dor A	69
6.1	Observations and data analysis	69
6.1.1	Quiescent emission	69
6.1.2	Flare analysis	69
6.2	Results	70
6.2.1	Global flare properties	70
6.2.2	Comparison with scaling laws	72
6.2.3	The event distribution	75
7	A solar-like magnetic activity cycle on the active ultra-fast rotator AB Dor A?	77
III	Conclusions	89
8	Concluding remarks	91
8.1	Summary and concluding remarks	91
8.2	Outlook	93
	List of Figures	97
	Bibliography	99

Part I

Introduction

Chapter 1

Solar-stellar connection

“The stars, they are as the Sun. Each star. Every star. And those spheres - they are worlds, realms, each one different yet the same.”

- **Steven Erikson**

The Sun displays amazing physical phenomena which continue to surprise us, despite the fact that solar physics is a mature scientific discipline. The Sun being the nearest star to us, permits uniquely sensitive measurements which cannot be easily performed on any other star. However, one of the major scientific challenges in solar physics is the complexity of the physical processes which is driven by the flow of energy generated in the solar interior to the atmospheres.

The fundamental questions associated with solar physics focus on understanding the magnetic field generation, emergence and its dynamical behaviour:

- What is the nature of solar dynamo generating magnetic fields?
- How does the magnetic field develop into dynamic loop structures in the solar atmosphere?
- Why is the solar corona hotter than the solar photosphere/chromosphere ?
- How are the short and long-term variability of the solar activity related to each other?
- How does the solar activity affect the Earth and its climate?
- How is the solar wind generated?

Solar physics has taken a major leap on answering these fundamental questions with the advent of space missions.

The Sun and most of the stars have the photosphere which is the lowest of the four layers of the solar atmosphere. Lying just above the photosphere is the chromosphere occupying few thousands of kilometres. In the case of the Sun, the outer layer of its atmosphere is the corona where the solar plasma is heated to millions of degrees. The layer of atmosphere between the chromosphere and the corona is a thin and a very irregular layer called the transition region. In this chapter I give a brief introduction of the observational features associated with the solar and the stellar photosphere, the chromosphere and the corona.

Aristotle postulated a concept that the Sun is constant and has a homogeneous surface. However, slight changes in the Sun were noticed even with the naked eye, way before Aristotle. Such variability of the Sun was later found to have several manifestations and is broadly termed as solar activity. Solar activity includes sunspots, prominences, flares, coronal mass ejection (CME'S), etc.. In this chapter I will also discuss the concept of activity associated with each layer of the atmosphere, with a special emphasis upon stellar X-ray flares.

1.1 Photosphere

The lowest of the four layers of the solar atmosphere is the photosphere which attributes to the optical surface of the Sun and the emergent spectrum is globally defined by a black body spectrum. Hence, using Wien's displacement law we know that the temperature of the solar

surface is ≈ 5800 K (Gray 2005).

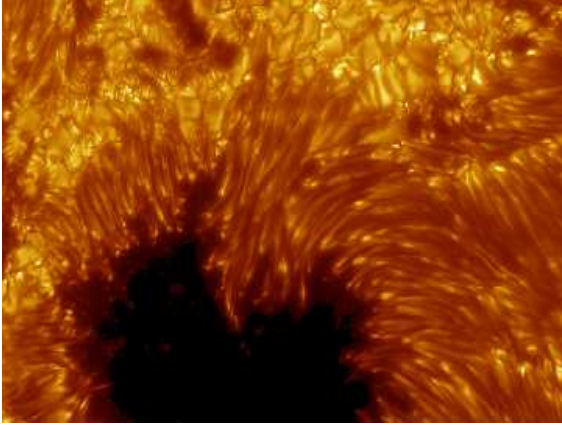


Figure 1.1: Giant spot on the surface of the Sun showing numerous granules, the dark umbral region and the light penumbral region. Image credit: SST, Royal Swedish Academy of Sciences.

Besides the temperature the photosphere is also characterised by its granulation. Granulation occurs as a result of convection currents occurring just below the photosphere. In addition to these granular structures, the Sun also comprises the dark sunspots, the bright faculae, etc..

A prominent and a well-studied feature associated with the solar photosphere are the sunspots. Sunspots are the easiest activity feature to detect on the solar surface. Naked eye observation of the sunspots are known from different cultures with the oldest record dating nearly 2000 years ago (Bray & Loughhead 1964; Wittmann & Xu 1987).

A typical sunspot consists of a central dark region called the umbra and a lighter surrounding region called the penumbra (see Fig. 1.1). Sunspots appears relatively dark when compared to the surrounding photosphere. The typical temperature of the solar photosphere is about 5800 K, whereas, the temperature of sunspots is around 4000 K (Solanki 2003). The reason for this difference in the temperature is the strong magnetic field associated with the spot. The temperature of the sunspot is thought to be lowered by the inhibition of convective energy by the magnetic field (see Solanki 1997 and references therein). Hence the

sunspot regions having strong magnetic field tends to be cooler than the surrounding region and hence appears darker.

The magnetic field associated with a sunspot is manifested by measuring the Zeeman splitting of the spectral lines. If the magnetic fields are present, then the energy levels of atoms, ions and molecules split into more than one level, and the amount of splitting depends on the strength of the magnetic field. This effect is called the *Zeeman effect* and the corresponding effect on the spectral lines are called the Zeeman splitting. If one measures the Zeeman splitting in the spectrum, then one can measure the strength of magnetic field associated with the splitting. The magnetic field strength B typically reaches peak values of 2000-3700 G in parts of the sunspot umbra for a large spot and drops steadily down to 700-1000 G at the edge of a visible sunspot (Martinez Pillet 1997; Solanki 2002).

1.1.1 Photospheric variability

In the year 1613, Galileo Galilei observed the sunspots which seemed to be carried around by the Sun's rotation. For centuries the question that puzzled observers was whether the spots were free-floating clouds in the Sun's atmosphere. However, we now know that they are not free-floating, but rather anchored to the solar surface.

During the 19th century two very important discoveries associated with the Sun were made:

- Sunspots have been monitored since the time of Galileo. A feature that emerged from this long-term data is that the sunspot numbers in a given year is cyclic (see bottom panel of Fig.1.2). In the year 1843, Heinrich Schwabe showed that the number of spots on the solar surface followed an 11 years cycle (Schwabe 1844). This cyclic behaviour is called the sunspot cycle.
- Richard C. Carrington showed that the sunspots migrated in latitude, i.e., during a sunspot minimum period the spots are at higher latitude and as the sunspot activity reaches maximum the spots migrate

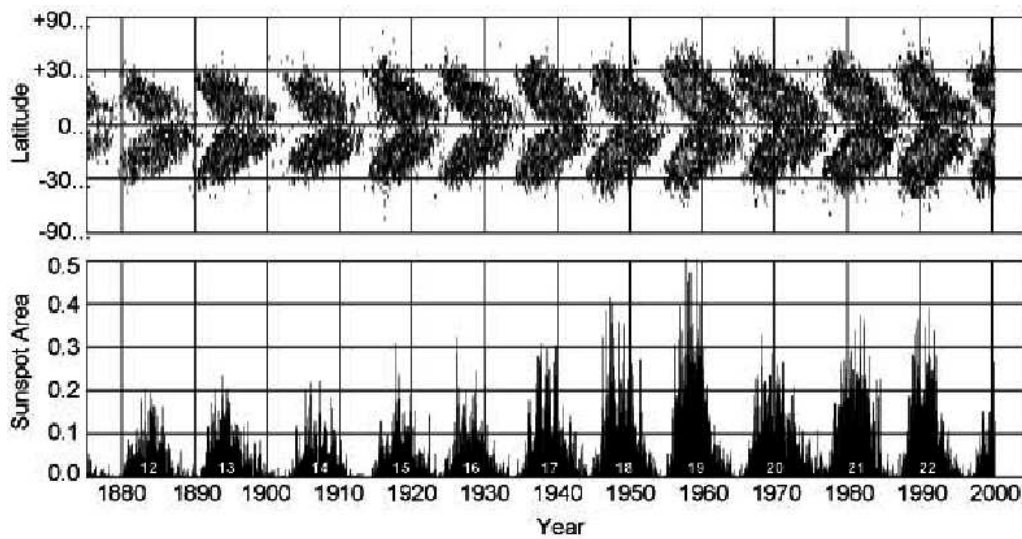


Figure 1.2: Top panel : Butterfly diagram of sunspots. This plot shows that the spots migrate towards the equator during a given cycle. Bottom panel: The total area of sunspots as a percent of the visible hemisphere which follows a 11-year cycle. Image credit: David Hathaway, NASA/MSFC.

towards equator. This gives rise to the famous *butterfly diagram* of the solar activity cycle (see top panel of Fig. 1.2).

1.1.2 Spots in other stars

Stars having stellar properties similar to those of the Sun, having different ages provide an ideal opportunity to study the time evolution of the Sun's magnetic activity. With this aim the spot activity and the associated cyclic behaviour in stars have been investigated for decades now. RS Canum Venaticorum and BY Draconis are well-known examples of spotted stars. They are believed to have large cool spots on their surface (Vogt 1981). However, spots are not restricted to only a few stars; all cool stars are expected to have spots on their surfaces (Strassmeier 2009). Spots in stars can be inferred by the periodic variations in the star's light as these spots move along the surface of the star as a result of stellar rotation.

A remarkable feature about the solar activity is its sunspot cycle, then the obvious question arises whether cyclic behaviour of spots can be noticed in other stars as well. Indeed star spots also show cyclic behaviour, Phillips & Hartmann (1978) reported the first evidence of

stellar photospheric cycle in two spotted dwarfs BY Dra and CC Eri. Additionally, Lockwood et al. (2004, 2007) also found clear evidence of a relation between the photospheric and chromospheric activity cycle. Several studies on the brightness variation due to cool spots on young solar analogs confirmed the detection of activity cycles (Messina & Guinan 2002; Järvinen et al. 2005) which resembles the 11 year sunspot cycle.

1.2 The magnetic cycle

In the early 20th century, George Ellery Hale demonstrated the magnetic nature of sunspots and the solar activity cycle. Magnetographic mapping of the Sun's surface magnetic field suggested that the solar poloidal magnetic field undergoes cyclic variation, changing polarities at the maximum of the sunspot activity. In other words, the magnetic field during the sunspot minimum exhibit mainly poloidal configuration as the cycle progresses to the maximum spot activity becomes mainly toroidal, and then turns into poloidal configuration with opposite polarity. Hence, a successful model needs to account for both the mechanism where the poloidal field is transformed into toroidal

and vice versa (Schrijver & Siscoe 2009).

The poloidal to toroidal configuration can be explained using a simple approach. The Sun exhibits differential rotation where the equator rotates faster than the poles. This differential rotation causes magnetic field lines to wind up around the rotation axis. Assuming that the poloidal magnetic field is already present, differential rotation should provide sufficient mechanism to convert the poloidal magnetic field into toroidal magnetic field – a process commonly known as the ω -effect. The ω -effect is thought to be located at the "tachocline", which is the interface layer between the uniformly rotating radiative core and the differentially rotating outer convective zone.

However, the regeneration of the toroidal field into the poloidal field is much more complicated. According to Parker (1955), a plasma sphere/bubble rises in the solar convective zone and they expand as they reach low density regions. As a result of the Coriolis forces these plasma spheres start to rotate. The inherent magnetic fields in these rotating spheres become twisted as they rise to the surface, hence small magnetic field perpendicular to the previous configuration are produced, which will yield a poloidal magnetic field configuration. This is called the classical α -effect. Babcock (1961) and Leighton (1969) proposed an alternative scenario where the α -effect is located near or at the solar surface. And the poloidal field is regenerated by the decay of active regions and they migrate poleward due to interaction with a meridional flow.

Yet another type of dynamo is the α^2 dynamo which can be applied to fully convective stars. Stars below $\approx 0.3M_{\odot}$ become fully convective, as a result, the mean field model allows dynamo which do not necessarily rely on a combination of α and ω effect, but can also transform the toroidal to poloidal field configuration purely by α effect. This suggests a change in the magnetic field which might lead to an abrupt change in the X-ray properties (see sect.1.4).

1.3 Chromosphere

The chromosphere is the second layer of the Sun's atmosphere sitting just between the photosphere and the transition region. In the 19th century, the first recorded observation of the chromosphere were made (Hall 2008). While engaged in observations of a total solar eclipse, just a few seconds after totality a bright red flash was observed close to the photosphere (Fig.1.3). Several spectroscopic observations began soon after this to confirm whether the origin of this bright phenomena were intrinsically solar or terrestrial. Subsequent work led to discovery of several spectral emission features of highly ionised species associated with the chromosphere and the corona. This indicated that the temperature above the photosphere rises to about $\sim 10\,000$ K (Vernazza et al. 1981) in the chromosphere and abruptly jumping to millions of Kelvin in the corona (see Sect.1.4).

In addition, chromosphere shows widespread cool gas like the carbon monoxide bands (CO band) at chromospheric heights (Solanki et al. 1994). The existence of CO bands implies a gas temperature of about 3700 K, however in the classical chromospheric temperature models the minimum temperature is located between 4200 K and 4500 K (Wiedemann et al. 1994). This indicates that the chromosphere is extremely in-homogeneous.

A typical chromospheric structure is the prominence (see van Ballegoijen & Martens 1989 and references therein), observed as dense cloud of material suspended through loops of magnetic fields above the solar surface. Prominences have been observed in $H\alpha$, ultraviolet (UV) and extreme ultra-violet (EUV) lines and their study is of great interest in the understanding the formation, stability, mass supply and the magnetic structure of the prominence. Such prominence activity was later observed in other stars as well (Dunstone et al. 2006; Korhonen et al. 2010; Parsons et al. 2011; Lalitha et al. 2013).

A ubiquitous feature of the chromosphere is the appearance and disappearance of "small

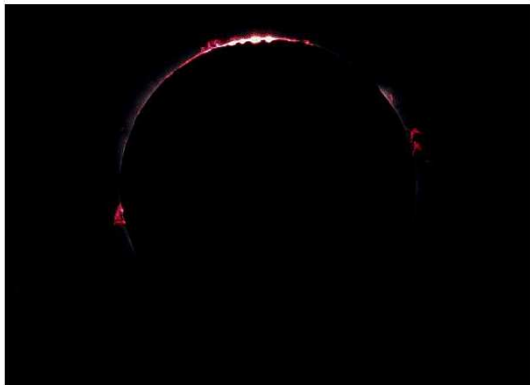


Figure 1.3: The solar chromosphere glowing in red around the edge of the moon. This image also shows the presence of prominence like structures around the limb of the Sun. Image credit: National Solar observatory.

spike" prominences called the spicules on time-scales of minutes. Spicules are bright in $H\alpha$, giving the chromosphere its pink colour. However, larger spicules are also prominent in extreme ultraviolet images.

1.3.1 Chromospheric activity

The strongest chromospheric spectral features observable from the ground are those dubbed by the H and K lines arising from singly ionised calcium and magnesium (Livingston et al. 2007). However, there are several other prominent well-studied lines associated with the chromosphere such as the D lines of neutral sodium, $H\alpha$, etc. – in this section, I will concentrate mainly on activity associated with the Ca II doublets.

A program aimed at answering if the strength of Fraunhofer lines in the solar integrated flux spectrum vary with time was initiated in the year 1974. Later White & Livingston (1978) carried out precise measurement of chromospheric Ca II H and K line profiles. Soon afterwards Skumanich et al. (1975) found a direct correlation between the magnetic field flux and the relative Ca II core strength in solar plages. Plages are the bright cloud-like features observed above the sunspots (Kelch & Linsky 1978). As the activity cycle progresses from minimum to maximum activity, the num-

ber of plages also increases, which in turn varies the strength of the Ca II and the Mg II emission lines. As a result, the strong doublet of the Ca II and the Mg II emission lines have become a diagnostic for the solar and stellar chromosphere studies.

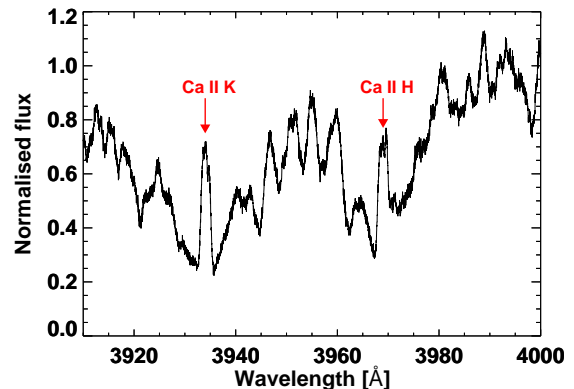


Figure 1.4: The spectrum of AB Dor A in the range of 3910-4000 Å around the Ca II H and K lines. Note the strong but very narrow emission in the cores of Ca II K (3933.7 Å) and Ca II H (3968.5 Å) lines.

1.3.2 Mt. Wilson program

In the case of the active stars the Ca II emission seems to increase with decreasing surface brightness (Lockwood et al. 2007). This raises an obvious question whether Ca II in solar-like stars exhibit a long-term trend which can be traced. In order to answer this question, Olin Wilson implemented a long-term program to monitor a sample of stars in the solar neighbourhood. For this monitoring, the telescope was equipped with a spectrophotometer to measure the strength of Ca II feature at Mt. Wilson observatory. The Mt. Wilson Ca II measurements are expressed in terms of the "S-index". The S-index is the ratio of Ca II H and K emission line cores to that in the nearby continuum bandpass on either side of the Ca II H and K lines (given as V and R) (see Fig.1.4). This is presented as

$$S \propto \frac{H + K}{V + R} \quad (1.1)$$

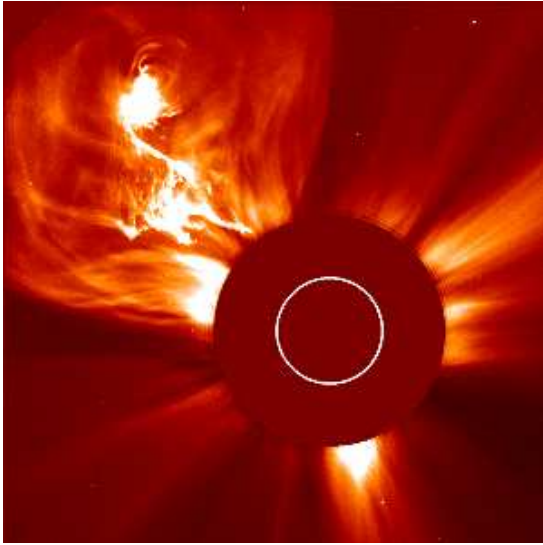


Figure 1.5: The elusive solar corona observed with Large Angle and Spectrometric COronagraph (LASCO) C2, showing the complex magnetic structure associated with it. Image credit: SOHO/EIT and SOHO/LASCO (ESA & NASA).

where $H+K$ is the counts in Ca II line cores, $V+R$ are counts in the violet and red continuum bands on both the sides of the Ca II doublets. Results of this systematic study were presented by Wilson (1978), indicating that all stellar chromospheres were indeed variable to certain extent, and that these stars could show cyclic variation analogous to the Sun. Baliunas et al. (1995) also showed that the solar S-index obtained in the context of Mt. Wilson project varied between 0.16 during activity minima to 0.22 during activity maxima. The "HK project" was continued by S. Baliunas for several years and this work remains the fundamental observation of stellar chromospheric activity. In addition, this program also resulted in several investigations on stellar chromospheric cycle (Baliunas & Vaughan 1985; Baliunas et al. 1995).

1.4 Coronae

The corona is the outer-most layer of the solar atmosphere extending into the interplanetary space. It is inhomogeneous (Rosner et al. 1978), hence a precise definition is very difficult. Consequently, one chooses to define the

corona based on the magnetic structures which seem to be ubiquitous and are found to be relatively independent of each other. These magnetic structures are basically loops anchored in the photosphere extending out into the interplanetary space or curving back into the photosphere (Aschwanden & Nightingale 2005).

The Solar corona was for the first time seen during a total solar eclipse. The corona is exceptionally faint when compared to the visible disk of the Sun. The ratio of coronal to the photospheric brightness is $\approx 10^{-6}$ and decreases by almost three orders of magnitude with increasing distance from the visible limb. Since the corona is optically thin at visible wavelength, many features observed initially were viewed only at the limb. With the advent of space borne instruments, it is now possible to view the corona on the solar disk in X-rays. Figure 1.5 shows a complex structure of outwardly-directed streamers at larger distances which is caused by the emergence of magnetic fields from inside the Sun.

One of the most important facts that we know about the solar corona is that the temperature is several million degrees. We know that the visible surface of the Sun, the photosphere, has a temperature of ≈ 5800 K. One expects that the temperature above the photosphere to drop. On the contrary, the temperature inversion occurs within few 10^3 's of kilometres with a rise from 5800 K to 10^6 K which is actually less than a thousandth of the solar radius (see Fig.1.6).

Do other stars have coronae?

If our Sun, a middle-aged main-sequence star has a corona and is an X-ray source, then one can ask if all other main-sequence stars also have a corona and are X-ray sources. This has been investigated for decades now and indeed other stars do emit X-rays. A survey published by Vaiana et al. (1981) after the first year of observations carried out by *Einstein* observatory, showed an X-ray Hertzsprung-Russell (HR) diagram similar to that of an optical HR diagram (see Fig. 1.7).

Rosner et al. (1985) depicted that all main sequence stars with spectral type F,G,K and

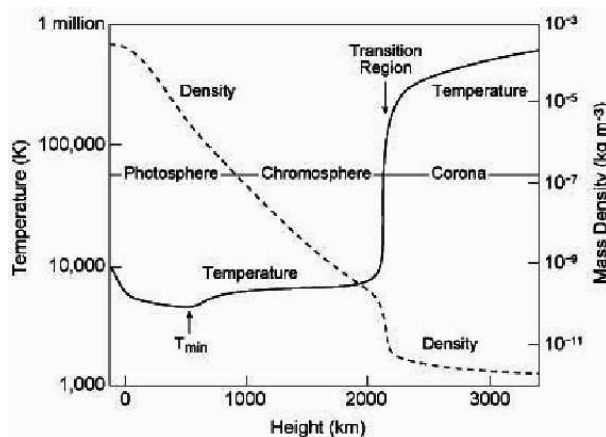


Figure 1.6: Temperature and density profile of the solar atmosphere as a function of height above the visible photosphere. Image credit: Eugene Avrett.

M are X-ray emitters, with luminosities in the range 10^{26-31} erg/s. Observations carried out by the *Einstein* observatory lead to an open question whether X-ray emission is really found for all-stars or whether there is possibility for an X-ray dark cool star to exist. To answer this question, a far more systematic study of the X-ray emission from cool stars were required. Schmitt (1997) used the data obtained during the ROSAT all sky survey and investigated the complete volume-limited sample of solar-type F and G stars within 13 pc, K stars within 10 pc and M dwarfs within 7 pc. This studies revealed that all the F-type stars from their sample were detected, whereas, the detection rate of the G-stars was more than 85%. This led to the conclusion that the formation of the corona on solar-like stars was indeed a universal phenomenon. Further, Rosner et al. (1985) also interpreted that all the stars earlier than about B5 are also X-ray emitters, they have emission levels of about 10^{29-34} erg/s. However, the corona in these stars are assumed to exist at the base of the stellar wind as a result the X-ray emission is mainly attributed to winds (Vaiana et al. 1981; Cassinelli et al. 1994; Berghoefler et al. 1997).

Depicted in Fig. 1.7 is the detected X-ray emission from thousands of stars within 25 pc around the Sun contained in the Bright Source Catalog (BSC). As can be seen, all types

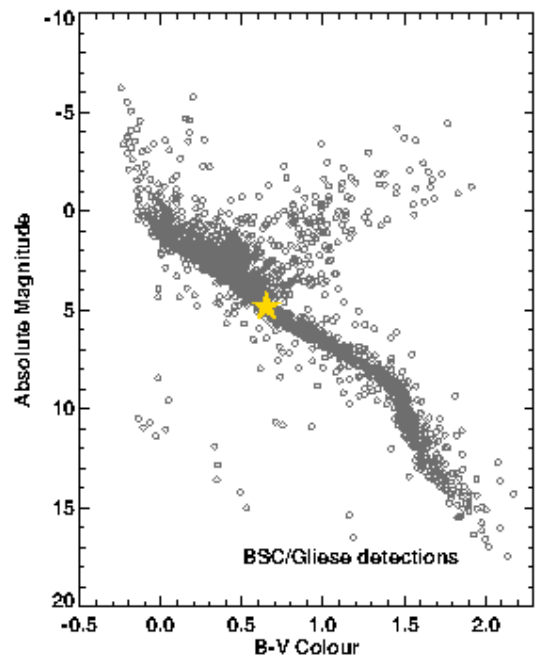


Figure 1.7: Colour-magnitude diagram of X-ray detected bright source catalog stars from Huensch et al. (1998); Hünsch et al. (1999). Depicted as yellow star is our Sun.

of stars in the colour-magnitude diagram are found to be X-ray emitters.

The stellar dynamo continuously generates magnetic fields, and a more intense dynamo action results in a more intense X-ray emission. If this picture is correct, then one expects correlation between the X-ray emission level and other stellar parameters like the rotation rate, depth of convective zone, etc.. One of the fascinating results obtained from X-ray astronomy is, that the X-ray luminosity decreases with an increase in the age of the star (Vaiana et al. 1981). This decrease in the X-ray emission with age could be explained as an effect of stellar spin-down with age. The relation between the X-ray luminosity (L_X) and the rotation rate ($v \sin i$) was demonstrated by Pallavicini et al. (1981) which in turn is a relation between the stellar age and activity.

1.4.1 Coronal activity

Coronal activity can be traced by a number of phenomena. However the most widely used in-

indicator is the solar flare. Solar flares are explosive events occurring as a result of magnetic reconnection. The energy released during such an explosion is about $10^{28} - 10^{32}$ erg. Historically the first flare observation was reported by Richard C. Carrington and Richard Hodgson in the year 1859. They were independently observing sunspots at the time; when they viewed a large flare in white light. However, most flares are not only manifested in the visible light; they reserve their strongest enhancements for spectral lines such as the $H\alpha$, the $Ca II$, and they also radiate an enormous amount of energy in extreme ultraviolet and soft X-ray wavelengths. Flares have been observed across the entire electromagnetic spectrum starting from the radio to the gamma rays.

General picture of a flare

The occurrence of flares is not distributed arbitrarily but rather they occur only in parts of the atmosphere where the conditions are right, like in an active region. A region is called an active region, when it exhibits excess $H\alpha$ emission in comparison to the surrounding atmosphere. However, this is an observationally biased definition, it provides a convenient means for observing flares. On the contrary, not all active regions produce flares, it requires certain pre-flare conditions. An important condition is the difference in the presence of strong magnetic field when compared to the quiet-Sun condition (Tandberg-Hanssen & Emslie 1988).

Kopp & Pneuman (1976) suggested that the flares have a filament associated with them and that the eruption of this filament produces magnetic instability (Fig. 1.8a and Fig. 1.8b). Filament is the same as the prominences, they are observed on solar disk as dark region, consequently prominences are seen above solar limb, where they appear as bright features against the dark background (Hirayama 1985). The magnetic instability produced by the eruption of filament leads to reconnection at large coronal heights. As a consequence of the magnetic reconnection, electrons are accelerated along the reconnected magnetic field towards the chromosphere (Fig. 1.8c). Thus, the chro-

mospheric material is heated to millions of degrees generating the optical continuum and line emissions (Fig. 1.8d). The evaporated chromospheric material fills up the coronal loop producing the soft X-ray emission.

1.4.2 Stellar flares

Historically, Joy & Humason (1949) reported the observation of M-type star using spectrogram which showed a brightening by approximately an order of magnitude in both the line emissions and the continuum emission. This star had the spectral classification dMe, where ‘d’ refers to dwarf and the ‘e’ refers to the emission line in the star’s spectrum. Features of this brightening were very similar to an intense white light flare observed on the Sun. Additionally, an increase in the optical luminosity by a factor of 2.5 was noticed. Since then intense flares are observed on a large number of K and M stars.

Stellar flares are observed across the entire electromagnetic spectrum from the radio waves and micro waves throughout the UV, and in X-rays similar to the solar flares. Solar and stellar flare show resemblance in the light curves as well (see Fig.1.9). Further, many stellar flares show a short duration spiky impulsive phase as a result of particle acceleration (Robrade & Schmitt 2005) and a long duration gradual phase as a result of thermal radiation of heated flare plasma similar to solar flares (Güdel 2004).

However, during a flare there have been observations which reveal that the luminosity increases by a factor of over 600. Optical flares on dMe stars are 10 to 10^3 times more energetic than the solar flares. This suggests that the dynamo action in the Sun and M stars might differ (see Sect. 1.2). In the Sun, the complex magnetic field associated with the solar photosphere favours the occurrence of large flares. Generalising this, the occurrence of large flares in M dwarfs and other solar-like stars may be attributed to dynamo action in the deep convective envelope producing irregular bipolar active regions in the stellar photosphere (Schrijver & Zwaan 2000).

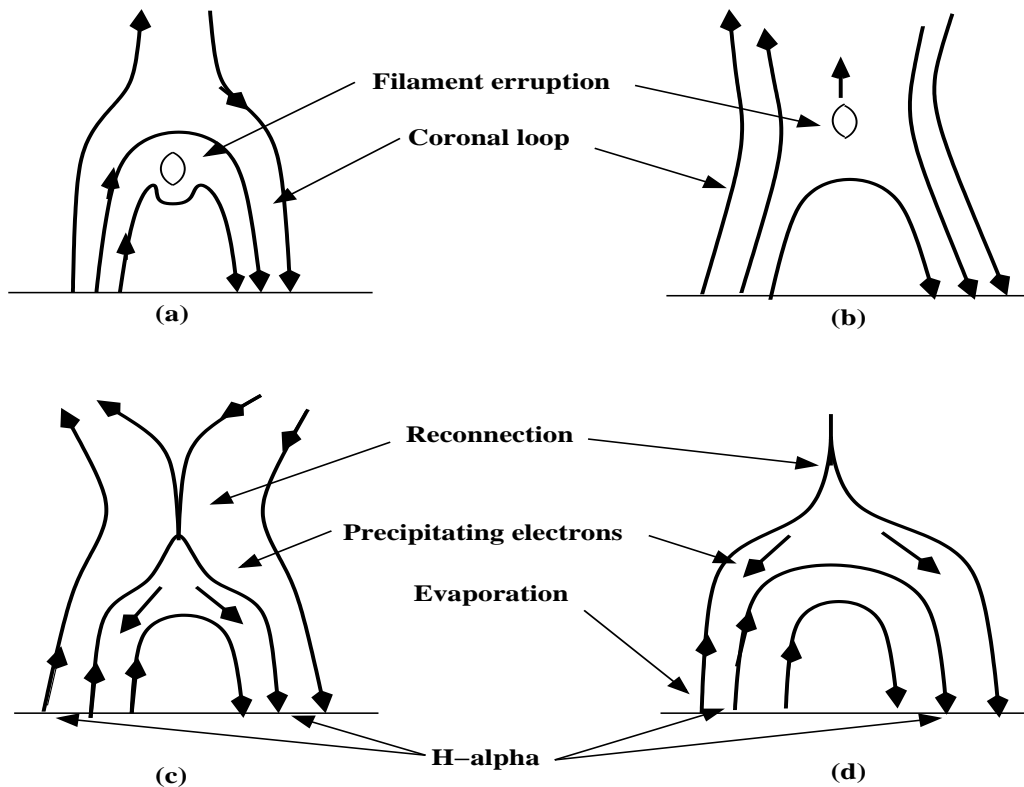


Figure 1.8: A schematic diagram of the general scenario of flares assuming energy release as a result of magnetic reconnection.

1.5 X-ray instrumentation for coronal observations

X-ray photons can penetrate the Earth's atmosphere at least a few meters, however the atmosphere is thick enough that virtually none of the X-ray photons are able to penetrate from space all the way to the Earth's surface. Hence to best solution to perform any X-ray observation is to get above the Earth's atmosphere. There have been several space-borne X-ray missions to observe both the Sun and the stars.

Few X-ray observatories used in the past for observations of the solar corona are the *Skylab* which carried two X-ray telescopes and an X-ray camera operated between 1973-1979 (Garrett & Tousey 1977).

A number of revolutionary scientific results were obtained by the *Yohkoh* spacecraft which operated between 1991 and 2005. The main objective of *Yohkoh* was to observe the solar flares during activity minimum and characterising the associated physical phenomenon of

the solar corona (Acton et al. 1992). When most of the space missions were concentrating only on the corona, a mission was designed to investigate the magnetic field associated with the photosphere, the transition region and the corona, providing a multi-wavelength view. This satellite operated between 1998 and 2010 and was called the *Transition Region and Coronal Explorer* (TRACE). It was launched with the aim to provide continuous coverage of solar phenomena.

A few of the active X-ray solar missions are the Solar and Heliospheric Observatory (SOHO), which was launched with a primary aim to study the Sun from its core to the outer most layer of the atmosphere, the corona and the solar wind (Domingo et al. 1995). Yet another satellite is the Reuven Ramaty High Energy Solar Spectroscopic Imager (*RHESSI*), operating since 2002 (Lin et al. 2002). *RHESSI* which was launched with an aim to explore the basic physics of the accelerated particle and energetics of solar flares. With *RHESSI*,

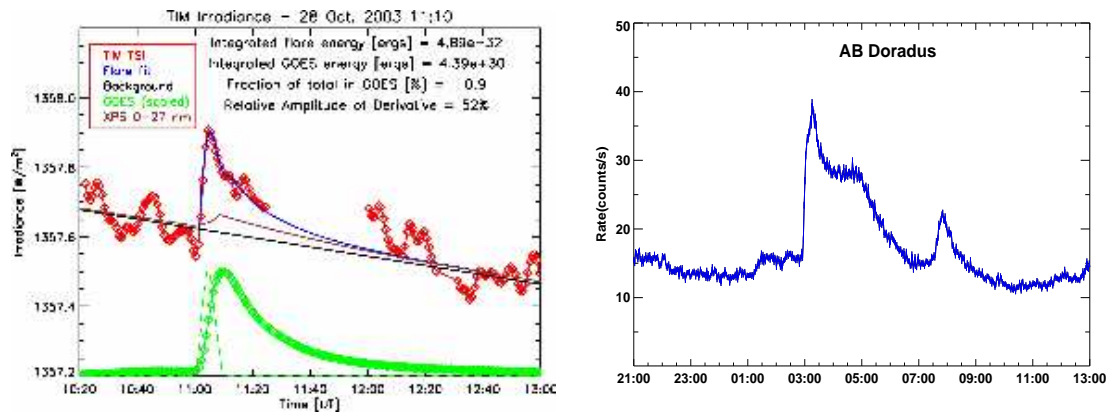


Figure 1.9: Left: A high energetic solar flare illustrating the abrupt increase in the flux to the peak followed by a gradual decrease in the flux (Kopp et al. 2005). Right: An X-ray flare observed on a low mass star AB Dor A (Lalitha et al. 2013).

flare spectra are obtained with both high spectral resolution as well as broad spectral energy range. This provides an unique opportunity to observe the hottest plasma and to compare its relation to the accelerated electrons producing non-thermal bremsstrahlung X-rays. Launched in 2010 is the Solar Dynamic Observatory (SDO), which is continuously measuring the properties of the Sun and the solar activity to provide a better insight into the Sun's variable magnetic field. In addition to all these dedicated Solar X-ray telescopes, Geostationary Satellite (GOES) 12 - 15 which is a weather monitoring satellite carries a solar X-ray imager has been continuously monitoring the Sun for over a decade.

Some of the future solar X-ray mission include Aditya - the solar coronagraph is expected to be launched in early 2015 (Singh et al. 2012); the Solar Orbiter is scheduled to be launched in early 2017. Once launched these missions are expected to address some of the outstanding fundamental questions in solar and heliophysics today.

The first non-solar X-ray satellite developed was *Uhuru* which operated between 1970 and 1973. *Uhuru* performed the first comprehensive and uniform all sky survey. However, the stellar X-ray astronomy saw a revolutionary breakthrough with the *Einstein* satellite named in honour of Albert Einstein, operated between 1978 and 1981. Aboard *Einstein* was an X-ray

telescope and an imaging proportional counter which provided a good sensitivity to observe a wide range of astronomical objects from stars to galaxy clusters. *Einstein* was amongst the first astronomical satellites to provide an opportunity for guest observer program. *Einstein* performed the first high-resolution spectroscopy and also detected several hundreds of X-ray sources (Sciortino et al. 1988).

The successor to *Einstein* observatory was the Roentgen Satellite (Truemper 1992), *ROSAT* which was launched in 1990 performed an all sky survey for the first six months and produced a catalogue of 150 000 objects; the following eight years it performed individual pointing observations and accumulated another catalogue of 100 000 serendipitous sources (Hünsch et al. 1999; Voges et al. 1999). *ROSAT* imaging was over 2° field of view which provided observations of supernova remnants, galaxy clusters, structure of interstellar medium, comets and the Moon. There were several other X-ray missions such as the Advanced Satellite for Cosmology and Astrophysics, *ASCA*, operated between 1993-2001, Rossi X-ray Timing Explorer (*RXTE*) operated between 1995 and 2012 (Levine et al. 1996), and *BeppoSAX* operated between 1996 and 2002 were used for several follow-up observations and long-term monitoring of the X-ray sources (Boella et al. 1997).

Currently we are in the era of observato-

ries such as the *Chandra* launched in 1999, the *XMM-Newton* launched in 1999 as well, the *Swift* launched in 2004 and more recently the *NuSTAR* launched in 2012. The cornerstone X-ray mission of early 2000 complementing each other is *Chandra* (Weisskopf et al. 2000) and *XMM-Newton* (Jansen et al. 2001), where *Chandra* is optimised for high angular resolution, while *XMM-Newton* has a high energy resolution.

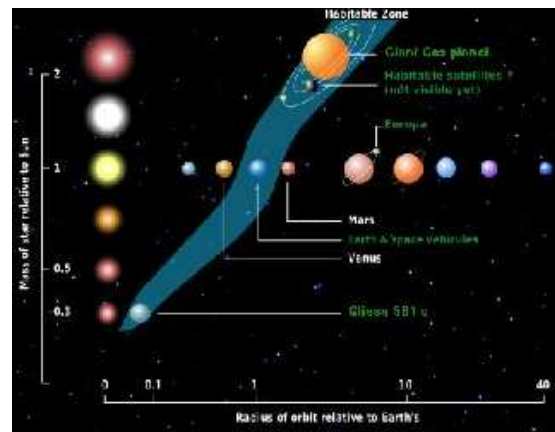
XMM-Newton is the primary database for this work. *XMM-Newton*, the X-ray Multi-Mirror mission consists of three co-aligned telescopes equipped with European Photon Imaging Camera (EPIC). The EPIC consists of two MOS and one PN CCD arrays with a sensitivity range of $\approx 0.5 - 15$ keV. The X-ray telescopes with the MOS detectors are equipped with reflection gratings (RGS) producing high-resolution X-ray spectra between 0.35 - 2.5 keV. The X-ray telescope with PN detector is equipped with optical monitor. The optical monitor on board *XMM-Newton* provide an opportunity to perform simultaneous observations in the X-ray and optical/UV regime from a single platform.

Chapter 2

Extra solar planets and habitability

The discovery of the first exoplanet, 51 Peg b, in 1995 (Mayor & Queloz 1995) marked the dawn of the new field called the exo-planetary science. To a great surprise, the first exoplanet was a Jupiter mass planet orbiting in close proximity to its host star — a so-called "hot Jupiter". Over 861 exoplanets (as of January 2013) have been discovered since 1995. While most of the known planets remain hot Jupiters, the frontier is inevitably approaching the Earth-mass regime having already reached the so-called super-Earths, i.e., planets with a mass between 1 and 10 Earth masses. However an ultimate goal has been to search for Earth-like planets in the habitable zone.

in or very close to the habitable zone of their host star (Udry et al. 2007a; Mayor et al. 2009a; Bonfils et al. 2013 and their references).



2.1 Habitable zone and its description

The habitable zone is a key concept in our understanding of the conditions under which the basic life can form and exist. We can find extreme conditions under which life exists on our very own Earth. Hence understanding the conditions in which life forms and evolves is important. The concept of habitable zone was for first time proposed by Huang (1959).

A simple definition of the habitable zone is, that it is the region around a star in which an Earth-like planet can possess liquid water on the surface and therefore possibly support life. Why water? Water appears to be the best solvent for life to emerge in. Water has a large dipole moment which readily forms hydrogen bonds stabilizing macromolecules (Kasting et al. 1993). Several potentially habitable planetary candidates have been discovered which are

Figure 2.1: Predicted location of the habitable zone around stars of different spectral class calculated based on stellar luminosity. Image credit: ESO.

A basic criterion for habitability of a planet, is its equilibrium temperature, which is accessible from observations. The equilibrium temperature is given by

$$T_{eq} = \left(\frac{(1 - A)F}{4\sigma} \right)^{\frac{1}{4}} \quad (2.1)$$

where A is the planetary albedo which is the reflecting power of the surface, σ the Stefan-Boltzmann constant and F the stellar flux at the orbital distance (d) of the planet. A crucial parameter for estimating the planetary effective temperatures is its albedo. Planets do not absorb all the incident light from its host; much of the light gets reflected and a fraction of the incident light reflected is called the albedo.

According to Selsis et al. (2007) and Kaltenegger & Sasselov (2011), a habitable planet should have a $T_{eq} \leq 270K$ to avoid the loss of the surface water. If T_{eq} is low near the outer edge of the habitable zone (e.g., in the case of GJ 581 d the model predictions suggest $T_{eq} \sim 190K$, see von Paris et al. 2010), a tremendous amount of greenhouse effect must be provided by the atmosphere to sustain habitable condition. An obvious example is that of Venus. Other than H_2O , CO_2 is the next most important greenhouse gas for determination of the outer border of habitable zone. At the outer boundary of the habitable zone, an increase in the CO_2 pressure leads to surface cooling rather than heating, due to increase in back-scattering of the incident stellar radiation.

In addition to temperature, water and CO_2 there are several other factors that decides the habitability of a planet. For example, the habitable zone of low mass stars are in orbital distances, where the planets are tidally locked. Figure 2.1 shows how the distance of the habitable zone from the host star as well as its width are dependent of the star's mass and its intrinsic luminosity. Due to close proximity to the host star these planets may have effects on the climates, plate tectonics may not develop in these planets and occurrence of super-volcanoes might affect the habitability (Bauer & Lammer 2004). Additionally, planets in the habitable zone around low mass stars are submitted to strong X-ray and UV irradiation and strong stellar winds from the host star (explained in chapter 4).

2.2 Exoplanet detection methods

According to the International Astronomical Union (IAU) working group on Extrasolar planets an object is classified as a planet if it meets the basic criteria – the mass of the object is less than or equal to 30 Jupiter masses. However, follow-up observations should be undertaken to account for the object to be false positive (Schneider et al. 2011). The main problem in searching extrasolar planets is its enormous distance from us, they are dark at optical wave-

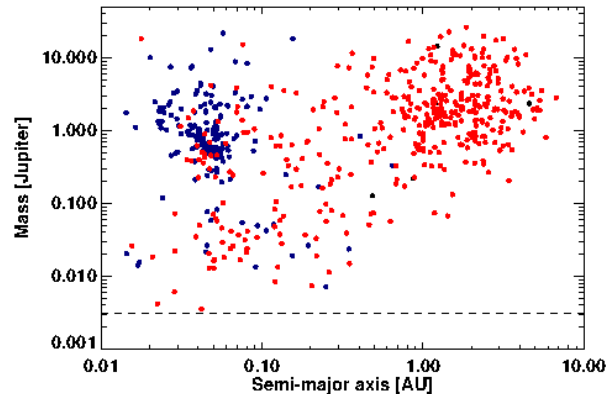


Figure 2.2: Logarithmic scatter plot of mass of planet versus the semi-major axis of known planets. Plotted in blue are exoplanet detections using transit method and in red are the detections using radial velocity method. The horizontal line indicate the mass of Earth in Jupiter masses.

lengths and they orbit a bright host. The discovery of an extrasolar planets rely on the following methods

- The transit method: In this method one observes the extrasolar planet crossing the stellar surface. When a planet does this, a part of the light from the star is blocked which translate into a shallow dip in the stellar light curve (Haswell 2010). The transit method is mainly described by three parameters: its depth, its duration and its shape. The depth is related to the fraction of the stellar disc covered by the planet. In other words, the change in the flux during the transit is related to the radius of the planet

$$\frac{\Delta F}{F_{\star}} = \frac{R_p^2}{R_{\star}^2}, \quad (2.2)$$

where ΔF is the observed change in the flux during the transit, F_{\star} is the out of transit flux measured from the star, R_p and R_{\star} are the radii of the planet and the star, respectively.

One of the straight forward estimates from a transiting exoplanet system is its orbital

period which is given by the ratio of the elapsed time between two observations of the same event and the number of cycles between the two occurrences. The orbital period (P) of a planet is related to the semi-major axis (a) based on Kepler's third law

$$\frac{a^3}{P^2} = \frac{G(M_\star + M_p)}{4\pi^2}. \quad (2.3)$$

In addition, the transit duration (d) is related to the orbital period (P), orbital radius (a) and the radius of the star (R_\star)

$$d = \frac{PR_\star}{\pi a}. \quad (2.4)$$

The above relation is valid only for planets in circular orbits. However, if the planet path does not pass through the centre of the stellar disc, it is essential to define a factor called the impact parameter (b). The impact parameter is the shortest distance from the centre of the stellar disk to the locus of the planet and is given by

$$b = \frac{a}{R} \cos i, \quad (2.5)$$

where i is the orbital inclination. So far 292 planets in 237 planetary system out of ~ 700 planetary candidates (until January 2013) have been detected by the transit method and confirmed with the radial velocity method. In Fig. 2.2 we show the distribution of mass of planets detected by the transit method (blue) as a function of semi-major axis ¹.

- Radial velocity (RV): Here one observes the periodic variation in the radial velocities of the host star as a result of an exoplanet orbiting the star. Based on the amplitude of radial velocity one can measure the semi-major axis, the mass of the planet, the orbital period and the eccentricity (details in Sect. 4.3). The mass of the planet is given by

$$M_p \sin i = K \left(\frac{M_\star^2 p}{2\pi G} \right)^{\frac{1}{3}}, \quad (2.6)$$

M_p is the mass of the planet, i is the orbital inclination, K is the amplitude of radial velocity variation, M_\star is the mass of the star, p is the orbital period and G is the gravitational constant.

A precise value of the inclination is obtained from modelling the transit shape. The RV method provided most of the known planets which is depicted in Fig. 2.2. Note that the RV favours detecting massive planets rather than larger planets (Wright & Gaudi 2013). Until January 2013, about 503 planets in 389 planetary systems have been detected by RV method.

- Astrometry: This method is related to the radial velocity detection technique. In this method the precise measurement of the position of a star is carried out, so that any wobbling induced by an orbiting planet can be directly detected (Wright & Gaudi 2013). Consequently, the astrometry method favours Jupiter mass planets with large semi-major axes. Since massive planet like Jupiter can produce large enough wobbling that can be detected with the current observational facilities. However, long-term monitoring is required to detect planets with large semi-major axes.
- Micro-lensing: This method is achieved using the lensing effect of general relativistic space-time curvature to detect the presence of planetary size objects. This method is sensitive to a wide range of star planet separation. So far 18 planets in 16 planetary system are detected by micro-lensing method.
- Direct imaging: An extremely challenging task is to image a planet around other stars. This method is limited to bright planets in distant orbit around a nearby faint star. For direct imaging of exoplanets, the well established method to block the light from solar disc – the

¹Plot is generated from data provided by the <http://exoplanets.org/table>

coronagraphic method is adopted (Wright & Gaudi 2013). If an exo-planetary system is close to us and is well resolved (the star and exoplanet), then a coronagraph may be used to image an exoplanet. An example is the discovery of a giant planet orbiting a brown dwarf (2MASSWJ 1207334-393254). With dedicated exoplanet imaging instrument like SPHERE (Spectro-Polarimetric High-contrast Exoplanet REsearch) several planets have been discovered. As of January 2013, 32 planets in 28 planetary system have been imaged. However, the detection of a planet by direct imaging depends on many variables like the semi-major axis and the size of the planet, age and distance to the star, etc. Therefore surveys based on direct imaging need to be carefully designed to maximize the chance of success.

The majority of known exoplanets are detected by the radial velocity method and followed by the transit method (if they are transiting system). In the past terrestrial exoplanets were detected by the microlensing method, nevertheless, now they are detected by both radial velocity and transit method.

2.3 Searches for habitable worlds

So far several surveys of exoplanets around stars of different spectral types have been carried out using both the transit method as well as the radial velocity technique. Such surveys have led to discoveries of gas giants, Neptune-like planets and super-Earths. In this section I explain some of such surveys conducted to search for Earth-like planets.

2.3.1 Space-based survey

Kepler

In 2009 NASA's Kepler mission was launched in space to search for transiting Earth-sized planets. Kepler performs high precision photometry

($\sim 0.01\%$) staring at the same field in Cygnus-Lyra region, observing $\sim 150\,000$ stars repeatedly over the last 4 years. Repeated observation of the same region of the sky is done mainly, because, if one has to detect an Earth-like planet in the habitable zone of a star like our Sun then that requires a long-base of observation. Kepler discovered a planet, Kepler 22b, with a 2.4 Earth radii, orbiting within the habitable zone of a solar-like star (Borucki et al. 2012). However, there are several other planetary systems discovered by Kepler, for e.g. Kepler-20 hosting two Earth-sized planets (Fressin et al. 2012), Kepler-36b a super-Earth system with an interior structure similar to Earth (Futó 2013), etc..

CoRoT

Convection **R**otation and planetary **T**ransits (CoRoT) was launched in 2006, with the primary goals of studying stars through asteroseismology and detecting transiting planets (Auvergne et al. 2009). During an observing run, nearly 12 000 stars can be simultaneously and continuously monitored over ~ 150 days. CoRoT is thus particularly well-suited to detecting planets with orbital periods shorter than 50 days. The first planet discovered by CoRoT in its initial run of observation is the CoRoT-Exo-1b, which was found around a G0V star of $V=13.6$ (CoRoT-Exo-1) with a period of 1.5 days and a depth of 2%. Several CoRoT planetary system have been discovered. Léger et al. (2009) reported on the detection of the first known transiting super-Earth, CoRoT-7b. CoRoT-7b orbits its host star every 0.85 days, has a mass of ~ 7.4 Earth masses, and a semi-major axis of 0.017 AU (Hatzes et al. 2011). Additionally, CoRoT-7 host yet another super-Earth (CoRoT-7c) with roughly twice the mass of CoRoT-7b and an orbital period of 3.7 days.

2.3.2 Ground-based surveys

MEarth

The MEarth project is a ground based project targeting typically mid-to-late M dwarfs using 40 cm robotic telescopes to perform photometric surveys. MEarth has been operational since

2008, with eight telescopes on Mt. Hopkins, Arizona. MEarth is expected to be sensitive to planets as small as 2 Earth radii with a period as long as 20 days (Nutzman & Charbonneau 2008). A transiting super-Earth system, GJ 1214 b, around a low mass M star, was discovered by MEarth survey.

The HARPS search of southern extrasolar planets

The HARPS search of southern extrasolar planets is a radial velocity survey performed with the HARPS spectrograph, which is mounted on the 3.6m ESO's telescope in La Silla (Mayor et al. 2003). It has discovered more than 150 exoplanets (January 2013), most of these planets are in the super-Earth mass range. (Mayor et al. 2011). For e.g., the multiple planet system with at least three super-Earths orbiting a M dwarf (GJ 581) was discovered by the precise radial velocity measurement using the HARPS survey (Udry et al. 2007*b*). Yet another multiple system with three super-Earths orbiting the K star HD 40307 was also discovered during HARPS monitoring (Mayor et al. 2009*b*). HARPS has been monitoring about 850 nearby solar-type stars since the beginning of the survey with RV precision of 1 ms^{-1} to detect low mass planets in the super-Earth regime.

CARMENES

CARMENES (Calar Alto high-Resolution search for M dwarfs with exo-Earths with Near-infrared and optical Echelle Spectrograph) is a next generation instrument built for 3.5m telescope at Calar Alto observatory. Its objective is finding habitable exoplanets around M dwarfs through radial velocity measurements (m/s level) in the near-infrared. CARMENES will conduct a five-year exoplanet survey targeting ~ 300 M dwarfs in solar neighbourhood (for detailed description on CARMENES see Chapter 4). CARMENES is expected to see its first light in 2014.

Chapter 3

Aim and outline of the thesis

Although magnetic activity has been observed and investigated for decades, the exact mechanism controlling the magnetic activity in the low mass stars are still not understood. Understanding magnetic activity of the low mass stars helps to place our Solar System in context with other planet host system. It illustrates the extent to which our Sun represents other stars and constraining whether majority of stars in the solar-neighbourhood are expected to host Earth-like habitable planet. There are several open questions associated with the magnetic activity in low mass stars, such as, what kind of magnetic dynamo operate in low mass stars, how does the heating of corona take place, what is the role of small-scale energy release events in heating of corona and how do they propagate, these are a few of the important questions that need to still be answered. Some of these outstanding questions concerning the coronal and the chromospheric activity are addressed in this thesis.

CARMENES

Chapter 4 deals with the activity characterisation of potential planet host stars for an upcoming planet search program — CARMENES (Calar Alto high-Resolution search for M dwarfs with Exo-Earths with a Near-infrared Echelle Spectrograph). CARMENES is optimised for the search for Earth-like planets around M stars and will carry out high precision radial velocity measurements of a sample these stars.

M dwarfs are faint stars, emitting the maximum of their radiation in the infrared and are intrinsically active. For planet search programs

using the radial velocity method, the effect of stellar activity on the spectral lines complicates the detection of planets. Hence to optimise the scientific return from CARMENES, a careful analysis of the target prior to the survey has to be carried out.

For activity characterisation the coronal fluxes of the CARMENES target stars are obtained based on the observations carried out by the ROSAT all-sky survey (RASS). About 30% of the stars from the CARMENES sample list were detected and for those stars not detected by RASS an upper-limit coronal flux is estimated. The distribution of the X-ray emitting plasma reveals the coronal characteristics of each of the target stars. Nearly 200 stars of the detected sample are active and are not suitable for CARMENES. Hence these stars were excluded from the CARMENES target sample.

Flares in low mass stars

Beside being strong X-ray source, low mass stars are capable of producing strong flares of short as well as long durations. They can show flares at a rate of several flares per hour. As the most numerous of potential planet hosts, it is essential to understand the properties of the flaring plasma, the associated energetics and the frequency of occurrence of such events. Since continued flaring activity can hinder the continuity of habitability.

Chapter 5 deals with the results obtained from our multi-wavelength campaign designed to cover the coronal and the chromospheric properties of two potential planet hosts Proxima Centauri and AB Doradus A by simultaneous observations in X-ray and optical

regime. Information from other wavelengths are used to understand in detail the propagation of energy release events through all layers of the stellar atmosphere.

Characteristics of flares on AB Dor A

The strong similarities between the solar flares, the low mass flare stars and the larger, brighter flare stars in stellar associations have baffled for many years. Using the Sun as an example one may explain the activity in low mass stars by comparing their properties.

In Chapter 6, I give a detailed investigation of the characteristics of the flares observed on AB Dor A over the last decade using observations carried out by *XMM-Newton*. The resulting flare properties are compared with solar flare properties and a common scaling law for each of the parameter is obtained. Despite the fact that the stellar flare emission measures is ~ 250 times higher than the solar flares they follow a common scaling law.

Many stellar flares release an energy of $E \sim 10^{34}$ erg, whereas the most energetic solar flare have $E \sim 10^{32}$ erg. The more energetic flares observed on low mass stars may suggest a different dynamo action from that in the Sun. In Chapter 6, I also present an analysis of the AB Dor A flare energetics. This dataset allows some interesting insight into the flare energies which suggests that the flare initiation in AB Dor A may be similar to that of the Sun.

A solar-like magnetic activity cycle on the active ultra-fast rotator AB Dor A?

An activity cycle analogous to the 11 year solar activity cycle has been found in CaII H and K emission lines for many stars in the Mt. Wilson project (Baliunas et al. 1995). However, coronal activity cycle are known for only a handful of samples since we lack X-ray data covering the typical activity cycle time scales of several years. For an ultra-fast rotator AB Dor A ($P_{\star} = 0.5\text{d}$), an activity cycle of 20 years has been derived from the optical V-band observations (Järvinen et al. 2005). In Chapter 7, I present a detailed analysis of AB Dor A's

coronal activity and its correlation with the optical brightness. The compiled observations in optical and X-rays of AB Dor A suggests a cyclic behaviour of activity. It is evident from the analysis that the X-ray luminosity of AB Dor A is indeed correlated to photospheric brightness variations. However, AB Dor A lacks high amplitude variations in X-rays during the expected activity maximum which supports the concept that AB Dor A posses a saturated coronae.

In chapter 8, I summarise my work. Additionally a short outlook into future possible work is given which includes some of my ongoing projects.

Part II

Scientific Contributions

Chapter 4

CARMENES

CARMENES, Calar Alto high-Resolution search for M dwarfs with Exo-earths with a Near-infrared Echelle Spectrograph, is a next generation instrument built for the 3.5 m Calar Alto Telescope, operated by a consortium of German and Spanish institutions. The main goal of CARMENES is finding habitable Earth-like planets around M dwarfs, using high-precision radial velocity measurements (1 ms^{-1}) in the near-infrared wavelength range, where M dwarfs emit the bulk of their radiation (Amado et al. 2012). CARMENES will carry out a survey of a sample of 300 M stars in search of low mass planetary companion over 600 nights. This survey will provide a good statistics of planets around M stars, especially on their frequency, masses and orbital parameters.

4.1 The instrument

The CARMENES instrument consists of two cross-dispersed échelle spectrographs covering both the visible ($0.53\text{-}1.05 \mu\text{m}$) and the near-infrared (0.95 to $1.7\mu\text{m}$) wavelengths at a spectral resolution of $R \approx 82\,000$. The spectrograph will be fibre-fed from the Cassegrain focus of the 3.5 m Calar Alto telescope. It will be located inside the temperature-stabilised vacuum chamber to enable a high-precision radial velocity measurement of 1 ms^{-1} (Quirrenbach et al. 2012). The wavelength calibration is one of the limiting factors for reaching RV-precision of $\sim 1 \text{ ms}^{-1}$. Thorium-argon lamps, the most successful calibration method, cannot be used in near-infrared with the same efficiency as in optical. Due to the smaller number of Thorium lines in the infrared wavelength, an alterna-

tive method, a Fabry-Perot interferometer illuminated by white light will be used for wavelength calibration (Schäfer & Reiners 2012). The advantage of a Fabry-Perot interferometer is its extremely high-resolution combined with multichannel spectrometer for measuring high-precision radial velocity variation.

4.2 How is CARMENES different from other survey?

The overall goal of CARMENES is to perform high-precision radial velocity measurements with long-term stability. The difference between CARMENES and previous surveys in search of Earth-like planets can be attributed as follows:

- So far, radial velocity surveys in search of Earth-like planets have mainly concentrated on Sun-like stars, whereas, CARMENES survey will concentrate on low mass stars mainly the M stars (for a detailed argument on why M stars see 4.3).
- CARMENES will be able to acquire data simultaneously in both optical and near-infrared wavelengths. Any activity induced velocity variation is expected to be wavelength dependent, however, this is not the case for orbital variation. Hence the concept of a dual-channel spectrograph will provide an opportunity to differentiate an activity induced period from the orbital variations.
- High-resolution as well as wide spectral coverage can be achieved.

- Since the monitoring will be for five years, this provides a guaranteed long time at the telescope, the characterisation of planets around M stars should be possible.

4.3 M dwarfs as host stars

M stars are much fainter, lighter and smaller than our very own host, the Sun. In fact none of the M dwarf is bright enough to be seen through naked eye. However, nearly 70% of the stars in our Galaxy comprise of M dwarfs making them the most common stars in the solar neighbourhood, in-turn, making them the most frequent planet hosts (Henry et al. 2004).

Due to extremely low luminosities the habitable zone around M dwarfs moves closer to the star (see Fig. 2.1). This means that habitable planets around M dwarfs produce a large radial velocity signal compared to a star like the Sun, since the semi-amplitude (K) of the radial velocity signal is given by

$$K = \left(\frac{2\pi G}{P_{orb}} \right)^{\frac{1}{3}} \frac{M_p \sin i}{(M_\star + M_p)^{\frac{2}{3}}} \frac{1}{\sqrt{1-e^2}}, \quad (4.1)$$

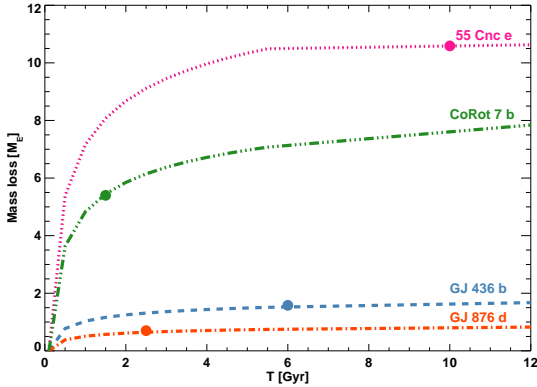


Figure 4.1: Evolution of mass loss for the detected super-Earths as a function of time. Plotted as thick point is the current age of the super-Earth systems.

where P_{orb} is the orbital period of the planet, M_\star and M_p are the masses of the host star and the orbiting planet, e is the eccentricity and i is the angle of inclination between the orbital plane and the line of sight. From the

above equation it is clear that the mass of the star and the radial velocity are inversely proportional. In other words, the lighter the star, the larger the radial velocity signal and vice versa. In the case of the Solar System, Jupiter produces a radial velocity signal of 12.4 ms^{-1} , whereas Saturn and Earth produce a signal of 2.8 ms^{-1} and 0.09 ms^{-1} , respectively. Assuming an super-Earth of a mass of $6 M_\oplus$ orbiting a star of a mass of $0.3 M_\odot$, the expected changes in the radial velocity of the star is calculated to be 3.2 ms^{-1} . As can be seen from Eqn. 4.1, for a given planet mass, the radial velocity amplitude increases with decreasing stellar mass. Hence M dwarfs are excellent targets for high-precision radial velocity planet search programs. Due to their lower primary mass, detection of very low mass planets is easier.

Despite the above mentioned properties of M dwarfs, they are not searched for planets as extensively as solar-like stars. This is mainly because of their low brightness in the optical, where most of the radial velocity searches are conducted. There are two major issues when we consider M dwarfs as potential exo-Earth hosts:

4.3.1 Hazardous M dwarfs

Due to intrinsically low luminosities of M dwarfs, habitable zones around them lie very close to the star ($\sim 0.2 \text{ AU}$ or less), making planets around these stars especially vulnerable to the effects of stellar activity (see Fig. 2.1). As pointed out by Lammer et al. (2003), the stellar X-ray and UV fluxes strongly determine the amount of gas lost from the outer atmospheres of close in exoplanets.

In the picture of energy-limited hydrodynamic mass-loss (Sanz-Forcada et al. 2010), the mass-loss rate, \dot{M} of a planet amounts to

$$\dot{M} = \frac{\pi R_p^3 \epsilon F_{XUV}}{G K M_p}, \quad (4.2)$$

where R_p is the planetary radius, F_{XUV} is the incident X-ray and UV flux, ϵ is the heating efficiency, G is the gravitational constant, M_p the mass of the planet, and K is a parameter

accounting for Roche-lobe filling. According to Valencia et al. (2010), the above expression remains valid even for strongly irradiated rocky planets, because the atmosphere is replenished by sublimation faster than it erodes. In the calculation below I assumed $\epsilon = 0.4$ as suggested by Valencia et al. (2010).

Figure 4.1 shows the mass-loss history of some of the well-studied super-Earths (CoRoT-7b, GJ 876d, GJ 436b, 55 Cnc e) derived using Eq. 4.2. To determine the incident X-ray and UV-flux I assumed the following relation between X-ray and UV flux (Sanz-Forcada et al. 2011):

$$\log L_{\text{EUV}} = (0.860 \pm 0.073) \log L_x + (4.80 \pm 1.99). \quad (4.3)$$

I assume that the XUV luminosity increases at young stellar ages by a factor $(\tau/\tau_\star)^{-1.23}$, where τ is the young stellar age when the stellar activity remains at a constant level (0.1 Gyr) and τ_\star is the current stellar age in Gyr (Ribas et al. 2005). Inserting the time variable XUV flux into Eq. 4.2 and integrating over current age of the system yields a total mass loss. The circle for each of the planet in Fig. 4.1 indicates the current age of the system. From Fig. 4.1 it is clear that UV/X-ray flux from the star must have evaporated substantial part of the mass of CoRoT-7b and 55 Cnc e in the past.

Further, stellar activity is also a concern for continuity of the habitability since active stars are known to flare at rates of several per hour (Gershberg 1989; Kowalski et al. 2009). Stellar flares can lead to coronal mass ejection and stellar winds which can compress the magnetosphere of Earth-like planets inside the close-in habitable zone, as well as affect the atmosphere and make it unstable (Fig. 4.2).

In addition, for a planet to remain within the habitable zone, it would have to orbit so close that tidal forces raised on the planet would cause the same hemisphere of the planet face the star all the time. As a result of this tidal locking, there would be no day-night cycle, and the planet's atmosphere on the dark side of the planet would freeze unless it is sufficiently thick or if there is strong wind associated with the planet similar to that of Jupiter in our Solar

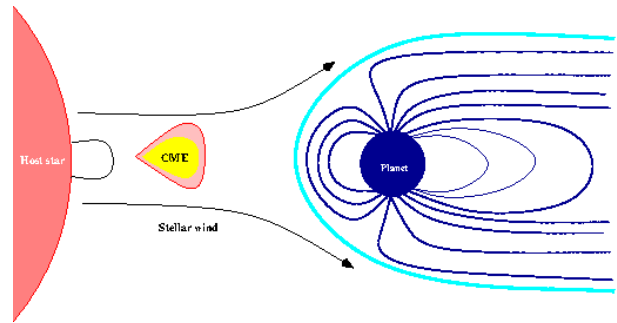


Figure 4.2: Schematic representation of Earth's magnetosphere. The shape of the magnetosphere is highly influenced by the solar activity. Image credit: Lalitha Sairam

System. This tidal locking results in an absence of the plate tectonics and presence of super-volcanoes that may affect the long-term habitability of the planet (Courillot 2002).

4.3.2 Observational difficulties

The radial velocity method of planet detection relies on measuring the parent star's orbital reflex motion which is typical of order of few ms^{-1} depending on the mass of the system. Such a shift may be imposed by either real velocity variations induced by an orbiting companion or by a cool spot on the surface of the star. An active region on the stellar surface can influence the line profile of stars introducing high noise levels or they may be misinterpreted as a RV variation due to the presence of a planetary companion (see Fig. 4.3). An active region on the surface of a star can cause radial velocity variations above 1 ms^{-1} depending on the surface velocity of a rotating star (Desort et al. 2007).

An important obstacle in detecting a low mass, long period planet may be a possible stellar magnetic cycle on similar time scales. Hence it is essential to characterise the activity properties of these low mass stars to disentangle RV variations due to spots and other stellar activity effects from the presence of planetary companions.

The influence of the active regions on the spectra of M dwarfs have not been studied systematically. However, Kürster et al. (2003) found an anti-correlation between the radial ve-

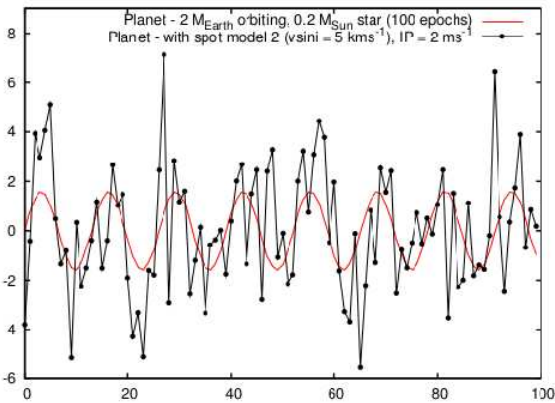


Figure 4.3: Simulated stellar radial velocity curve for a 2 Earth mass planet orbiting a M dwarf host (in red). Plotted in black is the radial velocity curve with added jitter due to starspots. Image credit: Barnes et al. (2011)

locity and the strength of the $H\alpha$ emission line in an inactive M dwarf. This raises the question to what extent is the influence of activity on detecting radial velocity variation induced by the orbiting planet. Reiners (2009) found that a moderate flare can cause a radial velocity jitter of $< 10 \text{ ms}^{-1}$. Further, he noticed that strong flares are easily recognisable from the spectra and those spectra affected by a flare should be neglected for planet searches. Hence flares on active M stars may not pose a substantial problem to radial velocity measurements. However, a co-rotating active region does have a strong influence on the precise radial velocity measurements.

4.4 Survey strategy & sample selection

CARMENES will carry out a survey for 5 years, during which selected 300 stars in the solar vicinity, lying just within 50 pc from the Sun, will be monitored. Given the final target sample of 300 stars, it is necessary to have to start with a larger list (in this case we start with ~ 1000 stars) and filter out those objects not suitable for high-precision radial velocity measurement. These non-suitable stars include the fast rotators, close binaries, very active stars,

etc..

The target list is based on the Palomar/Michigan state university (PMSU) catalogue (Reid et al. 1995, Hawley et al. 1996). Due to the limiting instrument magnitude and observation site, stars with $J > 11.5$ mag and $\delta < -23^\circ$ (i.e., zenith distance $> 60^\circ$) are discarded. Currently the CARMENES list consists of ~ 1000 objects and I will refer to them as pre-CARMENES target list in the following sections. To optimize the scientific return from CARMENES, a careful analysis of the stars prior to final selection has to be carried out to find the best suited objects. This includes the characterisation of the stellar properties, such as magnitudes, colours, luminosities, effective temperatures, projected rotational velocities, masses and radii, as well as activity properties such as chromospheric and coronal fluxes and photometric modulations. This characterisation of the stars helps to eliminate as many stars as possible that are not suited for high-precision RV work before the regular observations with CARMENES.

4.5 Activity characterisation

Magnetic activity strongly depends on the spectral type and the age of the stars (Reiners 2007; Reiners & Basri 2008, 2010). Solar chromospheric activity is traced mostly by Ca II H & K emission lines, Mg II and $H\alpha$, whereas, on low mass stars like M dwarfs activity can be traced by Balmer emission. In contrast to the Sun, Ca II H & K emission lines are not normally used in M dwarfs because these stars are so faint at that wavelength that it requires large telescopes for observation. However M dwarfs being intrinsically bright in the red, the $H\alpha$ line at 656.28 nm has become a primary diagnostic to trace chromospheric activity.

4.5.1 $H\alpha$ activity

The strength of activity can be characterised by the ratio of luminosity emitted in $H\alpha$ to bolometric luminosity ($L_{H\alpha}/L_{bol}$). The strength of activity varies as a function of spectral type. Reiners (2007) and Reiners & Basri (2010)

showed that multi-epoch spectral observations of active M dwarfs helps to explain the spread in activity in the M dwarf population and the variation on a single star.

4.5.2 X-ray activity

Studies of active low mass stars in non-optical wavelengths (X-rays, UV and radio emission) show that an enormous amount of energy can be released at these wavelengths. Hence it is necessary to understand the aspect that gives rise to such high energy emission (X-ray and EUV) in low-mass stars. This is particularly important for low-mass stars that host planets, where long duration exposure to high energy photons may significantly affect the atmospheres and habitability of close-orbiting worlds. Therefore, the pre-CARMENES targets are searched for such activity tracers and if a star is found to be substantially active then it is eliminated from the list.

4.6 X-ray activity characterisation of the pre-CARMENES targets

The primary database for X-ray analysis is provided by the ROSAT all-sky survey (RASS) which has produced a complete and unbiased sample of X-ray sources; moreover, I also considered X-ray data from the *XMM-Newton* and *CHANDRA* observatories.

The first six months in its orbit, ROSAT performed an all-sky survey in the 0.1-2.5 keV energy band. During its survey ROSAT discovered more than 120 000 X-ray sources. This all-sky survey is generally called the ROSAT All-Sky Survey (RASS). The RASS is the most complete X-ray scan of the sky to date. The scanning of the sky by RASS was along great circles perpendicular to the plane of the ecliptic. During a given scan, an X-ray source stays in the 2° field of view (FOV) of the ROSAT Position Sensitive Proportional Counter (PSPC) for up to 30 s.

For the analysis, I extracted 40' × 40' regions of the sky from the RASS data centred on the

position of every star in the list. The procedure employed here is the same as in Schmitt et al. (1995). Source detection was run on each of the X-ray images, and all sources found were deleted from the data. The spatial distribution of the remaining photons was fitted to create a background map. An X-ray source is detected by a maximum-likelihood method. For this all events within a 5' radius at the star's optical position are counted, this is done mainly to include all photons from a possible point source. Cross matching this way I identified ~ 30% of pre-CARMENES target stars as X-ray sources.

When no source was found, I calculated the number of counts needed above the background to detect a source with 95.6% (i.e. 2σ) probability, given the number of background counts expected in the extraction radius and the point spread function (PSF). These counts/upper limits are divided by the corrected exposure time from the exposure map at the position of the star in order to get the PSPC count rate / 2σ upper limit on the PSPC count rate. A conversion factor of 6×10^{-12} ergs cm⁻² counts⁻¹ was multiplied by the count rates to obtain the X-ray fluxes (Schmitt & Liefke 2004). Using the X-ray fluxes (F_x) and distances (d in pc) the X-ray luminosities are calculated ($L_x = 4\pi d^2 F_x$). For the determination of the X-ray luminosity the distance measurement plays an important role. The distance is calculated using the mean of the Hipparcos trigonometric parallax and the spectro-photometric parallax.

To characterise the strength of activity, I define a ratio of luminosity emitted in the X-ray to bolometric luminosity (L_x/L_{bol}). The bolometric corrected luminosity can be calculated using the following equation

$$L_{bol} = 10^{0.4(4.8 - m_v - bc + 5 \log(d) - 5)} L_{\odot}, \quad (4.4)$$

where m_v is the apparent visual magnitude, bc is the bolometric correction, d is the distance in parsec and L_{\odot} is the solar bolometric luminosity. Apparent magnitudes are obtained from the pre-CARMENES input list and the bolometric corrections are determined using Worthey & Lee (2011).

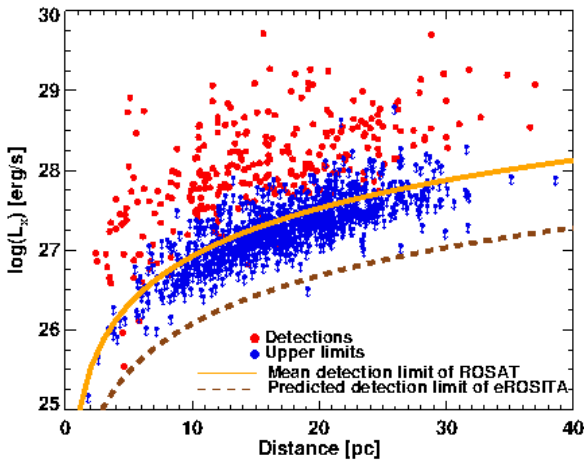


Figure 4.4: The X-ray luminosity of detected sources (red) and upper limits (blue) estimates for non-detections of the pre-CARMENES target sample plotted as a function of distance. Plotted as orange thick line is the mean limiting sensitivity achieved with ROSAT and as brown dashed line is the predicted detection limit of eROSITA.

4.7 Results

In order to investigate the X-ray properties of the pre-CARMENES target stars, I turn my attention to the observed X-ray luminosities and their relation to other stellar parameters of the program stars.

4.7.1 X-ray luminosities

In Fig. 4.4 I plot the X-ray luminosity (in erg/s) of the pre-CARMENES sample targets as a function of distance (in pc). Detections are represented in red, while non-detections are represented in blue. To avoid multiple marks for an X-ray source observed multiple times by different X-ray missions, only the observation with the longest exposure time was used. Nearly 40% of the pre-CARMENES target stars were detected in the ROSAT survey.

The RASS is a flux-limited all-sky X-ray survey with a mean limiting sensitivity of 7×10^{-14} ergs/s/cm² in the 0.3-2.4 keV pass band (plotted as orange line) corresponding to a mean limiting luminosity of $L_{X, \text{meanlim}} \sim 8.3 \times 10^{24} d_{pc}^2$ ergs/s. Therefore at larger distances only intrinsically brighter X-

ray sources can be detected. Many of those targets not detected by RASS can be detected by the future eROSITA survey according to its predicted detection limit. eROSITA is an X-ray mission to be launched in 2014. The primary aim of eROSITA is to perform an all-sky survey with unprecedented energy and angular resolution. In Fig. 4.4, notice that there are detections below the orange line because the all-sky survey was inhomogeneous, i.e., some parts of the sky were observed longer than others.

In order to see an overview of the X-ray luminosities for the pre-CARMENES sample targets I show in Fig. 4.5 the estimated X-ray luminosities as a function of absolute magnitude (M_v). Note that the median X-ray luminosity is decreasing with increasing absolute magnitude.

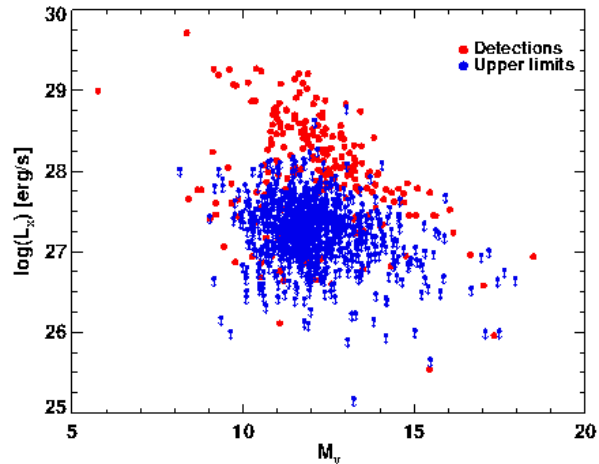


Figure 4.5: Plot of the X-ray luminosity vs absolute magnitude (M_v) for pre-CARMENES sample stars; red dots denote detections and blue dots represents upper limit estimates for non-detection.

All the detected targets with $5 \leq M_v \leq 10$ have X-ray luminosities exceeding $\approx 10^{27}$ ergs/s. For magnitude $10 \leq M_v \leq 15$ the X-ray detections range nearly four orders of magnitude. Furthermore, the faint stars with $M_v > 15$, the luminosities seem to be restricted to 10^{28} ergs/s. Here I note that there are no objects in the upper right corner and the lower left corner of Fig. 4.5 indicating that the pre-CARMENES sample list does not contain super saturated and X-ray dark M dwarfs, respectively.

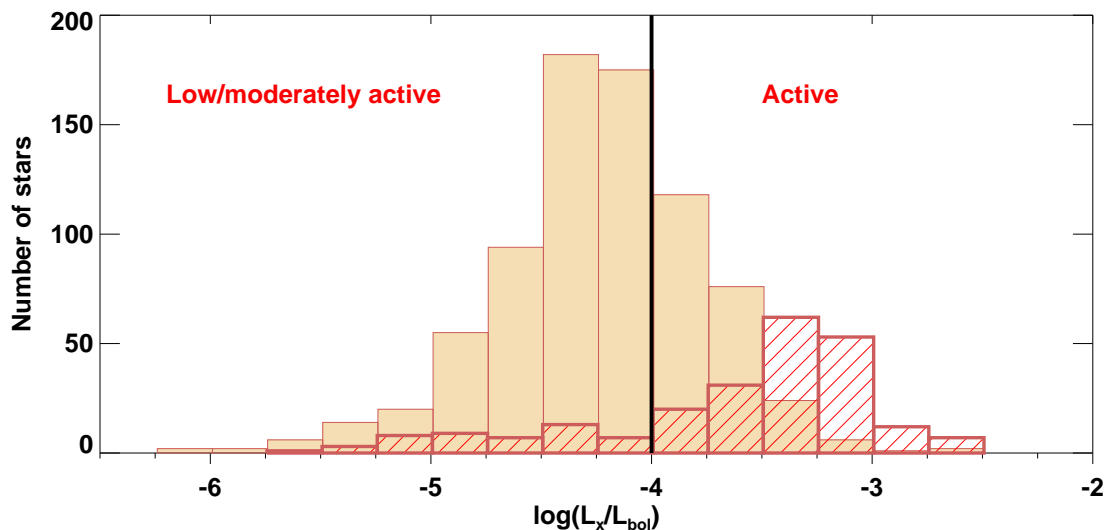


Figure 4.6: The distribution of $\log(L_X/L_{bol})$ for the X-ray detections (red) and the upper limits for non-detections (beige). The black thick line at -4.0 divides our sample into active and moderately active stars.

4.7.2 Coronal activity distribution

In Fig. 4.6 the distribution of $\log(L_X/L_{bol})$ for an X-ray detections and the upper limits for non-detections are plotted. Either there is a detection/ non-detection, I classify all the pre-CARMENES target stars with $\log(L_X/L_{bol}) < -4.0$ as low/moderately active sample. Not surprisingly, the detections are more active stars. Nevertheless, the majority of the detected stars have X-ray luminosities close to the saturation limit of -3; these can be definitely excluded from the pre-CARMENES sample list.

For about 70% of the sample stars from the pre-CARMENES input list, the derived upper limits do not rule out substantial activity. However, some of these upper limit stars may indeed turn out to be inactive. As a next step, these upper limit stars will be characterised based on chromospheric activity. This information will provide efficient tools to make a good selection of the final list of targets.

4.7.3 Chromospheric-coronal activity indicators

As seen earlier the most relevant chromospheric activity indicator is the $H\alpha$ emission in case of M dwarfs. In order to investigate the rela-

tion between coronal and chromospheric activity, I analysed the $\log(L_X/L_{bol})$ and $H\alpha$ equivalent widths of the target sample (plotted in Fig. 4.7).

As expected, large values of $H\alpha$ equivalent width always corresponds to X-ray emission near the saturation level (between -3 and -4). However, even for smaller values of the $H\alpha$ equivalent width, high levels of X-ray emission are encountered.

4.8 Discussion of preliminary results

The precise determination of properties of stars is important both to select the best planet-host candidates and to derive the properties of the exoplanets they may host. The objective of the work presented in this chapter is to characterise the activity properties of the M dwarf input list for the CARMENES survey. The characterisation of the coronal fluxes was carried out on sample of stars from pre-CARMENES target list. Nearly 30% (~ 300 stars) of the targets are detected; for non-detection (70% of the stars) an upper-limit X-ray flux was estimated.

Out of the 300 X-ray sources, nearly

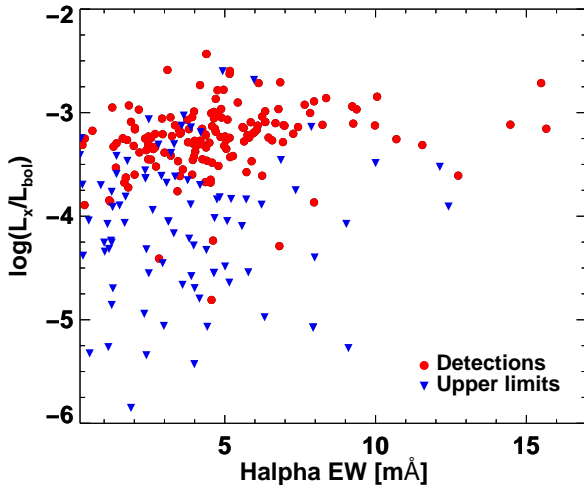


Figure 4.7: To understand the relation between chromospheric and coronal activity, $\log(L_X/L_{bol})$ and the $H\alpha$ equivalent width are plotted. The red circles indicate the detections in X-rays and the blue upside-down triangles indicate the upper-limit sample.

200 stars were found to be active with $\log(L_X/L_{bol}) > -4$ which will be dropped out of CARMENES sample list. Additionally, ~ 250 upper-limit sources were also found to have $\log(L_X/L_{bol}) > -4$, however, they may turn out to be inactive when detected. Hence activity characterisation of these poorly known stars can be approached alternatively by carrying out a systematic investigation of stellar chromospheric activity levels from various indicators. These chromospheric observations will allow the optimisation of the final list of potential planet hosts, which is to be observed with next generation spectrograph (CARMENES).

Chapter 5

Flares in low mass stars

In the following chapter, I reproduce a publication on Proxima Centauri (Fuhrmeister et al. 2011), which have been published in *Astronomy & Astrophysics* and a publication on AB Doradus A (Lalitha et al. 2013), which is submitted for publication in the same journal. Both these publications focus on the activity in low mass stars mainly focussing on multi-wavelength view of flares.

As each paper in this chapter lists several authors, I will provide an overview of my significant contribution.

5.1 My contribution

Proxima Centauri, the member of is the nearest neighbour to our Solar system with spectral type dM5e, is a well known example of optical flare star with substantial X-ray emission even in quiescent state (Haisch et al. 1978). This makes Proxima Centauri and ideal target to build an overall picture of the atmosphere from the chromosphere to the corona.

The publication reproduced in Sect. 5.2 (Fuhrmeister et al. 2011) of this thesis is based on the observational data obtained by Caroline Liefke using the *XMM-Newton* and the UVES spectrograph at Very Large Telescope (VLT) simultaneously. Section 5.2 in this chapter is the result of a collaborative work. Birgit Fuhrmeister reduced and analysed the VLT/UVES data (the optical data). I and Katja Popenhaeger reduced and analysed the X-ray and UV data obtained from the *XMM-Newton* observations. Natascha Rudolf analysed the optical data to investigate the magnetic field.

I analysed the simultaneous X-ray and op-

tical data covering a large flare and two small events on the active M dwarf Proxima Centauri with regard to the plasma properties in the corona and the geometry of the flaring structure. The temperature and density are enhanced by more than an order of magnitude compared to the quiescent corona at the flare peak, as expected from other events of similar strength observed in X-rays.

My main contribution is the analysis of the X-ray data to investigate the temporal variations and the spectral variations associated with flaring activity. I wrote the corresponding results in §3 and §4 of the paper and contributed to results and discussion to connect the flare in chromosphere and in coronae in §6. All results were reached in close co-operation with my supervisor Jürgen Schmitt.

The publication reproduced in Sect. 5.3 of this thesis (Lalitha et al. 2013) are based on the simultaneous multi-wavelength observations of AB Dor A obtained by Uwe Wolter, using the *XMM-Newton*, the UVES spectrograph at the Very Large Telescope and the Australia Telescope Compact Array. AB Dor A is an ultra-fast rotating late-type star. The observations were carried out with an intention to study highly time-resolved correlations of coronal, chromospheric and photospheric activity phenomena. This paper is result of a collective work where the major contribution was provided by myself and Birgit Fuhrmeister, again supported by Jürgen Schmitt. I reduced and analysed the X-ray and the UV data that we obtained from observations carried out by *XMM-Newton*.

In addition this project also provided me an opportunity to explore into the field of optical

spectroscopy. My contribution to the optical analysis include equivalent width determination and estimation of the black-body temperature during the flare, which, in-turn was used to determine the optical filling factor. This work helped us to build an overall picture of the atmosphere of AB Dor A from the chromosphere to the corona.

Of course, the other co-authors also provided contribution to the work, which I, nevertheless, will not explain in detail here.

A&A 534, A133 (2011)
 DOI: 10.1051/0004-6361/201117447
 © ESO 2011

**Astronomy
&
Astrophysics**

Multi-wavelength observations of Proxima Centauri^{★,★★}

B. Fuhrmeister¹, S. Lalitha¹, K. Poppenhaeger¹, N. Rudolf¹, C. Liefke^{1,2}, A. Reiners³,
 J. H. M. M. Schmitt¹, and J.-U. Ness⁴

¹ Hamburger Sternwarte, University of Hamburg, Gojenbergsweg 112, 21029 Hamburg, Germany
 e-mail: bfuhrmeister@hs.uni-hamburg.de

² Zentrum für Astronomie, Mönchhofstraße 12-14, 69120 Heidelberg, Germany

³ Institute of Astrophysics, University of Göttingen, Friedrich-Hund-Platz 1, 37077 Göttingen, Germany

⁴ XMM-Newton Science Operations Centre, European Space Agency (ESA/ESAC), 28691 Villanueva de la Cañada, Madrid, Spain

Received 9 June 2011 / Accepted 18 August 2011

ABSTRACT

Aims. We report simultaneous observations of the nearby flare star Proxima Centauri with VLT/UVES and *XMM-Newton* over three nights in March 2009. Our optical and X-ray observations cover the star's quiescent state, as well as its flaring activity and allow us to probe the stellar atmospheric conditions from the photosphere into the chromosphere, and then the corona during its different activity stages.

Methods. Using the X-ray data, we investigate variations in coronal densities and abundances and infer loop properties for an intermediate-sized flare. The optical data are used to investigate the magnetic field and its possible variability, to construct an emission line list for the chromosphere, and use certain emission lines to construct physical models of Proxima Centauri's chromosphere.

Results. We report the discovery of a weak optical forbidden Fe XIII line at 3388 Å during the more active states of Proxima Centauri. For the intermediate flare, we find two secondary flare events that may originate in neighbouring loops, and discuss the line asymmetries observed during this flare in H I, He I, and Ca II lines. The high time-resolution in the H α line highlights strong temporal variations in the observed line asymmetries, which re-appear during a secondary flare event. We also present theoretical modelling with the stellar atmosphere code PHOENIX to construct flaring chromospheric models.

Key words. stars: activity – stars: magnetic field – stars: chromospheres – stars: coronae – stars: late-type – stars: individual: Proxima Centauri

1. Introduction

Coronal heating of cool stars is thought to be driven by magnetic fields generated in the stellar convection zones. For stars from spectral type F to mid-M, the magnetic field production process can be modelled with an $\alpha\Omega$ dynamo (Parker 1955). However, stars of spectral type M3 or later are fully convective (Chabrier & Baraffe 1997; Dorman et al. 1989) and are not expected to undergo the same dynamo process as earlier-type stars (Browning 2008). Other processes such as turbulent or α^2 dynamos should not be as effective as the $\alpha\Omega$ dynamo and, indeed, many late M dwarfs have rather low X-ray luminosities in their states of quiescence (Robrade & Schmitt 2005). Nevertheless, the same stars are capable of producing strong flares of short as well as long durations (Stelzer et al. 2006; Robrade et al. 2010), so there must be some mechanism to allow violent releases of large amounts of magnetic energy. Magnetic flux densities are enormous in mid- to late-M stars, providing firm evidence of an efficient mechanism to produce and maintain strong magnetic fields (e.g. Reiners & Basri 2007, 2010). In summary, the magnetic activity processes in late M dwarfs are not yet thoroughly understood in

detail. Multi-wavelength observations cover different activity indicators and can therefore help us to reconstruct a picture of the whole stellar atmosphere. Examples of multi-wavelength observations can be found in e.g. Osten et al. (2005a), Berger et al. (2008), Kowalski et al. (2010a), and Fuhrmeister et al. (2008).

The energy released in flares is thought to originate from the interaction of magnetic fields in the convective zone of the star and photospheric motions that entangle the magnetic loops penetrating the stellar surface. The energy release is triggered by magnetic instabilities that cause the entangled magnetic field lines to reconnect in the corona leading to heating and particle acceleration in the reconnection region. Particles are accelerated downwards into the chromosphere where they collisionally heat the denser plasma, which in turn expands and evaporates into the corona. The coronal loop is filled by dense, hot plasma, which is then observable as a flare in soft X-rays (see e.g. Haisch et al. 1991).

Proxima Centauri, with a distance of only 1.3 pc (van Leeuwen 2007) the star closest to the Sun, is a magnetically active star of spectral type dM5.5. It has been frequently observed by various X-ray satellites: *Einstein* (Haisch et al. 1980), EXOSAT-IUE (Haisch et al. 1983), XTE (Haisch et al. 1998), ROSAT (Voges et al. 1999), ASCA (Haisch et al. 1995), *Chandra* (Wargelin & Drake 2002), and *XMM-Newton* (Güdel et al. 2004). Its quiescent X-ray luminosity varies in the range $L_X \approx (4-16) \times 10^{26}$ erg s⁻¹, which is comparable to that of the Sun despite its 50 times smaller surface area. Over the past 30 years, several X-ray flares of Proxima Centauri have been

* Based on observations collected at the European Southern Observatory, Paranal, Chile, 082.D-0953A and on observations obtained with *XMM-Newton*, an ESA science mission with instruments and contributions directly funded by ESA Member states and NASA.

** Full Table 6 is only available at the CDS via anonymous ftp to cdsarc.u-strasbg.fr (130.79.128.5) or via <http://cdsarc.u-strasbg.fr/viz-bin/qcat?J/A+A/534/A133>

A&A 534, A133 (2011)

observed, with the most extreme peak luminosities observed in a 2001 *XMM-Newton* observation (Güdel et al. 2004), which exceeded typical quiescent state X-ray fluxes by a factor of ≈ 100 . Here we present new data for Proxima Centauri's coronal and chromospheric properties, together with simultaneous measurements of its large-scale magnetic field strength.

Our paper is structured as follows. In Sect. 2, we describe our observations obtained with VLT/UVES and *XMM-Newton*. In Sect. 3, we compare the timing behaviour of Proxima Centauri in different wavelength bands. The coronal properties of Proxima Centauri such as temperatures and elemental abundances are presented in Sect. 4, while Sect. 5 describes the chromospheric and transition region properties of the star. Sections 6 and 7 contain a discussion of the presented findings and our conclusions.

2. Observations and data analysis

The multi-wavelength observations reported in this paper were obtained strictly simultaneously with *XMM-Newton* and ESO's Kueryn telescope equipped with the Ultraviolet-Visual Echelle Spectrograph (UVES) on 9, 11, and 13 March 2009 (labelled “night 1”, “night 2” and “night 3” in the following; see also Table 1). Due to the proximity of Proxima Centauri, interstellar absorption is negligible for the optical as well as for the X-ray data.

2.1. Optical UVES data

For our optical observations, the UVES spectrograph was operated in a dichroic mode leading to a spectral coverage from about 3290 Å to 4500 Å in the blue arm and 6400 Å to 10 080 Å in the red arm with a small gap from 8190 Å to 8400 Å caused by the CCD mosaic¹. For the red arm, a non-standard setup was used to ensure coverage of the H α line. We used exposure times varying from 1000 to 1800 s for the blue arm and of 90 to 450 s in the red arm due to variable seeing conditions. In the blue arm, we obtained 24, 17, and 15 useful spectra during the three nights and in the red arm 215, 168, and 179 useful spectra, respectively. The typical resolution of our spectra is $\sim 45\,000$. The red arm spectra were reduced using the UVES pipeline vers. 4.3.0 (Ballester et al. 2000)². The blue arm spectra could not be properly reduced with the pipeline software but had to be reduced manually using the IDL reduction software REDUCE (Piskunov & Valenti 2002) for several reasons. To obtain a simultaneous coverage with *XMM-Newton*, the star had to be observed at rather high airmass starting with a maximum of 2.4. Since the positioning of the star was accomplished with the red arm, a wider slit had to be used for the blue spectra, which resulted in an overlap of the bluest spectral orders. Therefore no dark exposure could be acquired and the flat-field and science spectra extraction had to be carried out with a fixed width and without scattered light. To complicate the spectral reduction even more, quite a number of spectra are contaminated by solar stray-light (from the Moon), which is outshone by the star in the red part of the spectrum but can be clearly recognised in the blue part of the spectrum.

The wavelength calibration in the blue arm was carried out with thorium-argon spectra with an accuracy of ~ 0.04 Å. Since the weather conditions and especially the seeing varied throughout the nights, no absolute flux calibration with a standard star

could be performed. To obtain an a posteriori flux calibration, we used synthetic stellar spectra provided by the stellar atmosphere program PHOENIX (Hauschildt et al. 1999). We determined the best-fit stellar model using a grid with T_{eff} varying from 2700 K to 3400 K in steps of 100 K and $\log g$ of 4.5, 5.0, and 5.5 and found that model to have $T_{\text{eff}} = 3100$ K and $\log g = 5.5$ in good agreement with the values derived by Demory et al. (2009), who had derived $T_{\text{eff}} = 3098 \pm 56$ K and $\log g = 5.2$ using the VLTI. For the blue spectra, only data at wavelength redward of 4000 Å were used for the calibration since at short wavelengths the data are dominated by chromospheric emission and thus the model spectra are unreliable. We estimate that our errors in the flux calibration in the blue band are about a factor of two. A comparison with a flux-calibrated spectrum of Proxima Centauri acquired by Cincunegui et al. (2007) and Cincunegui & Mauas (2004) shows that our fluxes are higher by about a factor of two for the blue band and by a factor of two to three in the red band. Since these authors used a standard star and low resolution spectra for their flux calibration, the main source of error in our calibration seems to be the model spectrum.

In addition to the spectral data, we obtained a blue and a red light curve using the UVES exposure-meters, i.e., one blue and red photometer located in the two arms of the spectrograph. These data are normally obtained for engineering purposes only and are not flux calibrated. We note that the flux bands of the exposure-meters are not identical to the spectral bands, the blue flux band in particular being “redder” than the blue spectrum.

2.2. X-ray data

Each of our VLT observations was accompanied by three simultaneous 30 ks observations conducted with *XMM-Newton*; the exact observation times with the ObsIDs being given in Table 1. On board *XMM-Newton*, there are three telescopes focusing X-rays onto three CCD cameras (one PN and two metal oxide semi-conductor (MOS) cameras with a sensitivity range of ≈ 0.2 –15 keV), which together form the European Photon Imaging Camera (EPIC). The X-ray telescopes with the MOS detectors are also equipped with reflection gratings. The two RGS (Reflection Grating Spectrometers) provide high-resolution X-ray spectroscopy ($E/\Delta E \approx 200$ –800) in the energy range of 0.35–2.5 keV capable of resolving individual X-ray emission lines. The X-ray instruments are accompanied by the Optical Monitor (OM), an optical/UV telescope that can be used with different filters for imaging and time-resolved photometry. Useful data of Proxima Centauri were obtained with the OM, EPIC, and RGS detectors, which were all operated simultaneously. The PN and MOS detectors were operated with the medium filter in full frame and large window mode, respectively. The OM was operated in fast mode with 0.5 s cadence using the *U* band filter covering a band pass of 300–390 nm.

All *XMM-Newton* data were reduced using the standard *XMM-Newton* Science Analysis System (SAS) software, version 10.0. The EPIC light curves and spectra were obtained using standard filtering criteria. We adopted an extraction radius of 15'' centred on the source; for background subtraction we used nearby source-free areas. Source counts with energies in the energy range 0.2–10 keV were considered for the scientific analysis. For the first two nights, the X-ray observations displayed only a low background level. During the third night, short phases with high background levels were present; these time intervals were excluded from our spectral analysis. The X-ray light

¹ A detailed description of the UVES spectrograph is available at <http://www.eso.org/instruments/uves/doc/>

² The UVES pipeline manual can be found at <ftp://ftp.eso.org/pub/dfs/pipelines/uves-cpl/uves-pipeline-manual-13.0.pdf>

B. Fuhrmeister et al.: Multi-wavelength observations of Proxima Centauri

Table 1. The three *XMM-Newton* observations of Proxima Centauri in March 2009.

ObsID	Start time	Duration (ks)	Label
0551120301	2009-03-10 02:23:34	28.7	night 1
0551120201	2009-03-12 02:11:19	30.7	night 2
0551120401	2009-03-14 02:20:45	28.7	night 3

curves are background-subtracted and binned by 100 s unless stated otherwise.

Spectral analysis was carried out with Xspec V12.5.0 (Arnaud 1996) for the overall fitting processes and CORA (Ness & Wichmann 2002) for fitting of individual spectral lines. For the overall analysis in Xspec, we used models with several temperature components assuming the same elemental abundance for each component. These models are based on a collisionally ionised optically thin gas calculated with the APEC code (Smith et al. 2001). Abundances are calculated relative to the solar photospheric values given by Grevesse & Sauval (1998).

3. Multi-wavelength timing behaviour

In Figs. 1–3, we present the background-subtracted X-ray light curves (taken with EPIC-PN) and the OM *U*-band light curve for our three Proxima Centauri observations, as well as the optical UVES blue-band flux and several chromospheric line fluxes; the X-ray light curves are binned in units of 100 s, and data for the OM in units of 10 s, while the UVES exposure-meter data are binned in units of 5 s.

3.1. Quiescence and small flares

In the optical (UVES exposure-meter and in the OM), flaring state and quiescent phases can easily be identified even for smaller flares. For the chromospheric emission line light curves and the X-ray light curves this is not so easy: the lowest parts of the X-ray light curve – as seen in Figs. 1–3 – show a typical count rate of ≈ 1 cps in the PN detector, comparable to the low count rate states found in the 2001 observations of Proxima Centauri (see Güdel et al. 2002). During these time intervals, the light curves also display some variability, i.e. do not remain constant. To be consistent with other authors, we nevertheless use the term “quiescence” and define it for our subsequent spectral analysis as those times with a PN count rate below 1.8 cps.

In addition to the low-level variability seen during quiescence, small flares are observed at 3:30 and 6:00 UT in the X-ray data from night 1 (see Fig. 1). Similarly, in the X-ray data from night 2 (Fig. 2), which have a slightly higher mean count rate, there is some low-level variation with small flares at about 4:40, 6:15 and 8:40 UT. Most of these flares are also visible in the OM light curves, while the UVES exposure-meter does not show significant variability. Apart from these small flares, the X-ray light curves also show some plateau-like structures and slow rises and decreases not seen in the OM light curve, which displays a constant quiescent level during these times.

Nevertheless, a comparison of the X-ray flux with several chromospheric line fluxes (see Figs. 1 and 2) shows quite good agreement, especially for the $H\alpha$ light curve, which can be studied with the much higher time-resolution of the red arm spectra. For instance, the first $H\alpha$ flare in night 1 at about 3:30 UT can also be identified in the X-ray light curve, although not in the optical (UVES) light curve. In addition, the flare in night 2 at 6:15 UT is found in X-ray, OM, and in the chromospheric

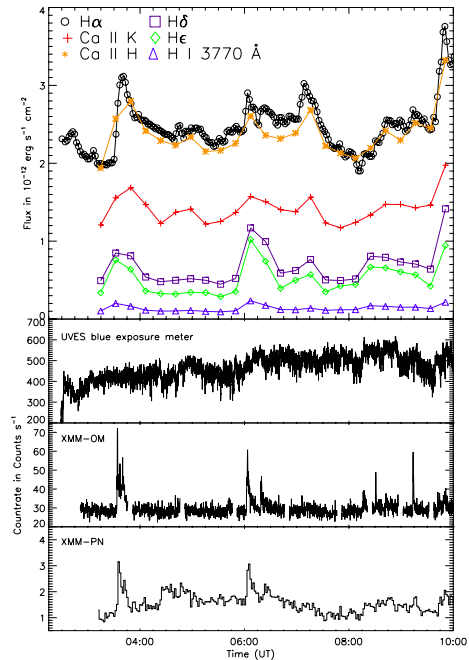


Fig. 1. Light curves of Proxima Centauri from night 1 as seen in the fluxes of characteristic chromospheric emission lines (top, note the better time binning provided by the $H\alpha$ line) as well as optical UVES, OM, and X-ray light curves (bottom).

emission lines, but is much more pronounced in the Ca II H & K line than in the Balmer lines. This shows that the chromospheric emission lines can also be affected by small flares, when the continuum exhibits no changes. Moreover, the chromospheric emission lines exhibit variability that is not seen in the X-ray band, thus should be confined to the chromosphere; for instance, in night 2, during the first two hours, the $H\alpha$ and other chromospheric emission lines display a flux decline, but the X-ray level is constant, and in night 1, the chromospheric lines show a peak at about 7:00 UT that is not noticed in the X-ray or continuum. This behaviour during flares has been found before. Osten et al. (2005b) found at radio, optical, and X-ray wavelengths for the flare star EV Lac flares with no counterparts at other wavelengths. In addition Hilton et al. (2010) searched for flares in the SDSS and found 243 flaring spectra of 63 flare stars with only two having an enhanced continuum. Continuum enhancement occurs especially for the strongest flares (see e.g. Kowalski et al. 2010a; and Hawley & Fisher 1992).

We also analysed Proxima Centauri’s integrated flux using PN spectra from the three individual *XMM-Newton* observations. The X-ray flux levels did not change significantly for the first and second exposure, whereas there is a significant change in the X-ray flux in the third exposure as can be seen in Fig. 4; here the X-ray flux was determined using the Xspec best-fit spectral models (see Sect. 4) integrated in the energy range 0.2 to 10.0 keV. Specifically, the night 1 EPIC PN exposure results in an X-ray flux of $3.0 \times 10^{-12} \text{ erg cm}^{-2} \text{ s}^{-1}$ ($L_x = 6.0 \times 10^{26} \text{ erg s}^{-1}$), the exposure of night 2 corresponds to $3.2 \times 10^{-12} \text{ erg cm}^{-2} \text{ s}^{-1}$ ($L_x = 6.4 \times 10^{26} \text{ erg s}^{-1}$), and the data from night 3 give

A&A 534, A133 (2011)

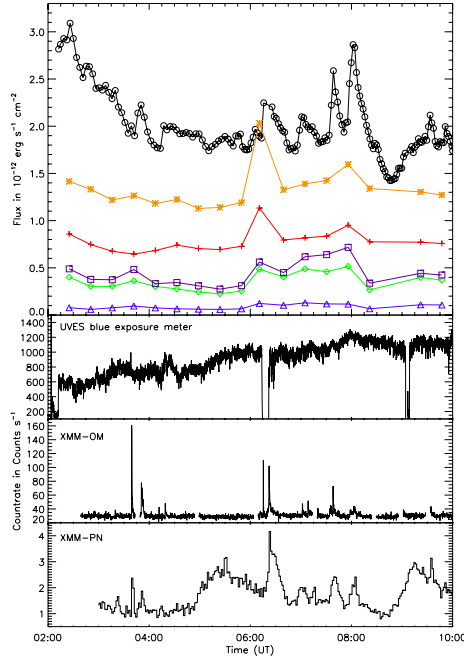


Fig. 2. As Fig. 1, but for night 2. The two gaps in the UVES light curve are due to technical problems that led to the loss of the guide star. The legend is the same as in Fig. 1.

$6.3 \times 10^{-12} \text{ erg cm}^{-2} \text{ s}^{-1}$ ($L_x = 1.2 \times 10^{27} \text{ erg s}^{-1}$). The higher value for the third night is caused by the strong flare.

During all three nights, the X-ray flux in the quiescent time intervals is at a level of $2.6 \times 10^{-12} \text{ erg cm}^{-2} \text{ s}^{-1}$ ($L_x = 4.9 \times 10^{26} \text{ erg s}^{-1}$). This is comparable to the lower boundary of the variable quiescent X-ray luminosity $4\text{--}16 \times 10^{26} \text{ erg s}^{-1}$ found by Haisch et al. (1990).

We can calculate the activity level of Proxima Centauri using the activity indicator $\log L_x/L_{\text{bol}}$. With infrared H and K band magnitudes of $m_H = 4.835$ and $m_K = 4.384$ and using the bolometric corrections given by Reid et al. (2001), Proxima Centauri's bolometric luminosity is $6 \times 10^{30} \text{ erg s}^{-1}$, i.e., slightly less than the $L_{\text{bol}} = 6.7 \times 10^{30} \text{ erg s}^{-1}$ found by Frogel et al. (1972). With an activity indicator of $\log L_x/L_{\text{bol}} = -4$ in non-flaring time intervals, Proxima Centauri is a moderately active star.

3.2. The large flare

The X-ray light curve from night 3 (Fig. 3) shows a large flare with a peak X-ray flux of $3.8 \times 10^{-11} \text{ erg cm}^{-2} \text{ s}^{-1}$ ($L_x = 7.2 \times 10^{27} \text{ erg s}^{-1}$), which is also evident in the OM and optical data. The optical UVES exposure-meter and OM light curves resemble those of a typical solar impulsive flare. The X-ray data and light curves of chromospheric emission lines show a more complex behaviour with two broad secondary events peaking at about 6:45 and 9:10 UT in the X-ray light curve. In the $H\alpha$ -emission, we find an even more complicated behaviour with several sub-peaks in the decay phase, which are not seen in any of the other light curves but are roughly associated with the two

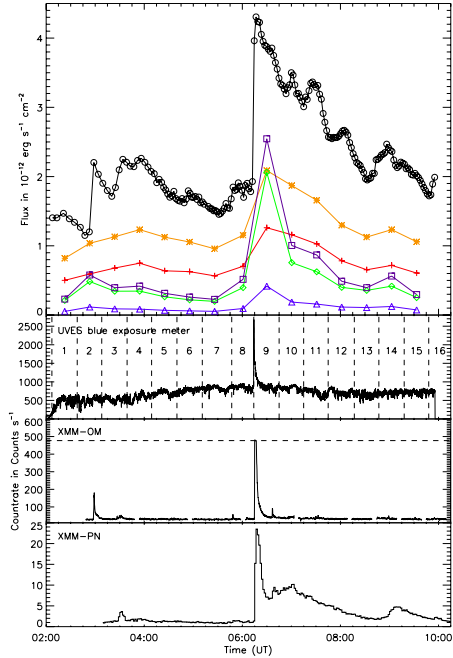


Fig. 3. As Fig. 1, but for night 3. The time intervals for the UVES blue arm spectra are also indicated for further reference. The dashed line in the OM panel marks the saturation limit that was reached in the flare peak. The figure legend is the same as in Fig. 1.

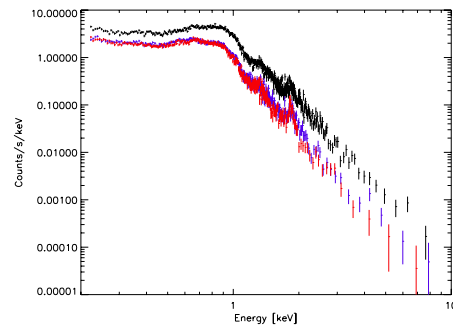


Fig. 4. PN spectra from night 1 (bottom/red), night 2 (middle/blue), and night 3 (top/black).

secondary peaks seen in X-rays. The two secondary peaks can also be identified in the other Balmer lines and the Ca II H and K lines despite their lower time resolution. The secondary peaks are found in neither the optical UVES light curve, nor the OM light curve. A similar event was described for Proxima Centauri by Güdel et al. (2002).

The flare rise to the maximum flux took place on a timescale of $\sim 500 \text{ s}$. With a 10 s binning for X-ray and optical data, we found that the optical peak as seen in the OM light curve precedes the X-ray peak by about two minutes. This can be explained in terms of the Neupert effect (Neupert 1968) known

B. Fuhrmeister et al.: Multi-wavelength observations of Proxima Centauri

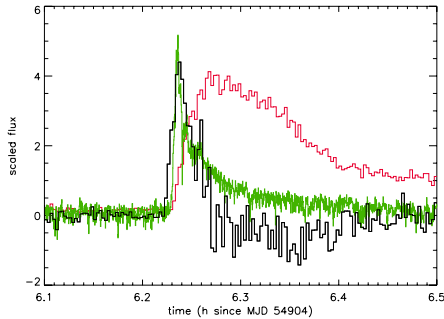


Fig. 5. Illustration of the Neupert effect during the large flare of Proxima Centauri on night 3. Depicted are the combined EPIC X-ray light curve in red, its time derivative (smoothed by five bins) in black, and the optical UVES light curve in green.

to occur in solar and a variety of stellar flares, where the time integral of emission due to particle acceleration, such as radio emission or blue continuum emission, resembles the rise of the flare light curve in soft X-rays. The explanation of this behaviour is that accelerated particles hit the dense chromosphere and that chromospheric material is heated and evaporates into the corona, where it accumulates and provides the emission measure of the subsequent soft X-ray emission.

This effect is also clearly seen in our data, because the time derivative of the combined EPIC (MOS1, MOS2 and PN) X-ray light curve during the flare rise (see Fig. 5) matches the shape of the optical light curve; we note that we cannot use the OM light curve for this analysis, since the OM data are saturated during the flare peak, but we use the light curve that is extracted from the UVES’s blue-arm photometer.

3.3. Average magnetic field

The average magnetic field Bf of Proxima Centauri is measured using our UVES red arm data by employing a method introduced by Reiners & Basri (2006) utilising an absorption band of molecular FeH close to $1 \mu\text{m}$. We provide a brief overview of the method here and refer to the paper by Reiners & Basri (2006) for a more detailed description of the procedure. The FeH band contains a large number of isolated lines, some of which are highly sensitive to the Zeeman effect, while others are not. Since Landé- g factors are unavailable, a direct determination of the Zeeman effect is difficult, although there have been some attempts to model FeH molecular lines theoretically (see Shulyak et al. 2010). We measure the magnetic field by comparing observed FeH lines to spectra of stars with known magnetic fields. These template stars are GJ 1002 (M5.5, no measured magnetic field) and GJ 873 (M3.5, $Bf \sim 3.9 \text{ kG}$, Johns-Krull & Valenti 2000). Before the spectra can be compared, the template spectra have to be scaled to match the strengths of the FeH absorption to the strength found in our spectra of Proxima Centauri. They also have to be adjusted to match in terms of rotational velocity. The observed spectrum is then modelled as a linear combination of the template spectra to determine Bf , thus it is assumed that the Zeeman broadening is linear in Bf and that the magnetic field strength is distributed similarly in all stars.

We measured the average magnetic field Bf for all three nights by using a χ^2 -minimisation to find the best-fit relation for

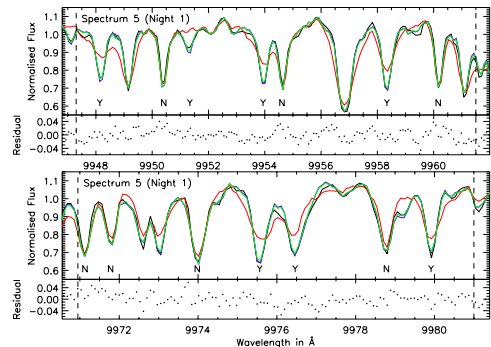


Fig. 6. Result of the fit for UVES red arm spectrum 5 from night 1 with $Bf = 400 \text{ G} \pm 110 \text{ G}$. *Black*: slope corrected Proxima Centauri data; *red*: scaled and broadened spectrum of magnetic reference GJ 873; *blue*: scaled and broadened spectrum of non-magnetic reference GJ 1002; *green*: best fit; *Y*: magnetically sensitive lines; *N*: magnetically insensitive lines; *vertical dashed lines* border the wavelength regions used for the fit.

the interpolation between the template stars and the UVES red arm spectra of Proxima Centauri. The fit was calculated in two wavelength regions, $9947.3\text{--}9961.5 \text{ \AA}$ and $9970.95\text{--}9981.0 \text{ \AA}$, containing 14 absorption lines of FeH with 7 being sensitive and 7 being insensitive to the magnetic field, respectively. A typical example of our fits is shown in Fig. 6. We compute a formal 1σ uncertainty in Bf by searching the range of Bf for which $\chi^2 < \chi^2_{\text{min}} + 1$ while varying the four other parameters. This results in an average uncertainty of $\overline{\Delta Bf} = 110 \text{ G}$. We note that it is only the statistical error that we use to compare individual differential measurements because the magnetically insensitive lines remain constant; thus they provide an accurate calibration particularly when intercomparing exposures. In addition to statistical errors, there are systematic errors and we estimate the true uncertainty in the absolute measurement of the magnetic field Bf to be of the order of a few hundred gauss. Hence, to accurately assess any trend in the data the statistical error has to be considered, while the systematic errors may offset the whole graph.

There is a relatively strong correlation between the seeing conditions and the derived values of Bf , especially in the second and third night with Pearson’s product-moment correlation coefficients r of $r_{N2} = 0.84$ and $r_{N3} = 0.64$. This was eliminated by dividing the Bf measurements by a polynomial describing the general trend of the seeing taken from the ESO archive. The resulting timing behaviour of Bf is shown in Fig. 7. The field has a mean level of $\overline{Bf} = 250 \text{ G}$ with a statistical error of 60 G . Reiners & Basri (2008) also measured the average magnetic field of Proxima Centauri with the same method using data taken in April 2004 and found magnetic field values in the range $450 \text{ G} < Bf < 750 \text{ G}$. This change of $\sim 350 \text{ G}$ over five years might well be real, but is close to the limits of our uncertainty. Hence, it is unclear whether this difference is real or a consequence of the measuring inaccuracy.

As mentioned above, we can use the statistical error in the χ^2 -minimisation to compare individual measurements, because we are only interested in a differential comparison and not in the absolute values of Bf . For the first and second nights, the magnetic field is consistent with a constant value within the error bars. For the third night, there is a dip in the magnetic field

A&A 534, A133 (2011)

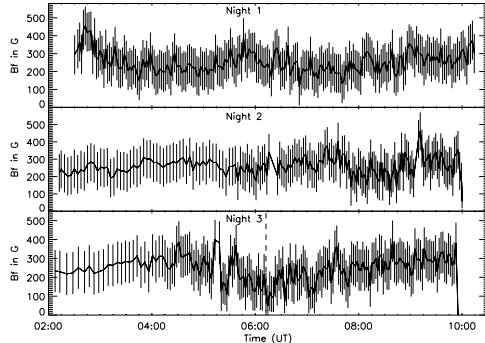


Fig. 7. Timing behaviour of the average magnetic field B_f for the three observed nights. The onset of the flare in the third night is marked by a vertical dashed line.

with its minimum roughly at the time of the flare onset (Fig. 7). In the context of the reconnection model for flares, a weak magnetic field at flare onset is what one would expect. However, we note that the measured fields refer to the photosphere, while the field annihilation is assumed to take place in the corona. In addition, the slow decay before the flare event is surprising for a catastrophic event such as magnetic reconnection, while after the flare the magnetic field recovers relatively quickly. In summary, it remains unclear whether there is a physical association of the magnetic field changes with the flare.

4. Coronal properties of Proxima Centauri

4.1. X-ray spectral analysis

Our X-ray observations of Proxima Centauri can be analysed to help us derive several time-variable properties of its corona such as temperatures, abundances, and densities, as we investigate in this section.

4.1.1. Spectral fits and elemental abundances

To visualise the spectral changes of Proxima Centauri associated with the large flare, we show the time evolution of the RGS spectra during night 3 in Fig. 8. The mean spectrum is shown in the uppermost part of the diagram, while the time evolution in the form of the light curve is depicted vertically at the right border. The mean spectrum resembles a typical RGS spectrum of M-dwarfs with O VIII Ly α being the strongest line and other prominent lines originating from Ne IX, Ne X, Fe XVII, O VII, and C VI. As expected, the diagram shows a brightening in the spectral lines with the flare onset. The higher plasma temperatures during the flare manifest themselves as a relative brightening of lines formed at higher coronal temperatures than the cooler spectral lines, for example O VIII vs. the O VII triplet. However, pronounced changes in the density-sensitive ratio of the O VII forbidden to intercombination line cannot be identified in this time-resolved plot for the flare and the pre-flare period; they are only evident in time-integrated measurements for the flaring and quiescent states (see Sect. 4.1.3).

There is particular interest in studying elemental abundances during a flare. Since flares transport chromospheric material into the corona by chromospheric evaporation, coronal abundance patterns can temporarily change during flares. We

determined the temperatures and abundances relative to solar values (Grevesse & Sauval 1998) with an iterative procedure of global Xspec fits to EPIC and RGS spectra with VAPEC plasma models. In these fits, the abundances and emission measure are inherently interdependent, hence we made our inferences from relative changes in the fit parameters for the three observations. The errors we give for the fitted parameters were calculated with Xspec's *error* command. The program Xspec calculates the confidence intervals for the desired parameter by fixing this parameter at a specific value and varying the other free parameters until the best fit is reached. New fixed values for the parameter of interest are chosen until the error margins that were requested in the *error* command are covered. The errors in these plasma fits are correlated; in particular for the emission measure and elemental abundances, there is a strong interdependence (see below). Thus, in the calculation of Xspec's error margins for an individual parameter, all other non-frozen parameters are also allowed to vary, yielding effectively larger error margins than if one (incorrectly) assumes the errors to be uncorrelated.

When fitting the EPIC spectra, we adopted the following method to obtain the abundances: the abundances of oxygen, neon, iron, magnesium, and silicon were allowed to vary freely and independently, but were constrained to be the same among all the VAPEC temperature components. The abundances of all other elements were frozen to the solar value because they cannot be well-constrained with EPIC spectra since they do not have prominent spectral lines at energies where EPIC has a large effective area. When fitting EPIC spectra together with RGS spectra, carbon and nitrogen abundances also were allowed to vary. To determine the number of VAPEC components with different temperatures, we added new components one by one until the addition of the next component did not improve the fit significantly.

In the following sections we used the RGS spectra with their much higher wavelength resolution for spectral fitting simultaneously to the MOS spectra. We combined the spectra from the quiescent states of all three nights (for a definition of quiescence, see Sect. 3.1) and compared them to the spectra obtained from the large flare during the third night. To compare these two states, we defined a fixed temperature grid consisting of the values 0.14, 0.4, and 1.0 keV (1.6, 4.6, and 11.5 MK). The resulting best-fit χ^2 values of the three-temperature VAPEC models along with average individual elemental abundances for the quiescent state and the flaring state are listed in Table 2. The quiescent state is characterised by dominant plasma components at 0.14 and 0.4 keV. During the flare, there was a pronounced enhancement of the emission measure at 0.4 and 1.0 keV. The emission measure at low temperatures is more weakly constrained than for the quiescent state; within the errors, the low-temperature emission measure is consistent in both fits.

4.1.2. The FIP effect

Similar to the Sun, inactive or low-activity-level stars show a normal first ionisation potential (FIP) effect where elements with a low FIP are enhanced in the corona compared to elements with a high FIP. A reversed pattern – the inverse FIP effect – with enhanced high-FIP elements and depleted low-FIP elements is frequently found in stars of higher activity (e.g. Brinkman et al. 2001, Audard et al. 2003). A FIP effect is common among stars with low activity levels ($\log L_X/L_{\text{bol}} < -4$). Owing to the activity level shown by Proxima Centauri, one would expect to observe the inverse FIP-effect. In the measurements for the quiescent state, the inverse FIP-effect might be observed but owing

A&A 534, A133 (2011)

Table 3. Model parameters for the flare spectra with variable Fe abundances.

Spect. No.	KT_1 [keV]	EM_1 [10^{50} cm $^{-3}$]	KT_2 [keV]	EM_2 [10^{50} cm $^{-3}$]	Fe	Red. χ^2	d.o.f	T MK	EM [10^{50} cm $^{-3}$]
1	0.75 $^{+0.05}_{-0.06}$	2.38 $^{+0.91}_{-0.63}$	1.90 $^{+0.28}_{-0.26}$	4.90 $^{+0.58}_{-0.72}$	0.58 $^{+0.15}_{-0.12}$	1.15	119	17.71 $^{+1.65}_{-1.95}$	7.28 $^{+1.49}_{-1.36}$
2	0.69 $^{+0.07}_{-0.09}$	3.23 $^{+1.12}_{-0.85}$	1.58 $^{+0.19}_{-0.17}$	6.39 $^{+0.81}_{-0.98}$	0.38 $^{+0.12}_{-0.07}$	1.10	148	14.88 $^{+1.44}_{-1.61}$	9.62 $^{+1.93}_{-1.83}$
3	0.61 $^{+0.03}_{-0.03}$	2.85 $^{+0.53}_{-0.44}$	1.60 $^{+0.11}_{-0.12}$	4.98 $^{+0.40}_{-0.42}$	0.54 $^{+0.11}_{-0.09}$	1.19	159	14.40 $^{+0.82}_{-0.91}$	7.83 $^{+0.94}_{-0.86}$
4	0.63 $^{+0.03}_{-0.09}$	3.61 $^{+1.47}_{-1.87}$	1.26 $^{+0.27}_{-0.15}$	2.85 $^{+1.71}_{-0.92}$	0.35 $^{+0.11}_{-0.09}$	0.95	93	10.60 $^{+1.89}_{-1.32}$	6.47 $^{+3.19}_{-2.80}$
5	0.58 $^{+0.07}_{-0.12}$	2.41 $^{+0.59}_{-0.54}$	1.22 $^{+0.48}_{-0.24}$	1.91 $^{+0.48}_{-0.62}$	0.33 $^{+0.07}_{-0.06}$	1.07	113	10.05 $^{+2.95}_{-2.17}$	4.32 $^{+1.07}_{-1.16}$
6	0.46 $^{+0.13}_{-0.10}$	1.80 $^{+0.75}_{-0.36}$	0.97 $^{+0.14}_{-0.13}$	1.71 $^{+0.38}_{-0.75}$	0.24 $^{+0.11}_{-0.07}$	0.92	96	8.26 $^{+1.57}_{-1.41}$	3.52 $^{+1.13}_{-1.12}$
7	0.38 $^{+0.09}_{-0.06}$	1.16 $^{+0.17}_{-0.18}$	1.06 $^{+0.11}_{-0.07}$	1.67 $^{+0.22}_{-0.11}$	0.37 $^{+0.20}_{-0.10}$	1.20	106	9.11 $^{+1.20}_{-0.75}$	2.84 $^{+0.40}_{-0.30}$
8	0.79 $^{+0.02}_{-0.03}$	2.72 $^{+0.34}_{-0.46}$	1.58 $^{+0.89}_{-0.46}$	0.79 $^{+0.45}_{-0.39}$	0.21 $^{+0.05}_{-0.03}$	1.00	135	11.28 $^{+6.05}_{-2.69}$	3.52 $^{+0.79}_{-0.85}$
9	0.64 $^{+0.02}_{-0.03}$	1.71 $^{+0.43}_{-0.44}$	1.01 $^{+0.12}_{-0.12}$	1.82 $^{+0.38}_{-0.35}$	0.26 $^{+0.04}_{-0.03}$	1.03	229	9.64 $^{+0.82}_{-0.97}$	3.53 $^{+0.82}_{-0.79}$
10	0.62 $^{+0.02}_{-0.12}$	2.86 $^{+0.39}_{-0.33}$	1.22 $^{+0.42}_{-0.27}$	0.92 $^{+0.28}_{-0.32}$	0.30 $^{+0.03}_{-0.03}$	1.03	222	8.88 $^{+2.27}_{-2.32}$	3.78 $^{+0.67}_{-0.65}$
11	0.46 $^{+0.03}_{-0.09}$	1.88 $^{+0.74}_{-0.69}$	0.76 $^{+0.13}_{-0.06}$	2.00 $^{+0.72}_{-0.87}$	0.27 $^{+0.05}_{-0.03}$	1.00	217	7.17 $^{+1.22}_{-0.91}$	3.89 $^{+1.47}_{-1.57}$
12	0.31 $^{+0.03}_{-0.04}$	1.52 $^{+0.32}_{-0.35}$	0.72 $^{+0.05}_{-0.04}$	1.72 $^{+0.34}_{-0.29}$	0.36 $^{+0.07}_{-0.06}$	0.92	193	6.21 $^{+0.52}_{-0.51}$	3.24 $^{+0.64}_{-0.62}$
13	0.24 $^{+0.05}_{-0.03}$	1.25 $^{+0.45}_{-0.34}$	0.64 $^{+0.05}_{-0.03}$	1.70 $^{+0.35}_{-0.37}$	0.38 $^{+0.07}_{-0.05}$	0.81	184	5.53 $^{+0.62}_{-0.43}$	2.95 $^{+0.80}_{-0.72}$
14	0.25 $^{+0.05}_{-0.04}$	1.04 $^{+0.30}_{-0.35}$	0.59 $^{+0.06}_{-0.03}$	1.42 $^{+0.38}_{-0.46}$	0.38 $^{+0.09}_{-0.07}$	0.97	162	5.23 $^{+0.73}_{-0.47}$	2.47 $^{+0.89}_{-0.82}$
15	0.22 $^{+0.03}_{-0.05}$	0.88 $^{+0.29}_{-0.40}$	0.57 $^{+0.04}_{-0.07}$	1.36 $^{+0.54}_{-0.29}$	0.34 $^{+0.08}_{-0.07}$	1.14	142	5.05 $^{+0.46}_{-0.74}$	2.25 $^{+0.83}_{-0.70}$
16	0.26 $^{+0.03}_{-0.01}$	1.67 $^{+0.12}_{-0.12}$	1.78 $^{+0.15}_{-0.09}$	0.40 $^{+0.20}_{-0.14}$	0.35 $^{+0.21}_{-0.17}$	0.75	134	4.28 $^{+1.30}_{-0.69}$	2.08 $^{+0.32}_{-0.27}$
17	0.24 $^{+0.01}_{-0.01}$	1.31 $^{+0.10}_{-0.11}$	0.78 $^{+0.19}_{-0.28}$	0.25 $^{+0.44}_{-0.09}$	0.37 $^{+0.05}_{-0.03}$	1.11	103	3.82 $^{+1.83}_{-1.61}$	1.57 $^{+0.55}_{-0.21}$
18	0.24 $^{+0.02}_{-0.02}$	1.15 $^{+0.14}_{-0.09}$	0.70 $^{+0.13}_{-0.09}$	0.25 $^{+0.11}_{-0.14}$	0.36 $^{+0.37}_{-0.17}$	1.02	91	3.78 $^{+0.83}_{-0.78}$	1.40 $^{+0.25}_{-0.24}$
19	0.31 $^{+0.09}_{-0.04}$	1.15 $^{+0.29}_{-0.30}$	0.68 $^{+0.35}_{-0.22}$	0.21 $^{+0.26}_{-0.19}$	0.29 $^{+0.07}_{-0.07}$	0.95	74	4.29 $^{+2.54}_{-1.39}$	1.37 $^{+0.56}_{-0.50}$
20	0.22 $^{+0.02}_{-0.02}$	0.79 $^{+0.08}_{-0.09}$	0.69 $^{+0.14}_{-0.06}$	0.15 $^{+0.09}_{-0.06}$	0.20 $^{+0.07}_{-0.11}$	1.24	62	3.48 $^{+1.01}_{-0.61}$	0.95 $^{+0.18}_{-0.16}$
21	0.13 $^{+0.03}_{-0.01}$	0.72 $^{+0.23}_{-0.19}$	0.47 $^{+0.14}_{-0.10}$	0.54 $^{+0.19}_{-0.30}$	0.24 $^{+0.05}_{-0.08}$	0.98	60	3.25 $^{+0.97}_{-0.54}$	1.26 $^{+0.43}_{-0.50}$
22	0.23 $^{+0.02}_{-0.03}$	0.70 $^{+0.19}_{-0.13}$	0.76 $^{+0.10}_{-0.10}$	0.45 $^{+0.15}_{-0.13}$	0.32 $^{+0.16}_{-0.12}$	1.03	77	5.14 $^{+0.73}_{-0.84}$	1.15 $^{+0.34}_{-0.26}$
23	0.40 $^{+0.08}_{-0.06}$	1.05 $^{+0.21}_{-0.13}$	0.91 $^{+0.07}_{-0.05}$	1.00 $^{+0.25}_{-0.17}$	0.33 $^{+0.08}_{-0.05}$	1.09	135	7.57 $^{+0.94}_{-1.05}$	2.05 $^{+0.46}_{-0.31}$
24	0.26 $^{+0.07}_{-0.04}$	0.76 $^{+0.31}_{-0.23}$	0.72 $^{+0.08}_{-0.05}$	1.22 $^{+0.25}_{-0.28}$	0.27 $^{+0.08}_{-0.06}$	0.84	129	6.38 $^{+0.90}_{-0.59}$	1.98 $^{+0.57}_{-0.52}$
25	0.19 $^{+0.03}_{-0.03}$	0.66 $^{+0.13}_{-0.14}$	0.63 $^{+0.04}_{-0.04}$	0.90 $^{+0.19}_{-0.17}$	0.32 $^{+0.09}_{-0.07}$	1.14	105	5.16 $^{+0.48}_{-0.44}$	1.56 $^{+0.32}_{-0.31}$
26	0.29 $^{+0.06}_{-0.05}$	0.94 $^{+0.22}_{-0.22}$	0.78 $^{+0.11}_{-0.14}$	0.38 $^{+0.21}_{-0.11}$	0.32 $^{+0.28}_{-0.15}$	1.22	85	5.09 $^{+1.02}_{-1.00}$	1.33 $^{+0.44}_{-0.34}$
27	0.26 $^{+0.06}_{-0.03}$	0.72 $^{+0.17}_{-0.18}$	0.68 $^{+0.12}_{-0.10}$	0.32 $^{+0.18}_{-0.10}$	0.32 $^{+0.18}_{-0.11}$	1.02	69	4.56 $^{+1.09}_{-0.72}$	1.04 $^{+0.36}_{-0.29}$
28	0.23 $^{+0.02}_{-0.11}$	0.65 $^{+0.09}_{-0.16}$	0.78 $^{+0.11}_{-0.16}$	0.25 $^{+0.21}_{-0.08}$	0.25 $^{+0.11}_{-0.20}$	1.14	66	4.49 $^{+1.03}_{-1.53}$	0.91 $^{+0.31}_{-0.25}$

and the flare temperature T is defined as an emission-measure weighted sum of the temperatures from each flare component

$$T = \sum_i \frac{T_i \times EM_i}{EM}$$

We infer that the iron abundance increases from a level of 0.30 ± 0.03 directly before the onset of the flare to a maximum value of $0.58^{+0.15}_{-0.12}$, when the flare peak is reached (see Table 3). As oxygen is another element that produces very strong emission lines in our X-ray spectra, we also investigated possible oxygen abundance changes during the flare in the same fashion, but found no evidence of a similar timing behaviour. This indicates that fresh plasma material is evaporated from the photosphere and chromosphere that has a different composition with a higher iron abundance than the quiescent coronal plasma. This scenario

fits very well with the measured $H\alpha$ asymmetries that indicate movements from the chromosphere in the direction of the corona (see Sect. 5.2). As can be seen from line shift measurements in Table 9, material is evaporated with a velocity of 44.3 km s^{-1} in the spectrum lasting from 6:12 to 6:14 UT. If one makes a conservative estimate that the material is accelerated only at the end of the exposure time, it can travel for about 90 seconds or about 4000 km before the measurement No. 1 of Table 3 starts (6:16:00 UT), which would place the material within the corona. For the second measurement of $H\alpha$ blue-shifts, the situation is not as clear because the blue-shifts persist for a longer time overlapping with measurement No. 3 (starting at 6:20:00 UT) of higher coronal iron abundance. If most of the material is evaporated at the beginning of the blue-shift, the material moves for about 210 s or about 2200 km before the X-ray measurement No. 3 starts, again putting the material into the corona.

B. Fuhrmeister et al.: Multi-wavelength observations of Proxima Centauri

Table 4. X-ray counts in the O VII triplet during quiescence (total integration time of 49 ks) and during the flare (total integration time of 7 ks).

Line	Counts (quiescence)	Counts (flare)
resonance (21.6 Å)	225 ± 17	96 ± 12
intercombination (21.8 Å)	60 ± 11	39 ± 8
forbidden (22.1 Å)	130 ± 13	48 ± 8

4.1.3. Coronal densities

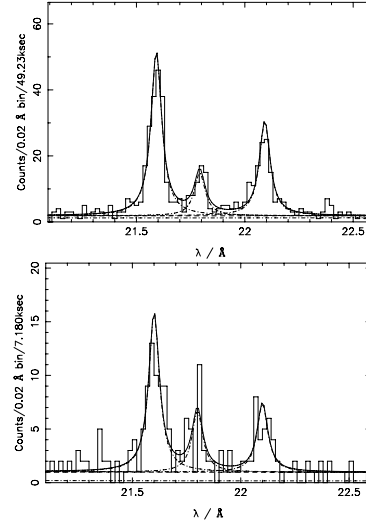
Electron densities can be inferred from line triplets of He-like ions. The RGS energy range contains density-sensitive He-like triplets of N VI, O VII, Ne IX, Mg XI, and Si XIII. These He-like triplets show in increasing order of wavelength a resonance (*r*), intercombination (*i*), and a forbidden line (*f*). If the electron collision rate is sufficiently high, ions in the upper level of the forbidden transition, $1s2s^3S_1$, do not return to the ground level, $1s^2^1S_0$, but the ions are instead collisionally excited to the upper level of the intercombination transitions, $1s2p^3P_{1,2}$, from where they decay radiatively to the ground state. Thus, the ratio of the *f* to *i* fluxes is sensitive to density (Gabriel & Jordan 1969).

The He-like triplet of O VII is strong enough in our observations to be used to obtain characteristic electron densities in the source region. We estimate the coronal plasma densities using the density-sensitive ratio of the forbidden to intercombination line of the O VII triplet in the quiescent and the flaring state. The measured *f*/*i* flux ratios are 2.17 ± 0.61 in quiescence and 1.23 ± 0.46 during the flare in the third night (see Fig. 10, Table 4). The errors in these line ratios are rather large and are caused by the weak intercombination line. Formally, the errors overlap, hence one could argue that the change in density is insignificant. However, the ratio $(f + i)/r$ is practically constant during quiescence (0.84 ± 0.17) and the flare (0.90 ± 0.28). This indicates that physically X-ray photons are only shifted from the forbidden to the intercombination line at high densities. Hence, the constant $(f + i)/r$ ratio suggests that the change in the *f*/*i* ratio is actually density-related and makes it less probable that it is a statistical fluctuation.

To convert the measured *f*/*i* ratios into coronal plasma densities, we approximated the flux ratio by $f/i = R_0/(1 + n_e/N_c)$, where R_0 is the low density limit and N_c is the critical density. We adopted the values from Pradhan & Shull (1981) of 3.95 and $3.1 \times 10^{10} \text{ cm}^{-3}$, respectively. We find electron densities of $n_e = 2.5 \pm 0.7 \times 10^{10} \text{ cm}^{-3}$ in quiescence and $n_e = 6.9 \pm 2.6 \times 10^{10} \text{ cm}^{-3}$ during the third-night flaring period. This suggests an increase in plasma density during the flare, as one expects from the standard flare model.

4.2. Interpretation: loop properties

Emission measure – temperature (*EM-T*) diagrams are useful for estimating physical quantities that are not directly observable. Since there is no direct information about the morphology of the involved coronal structures, we estimate the size of the spatially unresolved stellar coronal flaring region from the light curve, time-resolved temperature (*T*), and emission measure (*EM*) values obtained during the decay of the flaring loop. The decay time of an X-ray flare is directly related to the length of the flaring loop. However, if there is a significant amount of heating present during the decay of the flare, it can prolong the decay and lead to an overestimated loop length. We assumed

**Fig. 10.** Density-sensitive line triplet of O VII (resonance, intercombination, and forbidden line for increasing wavelength). The upper panel shows the best fit to cumulated RGS1 data during quiescence, while the lower panel shows the RGS1 triplet data during the large flare.

that the flare occurs inside a single coronal loop with a constant cross-section that is anchored in the photosphere. The plasma is confined to the loop, and the decay begins after the loop has reached a quasi-steady state, where the energy and plasma flow are negligible. According to this assumption, the decay time of the X-ray emission roughly scales with the plasma cooling time, which in turn scales with the length of the loop structure. Therefore, the longer the decay takes, the larger the loop structure becomes. Serio et al. (1991) derived a thermodynamic timescale for pure cooling of flaring plasma confined to a single flaring coronal loop. Reale et al. (1997) derived an empirical formula to determine the loop length considering the effect of sustained heating during the flare decay that uses the trajectory of the flare in the *EM-T* diagram, viz.

$$L = \frac{\tau_{LC} \sqrt{T_0}}{\alpha F(\zeta)} \text{ or } L_0 = \frac{\tau_{LC} \sqrt{T_{0.7}}}{120 F(\zeta)} \zeta_{\min} < \zeta \leq \zeta_{\max},$$

where τ_{LC} is the decay time derived from the light curve and $\alpha = 3.7 \times 10^{-4} \text{ cm}^{-1} \text{ s K}^{1/2}$. The observed maximum temperature must be corrected to $T_0(T - 0.7) = \xi T_{\text{obs}}^\eta$ (in units of 10^7 K), where T_{obs} is the maximum best-fit temperature derived from spectral fitting to the data. The unit-less correction factor is $F(\zeta) = \frac{c_a}{\zeta - c_a} + q_a$, where ζ is the slope of *EM-T* diagram. The coefficients ξ , η , c_a , ζ_a , and q_a depend on the energy response of the instrument. According to Reale (2007), for XMM/EPIC the values are $\xi = 0.13$, $\eta = 1.16$, $c_a = 0.51$, $\zeta_a = 0.35$, and $q_a = 1.35$.

We show the *EM-T* diagram of the flare on Proxima Centauri including the two secondary flares in Fig. 11. For the part of the flare evolution before the secondary events, the slope measured from the $\log T - 0.5 \log EM$ diagram in Fig. 11 is $\zeta = 1.07 \pm 0.29$. Given $T_{\text{peak}}[\text{MK}] = 33.26^{+7.73}_{-11.93}$, we determined the loop half length to be $L = 8.55^{+3.81}_{-2.86} \times 10^9 \text{ cm}$. Assuming that the volume $V \propto L^3$, we computed the volume of the flaring region $V_{\text{flare}} \approx 6.25^{+2.12}_{-0.22} \times 10^{29} \text{ cm}^3$. We also computed the loop-footprint area

A&A 534, A133 (2011)

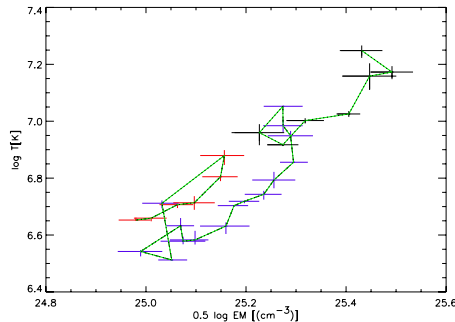


Fig. 11. Flare evolution in density-temperature. The green line represents the evolution of flare decay (black) and secondary events (blue and red).

$V/2L$ and an area filling-factor of the flare of three percent. We also note that in addition to this flare decay, there are two other secondary events. From the EM-T diagram for these events, the slopes measured from these secondary events are similar to the slope obtained for the first flare event. Thus, the derived loop lengths are of the same order of magnitude within the errors.

4.3. Optical Fe XIII emission

We also investigated the Fe XIII forbidden coronal line at 3388.1 Å in our spectra of Proxima Centauri. The stellar spectrum had previously been searched for this line but no clear conclusion had been drawn (Führmeister et al. 2004). In the new UVES data, there is indeed evidence of the forbidden line during and after flare activity for the first and the third night.

To isolate the forbidden coronal line emission at 3388.1 Å, we averaged at least three normalised spectra for the quiescent state, the flare state, and after-flare state. To emphasise the chromospheric and coronal changes between the averaged spectra, we subtracted the quiescent state from the flaring state and the post-flare state (and for testing purposes also from different quiescent states of the same night). These difference spectra of the different quiescent states usually contain only noise as expected. However, the differences between the spectra of flare states and quiescent states in the first and third nights show a weak broad excess at the position of the Fe XIII line beginning at about UT 6:00 for the first night. This line persists for the post-flare state. In the third night, the line can also be found directly before the large flare starting at UT 4:40, while no evidence of Fe XIII emission could be found for the second night. An example of the line can be found in Fig. 12, the fit parameters obtained with CORA can be found in Table 5. The derived fluxes have an error of about a factor of two because of the uncertainties in the flux calibration. For the first night, we used the spectra No. 3–7 as quiescent state, for the second night the spectra No. 4–6, and for the third night the spectra No. 1–5. The half width σ of the line is much larger than the typical measured half width of the chromospheric lines of 0.04 Å (see Table 6). Interpreting the line width as pure thermal Doppler broadening, we expect a half width of 0.04 Å, for a typical chromospheric temperature of about 10 000 K and a half width of about 0.17 Å for the coronal Fe XIII line with a peak formation temperature of about 1.6 MK. The measured half widths are larger for the forbidden Fe XIII line suggesting

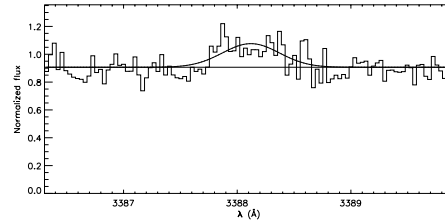


Fig. 12. Example of the fit to the averaged difference spectrum of the first night for the after-flare state at the end of the night for the Fe XIII line. The broad Gaussian is the line best fit obtained with CORA.

Table 5. Fit parameters of the Fe XIII line.

Averaged spectra No.	Central wavelength [Å]	Half width [Å]	Line flux ^a [erg s ⁻¹ cm ⁻²]
1st night			
13–17	3388.02 ± 1.32	0.25 ± 0.02	6.6 × 10 ⁻¹⁵
18–22	3388.07 ± 1.32	0.22 ± 0.02	6.6 × 10 ⁻¹⁵
23–26	3388.10 ± 1.32	0.25 ± 0.02	7.2 × 10 ⁻¹⁵
3rd night			
6–8	3388.13 ± 1.32	0.27 ± 0.03	1.0 × 10 ⁻¹⁴
9–11	3388.16 ± 1.32	0.20 ± 0.01	1.5 × 10 ⁻¹⁴
12–15	3388.15 ± 1.32	0.36 ± 0.03	1.7 × 10 ⁻¹⁴

Notes. ^(a) Flux errors are about a factor of two.

that there are additional line-broadening mechanisms; however, it must be kept in mind that the measurement of the line width is sensitive to the determination of the background, thus the given (formal) errors are probably underestimates.

The order of magnitude of the derived Fe XIII flux is consistent with our estimate derived from Proxima Centauri's coronal X-ray spectrum during the flare. The O VII triplet is formed at a similar temperature as Fe XIII ($\log T = 6.3$ and 6.2 , respectively). We calculate the flux in the O VII triplet during the flare from a CORA fit to the RGS1 spectrum to be $F_{\text{O VII}} = 4.32 \times 10^{-13} \text{ erg s}^{-1} \text{ cm}^{-2}$. The coronal abundance ratio of iron to oxygen is 0.67 during the flare (see Table 2), and from CHIANTI we calculate the ratio of the line emissivities of Fe XIII to the O VII triplet to be of the order of 0.25 in the temperature range $\log T = 6.2$ – 6.3 . From this, we derive an order-of-magnitude estimate of $F_{\text{Fe XIII}} \approx 10^{-15} \text{ erg s}^{-1} \text{ cm}^{-2}$, which is a little bit lower but given the uncertainties compatible with the flux computed from the optical spectra in Table 5.

The observation of the Fe XIII line during the larger flare in the third night seems to be counter-intuitive at first glance, since a flare should heat the corona and Fe XIII has its peak ionisation equilibrium at $T = 1.6$ MK. However, during the flare the emission measure for the low temperature component at 1.6 MK is slightly higher than for quiescent state (or, given the errors, comparable to the emission measure during quiescence) and the iron abundance is similarly higher, which is consistent with the forbidden Fe XIII line being seen during the flare. Moreover, for another M5.5 star, LHS 2076, the line was also observed only during a flare (Führmeister et al. 2004).

5. Chromospheric and transition region properties of Proxima Centauri

5.1. Identification of chromospheric emission lines

For the flare spectrum No. 9 in the blue arm and No. 76 in the red arm, respectively, we produced an emission line list containing 474 chromospheric emission lines, out of which 21 are from the red arm. In the blue arm, we analysed the flare spectrum directly, while in the red arm we subtracted the quiescent spectrum No. 74. The main part of spectrum No. 9 and spectrum No. 7 can be found in Fig. 13.

To access the line parameters, we fitted the background, central wavelength, half width σ , and line flux as free parameters using a Gaussian profile for every manually indicated emission line in a certain wavelength range. We typically chose 10 Å as the wavelength range size for the fitting process, since the background variations for such a short wavelength interval are negligible. The line fit parameters including a (possible) identification can be found in Table 6. We only show a few rows of the Table 6 in this paper as an example, while the whole table is provided only in electronic form.

The flux measurements given in the line catalogue may be affected by rather large errors mainly for the following reasons. First, the description with a Gaussian may give a poor fit quality if the lines have broad wings (and should be fitted with a Lorentzian/Voigt). Second, the background/quasi-continuum may be ill-defined. This is true for emission lines in a broader emission line wing, but also for emission cores of absorption lines and a variable background. Moreover, nine Balmer/Paschen and other lines could not be fitted at all because they are too broad or have an ill-defined background level (but the lines are clearly there). The absolute flux level is also estimated to have rather large errors as discussed in Sect. 2.1.

For the line identification, we generally used the catalogue of (Moore 1972). A few lines were identified using the NIST database³. For the identifications from the Moore catalogue, the multiplet is also given in Table 6. The spectra were first shifted to the rest wavelength for the identification process which should enable us to identify systematic line shifts caused by the flare.

Three lines could not be identified with any known line. Another 98 lines have only possible identifications for the following reasons: (1) the line was not found in the Moore catalogue, (2) the wavelength shift to the possible laboratory wavelength is large, (3) the line is blended severely with other lines, and (4) (most often) the line is the only one out of the multiplet. Since we excluded doubtful features from our line list, the list cannot be claimed to be complete, especially for weak lines. The identified lines belong in total to 32 different ions. The number of lines found for the individual ions is shown in Table 7. Statistically, all lines are blue-shifted by 0.01 Å.

We found Balmer lines up to number 19 during as well as outside the flare. The lines are only stronger during the flare. This indicates that the densities during the flare are not high enough to cause any Stark broadening of the lines, which would lead to the merging of higher order Balmer lines (Švestka 1972). This agrees well with the electron densities measured using the X-ray data (see Sect. 4.1.3), which have at most doubled during the flare compared to quiescence.

We compare the line list to that of the large flare on CN Leo (Fuhrmeister et al. 2008), which consists of 1143 chromospheric emission lines. The two catalogues overlap in the wavelength

region from 3280 to 3850 Å. In this range, we compared the proportion of lines found in the CN Leo flare to those found in this event. While for Fe I, Ti I, Mn I, Ni I, and Cr I, the proportion of lines found in the CN Leo flare compared to the lines found in the Proxima Centauri flare is (partially much) larger than 2, for the single ionised species of the same elements the proportion is 1–1.5. Moreover, nineteen lines in our present catalogue are not found in the CN Leo flare. These are 4 He I lines, 2 Fe I, 6 Fe II, 2 Zr II lines, 2 Co I, 1 V II, 1 Ti I, and 1 H I. This seems to indicate that the flare energy is deposited very effectively in the higher chromosphere/lower transition region, where helium and Balmer lines are formed, and also the lines of singly ionised metals should be formed.

5.2. Line asymmetries

During the flare, line asymmetries are found in both the blue and the red spectra. The Balmer lines, He I, and Ca II K show additional flux in the red wing. In the blue arm, we investigated the Balmer lines H γ , H δ , and the Balmer lines at 3889 Å and 3835 Å. We refrained from fitting He because of the heavy blending with the Ca II H line. We also failed to fit the higher Balmer lines because of the extreme width of these lines during the flare, the blending with multiple metal lines, and the low line amplitudes of the very highest Balmer lines. Unfortunately, all He I lines in the blue arm are weak or blended and decay very fast, so that in the spectrum No. 10 after the flare peak spectrum No. 9, the helium lines have almost vanished. The Ca II K line being an unblended strong metal line shows a clear red wing asymmetry. No other metal lines have clear asymmetries. In the red arm, we find an asymmetry for the He I line at 6678 Å in the flare peak spectrum No. 76, while in spectrum No. 77, the line has already faded too much to display any asymmetry. The other three helium lines in the red arm spectrum are either too weak or too complicated in their structure (blend with another helium line) to show unambiguous asymmetries. Hence, the only line for which we could study the asymmetries with higher time resolution of the red arm spectra is H α . This line shows indeed that the asymmetries have a strong time dependence that cannot be studied with the time resolution of the blue arm spectra. We fitted the line asymmetries with two Gaussians: one for the main (narrow) line component and one for the (broad) wing component. For all fits, we subtracted the quiescent spectrum directly before the flare. The shifts between the broad and the narrow Gaussian are listed in Table 8 for various lines and for the H α line with higher time resolution in Table 9. Although the formal errors found in the fitting process for the line shifts are small, we assume a ten percent error for all the line shifts.

The high time resolution of H α clearly shows that the asymmetries are a dynamical phenomenon as can be seen in Fig. 14. The asymmetries for the first secondary flare can be identified in the time map itself (elapsed time is about 1.3 h). In addition, it can be seen in the top panel of Fig. 14, where the yellow shaded spectrum shows the most prominent asymmetry in the wing. The third peak in this light curve also shows broad wings in the H α spectra, which are, however, weaker, thus could not be fitted. Starting with spectrum No. 149 (08:52:10 UT) and No. 150 with a blue asymmetry, the asymmetry turns to the red side in spectrum No. 152 and 153 (09:00:48 UT). These asymmetries can also be noted in the time map (elapsed time about 3.2 h in Fig. 14). While in the blue spectra there are only red asymmetries, in H α there are also blue ones. Indeed for the entire integration time of the blue spectrum No. 9, there are mostly

³ Available online under <http://physics.nist.gov/PhysRefData/ASD/index.html>

A&A 534, A133 (2011)

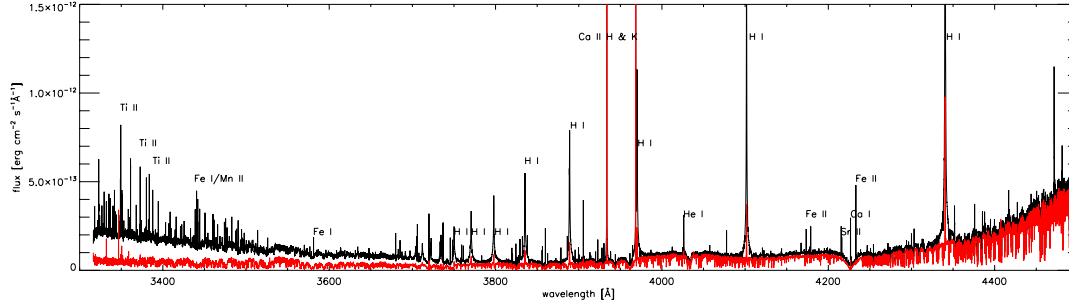


Fig. 13. Main part of the UVES blue flare (black) and quiescent (red/grey) spectrum. Several major chromospheric emission lines are identified in the plot.

Table 6. Ten rows of the line catalogue.

Central wavelength [Å]	Half width [Å]	Flux ^a [erg s ⁻¹ cm ⁻²]	Catalogued wavelength [Å]	Ion	Multiplet	Id flag	Comment
3495.35	0.06	8.70×10^{-15}	3495.285	Fe I	238	2	blend 3495.370 CrII 2
3495.82	0.04	1.25×10^{-14}	3495.831	Mn II	3	0	
3496.80	0.03	1.01×10^{-14}	3496.814	Mn II	3	0	
3497.09	0.04	3.93×10^{-15}	3497.115	Fe I	78	2	em
3497.51	0.03	7.56×10^{-15}	3497.536	Mn II	3	0	em
3497.83	0.03	1.21×10^{-14}	3497.843	Fe I	6	0	em
3500.33	0.04	8.34×10^{-15}	3500.340	Ti II	6	0	
3500.87			3500.852	Ni I	6	0	em, line not fitable
3503.46	0.05	7.53×10^{-15}	3503.474	Fe II	4	0	
3504.89	0.02	1.23×10^{-15}	3504.890	Ti II	88	0	

Notes. The whole table is accessible electronically at the CDS. ^(a) As discussed in Sect. 2.1, the absolute errors for the given fluxes are about a factor of two.

Table 7. Chromospheric emission line identifications.

Ion	No. lines ¹	Ion	No. lines ¹
H I	19(19)	Mg I	10(6)
He I	14(6)	K II	1(0)
Li II	1(0)	Ca I	1(0)
Sc II	7(4)	Ca II	7(7)
Ti I	3(0)	Cr I	5(4)
Ti II	58(53)	O I	3(3)
V II	2(0)	Ne I	1(0)
Cr I	9(7)	Ne II	1(0)
Cr II	30(26)	Al I	2(2)
Mn I	4(3)	Si I	2(0)
Mn II	9(8)	Si II	4(3)
Fe I	182(148)	Cl II	1(0)
Fe II	45(35)	Ce II	1(0)
Co I	5(2)	Sr II	2(2)
Ni I	31(28)	Zr II	3(2)
Ni II	5(5)	Y II	2(0)

Notes. ⁽¹⁾ In brackets we indicate the number of secure identifications.

blue-shifts for H α ; only for red spectrum No. 76 corresponding to the first few minutes exposure time of spectrum No. 9 there is a red shift (the spectrum No. 9 corresponds to elapsed time from 0.4 to 0.7 h in Fig. 14). Since the amplitude decays exponentially, the conditions at the beginning of the spectrum should dominate the spectrum. Therefore, blue spectrum No. 9 and spectrum No. 76 yield similar red shifts. After red spectrum

Table 8. Line shifts of the broad line component for diverse lines from the flare-only spectra.

Line	Velocity [km s ⁻¹]	Velocity [km s ⁻¹]	Velocity [km s ⁻¹]
	spec. No. 8(75) 05:47:14	spec. No. 9(76) 06:14:39	spec. No. 10(77) 06:45:12
H γ (4340 Å)	–	4.8	12.4
H δ (4101 Å)	3.9	4.9	10.2
H I 3889 Å	–	fit ambiguous	13.1
H I 3835 Å	2.1	fit ambiguous	9.4
Ca II K	–	5.1	21.4
He I 6678 Å	–	6.0	–

No. 80 (corresponding to an elapsed time of about 0.6 h), the asymmetries and large wings disappear – but re-appear in red spectrum No. 97–102 (corresponding to an elapsed time of about 1.1 to 1.3 h in Fig. 14). This agrees with the red wing asymmetries in blue spectrum No. 10, although the asymmetry in the red arm is invisible for the whole integration time of this spectrum. That the time scales on which the asymmetries evolve can be very short can be seen in red spectrum No. 75 and blue spectrum No. 8. While the red spectrum shows a clear blue-shift, in the blue spectrum the lines either cannot be fitted or show no real line shifts, but do display broad wings (see Tables 8, 9).

We interpret all these line shifts as manifestations of mass motions in the chromosphere as e.g. Fuhrmeister et al. (2008). The high velocity blue-shift at the flare onset corresponds to

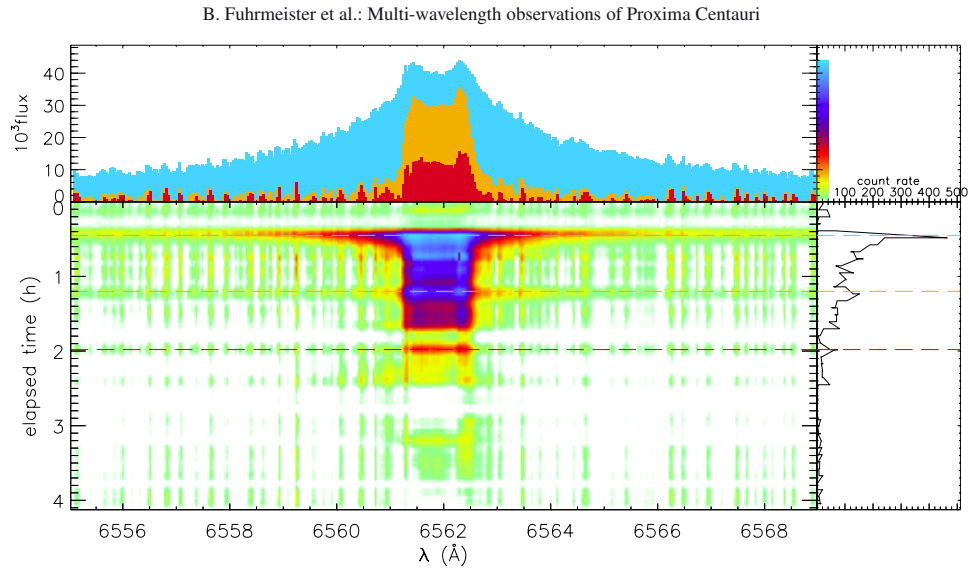


Fig. 14. The $H\alpha$ line variations in time with the quiescence spectrum No. 74 subtracted. The *top panel* shows three individual spectra as marked by the horizontal dashed lines in the time map below. On the *right hand panel*, we show the light curve of the integrated flux of the quiescence subtracted spectrum for the shown wavelength region. The time is measured in elapsed time since 5:50 UT.

Table 9. Line shifts of the broad line component for the $H\alpha$ line from the flare-only spectra.

Spectrum No.	Start time (UT)	Velocity [km s^{-1}]	Spectrum No.	Start time (UT)	Velocity [km s^{-1}]
75	06:12:16	-44.3	97	06:59:50	8.7
76	06:14:29	5.3	98	07:02:00	13.7
77	06:16:37	-10.5	99	07:04:09	13.7
78	06:18:48	-9.6	100	07:06:19	33.7
79	06:20:57	-5.9	101	07:08:28	32.9
80	06:23:06	1.4	102	07:10:37	3.7

evaporation of chromospheric material, while during the decay phase raining down as well as rising material can be found.

5.3. Theoretical modelling of the flare with PHOENIX

We modelled the flare spectra with theoretical PHOENIX chromospheric flare spectra. These spectra were originally computed to fit the mega-flare on CN Leo (Fuhrmeister et al. 2010). The stars CN Leo and Proxima Centauri have similar photospheric properties. While for Proxima Centauri, T_{eff} is about 3100 K, for CN Leo a T_{eff} of 2900 K was used for the underlying photosphere in the model calculation. Short & Doyle (1998) studied the influence of the underlying photosphere on a quiescent chromospheric model and found that a difference of 200 K in T_{eff} leads to uncertainties in the parameters of the column mass at the onset of the transition region as well as the column mass of the temperature minimum of about 0.3 dex. The finest step in our flaring model grid is 0.2 dex. Since we use a photosphere with a lower T_{eff} than is realistic, we should infer a too high column mass for the onset of the transition region and the temperature minimum. Details about the model construction can be found in Fuhrmeister et al. (2010). In this paper, we constructed the flaring model as a linear combination of a quiescent spectrum observed directly before the flare and a flaring model spectrum.

Table 10. Mean best-fit flare model parameters in time.

Spec. no.	T_{chrom} [K]	$\log c_{\text{mass}^{\text{chrom}}}$	$\log c_{\text{mass}^{\text{Tmin}}}$	grad TR	Filling factor
76	8400 ± 300	-2.5 ± 0.2	-0.3 ± 0.2	11.0 ± 0.1	2.0 ± 0.5
77	8400 ± 200	-2.5 ± 0.1	-0.3 ± 0.2	11.1 ± 0.3	2.0 ± 0.1
78	8300 ± 200	-2.7 ± 0.3	-0.4 ± 0.0	11.1 ± 0.3	2.0 ± 0.1
80	8200 ± 300	-2.7 ± 0.3	-0.4 ± 0.2	11.1 ± 0.3	2.0 ± 0.1
82	8300 ± 300	-2.9 ± 0.2	-0.9 ± 0.3	11.0 ± 0.4	4.0 ± 0.1
95	8000 ± 100	-3.0 ± 0.1	-1.1 ± 0.3	11.0 ± 0.4	6.0 ± 1.0
96	8400 ± 300	-2.6 ± 0.3	-0.2 ± 0.2	11.0 ± 0.1	2.0 ± 0.8
97	8400 ± 300	-2.5 ± 0.2	-0.3 ± 0.2	11.0 ± 0.1	1.5 ± 0.4
98	8400 ± 300	-2.7 ± 0.2	-0.3 ± 0.2	11.1 ± 0.3	1.5 ± 0.4
99	8400 ± 300	-2.7 ± 0.2	-0.3 ± 0.2	11.1 ± 0.3	1.5 ± 0.4
101	8200 ± 300	-3.0 ± 0.1	-1.1 ± 0.5	10.9 ± 0.3	4.0 ± 0.1
9	8500 ± 100	-2.5 ± 0.2	-0.3 ± 0.2	11.0 ± 0.4	0.8 ± 0.1
10	8400 ± 300	-2.9 ± 0.2	-0.8 ± 0.3	11.0 ± 0.1	0.9 ± 0.1

For the red and the blue arm respectively, we then used a global normalisation of the spectra and a grid of different filling factors of the flare model spectra to the quiescent observed spectra to help us find the best fit to the observed flare spectra. The filling factors used for the quiescent spectra are 0.85, 0.90, 0.93, 0.95, 0.96, 0.97, 0.98, 0.99, 0.995, and 0.999. The best fit was found using a χ^2 analysis again following Fuhrmeister et al. (2010). The mean best-fit parameters for the five best-fit flare models can be found in Table 10 with the standard deviation of the mean. Examples of the temperature structure of the best-fit models for a selection of different spectra can be found in Fig. 15. For a small wavelength range in the blue, a comparison between the observed spectrum and best-fit model spectrum can be found in Fig. 16.

The model parameters of the fitting process from the blue and the red arm agree well with each other with both exhibiting a shift towards flare models further out in the atmosphere later in the decay phase. For red models later than No. 82, no meaningful fit could be found with many models exhibiting nearly the same χ^2 . Even later during the secondary flare phase, a fitting of the flaring models also turned out to be possible again, starting at red

A&A 534, A133 (2011)

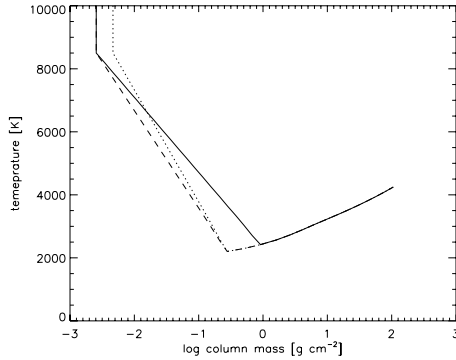


Fig. 15. Example of the temperature structure of the best-fit flare models for different spectra: black line: red spectrum No. 76 (flare onset); dotted line: red spectrum No. 97 (secondary flare); dashed line: blue spectrum No. 9.

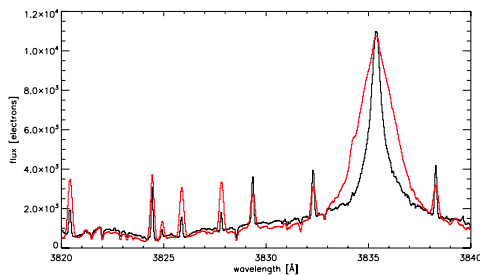


Fig. 16. Exemplary comparison between observed spectrum (black) and our best-fit model spectrum (red) for blue spectrum No. 9.

spectrum No. 95. The secondary flare can be seen in the models as a re-shift to higher-pressure chromospheric flare models. For the higher-pressure models, a higher temperature for the onset of the transition region is also found.

The only disagreement between model parameters can be found for the filling factor. Comparing red spectrum No. 76 to blue spectrum No. 9 shows that the blue spectrum has a lower filling factor. This may indicate that there is an error in the normalisation, which was done for the red arm where the influence of the flare on the continuum should be small and then applied to the blue arm. Another possibility of the different filling factors is a height dependence of the filling factor. The blue arm with its wealth of metal lines should trace the mid-chromosphere, while the red arm with the He I, Balmer, and Paschen lines should trace the upper chromosphere. The filling factor found for the red spectra models of about two percent agrees well with that found by the EM-T diagnostics from the X-ray data, which is three percent (see Sect. 4.2).

6. Discussion

The multi-wavelength character of the observations allows us to characterise general behaviour and energetics of the flare for various wavelength bands, hence different temperature regimes and also cross-check these using different instruments.

Table 11. Various fluxes and flare energetics for different wavelength regimes.

Wavelength band	Instrument	Flux ^a [erg s ⁻¹ cm ⁻²]	Energy [erg]
chrom. em. lines	UVES blue arm	1.2×10^{-11}	8.5×10^{28}
H α emission	UVES red arm	2.0×10^{-12}	1.6×10^{28}
blue excess em. (3300–3600 Å)	UVES blue arm	5.3×10^{-10}	3.8×10^{30}
X-rays (0.2–10 keV)	PN+RGS XMM	2.2×10^{-11} $\pm 0.2 \times 10^{-11}$	1.9×10^{29}

Notes. ^(a) The errors in the UVES fluxes are about a factor of two (see Sect. 2.1).

6.1. Flare energetics and excess emission

The flare exhibited a broadband excess emission in the far blue of the UVES spectral arm, which can be easily identified in Fig. 13. A similar excess was found for larger flares and could in these cases be ascribed to blackbody emission (Führmeister et al. 2008; Hawley & Fisher 1992). In the flare observed here, it was impossible to fit the excess emission with a blackbody model. We nevertheless calculated the excess flux, noting that the shape of the spectrum suggests that the bulk of the broadband emission is not covered by the UVES spectrum. We integrated the flare spectrum up to 3600 Å and subtracted (1) the quiescent flux, (2) the general flux increase seen in the blue arm during the flare, and (3) the chromospheric line flux in this wavelength interval for the flux excess calculation. We also calculated the total of the chromospheric line fluxes in the blue arm and in H α . We compared the H α line flux to the value one obtains using the χ method introduced by West & Hawley (2008), which is based only on the equivalent width of the line, the bolometric luminosity, and the distance of the star (so one needs no absolute flux calibration). Using the χ value of 0.176×10^{-4} for an M 6 dwarf, L_{bol} of 6.7×10^{30} erg s⁻¹, and a measured peak EW of 3.4, we evaluated the same flux of 2.0×10^{-12} erg s⁻¹ cm⁻² as in our flux calibration (or 1.8×10^{-12} erg s⁻¹ cm⁻² using L_{bol} of 6.0×10^{30} erg s⁻¹). The various fluxes can be found in Table 11 together with the resulting energies assuming a filling factor for the flare of two percent for the time range of the blue UVES spectrum No. 9 from 6:14 to 6:45 UT.

6.2. H α self-absorption

A comparison to the flux-calibrated spectrum of Proxima Centauri presented by Cincunegui et al. (2007) shows that the H α line amplitude in our spectra is extremely small during the whole three days of our observations. The line amplitude during the flare is comparable to the line amplitude of the spectrum from Cincunegui et al. (2007), which was taken during a quiescent state. This indicates that Proxima Centauri's chromosphere was generally in a low activity state during the observations. The occurring flare enhanced the H α line flux only to a level that can also be found during a quiescent state (at other times). This fits well with the relatively low X-ray flux found in our observations (see Sect. 3.1).

The H α line is heavily self-absorbed during our observations. This self-absorption is in most cases asymmetric. The line peak at the red side is higher than at the blue; this peak asymmetry should not be confused with the wing asymmetry described in Sect. 5.2 of this paper. Two examples can easily be noted in

B. Fuhrmeister et al.: Multi-wavelength observations of Proxima Centauri

the “flare only” spectra shown in the top panel of Fig. 14: while for the flare spectrum the two peaks are about of the same height and the line centre therefore symmetric, for the two spectra from the decay phase the red peak is higher than the blue peak. We note that the spectra of Cincunegui et al. (2007) have lower spectral resolution hiding a possible self-reversal. We therefore compared our data to processed HARPS data from the ESO archive facility⁴, which cover the spectrum of Proxima Centauri from 3782 to 6912 Å, in the time from 2004 to 2007. These spectra have not yet been published and show a wide variation in the H α line amplitude, with the spectra from Cincunegui et al. (2007) at the high end of measured H α line amplitudes and our observations at the low end. Like our spectra the HARPS spectra exhibit in most cases a self-reversal with more flux in the red side peak.

We checked the red peak asymmetries using our models, which also display H α self-absorption at the line centre that is in all cases symmetric. This would be expected for one-dimensional (1D) chromospheric models without mass motion, where the self-reversal is a pure non-local thermal equilibrium (NLTE) effect. Allred et al. (2006) computed 1D hydrodynamical models of M dwarf flares. For various evolutionary stages of the flare in their simulations, the H α line profiles show the red peak asymmetries also observed in our and the HARPS spectra. In the hydro-dynamical models, the peak asymmetry is caused by mass motions during the simulated flare. It appears reasonable to assume that similar mass motions are also common in the quiescent state to explain the observed peak asymmetries.

6.3. Magnetic field

The dip in the magnetic field coincides in time with the flare in the third night. We estimated the energetics as a consistency check, in case a physical connection were possible. The level of the magnetic field changes from $\approx 300 \pm 100$ G just before the flare to $\approx 100 \pm 100$ G at the time the flare starts in the optical. So, the nominal change in mean magnetic field is 200 G, although the errors are very large. As a consistency check however, we can calculate that this corresponds to a released magnetic energy density of

$$\eta = \frac{B^2}{8\pi} = 1.6 \times 10^3 \text{ erg cm}^{-3}.$$

In Sect. 4.2, we calculated the flaring volume to be $V_{\text{flare}} \approx 6.25 \times 10^{29} \text{ cm}^3$, yielding a total released magnetic energy of $1.0 \times 10^{33} \text{ erg}$. We computed the total X-ray energy released during the first 6.5 ks of the flare to be $1.5 \times 10^{31} \text{ erg}$ by integrating the flare and quiescent spectral models from Table 2 over the energy range 0.2–10 keV and calculating the difference between the two. This is two orders of magnitude less than our estimate for the total released magnetic energy. However, since the detailed loop configuration is not known and we simply estimated the flaring volume as $V = L^3$ with L being the loop half length, the volume itself can only be an order-of-magnitude estimate. Therefore, we interpret the derived numbers as a general confirmation that the emitted X-ray energy during the flare is within the energy budget of the theoretically released magnetic energy. The question, of whether the dip in magnetic field is really physically connected to the flare must unfortunately remain unsolved.

Other flare stars of similar spectral type do show higher quiescent activity levels. Although magnetic field measurements of

mid and late-type M dwarfs are still quite rare, there is a time series measurement for the M5.5 star CN Leo (Reiners et al. 2007) with mean magnetic field of 2.2 kG covering a large flare. A dip in Bf at the time of the flare is also seen in these data, although there are other field variations of similar amplitude that are not associated with flares. Thus, it remains unclear whether the change in magnetic field is associated with the flare.

Reiners et al. (2007) found a correlated change in the distributions of magnetic field Bf and H α emission in their data of CN Leo. We searched for a similar correlation in our data, but found no one, which is unsurprising as the magnetic field changes are only small. We note that the H α emission during the course of these observations are quite low (see Sect. 6.2) corresponding to a weak magnetic field. Unfortunately, the observation of Reiners & Basri (2008), which found a stronger magnetic field for Proxima Centauri (as described in Sect. 3.3) does not include the H α line.

6.4. Line asymmetries

Line asymmetries during flares have often been found in high resolution spectra mostly for H I and He I lines. Examples are red line asymmetries for a large flare on LHS 2034 (M6.5) (Fuhrmeister et al. 2005), blue line asymmetries for a flare on AT Mic (M4) (Gunn et al. 1994), and red line asymmetries for flares on AD Leo (M3.5Ve) (Crespo-Chacón et al. 2006, for further examples see also references therein). For the CN Leo mega-flare described by Fuhrmeister et al. (2008), blue-wing as well as red-wing asymmetries have also been found. Asymmetries were normally ascribed by these authors to mass motions, which were partially modelled with multiple kernels and compared to the chromospheric downward condensations (CDCs) observed in the Sun in the case of the red asymmetries. During the CN Leo flare, asymmetries in the wings of Ca II lines were also found for the first time. Surprisingly, we found asymmetries in the Ca II H and K line for this much smaller flare on Proxima Centauri, though Crespo-Chacón et al. (2006) found that larger flares have stronger asymmetries and found no asymmetry in the Ca II H and K line in their flare data (their longest flares lasted about 30 min).

In contrast to the CN Leo mega-flare we also found blue wing asymmetries during flare decay and for the first time a re-appearance of the asymmetries during the secondary flare phase. The vanishing and re-appearance of the broad wings combined with the asymmetries of the H α line coincides with the secondary flare process seen in the X-ray light curve (see Fig. 3 and Table 9). When the secondary flare started, the broad component vanished, but reappeared some time later. The reappearance of the broad wings can also be identified in the H α light curve (see Fig. 3) as the peak after the main flare peak. The data again illustrates the dynamic behaviour of the asymmetry phenomenon, which provides additional evidence of mass motions.

6.5. Theoretical modelling

The clear secondary flare found by the flare models for the chromosphere strengthens our confidence in this approach of mixing quiescent observations with flaring model spectra. However, the general caveats of the method presented by Fuhrmeister et al. (2010) still apply: the 1D models show (for simplicity reasons) a linear temperature rise, which can explain part of the difficulties in fitting large wavelength regions with the same model spectrum equally well. Moreover, the 1D models are a very

⁴ Based on data obtained from the ESO Science Archive Facility from program 072.C-0488(E).

A&A 534, A133 (2011)

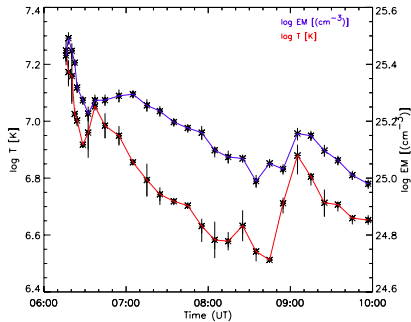


Fig. 17. Temporal evolution of flare temperature and emission measure.

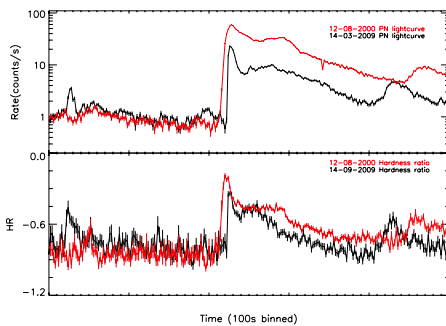


Fig. 18. Light curves with 100 s binning and hardness ratio of flares observed on Proxima Centauri by *XMM-Newton* on 12 August 2001 (red) and 14 March 2009 (black), respectively.

rough description of the horizontally as well as vertically highly complex temperature pattern (including shocks) of the (solar) chromosphere. Therefore, more physical chromospheric models should include hydrodynamic simulations and dynamic ionisation in either 1D or 3D.

6.6. Secondary flare events

The nature of this flare with its two secondary events following the first peak in the light curve raises the question of what kind of magnetic structure we are dealing with. There are two possibilities: it could be a single loop that experiences two additional heat pulses after the initial flare, or an arcade structure where several loops light up in sequence. The heat pulse refers to the process where the electron beam is accelerated in the coronal part of the magnetic flare loop, then propagates along the magnetic field lines down to the chromosphere, where the electrons are fully thermalised. A heat pulse represents the heating of the atmosphere by the electron beam. Reale et al. (2004) interpreted an earlier long-duration flare light curve of Proxima Centauri as being produced by two loops flaring in sequence, since the coronal temperature during the second peak was flat-topped and could not be adequately explained by a second heat pulse in the same loop. In our data however, the temperature and emission measure evolution follows the trend seen in the light curves closely as can be seen comparing Figs. 17 and 3.

From our analysis of the $EM-T$ diagram for this flare, we derive very similar $EM-T$ slopes for all three flare decays, each one indicating that a moderate amount of continuous reheating is present. The thus derived loop lengths are of the same order of magnitude. Even if the errors are rather large, there is a decreasing trend discernible within these three lengths; the lengths derived from the second and third peaks are comparable, while the length derived from the first peak seems to be larger by a factor of roughly two. This, and that the amount of reheating during the decays is very similar, suggests that we may see a series of similar loops in an arcade lighting up in sequence. However, owing to the large errors in the loop lengths, the possibility of a single loop with several heat pulses cannot be ruled out completely. A comparison of the X-ray and hardness ratio light curves for the mega-flare observed by Reale et al. (2004) and Güdel et al. (2004) and the flare presented here can be found in Fig. 18. The similarity of the light curves of the two events (despite the different count rates) is quite remarkable.

7. Summary and conclusions

We have presented multi-wavelength observations of the different activity stages of Proxima Centauri with particular emphasis on a long duration flare. We have tried to construct an overall picture of the atmosphere from the photosphere to the corona. We have determined a low average magnetic field, corresponding to low average X-ray and $H\alpha$ emission, with the latter being heavily self-absorbed. For the flare, we have compiled a chromospheric emission line list and found asymmetries in the broad wings of Balmer, He I, and Ca II H & K lines, which we ascribe to mass motions, which could explain coronal abundance changes. From the X-ray data, we have determined coronal densities, abundances, emission measures, and temperatures. The higher emission measure of the low temperature component and the higher Fe abundance during the flare fit well with the detection of a forbidden optical Fe XIII line during this time. The flare light curve is similar to the mega-flare for the same star described by Reale et al. (2004) and Güdel et al. (2004) exhibiting two bumps during the decay phase. The secondary flares are of a similar loop length as the main flare, show line asymmetries, and chromospheric flare modelling shows that the first one exhibits similar chromospheric parameters as the main one. All this indicates that the events are not independent of each other, but result from the same loop or at least an arcade with several arcade loops igniting consecutively. This seems to be a typical flare scheme for Proxima Centauri given, that it has been observed for the second time, and Reale et al. (2004) noted the similarity to solar flares. In contrast to Proxima Centauri, CN Leo, another well-observed M5.5 but more active dwarf never showed a comparable flare cascade during a long-duration flare. On the other hand, another highly active dM4.5e star, YZ CMi, also exhibited a series of secondary flares during a white light mega-flare as described by Kowalski et al. (2010b,a), who also speculated that the flare on YZ CMi originated in a complex arcade with a sequence of reconnecting loops. If these interpretations are correct, mid-type M dwarfs seems to have a flaring loop geometry that may be similar to the Sun, which will help to place constraints on turbulent dynamo theories.

Acknowledgements. S.L. acknowledges funding by the DFG in the framework of RTG 1351. K.P. acknowledges funding under project number DLR 50OR0703. N.R. acknowledges financial support by the DLR under project no. 50OR1002.

B. Fuhrmeister et al.: Multi-wavelength observations of Proxima Centauri

References

- Allred, J. C., Hawley, S. L., Abbett, W. P., & Carlsson, M. 2006, *ApJ*, 644, 484
- Arnaud, K. A. 1996, in *Astronomical Data Analysis Software and Systems V*, ed. G. H. Jacoby, & J. Barnes, ASP Conf. Ser., 101, 17
- Audard, M., Güdel, M., Sres, A., Raassen, A. J. J., & Mewe, R. 2003, *A&A*, 398, 1137
- Ballester, P., Modigliani, A., Boitquin, O., et al. 2000, *The Messenger*, 101, 31
- Berger, E., Gizis, J. E., Giampapa, M. S., et al. 2008, *ApJ*, 673, 1080
- Brinkman, A. C., Behar, E., Güdel, M., et al. 2001, *A&A*, 365, L324
- Browning, M. K. 2008, *ApJ*, 676, 1262
- Chabrier, G., & Baraffe, I. 1997, *A&A*, 327, 1039
- Cincunegui, C., & Mauas, P. J. D. 2004, *Boletín de la Asociación Argentina de Astronomía La Plata Argentina*, 47, 114
- Cincunegui, C., Díaz, R. F., & Mauas, P. J. D. 2007, *A&A*, 461, 1107
- Crespo-Chacón, I., Montes, D., García-Alvarez, D., et al. 2006, *A&A*, 452, 987
- Demory, B., Ségransan, D., Forveille, T., et al. 2009, in *AIP Conf. Ser.* 1094, ed. E. Stempels, 792
- Dorman, B., Nelson, L. A., & Chau, W. Y. 1989, *ApJ*, 342, 1003
- Frogel, J. A., Kleinmann, D. E., Kunkel, W., Ney, E. P., & Strecker, D. W. 1972, *PASP*, 84, 581
- Fuhrmeister, B., Schmitt, J. H. M. M., & Wichmann, R. 2004, *A&A*, 417, 701
- Fuhrmeister, B., Schmitt, J. H. M. M., & Hauschildt, P. H. 2005, *A&A*, 436, 677
- Fuhrmeister, B., Liefke, C., Schmitt, J. H. M. M., & Reiners, A. 2008, *A&A*, 487, 293
- Fuhrmeister, B., Schmitt, J. H. M. M., & Hauschildt, P. H. 2010, *A&A*, 511, A83
- Gabriel, A. H., & Jordan, C. 1969, *MNRAS*, 145, 241
- Grevesse, N., & Sauval, A. J. 1998, *Space Sci. Rev.*, 85, 161
- Güdel, M., Audard, M., Skinner, S. L., & Horvath, M. I. 2002, *ApJ*, 580, L73
- Güdel, M., Audard, M., Reale, F., Skinner, S. L., & Linsky, J. L. 2004, *A&A*, 416, 713
- Gunn, A. G., Doyle, J. G., Mathioudakis, M., Houdebine, E. R., & Avgoloupis, S. 1994, *A&A*, 285, 489
- Haisch, B. M., Harnden, Jr., F. R., Seward, F. D., et al. 1980, *ApJ*, 242, L99
- Haisch, B. M., Linsky, J. L., Bornmann, P. L., et al. 1983, *ApJ*, 267, 280
- Haisch, B. M., Butler, C. J., Foing, B., Rodono, M., & Giampapa, M. S. 1990, *A&A*, 232, 387
- Haisch, B., Strong, K. T., & Rodono, M. 1991, *ARA&A*, 29, 275
- Haisch, B., Antunes, A., & Schmitt, J. H. M. M. 1995, *Science*, 268, 1327
- Haisch, B., Kashyap, V., Drake, J. J., & Freeman, P. 1998, *A&A*, 335, L101
- Hauschildt, P. H., Allard, F., & Baron, E. 1999, *ApJ*, 512, 377
- Hawley, S. L., & Fisher, G. H. 1992, *ApJS*, 78, 565
- Hilton, E. J., West, A. A., Hawley, S. L., & Kowalski, A. F. 2010, *AJ*, 140, 1402
- Johns-Krull, C. M., & Valenti, J. A. 2000, in *Stellar Clusters and Associations: Convection, Rotation, and Dynamos*, ed. R. Pallavicini, G. Micela, & S. Sciortino, ASP Conf. Ser., 198, 371
- Kowalski, A. F., Hawley, S. L., Holtzman, J. A., Wisniewski, J. P., & Hilton, E. J. 2010a, *ApJ*, 714, L98
- Kowalski, A. F., Hawley, S. L., Holtzman, J. A., Wisniewski, J. P., & Hilton, E. J. 2010b [arXiv:1010.0452v1]
- Moore, C. E. 1972, *Nat. Stand. Ref. Data Ser.*, 40
- Ness, J.-U., & Wichmann, R. 2002, *Astron. Nachr.*, 323, 129
- Neupert, W. M. 1968, *ApJ*, 153, L59
- Osten, R. A., Hawley, S. L., Allred, J. C., Johns-Krull, C. M., & Roark, C. 2005a, *ApJ*, 621, 398
- Osten, R. A., Hawley, S. L., Allred, J. C., Johns-Krull, C. M., & Roark, C. 2005b, *ApJ*, 621, 398
- Parker, E. N. 1955, *ApJ*, 122, 293
- Piskunov, N. E., & Valenti, J. A. 2002, *A&A*, 385, 1095
- Pradhan, A. K., & Shull, J. M. 1981, *ApJ*, 249, 821
- Reale, F. 2007, *A&A*, 471, 271
- Reale, F., Betta, R., Peres, G., Serio, S., & McTiernan, J. 1997, *A&A*, 325, 782
- Reale, F., Güdel, M., Peres, G., & Audard, M. 2004, *A&A*, 416, 733
- Reid, I. N., Burgasser, A. J., Cruz, K. L., Kirkpatrick, J. D., & Gizis, J. E. 2001, *AJ*, 121, 1710
- Reiners, A., & Basri, G. 2006, *ApJ*, 644, 497
- Reiners, A., & Basri, G. 2007, *ApJ*, 656, 1121
- Reiners, A., & Basri, G. 2008, *A&A*, 489, L45
- Reiners, A., & Basri, G. 2010, *ApJ*, 710, 924
- Reiners, A., Schmitt, J. H. M. M., & Liefke, C. 2007, *A&A*, 466, L13
- Robrade, J., & Schmitt, J. H. M. M. 2005, *A&A*, 435, 1073
- Robrade, J., Poppenhaeger, K., & Schmitt, J. H. M. M. 2010, *A&A*, 513, A12
- Serio, S., Reale, F., Jakimiec, J., Sylwester, B., & Sylwester, J. 1991, *A&A*, 241, 197
- Short, C. I., & Doyle, J. G. 1998, *A&A*, 336, 613
- Shulyak, D., Reiners, A., Wende, S., et al. 2010, *A&A*, 523, A37
- Smith, R. K., Brickhouse, N. S., Liedahl, D. A., & Raymond, J. C. 2001, in *Spectroscopic Challenges of Photoionized Plasmas*, ed. G. Ferland, & D. W. Savin, ASP Conf. Ser., 247, 161
- Stelzer, B., Schmitt, J. H. M. M., Micela, G., & Liefke, C. 2006, *A&A*, 460, L35
- Švestka, Z. 1972, *ARA&A*, 10, 1
- van Leeuwen, F. 2007, *A&A*, 474, 653
- Voges, W., Aschenbach, B., Boller, T., et al. 1999, *A&A*, 349, 389
- Wargelin, B. J., & Drake, J. J. 2002, *ApJ*, 578, 503
- West, A. A., & Hawley, S. L. 2008, *PASP*, 120, 1161

A multiwavelength view of AB Dor's outer atmosphere [★]

Simultaneous X-ray and optical spectroscopy at high cadence

S. Lalitha¹, B. Fuhrmeister¹, U. Wolter¹, J. H. M. M. Schmitt¹, D. Engels¹ and M. H. Wieringa²

¹Hamburger Sternwarte, University of Hamburg, Gojenbergsweg 112, 21029 Hamburg, Germany

²CSIRO Astronomy & Space Science, Locked Bag 194, Narrabri, NSW 2390, Australia
e-mail: lsairam@hs.uni-hamburg.de

The date of receipt and acceptance should be inserted later.

ABSTRACT

Aims. We study the chromosphere and corona of the ultrafast rotator AB Dor A at high temporal and spectral resolution using simultaneous observations with *XMM-Newton* in the X-rays, VLT/UVES in the optical and the ATCA in the radio. Our optical spectra have a resolving power of $\sim 50\,000$ with a time cadence of ~ 1 min. Our observations continuously cover more than one rotational period of and include both quiescent periods as well as three flaring events of different strength.

Methods. From the X-ray observations we investigate the variations of coronal temperature, emission measure, densities, abundance and we interpret our data in terms of a loop model. From the optical data we characterise the flaring chromospheric material using numerous emission lines that appear in the course of the flares. A detailed analysis of the line shapes and line centers allows us to infer physical characteristics of the flaring chromosphere and to coarsely localize the flare event on the star.

Results. We specifically used the optical high-cadence spectra to demonstrate that both, turbulent and Stark broadening are present during the first ten minutes of the first flare. Also, in the first few minutes of this flare, we find short-lived (one to several minutes) emission subcomponents in the H α and Ca II K lines, which we interpret as flare connected shocks due to their large intrinsic velocities. Combining the space based data with the results of our optical spectroscopy we derive flare filling factors. Finally, comparing X-ray, optical broadband and line emission we find a correlation for two of the three flaring events, while for one event there is no clear correlation. Also, we do not find correlation of the radio data to any other observed data.

Key words. stars: activity – stars: magnetic fields – stars: coronae – stars: chromospheres – stars: late-type – stars: individual: AB Doradus A

1. Introduction

Low mass stars possess stratified atmospheres with coronae, transition regions, chromospheres and photospheres. All four layers exhibit characteristic temperatures and magnetically induced activity. Historically the first evidence of activity on the Sun – photospheric spots – were later complemented by observations in other wavelength bands like X-ray, UV, and radio, which trace different layers of the atmosphere and hence different activity phenomena. The different layers of the Sun's atmosphere are not independent, for e.g. during flares chromospheric material is mixed into the corona causing a temporary change in coronal metallicity (Sylwester et al. 1984, also see Phillips & Dennis 2012) and section 6 of Fletcher et al. (2011).

Moreover, for the case of the *spatially resolved* quiescent Sun, Beck et al. (2008) found propagating events between the photosphere and the chromosphere with travel times of about 100 s. The different layers are connected by magnetic flux tubes, which arc into the corona as loops (Fossum & Carlsson 2005; Wedemeyer-Böhm et al. 2009).

For the Sun, the heating mechanisms of the three outer layers are not well understood, yet (e.g. Wedemeyer-Böhm et al. 2012). For other stars, our knowledge is even sparser because their activity phenomena cannot be spatially resolved in most cases. Furthermore, stellar observations usually lack either the temporal or the spectral resolution required to follow the fast changing and complex phenomena in active regions.

To our knowledge our study is the first that combines high resolution ($R \sim 50\,000$) and high-cadence (~ 50 s with 25 s exposure time) optical spectra with simultaneous X-ray data that also offer such a temporal resolution. Other flare studies usually concentrate on high resolution *or* high cadence; e.g. Crespo-Chacón et al. (2006) studied flares on AD Leo with a

Send offprint requests to: lsairam@hs.uni-hamburg.de

[★] Based on observations collected at the European Southern Observatory, Paranal, Chile, 383.D-1002A and on observations obtained with *XMM-Newton*, an ESA science mission with instruments and contributions directly funded by ESA Member states and NASA.

cadence of typically 3 min, but with R of ~ 3500 in the wavelength range of 3500 to 5176 Å. Also Kowalski et al. (2010) observed a white light mega-flare on YZ CMi with a resolving power below 1000 but a cadence of 30 seconds covering a wavelength range from 3350 to 9260 Å. Prominent examples of good spectral resolution but lower cadence are Montes et al. (1999), who observed a major flare on LQ Hya during decay and about half an hour before its onset with $R \sim 35\,000$ and a cadence of 6 to 7 minutes in the wavelength range between 4842 to 7725 Å. Fuhrmeister et al. (2008) observed CN Leo during a mega flare with a cadence of about 15 minutes and $R \sim 50\,000$.

Achieving both, high spectral resolution and high cadence, in our study, is only possible through the combination of the instruments used and a bright target – AB Dor A, an extremely active, young K-dwarf and the closest ultra-fast rotator. ($P_{rot} = 0.52$ days, $d = 15$ pc, $m_v = 6.9$ mag, see Guirado et al. 2011 and their references). It has been a well studied target across all wavelengths demonstrating its high activity level. At longer wavelengths, AB Dor A was found to be a highly variable radio source by White et al. (1988). It also showed strong evidence of rotational modulation in the radio emission (Lim et al. 1992). At shorter optical wavelengths, signs of photospheric activity were found, e. g. long lived spots (Pakull 1981; Innis et al. 1988), and by detecting magnetic regions with a typical field strength of ≈ 500 G covering about 20% of the surface (Donati & Collier Cameron 1997). At shortest wavelength in X-ray AB Dor A was observed regularly since the detection by the Einstein observatory (Pakull 1981; Vilhu & Linsky 1987). Later observations were carried out with *XMM-Newton* (Güdel et al. 2001; Sanz-Forcada et al. 2003) and *Chandra* (Sanz-Forcada et al. 2003; Hussain et al. 2007; García-Alvarez et al. 2008). The corona of AB Dor A shows a high level of variability on timescales from minutes to hours. Vilhu et al. (1993) estimated an average of at least one flare per rotation on AB Dor A's surface.

Our paper is structured as follows: In Section 2 we describe our observations obtained with VLT/UVES, *XMM-Newton*, and ATCA. In Section 3 we compare the temporal behaviour of AB Dor A at radio, optical and soft X-ray wavelengths. We present the coronal properties of AB Dor A in quiescence as well as during flaring state in Section 4, while in Section 5 we describe the chromospheric properties of the star. Section 6 and 7 contain the discussion and our conclusions.

2. Observations and data analysis

The data on AB Dor A discussed in this paper were obtained simultaneously with *XMM-Newton*, ESO's Kueyen telescope equipped with the Ultraviolet-Visual Echelle Spectrograph (UVES) and the Australian Compact Array (ATCA)¹ on 25/26 November 2009.

¹ The Australia Telescope Compact Array is part of the Australia Telescope National Facility which is funded by the Commonwealth of Australia for operation as a National Facility managed by CSIRO.

2.1. Optical UVES data

For the optical data the UVES spectrograph was operated in a dichroic mode leading to a spectral coverage from 3720 Å to 4945 Å in the blue arm and 5695 Å to 9465 Å in the red arm with a small gap from 7532 Å to 7655 Å due to the CCD mosaic.² Data were taken on the 26 November 2009 between 2:00 UT and 9:30 UT. We used an exposure time of 25 s, i.e. a timing resolution of about 50 s due to the CCD readout, resulting in 460 spectra for the whole night. The resolution of our spectra is $\sim 40\,000$ for the blue spectra and $\sim 60\,000$ for the red spectra. There are two short gaps in the data, one at about 6:55 UT due to technical problems, where 2 spectra were lost and one at about 8:00 UT due to observations of AB Dor B. The spectra were reduced using the UVES pipeline vers. 4.4.8³ including wavelength and flux calibration.

We removed the telluric lines around $H\alpha$ line using a table of telluric water lines (Clough et al. 1992). We broadened the lines with a Gaussian representing the instrumental resolution and used a telluric reference line at 6552.61 Å for fitting the FWHM of the instrumental Gaussian and the depth of the line to each of our spectra and then subtracted the telluric spectrum.

2.2. X-ray data

The X-ray data were obtained using the *XMM-Newton*⁴ observatory. *XMM-Newton* consists of three co-aligned X-ray telescopes. Each of the three telescopes is equipped with a CCD camera which together form the European Photon Imaging Camera (EPIC); one of the telescopes is equipped with a pn CCD and the other two telescopes carry a MOS (Metal Oxide Semiconductor) CCD each with sensitivity between ~ 0.2 keV and 15 keV. These X-ray CCD detectors provide medium-resolution imaging spectroscopy ($E/\delta E \sim 20-50$) and a temporal resolution at sub second level. The telescopes with the MOS detectors are equipped with reflection gratings that provide simultaneous high resolution X-ray spectra between 0.35 and 2.5 keV with the Reflection Grating Spectrometer (RGS). In addition *XMM-Newton* carries an Optical Monitor (OM), an optical/UV telescope with different filters for imaging and time-resolved photometry.

Our *XMM-Newton* observations have a duration of 58 ks starting at 21:00 UT on 25 November 2009 (Obs ID: 0602240201), covering the entire time span of our optical observations. Useful data of AB Dor A were obtained with the OM, EPIC and the RGS detectors, which were all operated simultaneously. The pn and MOS detectors were operated with the medium filter in imaging and small window mode. The OM was operated in fast mode with 0.5 s cadence using the UVM2 band filter covering a band pass of 205 - 245 nm.

² A detailed description of the UVES spectrograph is available at <http://www.eso.org/instruments/uves/doc/>

³ The UVES pipeline manual can be found at <ftp.eso.org/pub/dfs/pipelines/uves-cpl/uves-pipeline-manual-13.0.pdf>

⁴ A detailed description of the instruments onboard *XMM-Newton* is available at http://xmm.esac.esa.int/external/xmm_user_support/documentation/technical/

All X-ray data were reduced with the *XMM-Newton* Science Analysis System (SAS) ⁵ software, version 12.0.1. EPIC light curves and spectra were obtained using standard filtering criteria. Spectral analysis was done with Xspec version 12.5.0 (Arnaud 1996) for the overall fitting processes. The models we used for fitting assume a collisionally ionised optically thin gas as calculated with the APEC code (Smith et al. 2001), elemental abundances are calculated relative to the solar photospheric values of Grevesse & Sauval (1998).

2.3. Radio data

AB Dor was observed with the Australian Compact Array (ATCA) on the 25 November 2009 from 19:00 UT until 26 November 2009 18:00 UT with a major interruption between 00:08 and 06:18 UT on the 26th (for details on the instrument Wilson et al. 2011). The array was in configuration 6B with baselines up to 6000 meters giving a spatial resolution of 1–2 arcsec for the observed frequencies. The backend was centered on 5.5 and 9.0 GHz and the bandwidth was 2 GHz in both cases. Data was taken every 10 sec. with breaks for calibrator (PKS 0515-674) scans every 7-15 minutes, depending on the weather conditions.

Data reduction was performed using the Miriad package (Sault et al. 1995). Time periods with bad phase stability and frequency channels affected by radio-frequency interference (RFI) were flagged. Bandpass calibration was performed using PKS 0823-500 for the first half of the data and PKS 1934-638 for the second half. Phase and gain calibration was performed using the frequent observations of PKS 0515-674. Absolute amplitude calibration was performed using PKS 1934-638, assuming a flux density of 4.97 Jy at 5.5 GHz and 2.70 Jy at 9.0 GHz.

Images were made at both frequencies using the full data set. The two strongest sources detected were at $\alpha=05:28:44.95$ $\delta=-65:26:53.5$ and $\alpha=05:28:44.61$ $\delta=-65:26:44.7$ (J2000), which we identify as AB Dor A and B, respectively. The mean flux densities were 4.2 mJy (5.5 GHz) and 3.0 mJy (9.0 GHz) for the primary star and 2.0 mJy (5.5 GHz) and 1.6 mJy (9.0 GHz) for AB Dor B. The noise level in the images was 11 μ Jy and 12 μ Jy at 5.5 and 9.0 GHz respectively.

Separate lightcurves in radio wavelength were produced for the two stars (AB Dor A and AB Dor B). They were phase shifted to the field centre and then self-calibrated (three iterations on the phases). After subtracting all other sources in the field, the data was vector averaged over a time interval of 120 sec over all baselines and channels.

3. Temporal Analysis

In Fig. 1 we provide a summary of our observations carried out as a multi-wavelength campaign designed to cover the coronal and chromospheric properties of AB Dor A. Specifically, from top to bottom we plot the radio light curve recorded at 5.5 GHz in Fig.1(a) with 120 s binning. The 9.0 GHz light curve is not

⁵ The *XMM-Newton* SAS user guide can be found at http://xmm.esac.esa.int/external/xmm_user_support/documentation/

Table 1. Integrated energies of individual flare events in *XMM-Newton*'s EPIC and OM.

Instrument	energy [erg]	energy [erg]
	event 1 + event 2 2:50-6:40 UT	event 3 7:30-8:58 UT
OM	4.20×10^{30}	1.40×10^{30}
EPIC	3.57×10^{33}	9.40×10^{32}

shown, since it is very similar to the 5.5 GHz light curve. In Fig. 1(b) and Fig. 1(c) we show the measured UVES Ca II K and H α equivalent widths (EW) as two examples of strong chromospheric emission lines, which originate from the lower and upper chromosphere, respectively. In Fig. 1(d) and Fig. 1(e) we plot the *XMM-Newton* OM and EPIC (pn and MOS combined) light curves with a binning of 100s. To identify heating events we defined a hardness ratio (HR) for the EPIC-pn as $HR = \frac{H-S}{H+S}$, where H is the number of counts between 1.0 and 10.0 keV (hard band) and S is the numbers counts between 0.15 and 1.0 keV (soft band) and plot the time-dependent hardness ratios (HR) in Fig. 1(f). The most extensive data set comes from *XMM-Newton*, which observed AB Dor for a total of 16 hours contiguously (from Nov 25 21:00 to Nov 26 13:00). UVES data are available for the time span between Nov 26 2:00 to 9:30, radio data is available from Nov 25 21:00-24:00 and Nov 26 6:00-13:00.

The most notable feature in the AB Dor light curve is a large flare or sequence of flares lasting from about Nov 26 3:00 - 9:00, which was covered by both *XMM-Newton* and UVES simultaneously, while the major part of the flare was unfortunately missed in radio wavelengths. A rough estimate of the flare energetics is given in Tab. 1. There are in addition a number of small scale events visible in the *XMM-Newton* OM and EPIC light curves as can be seen in Fig. 1(e), however, we concentrate on the large events in this paper.

For purposes of discussion we distinguish the following events, which need not necessarily be physically disconnected:

- Event 1: The first and main flare starts at 02:57 UT, consistently seen in the X-ray as well as in the UV light curve; also many chromospheric emission lines go into emission at this instance. For the flare, the count rate increased from a quiescent value of ~ 14 cts/s in the pn and ~ 5 cts/s in the MOS detector to ~ 38 cts/s and ~ 15 cts/s in the pn and MOS detectors, respectively at flare peak. In the HR we find a clear hardening to ≈ -0.2 during the large flare.
- Event 2: The second event is immediately following event 1 and rather broad; it occurs between 04:20 UT and 6:40 UT. This events 2 may be connected with the decay of the event 1, however, event 2 is not seen in the OM data, and is seen only rather weakly in the chromospheric lines (see Sect. 6.1). From the light curve it is not clear whether this event 2 is associated with event 1 as a reheating episode or whether it is independent; we will pursue this issue further in Sect. 6.
- Event 3: The third event starts at 07:34 UT and lasts until at 8:58 UT; this event can be traced through the X-ray, OM, and the chromospheric emission lines. It is the only event

4

S. Lalitha et al.: AB Doradus - outer atmospheres

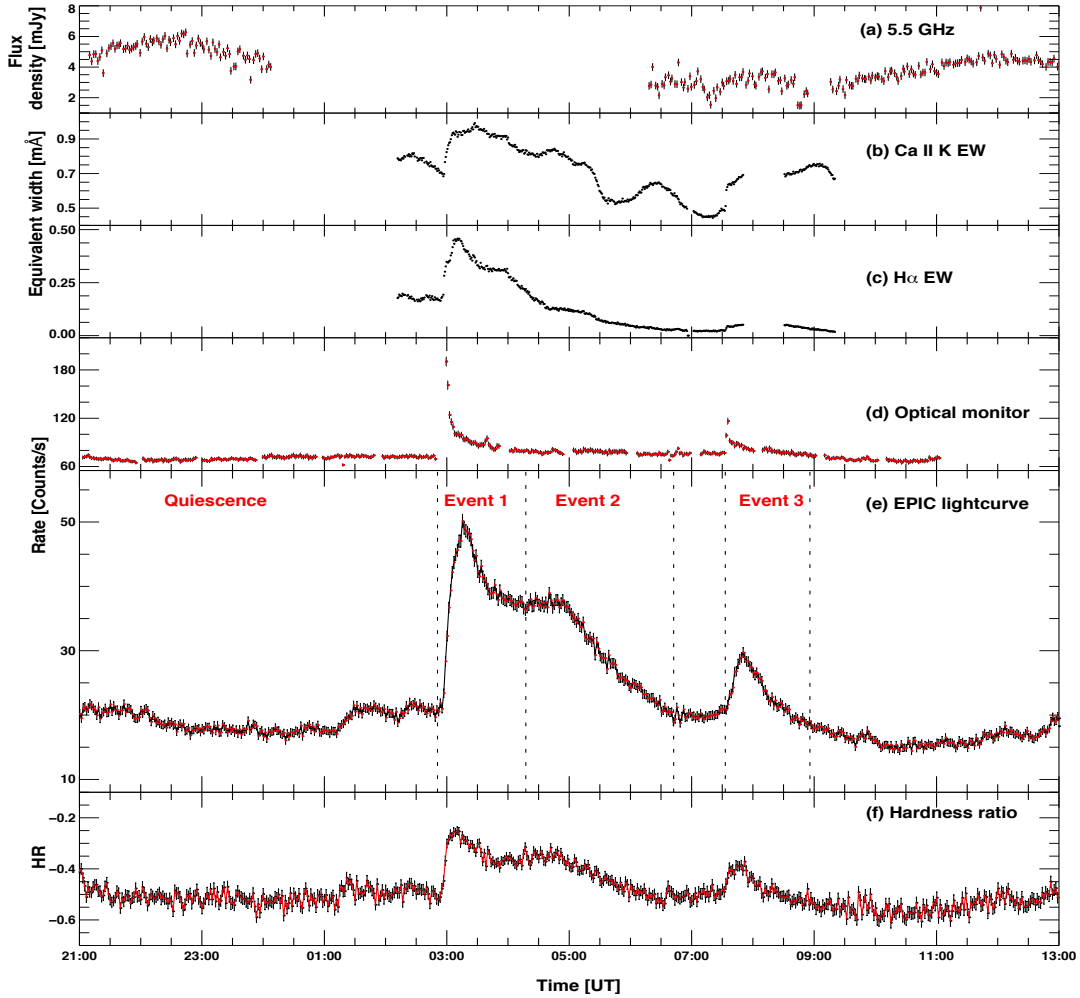


Fig. 1. Light curves of AB Dor A observed on 25 Nov 2009: (a) 5.5 GHz radio flux from ATCA observations binned to 120 s, (b) and (c) Ca II K flux and $H\alpha$ equivalent widths calculated from UVES spectra, (d) OM light curve, (e) EPIC (combined MOS and pn) light curve, (f) the EPIC hardness ratio. Light curves (d) to (f) are binned to 100 s. The vertical lines in panel (e) indicate the time segment corresponding to the events discussed in the article.

simultaneously covered by our radio observations, however, the radio light curve shows no clear response compared to the flare data in the other bands.

In addition to the observed flaring, the Ca II K EW curve between 5:00 UT and 8:00 UT shows two dimming events, which we interpret to be caused by prominence crossings. The radio light curve does exhibit a dip parallel to the second prominence crossing. Since the first prominence crossing was not covered in radio data and the radio light curve shows signs of another dip at about 9:00 UT when no prominence is noted in other diag-

nostics, it is hard to decide whether indeed the radio signal is physically connected to the prominence or only a chance coincidence. Such prominence crossings are observed typically in the $H\alpha$ line and were first noted on AB Dor and described in detail by Collier Cameron & Robinson (1989). In our $H\alpha$ EW light curve the information about the prominences is lost due to the large line width chosen for determining the EW in order to cover the broad emission component emerging during event 1. The EW light curve is totally dominated by this broad line component during event 1, however, the prominence crossing

can be seen in $H\alpha$, nevertheless, e. g. in Fig. 7, where we provide a more detailed discussion.

4. X-ray spectral analysis

In the following section we provide a detailed discussion of the X-ray observations.

4.1. Spectral fits and elemental abundances

4.1.1. Quiescent and flaring emission

The time span before 2:50 UT is free of any large temporal variations and we therefore denote this period as the pre-flare quiescence state of AB Dor A. The comparison of EPIC-MOS spectra of quiescence and of the flare rise phase shows the expected flare-related changes in spectral energy distribution yielding a substantial increase of emission measure at higher temperature. During a flare fresh material from the photosphere and chromosphere is brought to the upper layers of the stellar atmosphere, hence one may additionally expect a temporary change of the coronal abundance.

We therefore performed a detailed spectral X-ray analysis to determine plasma temperatures, emission measures and abundances in different states of activity for AB Dor A. We specifically determined the abundances relative to solar values (Grevesse & Sauval 1998) with an iterative procedure of global Xspec fits to EPIC and RGS spectra with VAPEC plasma models. In these fits, the abundances and emission measures are inherently interdependent, therefore we make our inferences from the relative changes of the fit parameters in the observations.

We compare each of the events introduced in sec.3 with the quiescent state to allow a detailed comparison between the various states. We divide the RGS and EPIC-MOS spectra into the above defined quiescent and flaring states and fit each of these spectra in the energy range 0.2-10.0 keV separately. For this comparison, we defined a fixed temperature grid consisting of the values 0.3, 0.6, 1.2 and 2.4 keV (~ 3.5 , ~ 7.0 , ~ 14.0 and ~ 28.0 MK, respectively). These temperature grids are in agreement with the best fit temperatures obtained by Sanz-Forcada et al. (2003), where three years of observations of AB Dor A were analyzed. For fitting RGS spectra, the abundance of carbon, nitrogen, oxygen, neon and iron abundances were allowed to vary freely and independently, but were fixed among all VAPEC temperature components. Meanwhile for fitting EPIC-MOS spectra magnesium, silicon, sulphur and argon abundances were allowed to vary along with oxygen, neon and iron abundances, but carbon and nitrogen abundance were fixed to values obtained from RGS which is sensitive to strong individual lines; the resulting fit parameters for the various states of AB Dor A are given in Tab. 2. As revealed by an inspection of Tab. 2, satisfactory fits (from a statistical point of view) can be obtained. Further, the quiescent state is characterised by an enhanced temperature at 0.6 keV, while during the flare a pronounced enhancement of the emission measure at 2.4 keV (28 MK) is present, and to a lesser extent at the very softest energies. As far as the abundance pattern between flare and qui-

Table 2. Fixed 4-temperature grid fit to the quiescent and the flaring states with variable elemental abundances. The abundances are relative to solar photospheric abundances (Grevesse & Sauval 1998).

Parameters	Quiescence	Event 1	Event 2	Event 3
kT_1 [keV]			0.3	
EM_1 [10^{52} cm^{-3}]	1.43 ± 0.16	2.12 ± 0.32	2.29 ± 0.29	2.37 ± 0.16
kT_2 [keV]			0.6	
EM_2 [10^{52} cm^{-3}]	4.59 ± 0.26	4.35 ± 0.46	5.53 ± 0.43	4.34 ± 0.24
kT_3 [keV]			1.2	
EM_3 [10^{52} cm^{-3}]	1.98 ± 0.19	1.16 ± 0.44	2.11 ± 0.37	1.72 ± 0.16
kT_4 [keV]			2.4	
EM_4 [10^{52} cm^{-3}]	1.79 ± 0.11	11.06 ± 0.40	8.47 ± 0.29	5.03 ± 0.11
C	0.71 ± 0.10	0.82 ± 0.20	0.67 ± 0.13	0.69 ± 0.13
N	0.90 ± 0.14	0.82 ± 0.24	0.77 ± 0.19	0.96 ± 0.19
O	0.41 ± 0.02	0.38 ± 0.03	0.34 ± 0.02	0.35 ± 0.01
Ne	0.81 ± 0.04	1.02 ± 0.08	0.93 ± 0.05	0.96 ± 0.04
Mg	0.27 ± 0.03	0.22 ± 0.07	0.28 ± 0.05	0.32 ± 0.03
Si	0.22 ± 0.04	0.25 ± 0.08	0.33 ± 0.05	0.27 ± 0.03
S	0.31 ± 0.05	0.29 ± 0.09	0.31 ± 0.07	0.33 ± 0.04
Ar	1.02 ± 0.26	0.66 ± 0.40	1.13 ± 0.32	0.76 ± 0.20
Fe	0.25 ± 0.01	0.32 ± 0.02	0.26 ± 0.01	0.29 ± 0.01
red. χ^2	1.13	1.09	1.12	1.68
D.O.F.	1832	1229	1591	1464
$\log L_x$	30.01	30.33	30.31	30.17
[0.2 – 10keV]				

escent states is concerned, there is no clear difference except for the elements Fe and Ne, which are clearly enhanced during the flaring states. strongly enhanced temperature components at 0.3 and 0.6 keV.

4.1.2. The FIP effect

The measured abundance patterns of AB Dor A during flare and quiescence are shown in Fig. 2, where we plot the abundances with respect to solar photospheric abundances against the FIP (First Ionisation Potential) of the corresponding element. Inactive stars like the Sun show the so-called 'FIP effect', where low-FIP elements like Fe, Si, Mg, etc. are enhanced in the corona when compared to high-FIP elements like C, N, O, Ne, etc.. However a reverse pattern called the 'inverse FIP effect' (IFIP) is observed in active stars, where high-FIP elements are enhanced when compared to low-FIP elements (e.g. Brinkman et al. 2001, Audard et al. 2003). As can be seen in Fig. 2, the abundance pattern of AB Dor A for both quiescent and flaring state indicates the inverse FIP effect, consistent with the results of Güdel et al. (2001).

4.1.3. Coronal densities

Using our RGS spectra we can investigate the electron densities of the coronal plasma from an analysis of the density-sensitive line ratios of forbidden to intercombination lines of helium-like triplets (N VI, O VII, Ne IX, Mg XI and Si XIII); the

6

S. Lalitha et al.: AB Doradus - outer atmospheres

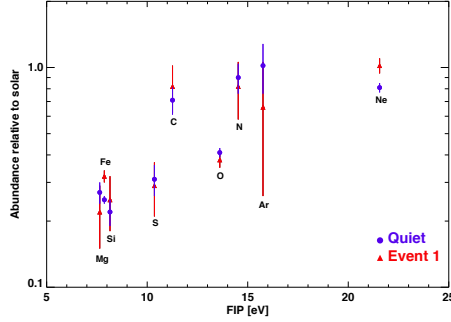


Fig. 2. AB Dor A's coronal abundance relative to solar photospheric values (Grevesse & Sauval 1998) as a function of the first ionisation potential (FIP) during quasi-quietness (blue) and event 1 (red).

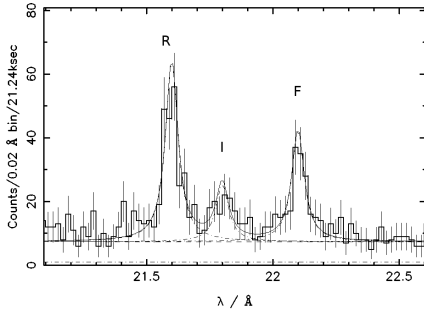


Fig. 3. The best fit density-sensitive line triplet of O VII (resonance, inter-combination, and forbidden line) for increasing wavelength) from cumulated quiescent RGS1 data .

theory of density-sensitive lines has been described in detail by Gabriel & Jordan (1969). Only the He-like triplet of O VII is strong enough in our data to be used to obtain the characteristic electron densities in the source region. In Fig. 3 we show the quiescent RGS spectrum centered on the O VII triplet, together with the best fits to the triplet lines r (resonance), i (inter-combination), and f (forbidden) provided by the CORA program (Ness & Wichmann 2002). The measured line counts and the deduced f/i ratios are listed in Table 3 for quiescence (integration time of 18 ks) and the flaring events.

In order to convert the measured f/i ratios to electron densities n_e , we approximated the flux ratio by

$$\frac{f}{i} = \frac{R_o}{1 + \frac{n_e}{N_c}}$$

where R_o is the low density limit and N_c is the critical density. We adopted the values from Pradhan & Shull (1981) of $R_o=3.95$ and $N_c=3.1 \times 10^{10} \text{ cm}^{-3}$. The errors are large in the line ratios due to the weak inter-combination line and they overlap. Hence there is – formally – no significant change in density. However, the above density estimate during flare is not

Table 3. X-ray counts measured by best fit to lines and f/i ratios deduced from the O VII triplet.

line	Quiescence ~18 ks	Event 1 ~5.5 ks	Event 2 ~8.4 ks	Event 3 ~ 5.5 ks
R (21.6 Å)	259 ± 20	101 ± 13	145 ± 15	178 ± 16
I (21.8 Å)	82 ± 14	43 ± 10	62 ± 12	63 ± 11
F (22.1 Å)	160 ± 17	49 ± 10	92 ± 13	85 ± 12
f/i	1.94 ± 0.40	1.15 ± 0.36	1.46 ± 0.36	1.35 ± 0.32
n_e [10^{10} cm^{-3}]	4.16 $^{+0.50}_{-0.65}$	5.68 $^{+0.82}_{-1.15}$	4.96 $^{+0.63}_{-0.86}$	5.20 $^{+0.62}_{-0.82}$

accounted for quiescence emission. If one takes into account the quiescent emission then the f/i ratio decreases to 0.2 ± 0.6 , 0.8 ± 0.7 and 0.4 ± 0.7 for event 1, 2 and 3 respectively, then the density could indeed be very high. However, with the current observation it is too difficult to evaluate the density variation due to the flare.

4.1.4. Emission measure, temperature, and iron evolution

In our previous investigation we only consider the integrated flare spectra. In order to investigate the temperature, the emission measure and the abundance variations in more detail, we divided the flare data into several time intervals and created spectra for each of these intervals. The first spectrum covers the flare rise and the following time intervals cover the different phases of the decay with 300s and 600s bins. Each of these spectra were fitted with 4-T APEC models, but now we kept the elemental abundances fixed except for the iron abundance, which was allowed to vary. Our models always include quiescent emission, i.e. the first two temperature components and its parameters are fixed to plasma properties of the quiescent spectrum before the flare. With this approach, we can account for the contribution of the quiescent coronal plasma to the overall X-ray emission.

In Fig. 4 we plot the evolution of the temperature, the emission measure and the Fe abundance. The temperature and the emission measure evolution exhibits a decay-like light curve and also the iron abundance increases from the quiescence level directly before the flare to a maximum during the flare peak (Fig. 4 right panel) and then decreases to pre-flare values. This can be explained by fresh plasma material which is evaporated from the photosphere and chromosphere during the flare onset. Since this evaporated plasma has a different composition with higher iron abundance compared to the quiescent coronal plasma, the iron abundance in the corona can change during a flare. For event 3 we also checked for iron abundance changes, but because of lower signal to noise in the data we find no significant change in iron abundance compared to the quiescent state.

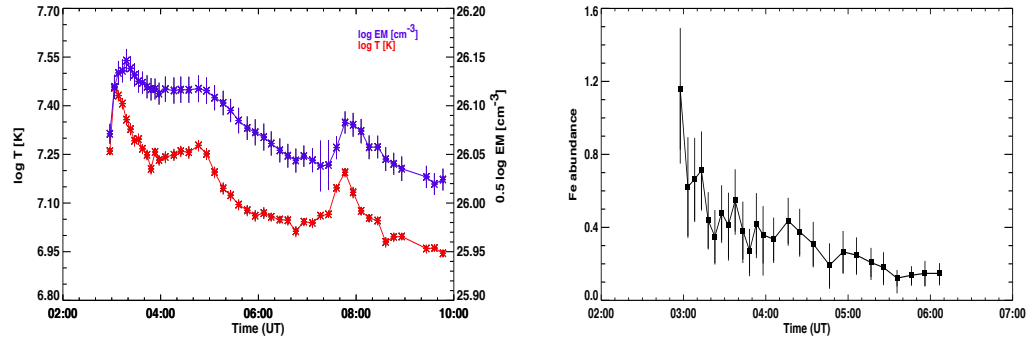


Fig. 4. Temporal evolution of flare temperature, emission measure in (left panel) and Fe abundance (right panel).

4.2. Loop properties

Observations of solar and stellar flares have revealed a correlation between the emission measure and the peak temperature of the flare. The Emission measure - Temperature (EM-T) diagram is a useful diagnostic to estimate physical quantities which are not directly observable. In order to interpret this diagram correctly, physical models are required. Hence we assume that the stellar flare is similar to a solar flare, which occurs in a localised region in the corona in a simplified geometry (single loop structure) and remains mostly unchanged during the flare evolution. As a result of decay, plasma cools down by radiation and thermal conduction to the chromosphere with characteristic cooling times. The plasma cooling time explicitly depends on the confining loop structure in particular the loop length and implicitly on density (Reale et al. 1997). Serio et al. (1991) derived a thermodynamic decay time scale of the flaring plasma confined to a single flaring coronal loop. However if there is a significant amount of heat released during the decay this may increase the decay time and therefore leads to a significantly overestimated loop length. Hence a correction factor has to be applied considering such heating during decay. Reale et al. (1997) derived an empirical formula to estimate loop lengths considering a correction factor due to significant reheating by a hydrodynamic simulation of the loop decay. We use this formula to estimate of loop lengths which has been explained in detail by Fuhrmeister et al. (2011).

Fig. 5 shows the evolution of the large flare and the two events 2 and 3 in the EM-T plane. We determine the loop half lengths L by making use of the peak temperature, the decay time derived from the light curve and the slope ζ measured from Fig. 5 for each of these events. The derived temperature from the spectral fitting of the data is corrected using the correction factors given in Reale (2007). From the EM-T diagram, the slopes measured for the event 2 and 3 are similar, hence the derived loop lengths are of the same order of magnitude (see Table 4). The derived loop length for event 1 is a factor of two greater than the stellar radius ($0.96 \pm 0.06 R_{\odot}$, Guirado et al. 2011). This is very large and this over estimate could be due to the simple model used to estimate the loop lengths. According

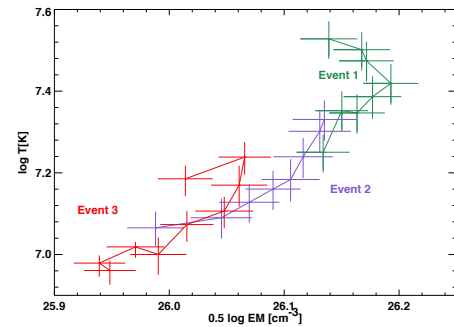


Fig. 5. Flare evolution in density and temperature for event 1 (green), events 2 (blue) and event 3 (red).

Table 4. The decay time τ_{LC} derived from the light curve, slopes (ζ) from the EM-T diagram, flare peak temperature T and deduced loop lengths L for each of the event.

Parameters	Event 1	Event 2	Event 3
τ_{LC} [ks]	8.60 ± 0.02	7.72 ± 0.03	1.90 ± 0.01
ζ [slope in Kcm^3]	1.67 ± 0.05	1.90 ± 0.12	1.80 ± 0.12
T [MK]	77.47 ± 1.04	65.79 ± 1.31	55.43 ± 1.85
L [$10^{10} cm$]	12.21 ± 0.08	8.86 ± 0.05	2.21 ± 0.04

to this model we assume that the flare occurs in a single loop with no further reheating, however its clear from the light curve that this flare occurs in a much more complicated geometric loop.

5. Chromospheric properties of AB Dor A

Optical lines, sensitive to chromospheric activity are found throughout our UVES spectra, most of them in the blue wavelength range up to about 4000 \AA . For AB Dor A, the strongest among them (Balmer lines, Ca II H & K and Na I D lines) show variations also outside of flares, but only during flares shall

low metallic emission lines show up. To illustrate that effect, we show in Fig. 6 for event 1 an arbitrarily chosen wavelength range both as an original spectrum and with a quiescent spectrum subtracted. The emission lines can only be noticed in the subtracted spectrum. This is in contrast to active mid M-dwarfs like Proxima Centauri or CN Leo, where the quiescent continuum in the blue wavelength range is so weak, that the emission lines easily outshine the continuum, especially during flares. Also, the relatively strong photospheric continuum explains, why in comparison to these very late-type stars, fewer emission lines are found in the spectrum of AB Dor A (Fuhrmeister et al. 2008, 2011). Moreover, the high rotational velocity strongly broadens the lines leading to a lower amplitude. On the other hand, the rotationally broadened emission lines offer the chance to identify emission of single active groups, if strong lines show subcomponents.

In the following we first comment on the evolution of strong lines and present an emission line catalog for events 1 and 3. Then we concentrate on the analysis of some selected lines.

5.1. Chromospheric line evolution overview

As an example of the development of an emission line throughout our observations we show an intensity map for the $H\alpha$ and the Ca II K lines in Fig. 7. For the $H\alpha$ line we subtracted a PHOENIX spectrum ($T_{eff}=4900$ K and $\log g=4.5$, for more details see below), while for the Ca II K line we show the original spectrum. The main flare onset can be noted as a bright horizontal line directly before 3:00 UT. For both lines one can see the line broadening directly after flare onset; for the $H\alpha$ line, there is a dizzy brightening on the red side up to 6575 Å, while for the Ca II K line the core is broadened. The Ca II K line shows its strongest brightening directly at flare onset. In contrast, the $H\alpha$ line shows the strongest brightening about half an hour later and it seems to be drifting from blue to red, making it questionable, that the brightening is really related to the main flare. Also the third event shows up in the intensity map, starting at about 7:30 UT, directly before the second observation gap and extending to the end of the observations.

Beside these brightening events, a few dim structures can be noted in the intensity map: between 5:00 and 7:30 UT, there are two large prominences seen as absorption features drifting across the line profile. This phenomenon was first described in detail by Collier Cameron & Robinson (1989). We note that in our spectra the prominences are not only seen in $H\alpha$ – which is the line, which most authors use to analyse such prominences – but also in the Ca II K line. The latter line is used by very few authors, e.g. Parsons et al. (2011) and Dunstone et al. (2006). We also searched for X-ray absorption at the time of the crossings of the prominences, but could not find evidence for an X-ray imprint. However, using the X-ray data, we could estimate an upper-limit to the hydrogen column density of the prominence as $n_H=9\times 10^{18}$ cm⁻³.

Judging from the $H\alpha$ line, and compared to previous observations, AB Dor A is in a state of medium activity during the whole observation. The absorption transients in the orig-

inal spectra reach a depth of about 0.8-0.85, which seems to be quite typical compared to the findings of Collier Cameron & Robinson (1989) and Vilhu et al. (1991). The latter detected also significant $H\alpha$ emission in the unsubtracted spectra, which they ascribe to flaring activity or a high density prominence. The flaring activity in our observations does not exhibit such a pronounced $H\alpha$ emission line, in line with the X-ray observations, which would also suggest a medium activity state during our observations.

5.2. Line fitting procedure

To access the properties of individual chromospheric emission lines, we performed fits using up to three Gaussian components with width σ , amplitude and central wavelength as free parameters for each component. Since we are dealing with 460 spectra the lines were fitted semi-automatically, i.e., we checked the fit quality by eye for each spectrum and line, and if the fit did not represent the line well, we changed starting parameters and/or the parameter restrictions. The lines could not be fitted in the original spectra, because the line shapes are often too complicated, e.g. the Na I doublet being an absorption line with some filling in, but showing no emission core. We checked the possibilities of subtracting either an observed quiescent spectrum or a PHOENIX photospheric model spectrum (Hauschildt et al. 1999). For the latter we determined the best fitting PHOENIX spectrum for different quiescent spectra of AB Dor A using a model grid with T_{eff} ranging from 4700 to 5200 K in steps of 100 K, with $\log g$ ranging from 3.5 to 5.0 in steps of 0.5, and with the rotational velocity ranging from 60 to 120 km s⁻¹ in steps of 10 km s⁻¹. We used solar metallicity. Our best fitting values are a $\log g$ of 4.5 and 4900 ± 100 K for the effective temperature. We find 100 ± 10 km s⁻¹ for the projected rotational velocity, in agreement with the value of 91 km s⁻¹ adopted by Jeffers et al. (2007). The PHOENIX model spectrum describes the photospheric lines generally well, though the amplitude of individual lines differ in most cases.

As individual lines we fitted the Ca II K line (the H line is too complicated due to blending with Balmer line emission), the Na I doublet at 5889 and 5895 Å, the He I D₃ line, $H\alpha$, $H\beta$, $H\delta$, and as an example of a shallow metal line the Si I line at 3905 Å. The Si I and the He I D₃ line were both fitted using a running mean, i.e. for each fit two consecutive spectra were averaged, nevertheless stepping through every spectrum.

5.2.1. Observed vs. simulated spectrum as quiescent template

As shown in Fig. 6, a quiescent template spectrum must be subtracted from the flaring spectra in order to identify and analyse the emission lines. Using a model spectrum or an observed spectrum as quiescent standard, has both advantages and disadvantages.

When subtracting a PHOENIX model spectrum, the deviations of the model from the observed photosphere may be as large as the amplitudes of the low amplitude metallic chromospheric emission that emerges during the flare. Therefore,

S. Lalitha et al.: AB Doradus - outer atmospheres

9

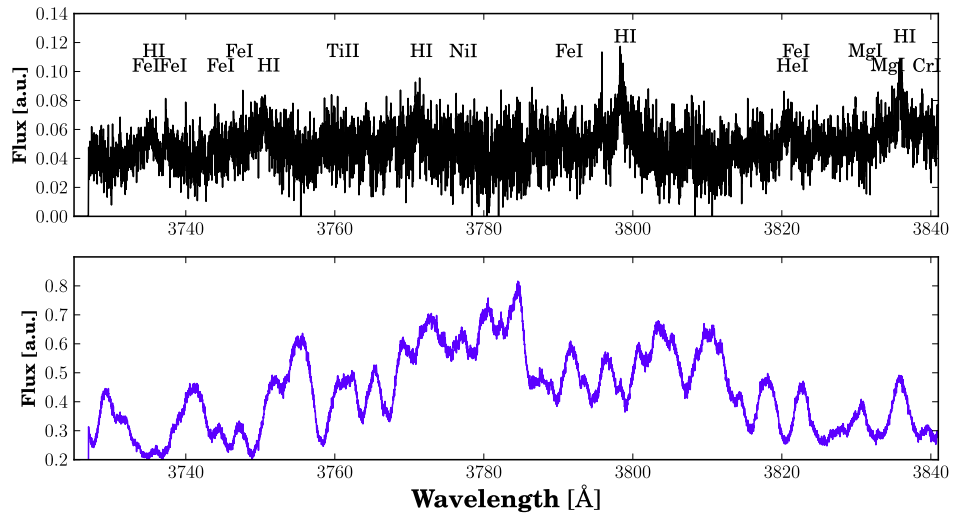


Fig. 6. Flare onset spectrum of AB Dor A in an arbitrary chosen wavelength range covering the blue end of our observations including the Balmer lines H9 – H13. Top: The flare spectrum with a quiescent spectrum subtracted. The identified emission lines are labelled. Bottom: The original flare spectrum.

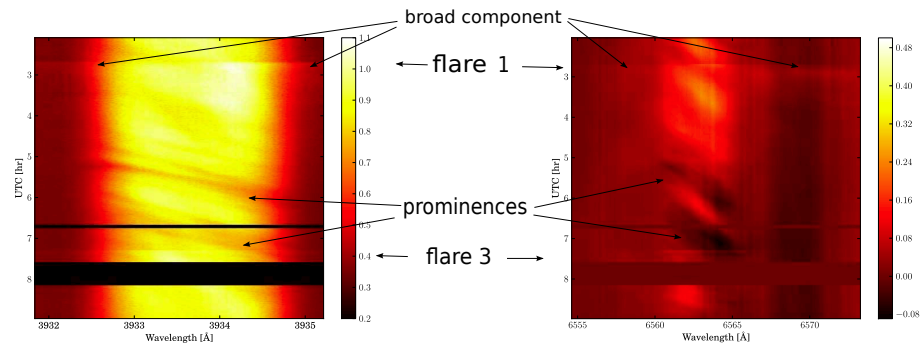


Fig. 7. Intensity map of the H α line (right – with a PHOENIX photospheric spectrum subtracted) and for the Ca II line (left – original spectrum, no spectrum subtracted). The two horizontal bars indicate observational gaps.

a PHOENIX model can only be used for strong emission lines. For these lines the general chromospheric emission leading to the filling-in of the lines (or to emission cores), is often so large that after subtracting the PHOENIX spectrum one ends up with a strong emission line, with the flare and emission of single active regions playing only a minor role, that cannot be properly modelled with an automatic fit. This is only possible for H α line, where the emission of the flare and single components is strong enough to show up against the emission core.

Subtracting an observed non-flaring spectrum as a proxy for the quiescent spectrum has the disadvantage that the spectra change significantly on short time scales (about 10 minutes), with single features of the line moving either in central

wavelength or changing in amplitude. For example, in the H α line, subtracting an average of the first three spectra from each single spectrum, after only about 10 minutes of observations an additional emission feature is turning up, and again about 10 minutes later, an absorption component manifests itself, but these features are only defined relative to the subtracted averaged spectrum. E.g. the absorption feature is caused by dimming and shifting of a strong emission component in the averaged quiescent spectrum, and therefore not a 'real' absorption component. This effect is illustrated for H α line in Fig. 8, where the PHOENIX subtracted lines are shown and one can note the shifting and dimming. An example of an absorption artefact can be found in Fig. 12 in the last two sub-frames. This subject

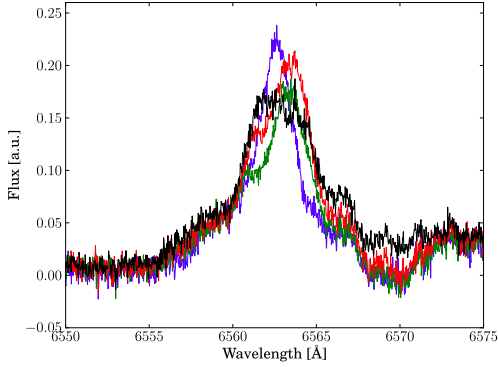


Fig. 8. Examples from the evolution of the $H\alpha$ line after subtraction of a PHOENIX spectrum in the first hour of observations, covering the main flare. Blue: spectrum at 2:13 UT (first spectrum taken), green: spectrum at 2:48 UT, red: spectrum at 2:58 UT (flare onset), black: spectrum at 3:05 UT. The additional flux in the black spectrum (best seen at about 6557 and 6570 Å) is caused by the broad line component.

of the distributed and fast changing chromospheric emission is also discussed in Sect. 6.5.

Nevertheless, for several lines the fitting process is best done using an observed quiescent spectrum. This method gives reliable results for the lines that are not present before the flare or show up only shortly before the flare (all lines and broad line components except the Balmer lines and the Ca II K narrow line components).

In the following sections we present our findings from the line fitting.

5.3. Catalogue of emission lines

For events 1 and 3, a number of chromospheric metal lines besides Ca II H & K show up in the spectrum. Event 2 does not influence the shallow metal lines. Therefore, we compiled an emission line list for events 1 and 3. For the line identification we generally used the Moore catalogue (Moore 1972). The line fit parameters – central wavelength, half width, and flux in arbitrary units – and (tentative) identifications including some comments can be found in Table 5. We only show a few rows of this table in the paper as an example, while the whole table is provided in electronic form at CDS.

5.3.1. Event 1

For accessing the metal line properties, we averaged the first and second flare spectrum and subtracted an averaged quiescent spectrum made of the first three spectra of the night. The flare onset spectrum alone contains a number of emission line candidates that are lost in the average spectrum. However, these additional lines are very noisy and would only allow insecure identifications.

We identified 90 lines in the blue arm and 11 lines in the red arm spectra with a mean wavelength shift of 39.6 ± 9.6 km s⁻¹ (applying a radial velocity of 32.5 km s⁻¹). The rather large scatter is caused by blended lines, for which the (probable) components are given as a remark. A few lines have possible blends with an unknown line or rather insecure identification and are marked with 'blend??' in the remarks. Because of the high noise level the line list cannot be considered complete concerning weak emission features.

Most of the blue emission lines can be detected for between 20 and 50 minutes after flare onset. Only the Balmer line and Ca II H and K emission persist after an hour of flare emission, but the line shifts and the decay of the broad line suggest, that the main part of this emission is not flare-related any more.

5.3.2. Event 3

During event 3 only few emission lines appear; they are a subset of the lines found during event 1. Since the strong lines, that also react during the event 3, show strong changes in time, we took the average of the three spectra directly before the onset of event 3 as quiescent spectrum. We could detect a line flux for 17 emission lines. The lines have an average line shift of -23.9 ± 13.2 km s⁻¹, which differs by more than 60 km s⁻¹ from the velocity measured for event 1.

5.3.3. Comparison to other line catalogues

We compared our AB Dor A line list to that of Proxima Centauri given in Fuhrmeister et al. (2011), which have an overlap between 3720 and 4485 Å and between 6400 and 9400 Å. We found that most of the lines in the AB Dor A flare coincide with the strongest lines in the Proxima Centauri flare. Nevertheless, there are 21 lines in the AB Dor A flare not found in the Proxima Centauri flare (see remarks in the line table). We compare therefore the line list also to the one of the CN Leo mega-flare (Fuhrmeister et al. 2008), with which the wavelength overlap is much smaller, though. In the overlapping line region all lines not found in the Proxima Centauri list could be identified besides one line.

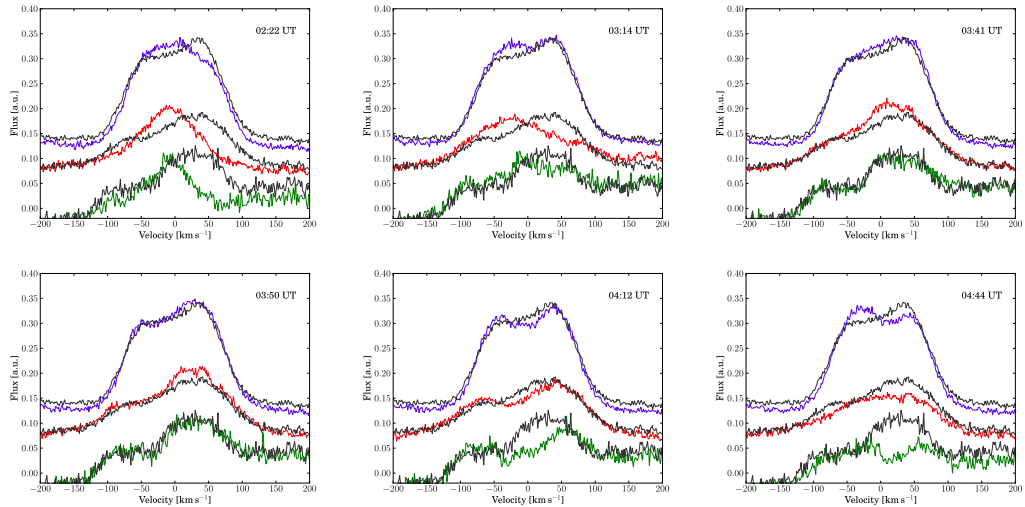
5.4. Timing behaviour of event 1

The flux in the three strong lines $H\alpha$, $H\beta$, and less pronounced for Ca II K, shows a slow increase and (later on) decrease well before the event 1 (see Fig. 11; the $H\alpha$ and Ca II K fluxes peak at about 2:30 UT, while the $H\beta$ flux peaks at about 2:40 UT).

A time series comparing the cores of the three strongest lines with a PHOENIX spectrum subtracted is shown in Fig. 9, where the lines are scaled for convenience. The lines in the spectrum taken at 2:22 UT show a single-peaked line center, that decays and develops a double-peaked structure *before the flare* for all three lines with one peak at about 40 to 45 km s⁻¹ and a second broader and shallower peak at about -80 km s⁻¹ for the $H\alpha$ and $H\beta$ lines and about -50 km s⁻¹ for the Ca II K line. This large difference in velocity cannot be explained only by different line forming heights and stays unexplained. This

Table 5. Section of the line catalogue corresponding to the wavelength interval shown in Fig. 6. The whole table is accessible electronically. See Sect. 5.3 for details.

central wavelength [Å]	half width [Å]	flux a.u.	catalogued wavelength [Å]	ion	multiplet	comment
3733.78	0.12	0.003	3733.319	FeI	5	
3735.18	0.47	0.017	3734.370	HI	3	blend with 3734.867 FeI 21
3737.42	0.13	0.007	3737.133	FeI	5	
3743.80	0.15	0.005	3743.364	FeI	21	
3746.32	0.27	0.005	3745.901	FeI	5	blend with 3745.561 FeI 5
3750.59	1.06	0.042	3750.154	HI	2	blend with 3749.487 FeI 21
3759.88	0.11	0.005	3759.291	TiII	13	
3771.09	0.45	0.026	3770.632	HI	2	
3776.35	0.13	0.006	3775.572	NIi	33	blend?? not in ProxCen list, but in CNLeo list
3790.58	0.10	0.005	3790.095	FeI	22	not in ProxCen list, but in CNLeo list
3798.44	0.43	0.030	3797.900	HI	2	
3820.25	0.09	0.005	3819.606	HeI	22	blend with FeI 20 at 3820.428
3821.03	0.32	0.020	3820.428	FeI	20	blend with HeI 22 at 3819.606
3829.88	0.05	0.002	3829.355	MgI	3	
3832.89	0.09	0.003	3832.303	MgI	3	
3835.95	0.32	0.029	3835.386	HI	2	
3836.52	0.25	0.008	3836.070	CrI	70	not in ProxCen and in CNLeo list
3838.86	0.07	0.002	3838.294	MgI	3	

**Fig. 9.** Spectra of $H\alpha$ (red), $H\beta$ (green), and $Ca II K$ (blue) with a PHOENIX spectrum subtracted and scaled for convenience. For comparison the PHOENIX-subtracted flare spectrum (2:58 UT) of each line is over-plotted in black. A different behaviour of the lines is seen, e.g. at 3:14 UT, where the $Ca II K$ is still double peaked, while in $H\alpha$ and $H\beta$ the peak at 40 km s^{-1} has already decayed. Also, the rotationally induced shift of line components is seen, e.g. in $H\alpha$ the main component which moves from about -40 (3:14 UT) to $+20$ (3:41 UT), $+30$ (3:50 UT), and finally to $+50 \text{ km s}^{-1}$ (4:12 UT).

second peak can be seen at 6561 \AA in Fig. 8 for the $H\alpha$ line in the green spectrum taken at 2:48 UT. Also it can be seen in the flare spectrum in Fig. 9, since the blue peak is nearly undisturbed by the flare. One can see the blue feature migrating redwards until it reaches $40\text{-}50 \text{ km s}^{-1}$ at about 4:10 UT (see Fig. 9 or Fig. 7). We interpret the blue peak as the signature of an active region rotating into view.

Event 1 occurred in the red-shifted half of the line, while the blue emission peak is nearly undisturbed. After event 1, for $H\alpha$ and $H\beta$, the line flux in the flaring component decays rapidly below the flare onset amplitude, while for the $Ca II K$ line the amplitude stays at the level of flare onset (see Fig. 9, 3:14 UT). This indicates that the heating of the flare site diminishes in the upper chromosphere, while in the lower chromo-

mosphere the heating persists. This state persists for about 40 minutes during which the blue shifted component brightens considerably and shifts red ward with a drift velocity of about 90 km s^{-1} per hour and eventually reaches the about 50 km s^{-1} of the original flare site at the stage it also reaches maximum brightness (about 3:47 UT). In Fig. 9 this corresponds to the peaks seen in $H\alpha$ and Ca II K starting at flare peak at about -70 (-50 for Ca II K) km s^{-1} , seen at 3:14 UT at about -40 km s^{-1} , at 3:41 UT (and 3:50 UT) the peak reaches about 40 km s^{-1} . This drift is better seen in the shift of the fitted Gauss kernels for the lines. This brightest episode in $H\alpha$ at about 3:45 UT can also be noted in the intensity map. Furthermore, another active region rotates into view in the blue line wing, which can be seen in the spectrum taken at 4:12 UT (Fig. 9). The difference between $H\alpha$ and $H\beta$ (the $H\alpha$ amplitude is similar to the one during the flare, while the amplitude of $H\beta$ is well below the flare values) may be explained by a different optical depth of the two lines. While for $H\alpha$ and $H\beta$ both components decay further, the blue component of the Ca II K line brightens until about the spectrum taken at 4:45 UT, which again indicates the different heating at different heights.

In the following we discuss the behaviour of the lines during event 1 in more detail.

5.4.1. Broad line components

During the event 1 the Balmer lines, He I D_3 , as well as the Ca II H and Ca II K lines show a very broad component, whose velocities and lifetimes differ significantly from the narrow components. For the He I lines at 3819.6 , 4026.2 , and 6678.1 \AA the amplitudes are not strong enough to reveal a broad component, although the latter shows at least a second component. Such a broad component has been noticed mostly in M dwarf flares (Crespo-Chacón et al. 2006; Fuhrmeister et al. 2008, 2011), however, also for young K-dwarfs (Montes et al. 1999 and references therein). Such broad line components, which can be blue- or (more often) red-shifted, are often ascribed to a moving turbulent plasma component. Broadening, especially of hydrogen lines, may also be caused by the Stark effect. E. g. for a flare on Barnards star, Paulson et al. (2006) attributed a symmetric line broadening to the Stark effect. Also for the Sun, Johns-Krull et al. (1997) found evidence for Stark broadening in higher order Balmer lines during a strong flare.

In Fig. 10 we show the results of our Gaussian fit to the broad component of the lines discussed above. All broad line components exhibit red shifts and no blue shifts. The larger shift of the $H\alpha$ line that starts few minutes after flare onset is most probably caused by additional red shifted narrow line components, that are not included in our model but influence the fit of the broad component (see Fig. 12).

The fluxes of the Ca II K and the He I D_3 line peak later and more gradually than the Balmer lines. For the Ca II K line the observed behaviour could be explained by a height effect and corresponds directly to the behaviour of the main component (see below). For the He I D_3 line the broad component is shallow and therefore noisy, which may hide a true peak directly after the flare onset (the earlier flare onset for this line is

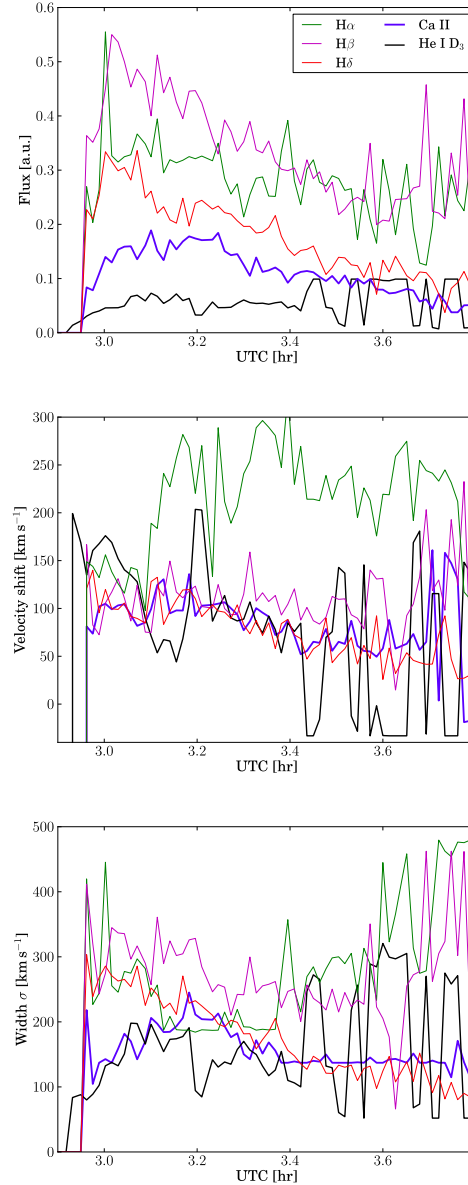


Fig. 10. Characteristics of the broad line component: Top: Flux amplitude; Middle: Velocity shift of the line centre; Bottom: Gaussian width in km s^{-1} . The legend applies to all panels. The earlier rise in the He I D_3 line is caused by using a running mean for the fitting process. The large velocity shifts in $H\alpha$ are caused by line subcomponents influencing the fit.

an artefact of the running mean used for the fitting and not of physical origin).

The broad component vanishes about an hour after flare onset as illustrated by the decaying line flux seen in Fig. 10.

5.4.2. Stark broadening versus turbulent broadening

Although the uncertainties of the fitted Gaussians are rather large, as can be seen from the scatter of the measurements, we can discern Stark broadening from turbulent broadening in our data. As seen in Fig. 10 there is a clear trend, that from flare onset until about 3.1 UT the Balmer line widths are larger than the widths of the helium and Ca II K lines. We ascribe this difference to Stark broadening. For a notable Stark broadening of helium lines, very high densities of at least 10^{16} cm^{-3} would have to be reached (Ben Chaouacha et al. 2007), which is not expected for this smaller flare. Therefore, we argue that the broadening observed in the He I D₃ and Ca II K is turbulent broadening, while the additional broadening observed in the Balmer lines is caused by Stark broadening.

We note that Stark broadening should affect higher members of the Balmer series more strongly (Švestka 1972; Worden et al. 1984). While H β is as broad as or even broader than H α , this is not found for the H δ line. However, the signal to noise of the spectra is decreasing towards the blue as is the amplitude of the Balmer lines with increasing order. Therefore, even broader tails may be hidden in the noise. For even higher members of the Balmer series it is not clear, if their broad line components start to merge. Moreover, also Paulson et al. (2006) found less broadening in higher Balmer lines and gave NLTE effects as possible reason, which affect low order lines most.

Although Stark broadening is present in the Balmer lines, we choose to fit the lines with two or three Gaussian components, instead of a Voigt profile. Asymmetric Stark profiles are expected for moving plasmas, but would have to be calculated with a full 3D hydrodynamic and radiative transfer code, as done by Allred et al. (2006), which is beyond the scope of this work. To obtain estimates of the velocities of the plasma movements a Gaussian approximation should be sufficient.

5.4.3. Narrow line component

The evolution of the flux of the main narrow line emission component is shown in Fig. 11. The H α line is fitted after subtracting a PHOENIX spectrum and scaled by 0.43, while all other lines were fitted using a quiescent spectrum of AB Dor A for subtraction. Also, since the H α line displays more than one narrow component, the fit switches to another component directly after flare onset, which is marked in light green in Fig. 11. Also, the dip between 3.5 and 4.0 UT in H α flux is not real but is caused by the fit shuffling flux from one to another fit component (the total H α flux peaks at about 3.75 UT).

5.4.4. Subcomponents of the H α line

We also searched for weaker subcomponents in the H α line. As discussed in Sect. 5.2.1 they are more pronounced, when sub-

tracting a quiescent spectrum of the star instead of a PHOENIX spectrum. Fig. 12 shows the evolution of the H α line *only during a few minutes* around flare onset; for all panels the averaged spectrum taken between 2:56 and 2:58 UT has been subtracted as a proxy for the quiescent state. The figure nicely illustrates the complex and rapidly evolving multi-component structure of the chromospheric emission during the impulsive phase of the flare. Obviously, for most spectra a fit with only three components is not sufficient to cover all components. However, a fit with four or more components is even more unstable than a fit with three components and can usually not be constrained by the data. Beside the main flaring component, there are several short-lived and a few longer lived narrow components of which the bluest at about 6561 Å is growing stronger during the decay of the flare. At 3:05 UT, about ten minutes after flare onset, an absorption component appears to emerge. However, it is most likely an artefact, i. e. it results from changes in the non-flaring line components relative to the pre-flare state. On the other hand we argue, since notable changes in the non-flaring spectrum seem to appear on time scales of about 10 minutes, that the subcomponents in H α during the first few minutes of the flare are real. Their development (appearing, shifting, and disappearing) takes place on much shorter time scales.

We interpret these weak subcomponents of the H α line as signatures of shock waves in the chromosphere. Alternatively they could be small dense 'blobs' created during the flare, moving at high intrinsic velocities. Some of them can only be identified in one or two consecutive spectra, translating into a life time of one to two minutes. We counted up to six such subcomponents in a single spectrum (2:59 UT, two spectra after flare onset), moving with velocities ranging from -270 km s^{-1} to $+260 \text{ km s}^{-1}$. If these subcomponents are present in more than one spectrum they normally decelerate, i. e. blue shifted features shift red wards, while red shifted features show a drift to bluer wavelengths. This strengthens our confidence that these features are not artefacts. The only other line besides H α with a sufficient signal to noise level to identify subcomponents is the Ca II K line. There we find a comparable number of subcomponents, but we cannot identify any of the Ca II subcomponents with H α subcomponents even for the stronger ones. This is caused partly, by the different velocity scatter ranging from -390 to $+190 \text{ km s}^{-1}$. Actually, this is not surprising, if these subcomponents are indeed tracers of material of different temperature potentially at different heights of the atmosphere.

6. Discussion

6.1. Comparison between X-ray and optical signatures

During the 58 ks exposure of XMM-Newton, three medium sized flares occurred in a time interval of only 22 ks, while the remaining light curve showed no major flux enhancement. In the same time interval also the OM light curve shows flux variations, coinciding with the X-ray events. The chromospheric emission lines show more complex variations, but it is certainly straightforward to assume that these different wavelength bands trace the same events in different parts of the atmosphere. Furthermore, one may ask, whether the three events originate

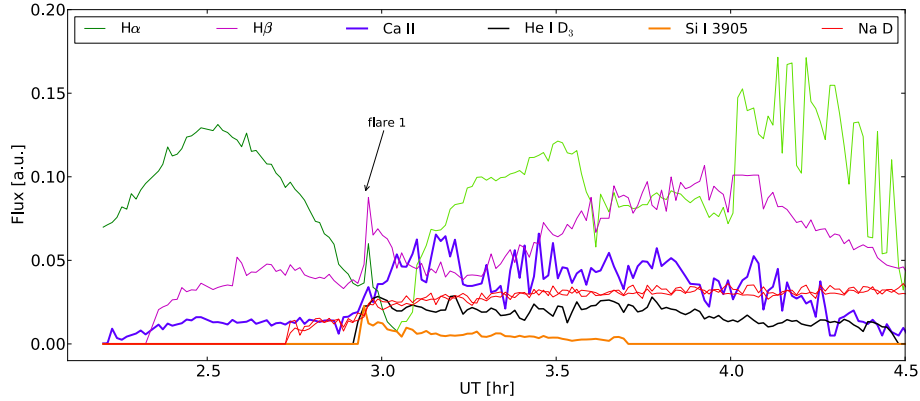


Fig. 11. Amplitude of the Gaussian fit for the strongest chromospheric emission lines. In case of multiple line components, the strongest narrow fitting component is shown ($H\alpha$, $H\beta$, Ca II K). The time interval covers the first 2.3 hours of observations, including the flare onset at 2:58 UT. For fitting $H\alpha$ a PHOENIX spectrum has been subtracted; the change of the green hue indicates, that the fit switched to another line component (see text). Colours are indicated in the legend; both Na I D lines are denoted in red.

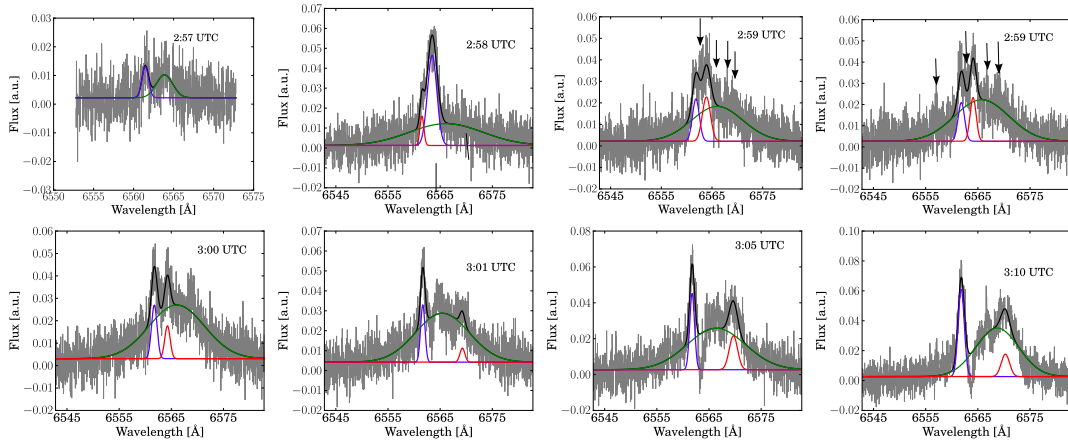


Fig. 12. Fit examples of the $H\alpha$ line with the observed quiescent spectrum subtracted. The data is shown in grey, the fit components are shown in green, blue, and red, and the resulting fit is shown in black. The data contains additional narrow short-lived line components, which are not fitted here, but are indicated by arrows for the two most complicated spectra at 3:59 UT. Between 3:00 and 3:01 UT the fit switches to another line component. The second spectrum in the upper row shows the flare onset. In the last two spectra one can note an absorption artefact at about 6563 Å which is caused by the dimming of a pre-flare line component.

from the same loop or arcade. In the following we discuss this for each of the events.

6.1.1. Event 1

The onset of the main flare shows strong evidence for the Neupert effect when comparing X-ray and optical/UV light curves. The chromospheric emission lines start to react and also peak at 2:58 UT while the X-ray emission peaks at 3:16 UT.

During a flare, the time integral of emission due to the accelerated particles (like $H\alpha$ emission, white-light emission) resembles the rise of the flare light curve in the soft X-rays which is called the Neupert effect. In Fig. 13, we plot the time derivative of the soft X-ray light curve (only EPIC) and the optical light curve. Since there is no data available from the OM during the flare rise we obtained the optical light curve using the UVES continuum spectra between the wavelengths 3895 Å - 3920 Å. We note that during flare rise the derivative of the X-ray light

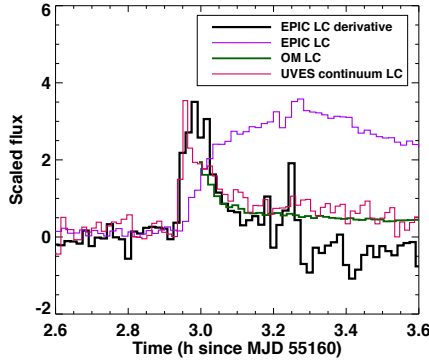


Fig. 13. Neupert effect observed during the large flare on AB Dor A. Depicted are the combined EPIC X-ray light curve in violet, its time derivative (smoothed by five bins) in black, the OM light curve in green and the UVES continuum light curve in red.

curve matches the shape of the optical light curve. It is also clearly seen, that the optical/UV peak precede the X-ray peak (see Fig. 13).

The chromospheric lines do not react strongly to the flare in amplitude. In contrast to the X-ray and optical/UV light curve they exhibit stronger emission before and after the flare events; i. e. the flare does not dominate the chromospheric line emission. Despite the weak reaction of the chromospheric lines in amplitude, the strong lines show turbulent broadening, the Balmer lines even show Stark broadening and in the $H\alpha$ line on top of that single short-lived shocks can be identified. All this is accumulating evidence that for this event, the above mentioned picture of a flare affecting different atmospheric layers is certainly correct.

6.1.2. Event 2

Event 2 has its broad X-ray maximum between about 4:20 and 4:50 UT followed by a slow decay until about 6:00 UT. Between about 4:15 and 4:45 UT there is a slight brightening in a component of $H\alpha$ at a velocity of about -35 km s^{-1} , which is not strong enough to be noticed in the intensity map (Fig. 7) nor in the main component (Fig. 11). It is most pronounced in the Ca II K line, where it even shows up in the intensity map as a slight brightening. As an example we show the central part of the Ca II K line covering the times of interest in Fig. 14. The feature is not seen in $H\beta$, which may be due to the noise level in this line.

Because of the slow rise and decay of the peaks in the X-ray and the chromospheric lines light curves, it is hard to decide, whether this brightening of the chromospheric lines is physically connected to the X-ray brightening.

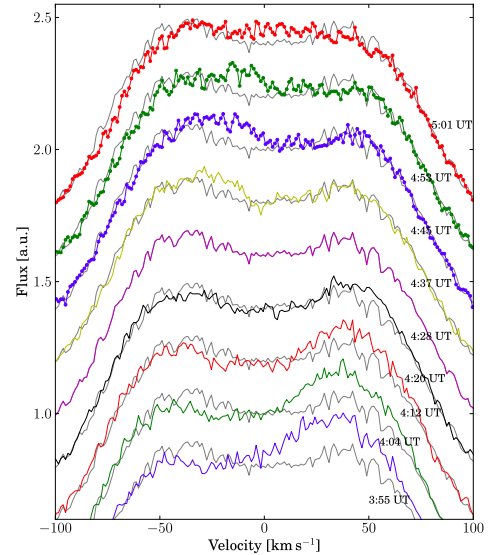


Fig. 14. Central part of the Ca II K emission line for different times. The spectra are offset for convenience. A PHOENIX spectrum is subtracted. The spectrum taken at 4:28 UT is always over-plotted for better comparison.

6.1.3. Event 3

Event 3 is characterised by a peak at 7:46 UT in X-rays, starting at 7:34 and lasting until 8:16 UT. Unfortunately, the third flare falls partly in a gap of the UVES observations. Nevertheless, the flare onset is covered and observed at about 7:34 UT, both, in the OM and in the chromospheric emission lines. The chromospheric emission lines all show a rather weak reaction compared to X-rays and the OM. They exhibit a very broad peak with the Na I D lines showing increasing flux until the end of the observations at about 9:20 UT. Ca II K is peaking at about 9:00 UT, while $H\alpha$ appears to peak during the observational gap.

6.2. Comparison to the radio data and to other work

While the X-ray and optical lightcurve show clear correlation for two of the three events, the radio data covering event 3 shows no flaring activity. Also the correlation between the radio data and the EW of the chromospheric lines during the second prominence crossing is ambiguous.

The timing of different flares for multi-wavelength observations has been extensively discussed by Osten et al. (2005), who compare parallel radio, optical, UV, and X-ray observations for the young flare star EV Lac and found that flares in different wavelength bands need not have counterparts in any

other wavelength bands. Also Kundu et al. (1988) found little correlation between radio and X-ray variations on the flare stars UV Cet, EQ Peg, YZ CMi, and AD Leo. While these two studies found no strong correlation between different wavelength bands, other studies did. E. g. Liefke et al. (2009), for the flare star CN Leo found correlations between X-rays, chromospheric lines, and the photospheric continuum at least for the larger events, while smaller events were not seen in all wavelength bands. The present study is in line with the latter: For the larger events 1 and 3, there is a reaction in X-rays, OM, and the chromospheric lines. For event 2 there is only a very small reaction in the OM and in the chromospheric lines, which are not clearly linked to the broad X-ray event 2. Therefore, the event appears to be largely confined to the corona. As the above mentioned authors, we could not find a correlation between the radio data and other wavelength bands for event 3.

6.3. Location of the flaring regions

During event 1 the chromospheric lines show the same velocity shift of $39.6 \pm 9.6 \text{ km s}^{-1}$. Most of these lines appear during the flare onset, but the Balmer lines and other strong lines can be identified before the flare as well. These strong lines show a slow velocity drift over a long time interval, but no discrete jump in their velocity at flare onset. This suggests, that the projected rotational velocity of the star and not the intrinsic velocity of the flaring material dominates the velocity of the main line component. This is further supported by observations of slowly rotating M dwarfs, for which line shifts during flares are normally not observed. E. g. Reiners (2009) searched for radial velocity jitter in UVES observations in the M dwarf CN Leo and found a jitter of below 1 km s^{-1} even during the observed mega flare.

Under the assumption, that the velocity shift in the chromospheric lines is dominated by rotation and the chromospheric line emission originates in a region very near the stellar surface, one can try to locate the flaring active region. Using an inclination of 60° of the stellar rotational axis (Kuerster et al. 1994; Donati & Collier Cameron 1997) and 90 km s^{-1} as projected rotational velocity, the active region would be about 25° off the center of the stellar disk in terms of longitude, if it is located at equatorial latitude and at about longitude of 60° , if located at 60° latitude. Thus, the active region could in principle be also circumpolar, with 60° being the lowest circumpolar latitude and therefore could allow to follow the flare site of event 1 rotating onto the 'rear' hemisphere (i. e. the hemisphere behind the pole as seen from Earth). This would imply a reversal in the velocity shift, yet, we see no such reversal of the velocity shift and the fitted Gaussian components all show increasing velocity (although the fit occasionally switches to other components, which may hide such a reversal). Also, the line velocity of about 40 km s^{-1} puts the active region below 64° , allowing it to be only marginally circumpolar. Therefore we exclude a high latitude, circumpolar active region.

To restrain the location of the active region further in latitude, we computed the times, for which the flare would still be visible for different latitudes. However, for the 45 minutes

flare duration (the time span for which the metal lines and the broad line component can be identified), only latitudes lower than about -30° are excluded. As another approach we measured the *drift velocity* of the lines to be about $20 \text{ km s}^{-1} \text{ h}^{-1}$ during event 1. This drift velocity implies a latitude of about 60° . However, the highest possible velocity for this latitude at the surface of the star is about 45 km s^{-1} , which is exceeded by far by the measured velocities of about $60\text{-}70 \text{ km s}^{-1}$ (for the Na D lines). A possible solution is, that the active region is located at some distance to the stellar surface. But distances up to 1 stellar radius do also not give consistent results. So there seems to be some inconsistency in the drift velocity, which may be influenced to some extent by the line profiles. We summarize, that we cannot consistently locate the active region of the event 1.

For events 2 and 3 the measured velocities are -35 and -24 km s^{-1} , respectively. If these velocities are dominated by the stellar rotation and the active region of event 1 is not circumpolar, then event 2 and 3 cannot stem from the same active region as event 1, since the star has completed less than half a rotation, which does not suffice to move the site behind the star and back to the visible hemisphere to reappear with a blue shifted velocity.

For event 2 there is nevertheless the possibility, that the weak reaction of the chromosphere and the strong coronal signal are not physically connected. Therefore, the X-ray signal may stem from a reheating event, while in the chromosphere a different active region undergoes a brightening that only coincides in time with the coronal activity.

The event 2 and 3 can in principle originate in the same active region. Since they exhibit only slightly different velocities, the active region must be located at high latitude then. For low latitudes, the expected velocity shift in the 3 hours between the two flare events would exceed the measured difference by far. Also the intensity map (see Fig. 7) suggests no dependency for the two events.

6.4. Geometry of the flaring region

The continuum of the flare optical spectra shows a well-defined slope which suggests a blackbody origin. For computing the blackbody temperature we use the flare spectrum and subtract the quiescent flux. The blackbody fit gives a temperature estimate of $16\,000 \text{ K}$ during the flare peak. Fig. 15 shows the best-fit blackbodies as solid line (green); blackbody fits with fixed temperatures at $14\,500\text{K}$ and $17\,500\text{K}$ for comparison as dotted lines (red).

Using the UV light curve obtained with the OM one can estimate the optical filling factor. For this we obtain the mean count rate of 70 cts/s during the quiescent phase between 21:00 UT and 01:00 UT. Additionally we obtain the count rate of 190 cts/s at the flare peak (event 1). Using the count-to energy conversion factor of $1.66 \times 10^{-15} \text{ erg/cm}^2/\text{s}$ for a star of spectral type K0 from the *XMM-Newton* handbook, we calculated a flux of $1.1 \times 10^{-13} \text{ erg/cm}^2/\text{s}$ and $3.1 \times 10^{-13} \text{ erg/cm}^2/\text{s}$ during quiescent and event 1 in the covered band of the UVM2 filter. Combining this flux with a distance of $\approx 15 \text{ pc}$, we obtain a lu-

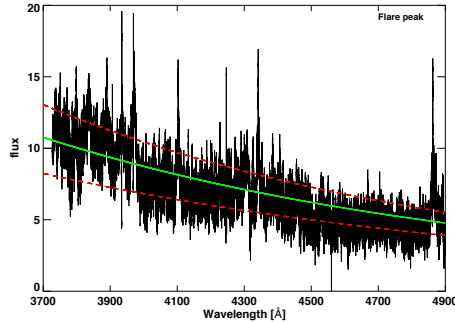


Fig. 15. Blue UVES spectrum with the quiescent flux subtracted, covering the peak of flare event 1. Overlaid in green and red are different blackbody fits.

minosity of 3.2×10^{27} erg/s and 8.6×10^{27} erg/s during quiescent and flare event 1, respectively. Using the derived temperature and the ratio of flare luminosity to the quiescent luminosity, an areal filling-factor of the flare of $\approx 2.3\%$ can be estimated.

Furthermore, one can attempt to estimate the volume of the flaring region in X-rays making use of the emission measure which is defined by $EM \sim n_e^2 V$, where n_e is the electron density. Using the EM of the hottest component from Table 2 and n_e from Table 3 we computed their loop-footpoint area $A = \frac{V}{L}$, where L is the loop length from Table 4. The resulting areal filling factor of each of the flaring events range between 1 – 3%, which is consistent with the estimate from the UV emission.

6.5. Quasi-quietness in the chromospheric lines

As discussed in Sect. 5.2.1, throughout our observations we find significant variations in line shape and amplitude in $H\alpha$, $H\beta$, and the Ca II K lines on a timescale of 10 minutes and less. These strong chromospheric lines also exhibit subcomponents in their cores. This indicates, that they trace emission from different active regions, which are partially resolved in wavelength due to the high rotational velocity of AB Dor A. The line emission thus results from the superposition of fluxes emitted by the different active regions. The flux of the different active regions vary in time, e.g. due to small flares and therefore lead to the very dynamic line behaviour. While the line shape is most affected by this phenomenon, even the overall fluxes in strong lines vary outside the flare events as can be seen in Fig. 7. This is comparable to the situation in X-rays, where many active flare stars do not exhibit a truly quiescent emission level, but some sort of flickering, sometimes called quasi-quietness (Robrade & Schmitt 2005). Moreover, the chromospheric emission in the strong lines is dominated by many active regions and not by the narrow component emission of the flare. Especially in $H\alpha$ the flare emission only plays a minor role compared to the overall signal.

6.6. Rotational modulation

Our observations cover about 16 hours, translating into ≈ 1.3 stellar rotation periods. Furthermore, an analysis of rotational modulation in our data is hampered by the fact that much of it is highly influenced by flares. Visual inspection of the radio and X-ray light curves suggests that AB Dor A's emission is rotationally modulated *outside* Events 1 to 3, see Fig. 1. However, closer inspection shows that the estimated maxima of the radio emission do not match the rotation period of 0.52 d by an hour or more. The same applies to the minima of the X-ray signal. Thus we conclude that we do not see any significant rotational modulation during our observations.

7. Summary and conclusions

We report on the temporal correlation of activity in different atmospheric layers of AB Dor A, with an emphasis on long duration flare events. From the X-ray data we determined the coronal abundances, temperature, emission measure and densities during different activity stages. The flare light curve shows a striking similarity to the flares observed previously on the same star described by Güdel et al. (2001). Such clustered events suggest that they originate in the same loop or arcade similar to what is observed on the Sun (see Kołomański 2007 and their references). However, our optical data clearly implies that these events originate in different active regions at least for the chromosphere. If there is a physical connection between the re-heating like event 2 in X-rays and the coincidental event in the chromospheric lines is not clear, though. Nevertheless, event 1 and 3 have clear counterparts in the different wavelength bands except for the radio emission that is not covered or exhibit no flaring activity, respectively.

Additionally, we found strong prominence absorptions in the chromospheric line profile, however, we find no clear evidence for an X-ray absorption by these prominences. Also we found no signs of rotational modulation neither in X-ray nor in radio emission.

In our high time cadence spectral series we could identify shallow emission subcomponents in the $H\alpha$ and Ca II K lines during the first few minutes of the flare, which we interpret as the signature of the strongest chromospheric shocks caused by the flare. Moreover, to our knowledge for the first time, we could show that during the early phase of the large flare, both, turbulent broadening for the helium and metal lines and Stark broadening for the hydrogen lines is at work; later on only turbulent broadening seems to be present. Our findings demonstrate the importance of high time-cadence on the one hand and high spectral resolution on the other hand for stellar flare studies.

Acknowledgements. S. L. acknowledges funding by the DFG in the framework of RTG 1351.

References

Allred, J. C., Hawley, S. L., Abbett, W. P., & Carlsson, M. 2006, *ApJ*, 644, 484

- Arnaud, K. A. 1996, in ASP Conf. Ser. 101: Astronomical Data Analysis Software and Systems V, ed. G. H. Jacoby & J. Barnes, 17–+
- Audard, M., Güdel, M., Sres, A., Raassen, A. J. J., & Mewe, R. 2003, *A&A*, 398, 1137
- Beck, C., Schmidt, W., Rezaei, R., & Rammacher, W. 2008, *A&A*, 479, 213
- Ben Chaouacha, H., Sahal-Bréchet, S., & Ben Nessib, N. 2007, *A&A*, 465, 651
- Brinkman, A. C., Behar, E., Güdel, M., et al. 2001, *A&A*, 365, L324
- Clough, S. A., Iacono, M. J., & Moncet, J.-L. 1992, *J. Geophys. Res.*, 97, 15761
- Collier Cameron, A. & Robinson, R. D. 1989, *MNRAS*, 236, 57
- Crespo-Chacón, I., Montes, D., García-Alvarez, D., et al. 2006, *A&A*, 452, 987
- Donati, J.-F. & Collier Cameron, A. 1997, *MNRAS*, 291, 1
- Dunstone, N. J., Collier Cameron, A., Barnes, J. R., & Jardine, M. 2006, *MNRAS*, 373, 1308
- Fletcher, L., Dennis, B. R., Hudson, H. S., et al. 2011, *Space Sci. Rev.*, 159, 19
- Fossum, A. & Carlsson, M. 2005, *Nature*, 435, 919
- Fuhrmeister, B., Lalitha, S., Poppenhaeger, K., et al. 2011, *A&A*, 534, A133
- Fuhrmeister, B., Liefke, C., Schmitt, J. H. M. M., & Reiners, A. 2008, *A&A*, 487, 293
- Gabriel, A. H. & Jordan, C. 1969, *MNRAS*, 145, 241
- García-Alvarez, D., Drake, J. J., Kashyap, V. L., Lin, L., & Ball, B. 2008, *ApJ*, 679, 1509
- Grevesse, N. & Sauval, A. J. 1998, *Space Sci. Rev.*, 85, 161
- Güdel, M., Audard, M., Briggs, K., et al. 2001, *A&A*, 365, L336
- Guirado, J. C., Marcaide, J. M., Martí-Vidal, I., et al. 2011, *A&A*, 533, A106
- Hauschildt, P. H., Allard, F., & Baron, E. 1999, *ApJ*, 512, 377
- Hussain, G. A. J., Jardine, M., Donati, J.-F., et al. 2007, *MNRAS*, 377, 1488
- Innis, J. L., Coates, D. W., & Thompson, K. 1988, *MNRAS*, 233, 887
- Jeffers, S. V., Donati, J.-F., & Collier Cameron, A. 2007, *MNRAS*, 375, 567
- Johns-Krull, C. M., Hawley, S. L., Basri, G., & Valenti, J. A. 1997, *ApJS*, 112, 221
- Kołomański, S. 2007, *A&A*, 465, 1021
- Kowalski, A. F., Hawley, S. L., Holtzman, J. A., Wisniewski, J. P., & Hilton, E. J. 2010, *ApJ*, 714, L98
- Kuerster, M., Schmitt, J. H. M. M., & Cutispoto, G. 1994, *A&A*, 289, 899
- Kundu, M. R., White, S. M., Jackson, P. D., & Pallavicini, R. 1988, *A&A*, 195, 159
- Liefke, C., Fuhrmeister, B., & Schmitt, J. H. M. M. 2009, in American Institute of Physics Conference Series, Vol. 1094, 15th Cambridge Workshop on Cool Stars, Stellar Systems, and the Sun, ed. E. Stempels, 608–611
- Lim, J., Nelson, G. J., Castro, C., Kilkenny, D., & van Wyk, F. 1992, *ApJ*, 388, L27
- Montes, D., Saar, S. H., Collier Cameron, A., & Unruh, Y. C. 1999, *MNRAS*, 305, 45
- Moore, C. E. 1972, *Nat. Stand. Ref. Data Ser.*, 40
- Ness, J.-U. & Wichmann, R. 2002, *Astronomische Nachrichten*, 323, 129
- Osten, R. A., Hawley, S. L., Allred, J. C., Johns-Krull, C. M., & Roark, C. 2005, *ApJ*, 621, 398
- Pakull, M. W. 1981, *A&A*, 104, 33
- Parsons, S. G., Marsh, T. R., Gänsicke, B. T., & Tappert, C. 2011, *MNRAS*, 412, 2563
- Paulson, D. B., Allred, J. C., Anderson, R. B., et al. 2006, *PASP*, 118, 227
- Phillips, K. J. H. & Dennis, B. R. 2012, *ApJ*, 748, 52
- Pradhan, A. K. & Shull, J. M. 1981, *ApJ*, 249, 821
- Reale, F. 2007, *A&A*, 471, 271
- Reale, F., Betta, R., Peres, G., Serio, S., & McTiernan, J. 1997, *A&A*, 325, 782
- Reiners, A. 2009, *A&A*, 498, 853
- Robrade, J. & Schmitt, J. H. M. M. 2005, *A&A*, 435, 1073
- Sanz-Forcada, J., Maggio, A., & Micela, G. 2003, *A&A*, 408, 1087
- Sault, R. J., Teuben, P. J., & Wright, M. C. H. 1995, in Astronomical Society of the Pacific Conference Series, Vol. 77, Astronomical Data Analysis Software and Systems IV, ed. R. A. Shaw, H. E. Payne, & J. J. E. Hayes, 433
- Serio, S., Reale, F., Jakimiec, J., Sylwester, B., & Sylwester, J. 1991, *A&A*, 241, 197
- Smith, R. K., Brickhouse, N. S., Liedahl, D. A., & Raymond, J. C. 2001, in ASP Conf. Ser. 247: Spectroscopic Challenges of Photoionized Plasmas, ed. G. Ferland & D. W. Savin, 161–+
- Sylwester, J., Lemen, J. R., & Mewe, R. 1984, *Nature*, 310, 665
- Švestka, Z. 1972, *ARA&A*, 10, 1
- Vilhu, O., Gustafsson, B., & Walter, F. M. 1991, *A&A*, 241, 167
- Vilhu, O. & Linsky, J. L. 1987, *PASP*, 99, 1071
- Vilhu, O., Tsuru, T., Collier Cameron, A., et al. 1993, *A&A*, 278, 467
- Wedemeyer-Böhm, S., Lagg, A., & Nordlund, Å. 2009, *Space Sci. Rev.*, 144, 317
- Wedemeyer-Böhm, S., Scullion, E., Steiner, O., et al. 2012, *Nature*, 486, 505
- White, G. L., Jauncey, D. L., Batty, M. J., Peters, W. L., & Gulkis, S. 1988, *PASP*, 100, 825
- Wilson, W. E., Ferris, R. H., Axtens, P., et al. 2011, *MNRAS*, 416, 832
- Worden, S. P., Schneeberger, T. J., Giampapa, M. S., Deluca, E. E., & Cram, L. E. 1984, *ApJ*, 276, 270

List of Objects

‘AB Dor A’ on page 1

Chapter 6

Characteristics of flares on AB Dor A

AB Dor A is an active young K dwarf with an age of $\sim 40\text{-}50$ Myr (Guirado et al. 2011). It rotates rapidly with a rotational velocity $v\sin i \approx 90$ Km/s (Kuerster et al. 1994) and a rotation period of 0.514 days, hence covering ~ 2 rotation cycles in just over a day.

Being located as a foreground star of the large magellanic cloud (LMC), AB Dor A has an advantage of being observed at all times by most of the X-ray satellites. Additionally, AB Dor A has been repeatedly observed in the last decade; since it is a calibration source for RGS on board *XMM-Newton*. Occasionally the pn was also operational during these calibration observations. During these observations several flares on AB Dor A have been observed providing an ideal opportunity to characterise each of the flares and compare its properties to that of Solar flares.

6.1 Observations and data analysis

Useful X-ray data were obtained by focussing X-rays onto three EPIC (European Photon Imaging Camera) cameras (one PN and two MOS cameras) with a sensitivity range of $\approx 0.5 - 15$ keV. The X-ray telescopes with the MOS detectors are equipped with reflection gratings (RGS) producing high-resolution X-ray spectra between 0.35 - 2.5 keV. All X-ray data were reduced using the standard XMM-Newton Science Analysis System (SAS) software, version 11.0. EPIC light curves and spectra were obtained using standard filtering criteria. Spectral analysis was done with XSPEC version 12.5.0 (Arnaud 1996), mak-

ing use of multi-temperature component models with coupled abundances for each component. Abundances are calculated relative to the solar photospheric values from Grevesse & Sauval (1998).

6.1.1 Quiescent emission

A quiescent emission level was calculated for each of the observations. The observed flux were converted into X-ray luminosity in the spectral band 0.2-10.0 keV and 0.3-2.7 keV for pn and RGS, respectively. The derived quiescent luminosity range between $29.96 \leq \log(L_x) \leq 30.13$. However, I define the quiescent level as the time duration in which no energetic event is detected in the light curve. If there are events occurring below the detection threshold there is no way to discriminate the quiescent and the mean level.

6.1.2 Flare analysis

I analyse the brightest X-ray flares from AB Dor A using *XMM-Newton* observations. I define an event as a flare when there is an anomaly in the count rate. In other words I identify an event flare when the peak count rate increases by 50 or more percent when compared the typical pre-flare/quiescent level. This results in over 17 flares from XMM's pn and 27 flares from the RGS over last decade. The difference in the number of flares detected by the PN and the RGS is because AB Dor A is a calibration source for the RGS and has been observed for longer period when compared to the PN.

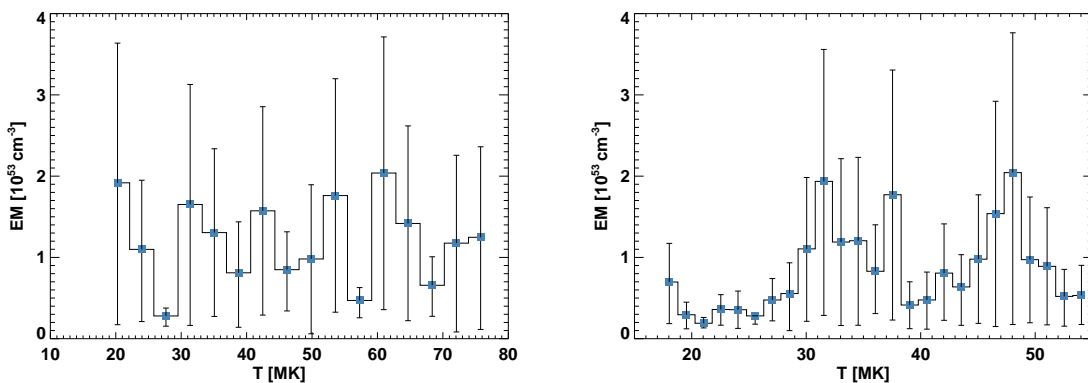


Figure 6.1: Distribution of flare peak emission measure plotted as a function of flare peak temperature for PN (left panel) and RGS (right panel) data.

6.2 Results

6.2.1 Global flare properties

During a flare fresh material from the chromosphere is brought to the upper layers of the stellar atmosphere, changing the coronal abundance, temperature and emission of coronal plasma temporarily (Güdel 2004). I perform a spectral analysis and determine plasma temperatures, abundances and emission measures in different states of activity for AB Dor A.

6.2.1.1 EM and T evolution

From X-ray point of view, the general flare scenario implies a characteristic evolution of the flare emission measure (EM) and the temperature (T). To investigate this, I divide each of the flare light curves into smaller time bins and create a spectra for each of these bins. The first spectrum covers the flare rise and the following time intervals covers the different phases of the decay. Each of the spectra is fitted with combinations of APEC models.

In addition I generated quiescent spectra before and after the flare for each of the observation and fitted with two-temperature component APEC models. While the fit improved with a three-temperature component model. I obtain a global quiescent emission I used only those observation which has both the RGS and the PN data. For fitting quiescent RGS spectra, the abundance of carbon, nitrogen, oxygen, neon and iron abundances were allowed to

vary freely and independently, but were fixed among all VAPEC temperature components. Further, I allowed the temperature components to vary independently. For fitting EPIC-PN spectra the magnesium, silicon, sulphur and argon abundances were allowed to vary along with oxygen, neon and iron abundances, but carbon and nitrogen abundance were fixed to values obtained from RGS which is sensitive to strong individual lines. As far as quiescent emission is concerned for different observations I notice that the properties of the for different quiescent spectra are very similar. Hence I created an average quiescent emission i.e. temperatures ($kT_1 = 0.29 \pm 0.04$ keV, $kT_2 = 0.69 \pm 0.08$ keV and $kT_3 = 2.29 \pm 0.15$ keV) and emission measures ($EM_1 = 1.48 \pm 0.17 \times 10^{52} \text{ cm}^{-3}$, $EM_2 = 4.98 \pm 0.26 \times 10^{52} \text{ cm}^{-3}$ and $EM_3 = 2.18 \pm 0.19 \times 10^{52} \text{ cm}^{-3}$). While the individual elemental abundances occurred with the abundances treated as free parameters are C/H= 0.71 ± 0.10 , N/H= 0.90 ± 0.14 , O/H= 0.42 ± 0.02 , Ne/H= 0.81 ± 0.04 , Mg/H= 0.28 ± 0.03 , Si/H= 0.25 ± 0.05 , S/H= 0.25 ± 0.05 , Ar/H= 1.04 ± 0.28 , and Fe/H= 0.28 ± 0.01 relative to the solar photospheric values of (Grevesse & Sauval 1998).

In the flare spectra models, I always include the quiescent emission, i.e. the parameters of the first three temperature components are fixed to the plasma properties of the quiescent emission. Hence during the flare I used five temperature component where the 4th and the 5th temperature component defines the con-

tribution from the flare (1^{st} - 3^{rd} temperature components represent the quiescent emission). With this approach one accounts for the contribution of the quiescent emission to the overall X-ray emission.

To improve the fit and to emancipate the temperature and abundance variation, single elemental abundance was introduced as additional free parameter. With the iron abundance as a free parameter I notice a clear improvement in the fit. I apply a similar spectral model to each data set to perform a self-consistent analysis.

In order to obtain the plasma properties I make use of the total emission measure (EM) and flare temperature (T),

$$EM = \sum_i EM_i \quad T = \sum_i \frac{T_i \times EM_i}{EM}, \quad (6.1)$$

where the total emission measure is the sum of the emission measures of each temperature component and the total flare temperature is the emission measure weighted sum of the temperatures from each flare component. Two flare temperature components give a reasonable fit for all bins during the flare decay, this in-turn supports that our assumption of low temperature component is not changing during the flare is correct. In Figure 6.1, I plot the distribution of flare emission measure derived from XMM-PN (left panel) and XMM-RGS (right panel) data. As seen in Fig 6.1, the estimated EM from PN and RGS are consistent within the errors. However, I note that the high energy component of the XMM-RGS data yields a large error since the instrument is not sensitive at those energies. Hence, it is not meaningful to compare the high temperature component estimated from the RGS with the PN observations.

6.2.1.2 Fe abundance evolution

In Figure 6.2, I plot the time series of the iron abundance relative to the solar photospheric abundance (Grevesse & Sauval 1998), here each colour indicates a different flare. The first point for each curve represent the abundance at flare peak. Plotted as thick black line is a simple exponential decay fit to the entire data set.

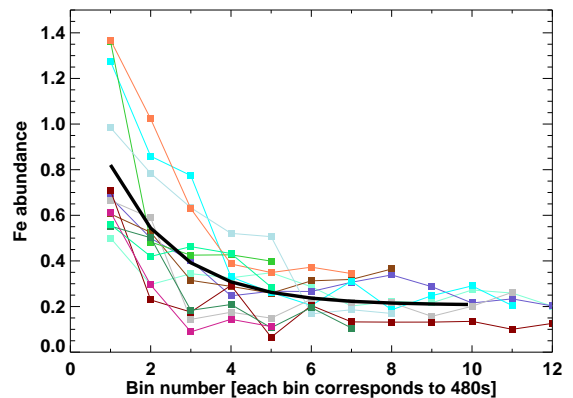


Figure 6.2: Evolution of Fe abundance for a subset of flares observed on AB Dor by XMM-PN. Plotted as thick black line is a simple exponential fit showing the expected evolution.

When neon abundance is set as free parameter instead of iron, the neon abundance does not give a clear pattern like the iron abundance. This could be due to contamination with highly ionized iron during the flare which is too strong to give any conclusive result. This was repeated with oxygen as well as silicon abundance as free parameters, a large scatter in the abundance over time for these later elements was noticed. Hence iron seems to be the only element which shows a clear trend in variation of elemental abundance as a result of a flare. In the general picture of a stellar flare, the evidence of the change in the iron abundance indicated that during the flare fresh material is evaporated from the photosphere and chromosphere which intrinsically shows a different composition with higher iron abundance than the quiescent coronal plasma.

AB Dor A being an active star, its quiescent corona is expected to show the inverse first ionisation potential (IFIP) effect (Lalitha et al. 2013). The above trend of increase in the Fe abundance confirms the findings of Nordon & Behar (2008) that IFIP-biased coronae tend to show FIP bias during flares with respect to Fe abundance.

In addition, I note that the decay time-scale of the iron abundance is faster when compared to evolution of the EM or T or the count rate. The iron abundance goes back to its respective

pre-flare value. This suggests two possibilities:

- the existence of some kind of iron-depleting mechanism occurs during the flare, or
- during the early and later stages of the plasma evaporation different regions of lower atmosphere with different abundance levels are affected.

6.2.1.3 Loop modeling

One of the major objective of flare analysis is determining the length scales of flaring loop. Unlike solar coronal loops, the stellar coronal structures are spatially unresolved. One can estimate the size of the stellar coronal flaring region from the light curve, the time resolved temperature and the emission measure values obtained during the decay of the flaring loop. Emission measure - Temperature (EM-T) diagram is a useful tool to estimate unobservable physical quantities such as flare loop length, total energy and magnetic field strengths. An empirical formula to determine loop lengths has been obtained by Reale et al. (1997) based on hydrodynamic approach making use of information from the light curves and EM-T diagram.

To calculate the loop length I follow the same procedure as in Sect. 5.2. The flare is assumed to occur in a single loop with a constant cross-section anchored in the photosphere. The plasma is confined to this single loop and the decay is said to occur once the loop reaches a steady state where further flow of energy and plasma are negligible. From these assumptions it is clear that the decay time of X-ray emission roughly scales to the plasma cooling times, which in turn scales to the loop length. In Figure 6.3, I plot the distribution of the estimated loop lengths for both PN (in black) and RGS (in grey). These estimated loop lengths for the flares vary between $0.02-1.8 R_{\star}$ ($0.96 \pm 0.06 R_{\odot}$, Guirado et al. 2011).

6.2.2 Comparison with scaling laws

In this section, an overview of our knowledge and understanding of the solar flares and comparisons with observations of stellar flare are

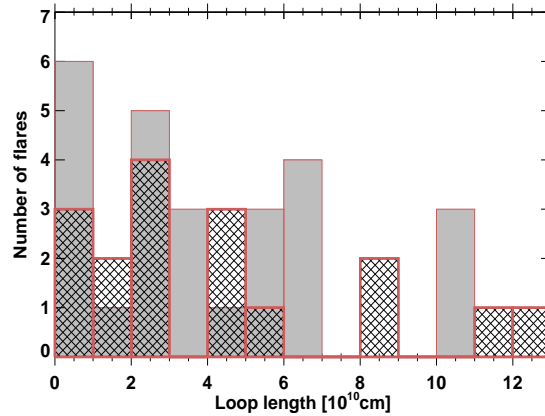


Figure 6.3: The distribution of loop lengths for the flares observed by PN only in black and the flares observed by the RGS in grey.

presented and some implications for our understanding of stellar flare variations are deduced.

6.2.2.1 Flare peak emission measure versus flare peak temperature

Flares on the Sun and other stars have been studied for a long time using both ground and space-based observations (see reviews by Benz 2008; Fletcher et al. 2011). A remarkable correlation between the temperature (T) during the flare peak and the emission measure (EM) was noticed using the space-based observations of solar flares (Shimizu 1995; Yuda et al. 1997). Apparently this correlation can be extrapolated to stellar flares as well (Stern et al. 1992; Feldman et al. 1995).

Shibata & Yokoyama (1999) presented a simple theory based on magnetohydrodynamic simulation of reconnection together with heat conduction and chromospheric evaporation to explain the correlation between the flare peak temperature and the emission measure. According to this $EM \propto B^{-5} T^{17/2}$ where B is the magnetic field strength. This equation means that the observed correlation between the temperature and emission measure is explained if B is nearly constant. Hence, the observed EM-T diagram may be an useful tool for estimating the magnetic field strength of stellar flares, which is observationally very difficult for other stars.

Table 6.1: Flare interpretation and summary of flare properties.

	$\log L_X$ [erg/s]	EM [10^{52}cm^{-3}]	T_{max} [10^6 K]	ζ [slope in Kcm^3]	τ_f [s]	L [10^{10} cm]	
	1	30.36	6.97 ^{2.22} _{1.85}	24.15 ^{20.53} _{6.50}	1.68±0.06	5220.02±27.10	5.78±0.05
	2	30.26	2.94 ^{1.40} _{1.21}	22.00 ^{28.54} _{14.91}	1.68±0.07	2520.00±6.33	2.64±0.04
	3	30.21	1.89 ^{1.18} _{1.32}	23.00 ^{16.24} _{8.31}	1.57±0.04	5580.01±30.96	6.43±0.08
	4	30.28	3.59 ^{1.77} _{1.66}	35.85 ^{23.10} _{20.23}	1.74±0.12	211.597±185.30	0.28±2.04
	5	30.27	3.56 ^{1.26} _{1.27}	30.84 ^{23.86} _{15.16}	2.15±0.45	10800.1±115.39	10.75±2.44
	6	30.26	2.80 ^{2.79} _{1.78}	38.54 ^{37.74} _{34.58}	2.15±0.45	5640.03±31.63	6.39±1.39
	7	30.31	4.76 ^{2.12} _{2.19}	23.48 ^{41.11} _{9.25}	5.02±13.28	355.260±278.07	0.13±2.15
	8	30.30	15.01 ^{2.92} _{2.76}	37.35 ^{18.55} _{7.90}	—	—	—
	9	30.31	5.55 ^{1.76} _{1.00}	30.20 ^{12.19} _{9.13}	2.42±0.64	2700.51±7.27	2.36±0.10
	10	30.40	12.21 ^{3.43} _{3.13}	28.91 ^{12.03} _{16.67}	—	—	—
	11	30.46	11.04 ^{2.26} _{2.13}	22.24 ^{5.11} _{3.99}	1.84±0.08	6998.83±879.64	6.75±1.35
	12	30.60	19.35 ^{3.11} _{2.86}	26.52 ^{5.87} _{4.30}	2.90±0.82	7428.76±305.07	5.03±1.94
	13	30.47	11.89 ^{1.63} _{1.62}	22.86 ^{8.14} _{4.14}	1.69±0.031	3000.30±8.97	3.20±0.01
RGS	14	30.48	12.05 ^{1.79} _{1.65}	22.17 ^{10.99} _{3.58}	1.84±0.084	6180.09±37.95	5.95±0.05
	15	30.42	8.29 ^{2.58} _{3.08}	17.29 ^{6.89} _{3.51}	1.80±0.12	3000.30±8.97	2.55±0.02
	16	30.57	17.71 ^{2.37} _{2.29}	26.07 ^{6.08} _{3.77}	1.89±0.16	563.552±171.40	0.58±0.46
	17	30.29	4.14 ^{1.28} _{1.23}	21.22 ^{26.09} _{5.96}	1.58±0.04	877.770±191.67	0.95±0.33
	18	30.31	4.76 ^{1.33} _{1.17}	21.23 ^{11.46} _{4.62}	8.92±7.22	5141.55±617.50	0.99±4.31
	19	30.34	8.07 ^{2.01} _{2.26}	24.70 ^{11.75} _{3.34}	1.71±0.07	3004.05±638.31	3.31±0.88
	20	30.34	6.36 ^{2.40} _{1.64}	53.92 ^{22.26} _{27.82}	1.56±0.05	3583.28±1690.30	6.81±12.12
	21	30.44	9.78 ^{1.87} _{1.88}	19.96 ^{8.77} _{4.10}	1.90±0.07	4020.10±16.09	3.51±0.02
	22	30.34	30.54 ^{3.11} _{4.23}	43.62 ^{10.13} _{4.76}	—	—	—
	23	30.52	15.38 ^{1.56} _{1.49}	31.73 ^{12.53} _{5.44}	2.78±1.06	1323.00±653.88	1.03±6.83
	24	30.58	20.43 ^{3.22} _{1.74}	43.37 ^{8.31} _{7.70}	1.81±0.10	7080.05±49.77	10.24±0.15
	25	30.42	9.72 ^{2.01} _{1.96}	29.04 ^{13.28} _{5.59}	1.85±0.11	4080.13±16.58	4.57±0.04
	26	30.40	8.90 ^{1.68} _{1.70}	34.92 ^{21.94} _{8.84}	9.33±7.46	9024.70±792.94	2.23±8.09
	27	30.29	5.20 ^{1.87} _{1.54}	26.67 ^{21.34} _{6.41}	1.56±0.05	8117.54±1304.19	10.25±2.88
	28	30.32	5.32 ^{1.61} _{1.75}	31.35 ^{52.81} _{12.59}	1.55±0.08	2040.03±4.15	2.84±0.02
	1	30.56	19.18 ^{1.99} _{1.72}	37.20 ^{1.89} _{2.26}	2.68 ± 0.42	2640.05 ± 6.95	2.35 ± 0.02
	2	30.41	10.98 ^{2.48} _{2.10}	75.97 ^{69.26} _{11.83}	2.08 ± 0.36	2961.34 ± 218.21	5.14 ± 2.07
	3	30.10	2.80 ^{1.83} _{1.53}	28.57 ^{50.34} _{12.35}	1.78 ± 0.17	9853.38 ± 2943.83	11.34 ± 29.70
	4	30.57	16.51 ^{1.74} _{1.63}	46.87 ^{3.51} _{3.65}	1.78 ± 0.15	5520.01 ± 30.30	8.47 ± 0.06
	5	30.44	13.05 ^{2.73} _{2.73}	28.97 ^{5.07} _{3.54}	2.48 ± 0.60	2640.05 ± 6.95	2.20 ± 0.03
	6	30.33	8.10 ^{1.83} _{1.40}	23.33 ^{2.02} _{2.62}	4.85 ± 2.47	4440.00 ± 19.62	1.67 ± 0.09
	7	30.46	15.73 ^{2.92} _{2.90}	18.42 ^{12.11} _{5.30}	1.60 ± 0.11	2333.91 ± 194.43	2.31 ± 0.81
	8	30.26	8.49 ^{3.83} _{3.41}	23.56 ^{27.55} _{9.69}	1.86 ± 0.23	1501.50 ± 2.25	1.47 ± 0.02
PN	9	30.37	9.80 ^{0.67} _{0.60}	30.41 ^{1.63} _{1.58}	8.92 ± 4.62	1740.04 ± 3.02	0.41 ± 0.01
	10	30.48	17.60 ^{3.23} _{3.25}	34.76 ^{5.94} _{4.21}	2.72 ± 0.76	4920.05 ± 24.08	4.16 ± 0.14
	11	30.30	28.52 ^{4.34} _{4.35}	25.98 ^{2.31} _{1.91}	—	—	—
	12	30.27	4.70 ^{3.12} _{2.57}	42.06 ^{23.33} _{11.84}	4.61 ± 2.11	893.224 ± 5.46	0.49 ± 0.08
	13	30.57	20.38 ^{3.64} _{3.57}	36.71 ^{3.55} _{2.98}	1.67 ± 0.05	8604.89 ± 21.17	12.21 ± 0.01
	14	30.44	14.17 ^{2.17} _{2.21}	31.89 ^{4.89} _{3.56}	1.90 ± 0.12	7720.81 ± 34.82	8.86 ± 0.06
	15	30.28	6.571 ^{3.06} _{2.75}	27.51 ^{8.02} _{4.22}	1.80 ± 0.12	1992.86 ± 19.89	2.21 ± 0.04
	16	30.47	11.75 ^{0.94} _{0.83}	31.10 ^{2.71} _{2.13}	1.69 ± 0.12	3431.52 ± 346.09	4.38 ± 0.47
	17	30.50	12.47 ^{1.33} _{1.13}	42.77 ^{3.83} _{3.20}	3.80 ± 1.34	7038.09 ± 873.87	4.81 ± 3.21

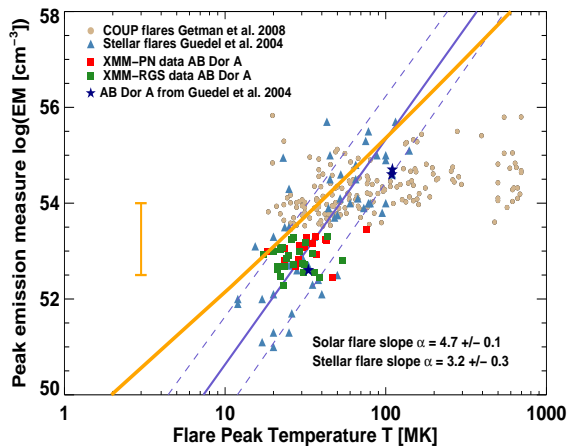


Figure 6.4: Plot of flare peak emission measure vs. flare peak temperature for the flares observed by *XMM-Newton*. Also depicted are the AB Dor A flares observed with pn (red square) and RGS (green squares). Plotted as beige circles are COUP flares compiled by Getman et al. (2008). Flares observed in other stars compiled by Güdel (2004) are depicted as blue triangles. The linear regression obtained by Aschwanden et al. (2008) is plotted as blue thick line with 1σ range (blue dashed line). AB Dor A flares, other stellar flares and solar flares fit a similar correlation $EM_f \propto T_f^{4.7}$. Plotted as yellow thick line is the linear regression, I obtained considering only stellar flares. The error bar indicate the 1σ range obtained from our analysis.

From comparison of solar and stellar flares Aschwanden et al. (2008) found a common scaling law between the flare peak emission measure (EM_f) and the flare peak temperature (T_f), $EM_f \propto T_f^{4.7 \pm 0.1}$ (plotted as blue thick line with 1σ range in Fig.6.4), despite the fact that the stellar flare emission is ~ 250 times higher than the solar flare emission. Further, Getman et al. (2008) found that about 60% COUP flares also follow the same trend as the solar and stellar flares (plotted as beige circles in Fig.6.4). Nearly, 40% of the COUP flares follow a shallow trend and hence for further analysis I neglect all the COUP flares.

In Figure 6.4, the comparison between the EM_f to T_f on AB Dor A observed by pn and RGS (red and green squares) and stellar

flares compiled by Güdel (2004) (blue triangle) is presented. Further, the AB Dor A flares from Güdel (2004) are over plotted as blue stars for comparing both the results. Previous flare observation of AB Dor A was carried out with *BeppoSAX* and *XMM-Newton*. The solar-stellar trend obtained by Aschwanden et al. (2008) is over plotted as thick blue line.

I performed a regression analysis on all the stellar flares and obtained a more shallow correlation between EM_f and T_f , $EM_f \propto T_f^{3.2 \pm 0.3}$. Plotted as yellow thick line is the scaling law between the flare peak temperature and emission measure obtained from the current analysis. However, one may notice that the flares observed on AB Dor A agrees well with the scaling law of Aschwanden et al. (2008) within errors.

6.2.2.2 Flare duration versus flare peak temperature

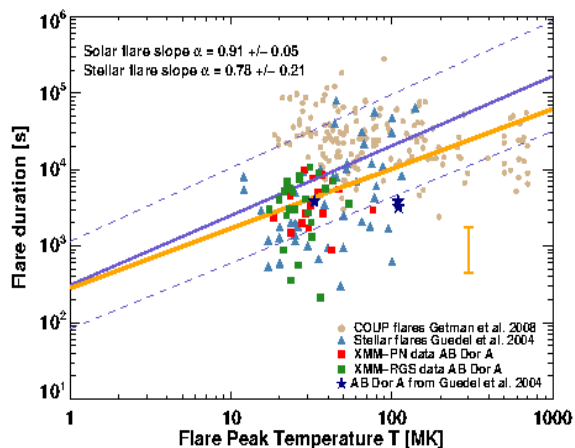


Figure 6.5: Plot of flare duration vs. flare peak temperature for the flares observed by *XMM-Newton*. Symbols and lines are as in Fig. 6.4. AB Dor A flares, other stellar flares and solar flares fit a similar correlation $\tau_f \propto T_f^{0.91}$.

In Figure 6.5, I show a comparison of the flare duration τ_f with the flare peak temperature (T_f) observed in AB Dor A flares (red and green squares), COUP flare compiled by Getman et al. (2008) (beige circles) and stellar flares compiled by Güdel (2004) (blue triangles). Previously the solar and stellar duration were fitted by a simple least square method,

this yielded a statistical correlation $\tau_f \propto T_f^{0.91}$. However, regression analysis of all the stellar flares including the flares observed on AB Dor A yield a slope of 0.78 ± 0.21 , which is consistent within errors with previous findings.

I note that for a certain value of temperature the flare duration seem to vary by three orders of magnitude. In other words, we know that the larger the loop the longer the decay time, then the size of the loop should also vary by three orders of magnitude for a constant temperature.

6.2.2.3 Flare length scales versus flare peak temperature

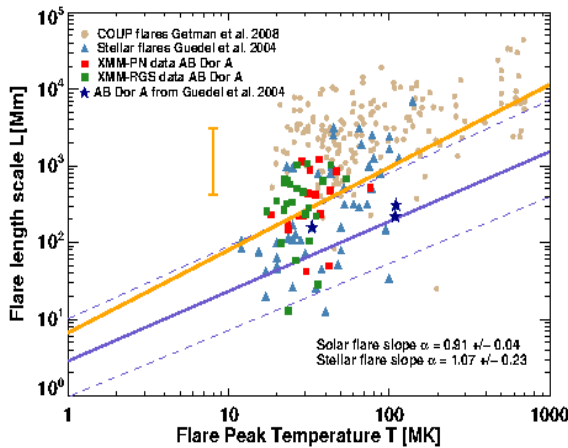


Figure 6.6: Plot of flare loop lengths vs. flare peak temperature for all the flares observed by *XMM-Newton*. Symbols and lines are as in Fig. 6.4.

Plotted in Figure 6.6 are the flare loop lengths (L) versus the flare peak temperature (T_f). Symbols are as in Fig. 6.4. The loci of stellar flares are plotted as thick yellow line and of solar flares are plotted thick blue line. The solar scaling law between flare loop length and the peak flare temperature is given by $L \propto T_{pk}^{0.91 \pm 0.04}$. However, for stellar flares (including AB Dor A flares and excluding COUP flares) we obtain $L \propto T_{pk}^{1.07 \pm 0.23}$. As can be noticed our estimate of the scaling law for the loop lengths and flare peak temperatures agree well when compared to the solar scaling law within the errors.

6.2.3 The event distribution

Despite decades of study, the source of heating of the solar and stellar coronae is still not understood (Schrijver et al. 1999; Reale 2010). There are several proposals on what may be the possible source of energy, but there are hardly any observational proofs to these theories. Parker (1988) introduced the term nanoflare for the Sun, which is defined as an impulsive event releasing energy less than 10^{27} erg which is minimum energy of a typical microflare event. Recent observations of the solar corona supports the possibility of coronal heating dominated by small-scale events with an average energy release of 10^{24} erg as suggested by Parker's nanoflare model (Parnell & Jupp 2000; Patsourakos & Klimchuk 2005). Solar microflares and milliflares energies follows a power law (Lin et al. 1984; Hudson 1991)

$$\frac{dN}{dE} = K E^{-\alpha}, \quad (6.2)$$

where K is proportionality constant, E is the energy of the flare (ergs) and α is the power law index.

The cumulative distribution for $\alpha > 1$ is defined by

$$N(> E) = \int_E^{\infty} \frac{dN}{dE} dE = K E^{-\alpha+1}. \quad (6.3)$$

According to Hudson (1991), it is crucial to understand if the solar and stellar flare rate distribution of energy steepens at lower energies. In solar context $\alpha = 1.5 - 1.6$ for a normal flare (Crosby et al. 1993); whereas $\alpha = 2.3 - 2.6$ for small events in the quiescent corona (Krucker & Benz 1998). Studies of stellar flare energy distribution in X-rays is rare because of scarcity of stellar flare statistics. Collura et al. (1988) found a power-law index $\alpha = 1.6$ for X-ray flares on M dwarfs using EXOSAT observations; on the other hand power-law index $\alpha = 2.2$ for solar analogs EK Dra and 47 Cas was determined by Audard et al. (1999). However, it is interesting to know the precise value of α , for example, if the power law is steep then the value $\alpha > 2$, which means that small impulsive events would be sufficient

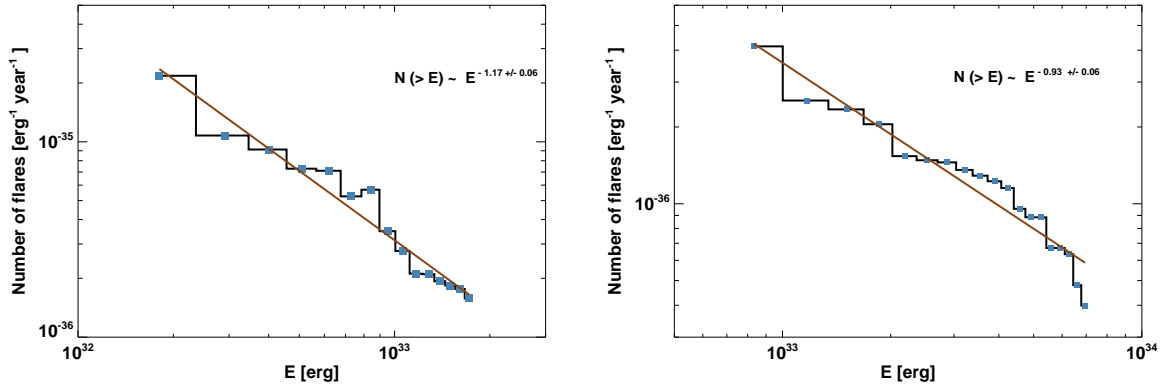


Figure 6.7: Frequency distribution of XMM-pn flares (left panel) and XMM-RGS flares (right panel) in AB Dor A as a function of total irradiated X-ray energy during the flare lifetime over spectral band 0.2-10 keV and 0.3-2.7 keV respectively. The straight line (in brown) is power-law fit to the distribution.

enough to account for the energy output of the entire corona.

The frequency distribution of flare energies, $N(E)$, is a crucial diagnostic to calculate the overall energy residing in flares contained in a given or expected energy range. For each detected flare event on AB Dor A, I estimated the energy radiated at X-ray wavelength above quiescent level for both pn and RGS separately. In Fig. 6.7, I plot the frequency distribution of the events as a function of total integrated energy during the flare. As can be seen, the slopes for PN and RGS are different since RGS cover more number of energetic flares when compared to PN. The above distribution yields a slope α between 1.93 and 2.17 for AB Dor A. Therefore, the large flares may not be contributing to the coronal heating. However, if we extend this distribution below detection threshold we would be able to explain coronal emission by stochastically occurring flares.

Chapter 7

A solar-like magnetic activity cycle on the active ultra-fast rotator AB Dor A?

S. Lalitha and J. H. M. M. Schmitt
submitted to *Astronomy & Astrophysics*

A solar-like magnetic activity cycle on the active ultra-fast rotator AB Dor A?

S. Lalitha and J. H. M. M. Schmitt

Hamburger Sternwarte, University of Hamburg, Gojenbergsweg 112, 21029 Hamburg, Germany
 e-mail: lalitha.sairam@hs.uni-hamburg.de

Received XXXX; accepted XXXX

ABSTRACT

Aims. Although chromospheric activity cycles have been studied in a larger number of late-type stars for quite some time, rather little is known about coronal activity cycles in other stars and their similarities or dissimilarities with the solar activity cycle. While it is usually assumed that cyclic activity is present only in stars of low to moderate activity, we demonstrate that the K-dwarf AB Dor, an ultra-fast rotator exhibiting substantial signs of magnetic activity in essentially all wavelength bands, possesses a photospheric activity cycle of about 17 years. We further use extensive X-ray data available on AB Dor to investigate whether also an X-ray activity cycle is present and to what extent any relations between X-ray and photospheric cycles exist.

Methods. We specifically used ROSAT and XMM-Newton X-ray observations of the nearby active ultra-fast rotator AB Dor A (K0) to study the long-term evolution of magnetic activity in this active K dwarfs over nearly three decades and searched for X-ray activity cycles and related photometric brightness changes.

Results. AB Dor A exhibits X-ray luminosities ranging between $29.8 < \log L_X [\text{erg/s}] \leq 30.2$ in the 0.3-2.5 keV. As a very active star AB Dor A shows frequent X-ray flaring, however, in the long XMM-Newton observations very often a kind of "basal state" is attained. This "basal state" is likely to vary with the photospheric activity cycle of AB Dor A, however, the X-ray variability amounts at most to a factor of ~ 2 , i.e., much smaller than the typical cycle amplitudes found on the Sun.

Conclusions.

Key words. stars: activity – stars: coroneae – stars: late-type – stars: individual: AB Dor

1. Introduction

One of the key characteristics of the Sun is its 11-years activity cycle, which was originally discovered from the periodic variation in the observed sunspot numbers (Schwabe 1844). However, the solar cycle also manifests itself in many other activity indicators such as the solar 10.7 cm radio emission, its chromospheric Ca II emission and its coronal X-ray emission (Gnevyshev 1967; Hathaway 2010). Ever since Hale (1908) discovered strong magnetic fields in sunspots, the magnetic character of solar activity and its cyclic variations is beyond dispute. With the advent of space-based astronomy vast amounts of solar X-ray data have been collected, which allow a better understanding of the evolution of coronal plasma temperature, emission measure, and structure over solar cycle (Orlando et al. 2000). As expected, the solar corona during activity minimum has a distinctly different appearance from that encountered at activity maximum. During a cycle the solar X-ray flux varies by a factor of 200 in the energy range of 0.6-1.5 keV (Kreplin 1970), while Stern et al. (2003) computed the solar soft X-ray irradiance variations as measured by the *Yohkoh* satellite in the 0.5-4 keV and found a maximum to minimum ratio of ~ 30 . In the softer energy range between 0.25-0.4 keV Tobiska (1994) estimated a factor of ~ 10 variation as the solar activity cycle progresses. Because of the absence of large active regions the solar corona during its activity minimum is much fainter than the solar corona during activity maximum (Golub 1980), however, the amplitude of these variations sensitively depends on the energy range considered and is much

smaller at softer energies. For example, Ayres (1997); Ayres et al. (2008) anticipated that through the 0.1-2.4 keV ROSAT band pass, the Sun should show variations between the minimum and maximum flux of a factor of 5-10. Peres et al. (2000) measured an X-ray brightness of $\log L_X = 27.5$ erg/s during activity maximum and $\log L_X = 26.5$ erg/s during activity minimum in the ROSAT 0.1-2.4 keV energy band, demonstrating an order of magnitude variation in the ROSAT band.

The question then immediately arises whether other late-type stars also show such a "solar-like" cyclic variability in their magnetic activity properties (Vaughan et al. 1978; Wilson 1978). Within the context of the Mt. Wilson HK program the long-term variability of stellar chromospheric activity of a larger sample of late-type stars was systematically studied over a few decades in the stellar Ca II emission cores and the cyclic activity of a larger number of stars in the solar neighbourhood was established (Baliunas et al. 1995). Specifically, Baliunas et al. (1998) found that about 60% of stars of the Mt. Wilson observatory survey stars exhibited periodic and cyclic variations, and, further, Lockwood et al. (2004, 2007) found evidence relating the photospheric and chromospheric activity cycles. Baliunas et al. (1995) employed the same technique used to study stellar activity to also monitor the solar activity cycle in integrated light and showed that the so-called S-index of the Sun varied between 0.16 and 0.22 between its activity minima and maxima; in fact, the Sun shows one of the best cycles in the whole stellar sample presented by Baliunas et al. (1998).

A related question is whether the stars with different cyclic properties in their Ca II emission show different behaviour with respect to their coronal emission. Hempelmann et al. (1996)

S. Lalitha et al.: A solar-like magnetic activity cycle on the active ultra-fast rotator AB Dor A?

compared the soft X-ray fluxes with the Ca emission in a sample of late-type stars and showed that the stars with cyclic variations in their calcium flux tend to show less X-ray activity than stars with irregular variability in their Ca II emission. Additionally, X-ray faint stars tend to show flat activity curves or low levels of short-term variability (see Wright et al. 2010 and references therein). On the other hand, X-ray bright, active stars are believed not to exhibit long-term cycles, instead they are thought to exhibit an irregular variation in their X-ray luminosity (Stern 1998).

Currently, only less than handful of stars have been found to have long-term X-ray cycles. With ROSAT, the monitoring of visual binary 61 Cyg A was begun and, later, continued with *XMM-Newton* (Hempelmann et al. 2006). Four more stars, i.e., the α Cen system, HD 81809 and τ Boo were also monitored by *XMM-Newton* (Favata et al. 2004, 2008; Robrade et al. 2007, 2012; Poppenhaeger et al. 2012) for possible magnetic cycles. Favata et al. (2004) found a pronounced cycle of 8.2 years and a clear evidence for large amplitude X-ray variability in phase with the chromospheric activity cycle for HD 81089. For 61 Cyg A, Robrade et al. (2012) found a regular coronal activity cycle in phase with its 7.3 yr chromospheric cycle, whereas they found no evidence of a clear coronal cycle for 61 Cyg B. Further, they also found that the two α Cen stars exhibit significant long-term X-ray variability, with α Cen A showing a cyclic variability over a period of 12-15 years; the α Cen B data suggest an X-ray cycle of a period of 8-9 years, the amplitudes of the variability for α Cen A and B were estimated to be an order of magnitude and about a factor six to eight, respectively. In addition they also concluded that the coronal activity cycles are a common phenomenon in older, slowly rotating G and K stars. Further Poppenhaeger et al. (2012) studied the activity cycle associated with τ Boo, a moderately active F star displaying a variation of ~ 1 year as anticipated from Zeeman Doppler imaging, however, they were unable to find any evidence of activity cycle with the available X-ray data.

In this paper we demonstrate a possible long-term cycle in the very active star AB Dor A both in its photospheric and coronal point activity. Our paper is structured as follows: in Sect. 2 we present the target stars and in Sect. 3 we describe the observations and data analysis. In Sect. 4 we discuss the optical and the X-ray light curves, we also discuss our investigation on the correlation between the photospheric and coronal activity cycles. In Sect. 5 we investigate the short-term variation induced by the star's rotation and we close with a summary in Sect. 6.

2. Our target star

AB Dor is a quadruple system consisting of the components AB Dor A, AB Dor Ba, AB Dor Bb and AB Dor C. AB Dor A is a magnetically active young dwarf star of spectral type K0, located at a distance of ~ 15 pc from the Sun as a foreground star of the Large Magellanic Cloud. It is a very rapid rotator with a period of $P = 0.514$ days and $v \sin i \approx 90$ Km/s (see Guirado et al. 2011 and references therein), resulting in very high levels of magnetic activity with an average $\log(L_x/L_{bol}) = -3$. Located $9.5''$ away from AB Dor A is the also active M dwarf AB Dor B (Rst 137B; Vilhu & Linsky 1987; Vilhu et al. 1989), which is about ~ 60 times fainter than AB Dor A and therefore only little or no contamination due to the presence of AB Dor V is expected in poor angular resolution studies. At radio wavelengths AB Dor B was serendipitously detected with the Australian Telescope Compact Array (ATCA) during an observations of AB Dor A (Lim et al. 1992). However, the binarity of AB Dor B

itself with a separation of only $0.7''$ (called as AB Dor Ba and AB Dor Bb) was detected after the advent of adaptive optics. Yet another low mass companion to AB Dor A is the AB Dor C Guirado et al. (1997), located about $0.16''$ away from AB Dor A.

The apparent magnitude of AB Dor A of $V=6.75$ (Amado et al. 2001) makes it a favourite target for optical observations to monitor photospheric spots and perform Doppler imaging (Rucinski 1983; Innis et al. 1986, 1988; Kuerster et al. 1994; Anders 1994; Unruh et al. 1995). Additionally Järvinen et al. (2005) noted evidence for a possible activity cycle of ~ 20 years along with presence of flip-flop cycle of ~ 5.5 years. Innis et al. (2008) repeated the cycle study with new data and determined a cycle period supporting the ~ 20 year period suggested by Järvinen et al. (2005). AB Dor A has not only been a target of interest for optical observations, but has been observed with many space based observatories across the UV, EUV and X-ray wavebands. The first X-ray detection of AB Dor A was obtained with the *Einstein* Observatory (Pakull 1981; Vilhu & Linsky 1987) and ever since then AB Dor A has been observed repeatedly by almost all X-ray observatories (Collier Cameron et al. 1988; Vilhu et al. 1993; Mewe et al. 1996; Maggio et al. 2000; Güdel et al. 2001; Sanz-Forcada et al. 2003; Hussain et al. 2007; Lalitha et al. 2013). The long term X-ray behaviour of the X-ray emission from the AB Dor system is dominated by AB Dor A (Güdel et al. 2001; Sanz-Forcada et al. 2003). AB Dor Ba and Bb cannot be separated with any current X-ray telescopes; the combined luminosities of the B-component is $\sim 2.8 \times 10^{28}$ erg/s in the 0.2-4.0 keV (Vilhu & Linsky 1987). Further, with *Chandra* ACIS observations Sanz-Forcada et al. (2003) obtained a luminosity of $\sim 3.4 \times 10^{28}$ erg/s in the 0.5-2.0 keV. Hence, the contribution of the companions to the X-ray emission of AB Dor A can be considered negligible, essentially because the quiescent X-ray emission of the companions scales as their bolometric luminosity.

The time evolution of AB Dor A has previously been studied by Kuerster et al. (1997), who compared the V-band brightness with X-ray observations (5 1/2 years of observations) carried out by ROSAT satellite, however, they did not find any pronounced long-term activity period from their analysis since the 5 1/2 years of data available at the time cover barely a part of the activity cycle.

3. Observations and data analysis

3.1. X-ray data

Being a foreground star of the Large Magellanic Cloud, AB Dor has the advantage of being well observable at all times with most X-ray satellites, and therefore quite a number of often serendipitously taken X-ray data of this source exist. In order to study the long-term evolution of AB Dor A's coronal X-ray emission we used the *Einstein* Observatory Catalog (EOSCAT) of IPC X-ray Sources, a database containing information on sources detected with the *Einstein* Observatory Image Proportional Counter (IPC) which was operated between 1978-1981. Additionally, we adapt the quiescent count rate of AB Dor A reported by Collier Cameron et al. (1988) using the *EXOSAT* Observatory; we also use the *BeppoSAX* observations reported by Maggio et al. (2000).

In addition to these individual observations we utilize a larger number of ROSAT observations obtained from the ROSAT PSPC source catalog from pointed observations with typical exposure time between 1 ksec and 3 ksec, and the ROSAT HRI source catalog from again pointed observations with typical ex-

posure times between 1 ksec and 6 ksec. Since the ROSAT satellite was in low Earth orbit, the typical contiguous and uninterrupted viewing intervals of any source are typically in the range 1 - 2 ksec, therefore longer exposures are composed of a number of shorter exposures with sometimes rather long intervening gaps. We specifically use the PSPC observations obtained between 1990 and 1993 and the HRI observations obtained between 1990 and 1998; the total PSPC exposure is 74.4 ksec, the total HRI exposure is 106.2 ksec; as can be seen from Table 1 the ROSAT observations comprise relatively little total exposure time compared to the *XMM-Newton* observations.

We therefore also carried out a detailed analysis of AB Dor A, using the data obtained by *XMM-Newton* Observatory. On board *XMM-Newton* there are three telescope co-aligned with three CCD cameras (i.e., one PN and two MOS cameras) with a sensitivity range between ≈ 0.2 and 15 keV, together forming the European Photon Imaging Camera - EPIC. The X-ray telescopes equipped with MOS detectors are also equipped with reflection gratings. These two reflection grating spectrometers (RGS) provide high spectral resolution ($E/\Delta E \approx 200-800$) in the energy range 0.35-2.5 keV. Useful data were obtained from the EPIC and the RGS detectors (Table 1).

AB Dor A, being a rather bright target with many emission lines, is fortuitously used as a calibration source for the *XMM-Newton* RGS. Hence this target has been repeatedly observed over last decade, giving us an ideal opportunity to assess the long term behaviour of AB Dor A. In these data there are either no observations or usually much less observation time covered by the EPIC instrument when compared to the RGS (see Table 1); we therefore restrict our analysis to the available RGS data. The data were reduced using standard *XMM-Newton* Science Analysis System (SAS) software V12.0.1. We used the meta-task *rgsproc* 1.30.3 to process the RGS data, this was followed by the spectral extraction and response generation. To create a combined light curve of the two instruments (RGS1+RGS2) the task *rgslccor* 0.52.1 is used¹.

In Figure 1 we provide all RGS light curves utilized for our analysis, and indicate the times of quiescence and the strong flaring. Since AB Dor A is an active star, flaring is indeed observed in almost all observations. When investigating the long-term behaviour of AB Dor A, we want to focus on the quiescent emission and excluded time periods of enhanced activity or strong flaring, particularly where the count rate increased from the quiescent level by about 50 or more percent. We thus excluded larger flares on the basis of the respective X-ray light curve and calculated the mean/median count rate for combined RGS (RGS1+RGS2) observations (see Col. 4 in Table 1).

3.2. Optical data

We compiled all publicly available photometric V-band data of AB Dor A, covering nearly 34 years of observations taken between 1978-2012 with a short gap between 1998-1999 and 2000-2001. The data taken between 1978-2000 has been presented by Järvinen et al. (2005); most of observations were carried out using the standard Johnson *UBVRI* filters. Additionally, we use an – unpublished – data set collected between 2001-2012 obtained in the context of the all-sky automated survey (ASAS)² in the V band (Pojmanski 1997; Pojmanski et al. 2005), which is publicly available.

¹ A detailed description of the XMM packages is available at <http://xmm.esac.esa.int/sas/current/doc/packages.All.html>

² The ASAS data are available at <http://www.astrouw.edu.pl/asas/>

Table 1. Observation log of *XMM-Newton* data used in this publication. Column 4 and 5 provides the mean RGS/median RGS count rate and the data dispersion for the RGS data.

Obs. ID	Date	Obs. time PN/RGS [ks]	Mean/median count rate [cts/s]	σ of the data points [cts/s]
2000				
0123720201	01/05	60.0/49.9	2.64/2.62	0.32
0126130201	07/06	41.9/58.9	2.58/2.57	0.29
0123720301	27/10	55.7/58.8	2.82/2.80	0.26
0133120701	11/12	6.2/8.8	3.07/3.00	0.18
0133120101	"	13.4/60.4	3.15/3.13	0.21
0133120201	"	4.2/20.8	3.03/3.03	0.21
2001				
0134520301	20/01	48.6/52.2	3.81/3.80	0.21
0134520701	22/05	48.2/49.5	2.58/2.57	0.38
0134521301	13/10	— /39.6	2.76/2.74	0.26
2002				
0134521501	12/04	15.9/53.1	3.63/3.66	0.28
0155150101	18/06	4.9/20.3	3.74/3.68	0.36
0134521601	"	21.3/47.8	3.80/3.77	0.350
0134521801	05/11	— /19.8	3.86/3.80	0.11
0134521701	15/11	— /19.8	2.50/2.50	0.32
0134522001	03/12	— /22.3	3.93/3.91	0.28
0134522101	30/12	— /48.8	3.31/3.31	0.30
2003				
0134522201	23/01	— /51.8	2.17/2.19	0.17
0134522301	30/03	— /48.8	3.64/3.59	0.38
0134522401	31/05	— /28.8	2.95/2.97	0.22
0160362701	23/10	— /26.5	2.79/2.80	0.23
0160362801	08/12	— /53.7	3.67/3.63	0.30
2004				
0160362901	27/11	— /56.3	2.60/2.59	0.28
2005				
0160363001	18/04	— /52.1	2.57/2.58	0.38
0160363201	16/10	— /50.1	2.54/2.51	0.25
2006				
0412580101	31/12	— /44.9	2.96/2.87	0.40
2007				
0412580201	19/07	— /48.8	3.32/3.35	0.42
2008				
0412580301	03/01	— /48.8	2.78/2.77	0.27
2009				
0412580401	04/01	47.0/48.8	2.56/2.53	0.32
0602240201	25/11	57.9/58.3	2.15/2.12	0.23
2010				
0412580601	11/01	9.9/49.8	2.21/2.20	0.24
2011				
0412580701	02/01	9.9/62.8	2.51/2.522	0.21
0412580801	31/12	9.9/61.8	2.68/2.67	0.22

The ASAS is a CCD photometric sky survey, monitoring both southern as well as a part of northern sky ($\delta < +28^\circ$) since 2000 up to now. The ASAS telescope is located in Chile, Las Campanas Observatory (LCO) at an altitude of 2215 m above sea level and consists of two wide field ($9^\circ \times 9^\circ$) cameras equipped

S. Lalitha et al.: A solar-like magnetic activity cycle on the active ultra-fast rotator AB Dor A?

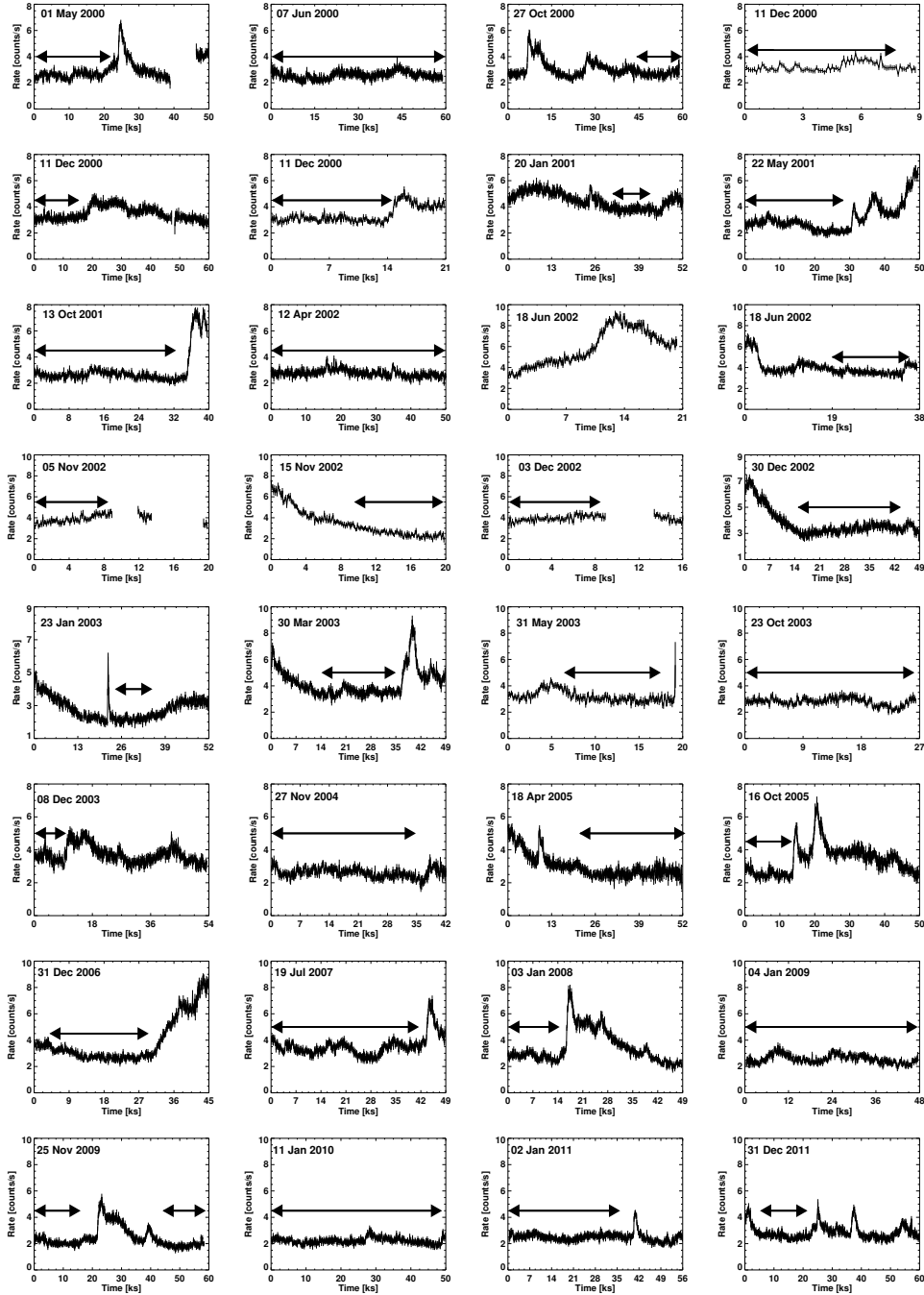


Fig. 1. The XMM-RGS light curves used for analysis. Quiescent time intervals are marked by arrows; see text for details. A log of the observations is provided in the Table 1.

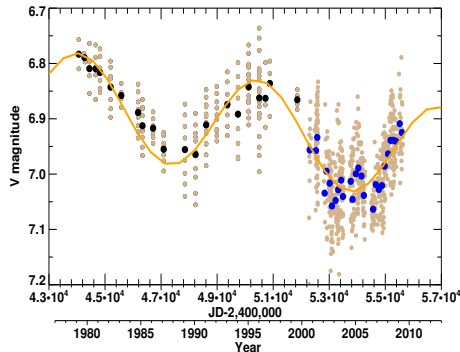


Fig. 2. AB Dor A's long-term V-band brightness evolution adapted from Järvinen et al. (2005) and ASAS observations. Plotted as thick line is the sinusoidal fit to the entire dataset with a period of ≈ 17 years.

with both V and I filters. For AB Dor A, we used observations carried out using only V-band data with exposure times of 180s for each frame. In general, the photometric accuracy of ASAS data for AB Dor A is about 0.05 mag.

4. Light curves

4.1. Optical light curves

In Fig. 2 we plot the V-band brightness of AB Dor A as a function of time; the brown circles denote all individual V band observations. We then subdivide the entire ~ 34 years of V-band observations into smaller time periods and estimate a median V magnitude over each of these time bins; the estimated median magnitudes are plotted as black and blue circles in Fig. 2 for the data from Järvinen et al. (2005) and the ASAS observations, respectively.

In order to search for any periodic variability we performed a periodogram analysis on the entire optical dataset using the generalised Lomb-Scargle periodogram in the form introduced by Zechmeister & Kürster (2009), which is a variant of the Lomb-Scargle periodogram. In Fig. 3 we show the resulting periodogram from the entire optical data set spanning nearly 34 years of observations. A clear peak around ≈ 6190 days (corresponding to 16.96 years) is apparent, which is highly significant, given the derived false alarm probabilities (FAP), also shown in Fig. 3. As a next step we fit a sine wave with a period of ~ 16.96 years to the entire data set presented in Fig. 2 after correcting for the linear trend in the Järvinen et al. (2005) and the ASAS data set (plotted as orange curve in Fig. 2).

In addition to the main peak in Fig. 3, we note another peak with a period ≈ 1 year showing up with $FAP \approx 10\%$. In order to check if this period is due to the activity cycle we recompute the periodogram after subtracting the best-fit sine wave with $P = 16.96$ years from the observed data. When comparing both the periodograms it became evident that the high peak with period of ≈ 1 year survives, hence this peak cannot be the result of considerable spectral leakage from the cycle frequency. Therefore, the nature of this peak remains unclear, yet we suspect that it is due to the seasonal distribution of the observations.

Additionally, in Fig. 4 we plot the mean of optical data folded with the cycle period of ≈ 17 years. Plotted in green and blue are mean of Järvinen et al. (2005) and ASAS observations,

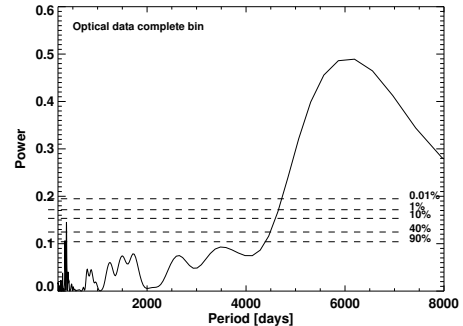


Fig. 3. Periodogram of complete data set of optical V-mag brightness. The highest peak indicate activity cycle period values of 16.96 years.

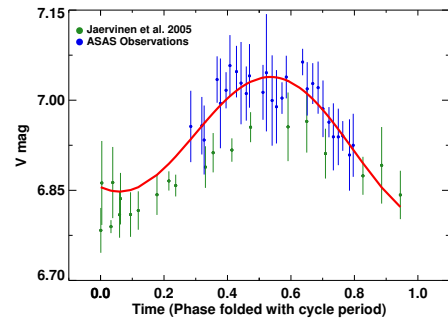


Fig. 4. Optical V-band brightness data of Fig. 2 folded with a cycle period of 16.96 years versus the phase interval [0.0,1.0].

respectively; the plotted error bar is actually depicting the brightness measurement distribution due to rotational modulation.

4.2. X-ray light curves

From the cyclic behaviour of the Sun we know that a decline in the photospheric brightness of a star implies that the surface of the star is dominated by spot activity, which in turn leads to increased X-ray emission from the star. If the same is true for AB Dor A, then, according to Fig. 2, one expects an increase in X-ray activity from minimum to maximum between 1979-1987 and 1996-2004, and a decline in X-ray activity between 1987-1996 and since 2005. In this section we investigate to what extent the available X-ray data support the view of such cyclic coronal activity in AB Dor A.

4.2.1. Overall X-ray behaviour

In Figure 5 we show the temporal behaviour of the soft X-ray luminosity as observed between 1979-2011 by various X-ray satellites. *Einstein* and *EXOSAT* count rates were converted into flux using the conversion factor used by Kashyap et al. (2008). Additionally, we converted the *ROSAT* PSPC and HRI count rates to X-ray fluxes using conversion factors 6×10^{-11}

S. Lalitha et al.: A solar-like magnetic activity cycle on the active ultra-fast rotator AB Dor A?

erg/cm²/count and 2.4×10^{-11} erg/cm²/count, respectively, for the *XMM-Newton*'s RGS the fluxes are obtained using XSPEC model on each observation individually.

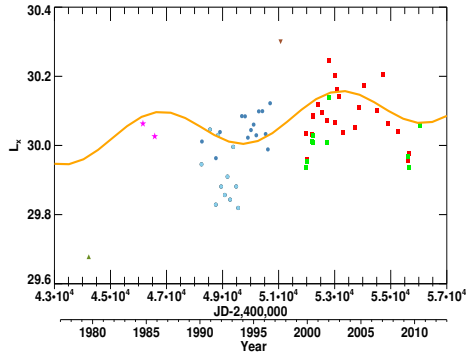


Fig. 5. The temporal behaviour of the soft X-ray luminosity of AB Dor A as observed by several X-ray missions between 1979 and 2011. Depicted as green triangle and magenta stars are *Einstein* and *EXOSAT* data, respectively; *ROSAT* PSPC data are plotted as light blue filled circles; *ROSAT* HRI data are depicted as navy blue filled circles; *BeppoSAX* is plotted as brown upside down triangle. The red and green squares represent *XMM-Newton* RGS and PN observations, respectively. Plotted as thick orange curve is sinusoidal fit to the X-ray data with optical cycle period of ≈ 17 years.

We note that *Einstein* observation data point is quite low when compared to rest of the data; this might be due to an intrinsically low flux or an error in the conversion factor used to convert the observed count rate to flux. In addition, we note that *BeppoSAX* is high when compared to other observations, this is likely due to the presence of strong flaring.

We performed a periodogram analysis on the X-ray light curve presented in Fig. 5, however, we were not able to obtain a significant peak indicating any preferred period. Subsequently we used the period obtained from the optical light curve assuming that the optical period also applies to the X-ray data. We folded the X-ray light curve with this period and obtained a sinusoidal fit to the X-ray data; this sine fit is plotted as a function of time in Fig. 5 as orange thick line. While such a sinusoidal curve provides a description of the data, it is far from unique and there is very large scatter around the fit curve, casting some doubt on any signatures of cyclic activity in the X-ray range.

4.2.2. Correlation between X-ray and optical data

In order to check whether the trends in the X-ray and optical are really correlated, we carried out a correlation analysis of the two data sets. In order to relate an optical magnitude to each X-ray observation, we use the value of the fitted optical light curve (see Fig. 2) at the time of each X-ray observation. The resulting scatter plot is shown in Fig. 6, which indicates a small, but positive slope of 0.30 ± 0.21 for the X-ray and optical brightness, implying that X-ray luminosity is higher when photospheric brightness is lower as expected from the solar analogy. Further, we also computed a linear Pearson correlation coefficient between (logarithmic) X-ray luminosity and photospheric brightness as 0.15 with a chance probability of 19%. These findings are clearly con-

sistent with the above mentioned picture of the star being X-ray bright when the surface brightness is small, however, the statistical significance of this correlation is uncomfortably low.

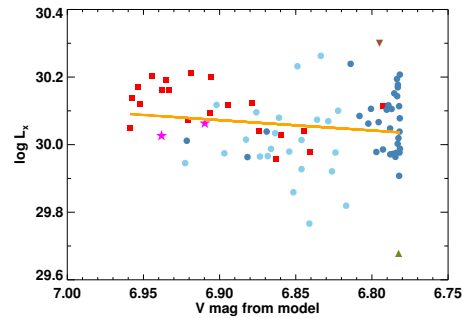


Fig. 6. Variation of X-ray luminosity as a function of the calculated V magnitude. The symbols here are the same as in Fig. 5; see text for details.

4.2.3. Individual light curves : ROSAT

While the overall X-ray light curve might be affected by errors in the instrumental cross calibrations, trends in individual instruments should be free from such effects and be real. In the following we therefore concentrate on the data taken with the *ROSAT* PSPC and the *ROSAT* HRI, from which a multitude of observations is available, to determine count rate trends individually for each instrument. The results of this analysis are listed in Tab. 2; we find a small negative and a positive slope with respect to time evolution of the count rates for the *ROSAT*-PSPC and HRI data, respectively (see column 2 in Table 2).

We used a simple bootstrap technique to estimate the error of the slope. For this we ran a Monte-Carlo simulation for the observing times carrying out linear fits to the simulated data sets. The count rates and their individual errors were randomly redistributed over the range of available observing times. Regression analysis on the re-sampled data was performed and repeated several times (5×10^5 times), thus providing an error at 1σ probability associated with the determined slope. The results of this analysis are listed in column 3 of Table. 2. For the PSPC data we find that in 72% of the cases slopes as small as the observed one are obtained by pure chance, whereas for the HRI data this is estimated to be in 61% of the cases.

Further, comparing the optical (Fig. 2) and the X-ray light curves (Fig. 5) one expects the *ROSAT* PSPC observations to be during the activity minimum, the *ROSAT* HRI to be during the constant/raise from activity minimum to maximum and the *XMM-Newton* covering almost two activity minimum periods. Our regression analysis of the individual PSPC and HRI data fits with the above picture, albeit at low significance. Due to the sparse sampling of the *Einstein*, *EXOSAT* and *BeppoSAX* observations we could not perform any regression analysis these data, however, these observations again appear to be consistent with the "expected" long term behavior.

Table 2. Results from the search for a long term variation in the X-ray data. The errors and the false alarm probability are obtained from bootstrapping the observed distribution of the measurements (BS).

Data set	best fit slope [cts/sec/yr]	Error BS	FAP %
<i>ROSAT</i>			
PSPC	-0.22	0.47	72
HRI	0.05	0.05	61
<i>XMM</i> RGS	-0.04	0.02	63

4.2.4. Individual light curves : *XMM-Newton*

Since AB Dor A was used as a calibration source for the RGS on board *XMM-Newton*, lots of data with much enhanced quality and large temporal coverage of AB Dor A have become available, which can be used for cycle studies. In particular, we can identify periods of flaring in the data stream and exclude such periods from analysis. In Fig. 7 we plot the evolution of the XMM-RGS count rate taking into consideration only the quiescent emission. Specifically, in the top panel of Fig. 7, we show the complete XMM-RGS count rate history of AB Dor A (as brown circles) after removing the flares from each observation. In addition we plot the median count rate over every observational run as black circles in the top panel of Fig. 7. In the lower panel of Fig. 7 we re-plot Fig. 2 to compare the optical and X-ray light curves. However, if the XMM-RGS data show a variation comparable to the optical data then 2000-2006 should represent activity maximum. While visual inspection suggests a possible anti-correlation between the optical and the X-ray data, we carry out some statistical tests to check whether these trends are significant or not.

A (parametric) regression analysis on this data similar to the ROSAT data is performed and the results are presented also in Table 2. We obtained a negative slope for the observed XMM-RGS count rates as a function of time, and again, similar to the ROSAT data we performed a simple bootstrap technique to estimate the error of the slope and FAP. A slope as small as the observed one for the XMM-RGS data by pure chance is estimated to be 63%. The negative slope fits with the overall picture of an expected decline in the activity, however the significance of this slope is very low.

We then decided to apply non-parametric correlation tests such as the Spearman ρ and Kendall τ test (Press 1992) on the mean and the median XMM-RGS data presented in Table. 1. For this purpose we divided the XMM-RGS data into two subsets, one covering the years 2000-2005, i.e., towards the anticipated maximum, and the second set between 2005-2011 with declining activity expected. The Spearman's rank correlation coefficient ρ is defined as

$$\rho = \frac{\sum(R_i - \bar{R})(S_i - \bar{S})}{\sqrt{\sum(R_i - \bar{R})^2} \sqrt{\sum(S_i - \bar{S})^2}}, \quad (1)$$

where R_i and S_i are the ranks of time and the minimum count rate values respectively. The significance of a non-zero value of ρ is computed from the value of t defined as

$$t = \rho \sqrt{\frac{N-2}{1-\rho^2}}, \quad (2)$$

where ρ is Spearman's rank and N is the sample size. Note that the significance t is distributed approximately as Student's distri-

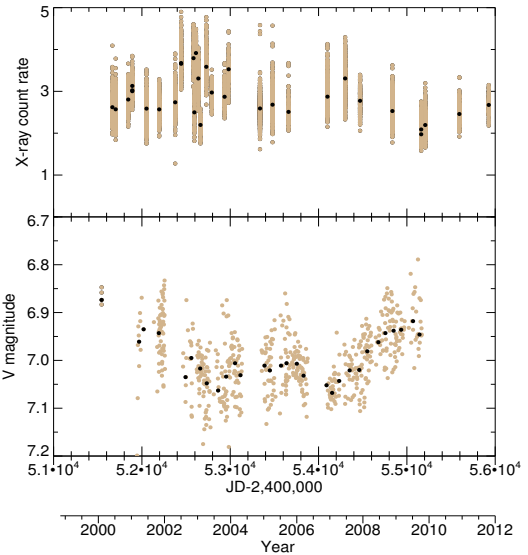


Fig. 7. Top panel: The temporal behaviour of the XMM-RGS count rate of AB Dor A as observed between 2000 and 2011. Bottom Panel: V-band data for AB Dor A.

bution with $N-2$ degrees of freedom (Press 1992); a small value of significance (p in Tab. 3) indicates a significant correlation.

An alternative non-parametric test is the Kendall's τ -test, which uses the relative ordering of the rank instead of the numerical difference of the ranks. Consider two samples (with n items each) of physical quantities, in our case the observing times t_i ($i = 1, N$) and the minimum count rate r_i ($i = 1, N$); we assume the times sorted so that $t_i < t_{i+1}$. The total number of possible pairs of time and count rates is $n(n-1)/2$. Now consider a pair of values of time t and count rate r . If the relative ordering of the ranks of two times is the same as the relative ordering of the two rates, the pair is called concordant, otherwise the pair is called discordant. Ignoring the problem of how to treat tied observations, the basic idea is to compare the number of concordant and discordant pairs, since that number should be statistically equal in the absence of correlations. Specifically Kendall's τ is given by

$$\tau = \frac{n_c - n_d}{n(n-1)/2}, \quad (3)$$

where n_c is the number of concordant and n_d the number of discordant pairs, normalized by the total number of pairs. Clearly, for a perfect correlation $\tau = 1$. On the null hypothesis of independence of time and count rate, i.e., no correlation, τ is expected to be normally distributed with zero expectation and a variance of

$$\text{Var}(\tau) = \frac{4N+10}{9N(N-1)}. \quad (4)$$

The results of our correlation analysis are provided in Tab. 3, where we also quote the two sided probability value (p -value) for a given t -value. Clearly, both tests and both the median and

S. Lalitha et al.: A solar-like magnetic activity cycle on the active ultra-fast rotator AB Dor A?

Table 3. Results from the correlation test performed on the mean and median XMM-RGS data. Column 3 shows the significance of a non zero value of the Spearman rank and Column 5 shows whether the observed value of τ is significantly different from zero.

Data set	Spearman ρ test			Kendall τ test	
	ρ	t	p-value	τ	σ^2
Mean RGS data					
2000-2005	-0.01	-0.07	0.94	0.02	0.02
2005-2011	-0.45	-1.33	0.22	-0.28	0.07
2000-2011	-0.36	-2.15	0.04	-0.22	0.01
Median RGS data					
2000-2005	-0.05	-0.22	0.82	0.01	0.02
2005-2011	-0.33	-0.94	0.37	-0.22	0.07
2000-2011	-0.35	-2.05	0.04	-0.20	0.01

mean RGS data yield no significant correlations for the 2000 - 2005 data, while both tests suggest significant correlations for both the median and mean RGS data between 2000 - 2011. If only the 2005 - 2011 data are considered, the τ -test suggests a significant correlation, while the correlation is marginal at best using Spearman's rank ρ . In all cases, however, there is an anti-correlation, i.e., the X-ray rate is decreasing according to "expectation". This results suggests that there is an influence of the cycle of the activity cycle on the X-ray emission, however, the observed X-ray variation is quite different than the X-ray variation measured for the Sun. It is of course difficult to assess this influence quantitatively, however, inspecting the values provided in Tab. 1 we find a maximum count rate of 3.93/3.91 cts/s from XMM-RGS data and a minimum count rate of 2.15/2.12 cts/s, from which we calculate a variation amplitude of at most ~ 1.8 in the X-ray emission between minimal and maximal activity in AB Dor.

4.3. Summary: Is there an X-ray activity cycle on AB Dor A ?

While a clear cyclic behaviour with a cycle length of ~ 17 years is observed for AB Dor A in its optical brightness variations, a similar variation in the available X-ray data is not immediately apparent. However, one does observe some anti-correlation between optical and X-ray brightness in support of the view of a variation in X-ray flux with the optical cycle (Fig. 6). The extensive and contiguous observations carried with the XMM-Newton RGS allow a much more refined assessment of the temporal variability of AB Dor A compared to previously available X-ray data. An inspection of Fig. 1, demonstrates that AB Dor A is variable at all times and does indeed produce frequent and significant flaring. However, the XMM-Newton RGS data also demonstrate that AB Dor A returns to a "basal" state at around approximately 3 RGS cts/sec. This "basal" state can be observed only in reasonably long and contiguous observations, and even then this "basal" state might not be attained. At any rate, in short and non-contiguous data as available from satellites in low Earth orbit such as ROSAT it is difficult to identify such "basal" state periods; still, taking the ROSAT data at face value, the data actually support a variation of X-ray flux with optical cycle in the anticipated way, however, the obtained correlations are not statistically significant.

Since the available XMM-Newton observations now cover the period between optical activity maximum and minimum we carried several statistical test to study a possible activity cycle associated with the XMM-RGS data. These tests indeed indicate an increase and decline in activity with an activity maximum

around 2005-2006. This change in activity manifests itself in a change in the flux of the "basal" state level, however, the amplitude change is at most a factor of two, and maybe even less. As a consequence the relative change is far less than the relative change observed in the Sun and other late-type stars and therefore the variability of the star's "basal" state is actually less than the typical X-ray variability (outside flares) in less active cool stars.

5. Rotational modulation

Out of the wealth of data of available XMM-Newton data on AB Dor A, we chose those subsets of data which cover more than one stellar rotation and are thus well suited for a short-term variability study. In Fig. 8, we depict the X-ray light curve after flares have been removed by eye for all XMM-RGS data sets with more than one rotational period and plotted vs rotational phase interval. Each colour in Fig. 8 represent different observations, the dashed line represent the first rotation and thick line during second rotation. Furthermore, the black filled circles in Fig. 8 represent the calculated mean count rate and the corresponding 2σ deviation at a certain rotation phase. We note substantial fluctuations as a result of an active corona. The seemingly irregular variability seen in individual light curves can be attributed to the low energy and short time scale flares, with no obvious sign of rotational modulation. We do point out that the data shown in Fig. 8 extend over ten years, yet the dispersion of the data is rather small, reemphasizing the existence of a "basal" coronal state in AB Dor.

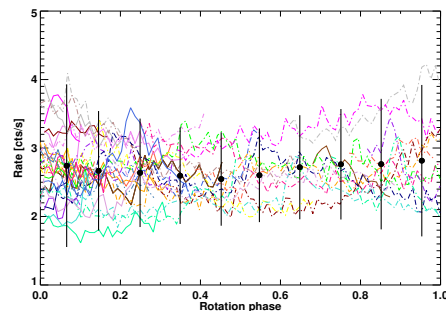


Fig. 8. X-ray light curve after removing the flares from a subset of XMM-RGS observation on AB Dor A folded with rotational period and plotted vs. the phase interval. Black filled circles mean count rate at a certain rotation phase with 2σ deviation.

6. Summary

The available X-ray observations of AB Dor, compiled for a period of more than thirty years, show X-ray variability on a variety of time scales. Since AB Dor is a very active star, it exhibits substantial short term variability and in particular frequent flaring activity. Such flaring activity may last for a couple of hours and therefore, in short and non-contiguous "snap shot" observations, as typically available from low Earth satellites, such variability is difficult to distinguish from variability on longer time scales. In the optical, long-term variability with a period of 16-17 years

and very reminiscent of the solar sunspot cycle could be established; with 20% the amplitude of the optical cyclic variations is quite substantial.

Because of its substantial variability on short time scales a correlation between X-ray and photospheric activity is difficult to establish with "snap shot" X-ray data. However, in sufficiently long X-ray observations AB Dor is observed, first, to attain a "basal" state of ≈ 3 *XMM-Newton* RGS cts/sec, and, second, we have presented evidence that this "basal" state flux may actually vary with the optical cycle of AB Dor in analogy to the solar activity cycle. However, for AB Dor A we estimate a factor of only ~ 1.8 variation in the X-ray emission in 0.3-2.5 keV range during its cycle, and therefore this very active star is in some sense much less variable than other solar-like stars (Robrade et al. 2012), albeit the basic picture that the X-ray flux is maximum, when the photospheric brightness is at minimal, also seems to apply to AB Dor.

Clearly, the time interval for which X-ray and optical data are available is rather short compared to the presumed cycle period of almost 17 years. Only two cycles have been covered so far, and a true periodicity as observed for the Sun is far from having been established. Further photometric monitoring of AB Dor and related objects in the next decades (!) is certainly in order to study whether the observed variations are truly cyclic with a well defined period. With more or less robotic facilities such monitoring can nowadays be carried out at relatively low cost. Similarly, extended X-ray observations of AB Dor and again similar objects would help to establish the existence of such "basal" states also in other stars, their relationship to stellar parameters and possible cycle variations.

Acknowledgements. S. L. acknowledges funding by the DFG in the framework of RTG 1351 "Extrasolar planets and their host stars".

References

- Amado, P. J., Cutispoto, G., Lanza, A. F., & Rodonò, M. 2001, in *Astronomical Society of the Pacific Conference Series*, Vol. 223, 11th Cambridge Workshop on Cool Stars, Stellar Systems and the Sun, ed. R. J. Garcia Lopez, R. Reboló, & M. R. Zapaterio Osorio, 895-900
- Anders, G. J. 1994, *Information Bulletin on Variable Stars*, 3985, 1
- Ayres, T. R. 1997, *J. Geophys. Res.*, 102, 1641
- Ayres, T. R., Judge, P. G., Saar, S. H., & Schmitt, J. H. M. M. 2008, *ApJ*, 678, L121
- Baliunas, S. L., Donahue, R. A., Soon, W., & Henry, G. W. 1998, in *Astronomical Society of the Pacific Conference Series*, Vol. 154, *Cool Stars, Stellar Systems, and the Sun*, ed. R. A. Donahue & J. A. Bookbinder, 153
- Baliunas, S. L., Donahue, R. A., Soon, W. H., et al. 1995, *ApJ*, 438, 269
- Collier Cameron, A., Bedford, D. K., Rucinski, S. M., Vilhu, O., & White, N. E. 1988, *MNRAS*, 231, 131
- Favata, F., Micela, G., Baliunas, S. L., et al. 2004, *A&A*, 418, L13
- Favata, F., Micela, G., Orlando, S., et al. 2008, *A&A*, 490, 1121
- Gnevyshev, M. N. 1967, *Sol. Phys.*, 1, 107
- Golub, L. 1980, *Royal Society of London Philosophical Transactions Series A*, 297, 595
- Güdel, M., Audard, M., Briggs, K., et al. 2001, *A&A*, 365, L336
- Guirado, J. C., Marcaide, J. M., Martí-Vidal, I., et al. 2011, *A&A*, 533, A106
- Guirado, J. C., Reynolds, J. E., Lestrade, J.-F., et al. 1997, *ApJ*, 490, 835
- Hale, G. E. 1908, *ApJ*, 28, 315
- Hathaway, D. H. 2010, *Living Reviews in Solar Physics*, 7, 1
- Hempelmann, A., Robrade, J., Schmitt, J. H. M. M., et al. 2006, *A&A*, 460, 261
- Hempelmann, A., Schmitt, J. H. M. M., & Stepień, K. 1996, *A&A*, 305, 284
- Hussain, G. A. J., Jardine, M., Donati, J.-F., et al. 2007, *MNRAS*, 377, 1488
- Innis, J. L., Budding, E., Olah, K., et al. 2008, *Information Bulletin on Variable Stars*, 5832, 1
- Innis, J. L., Thompson, K., & Coates, D. W. 1986, *MNRAS*, 223, 183
- Innis, J. L., Thompson, K., Coates, D. W., & Evans, T. L. 1988, *MNRAS*, 235, 1411
- Järvinen, S. P., Berdyugina, S. V., Tuominen, I., Cutispoto, G., & Bos, M. 2005, *A&A*, 432, 657
- Kashyap, V. L., Drake, J. J., & Saar, S. H. 2008, *ApJ*, 687, 1339
- Kreplin, R. W. 1970, *Annales de Geophysique*, 26, 567
- Kuerster, M., Schmitt, J. H. M. M., & Cutispoto, G. 1994, *A&A*, 289, 899
- Kuerster, M., Schmitt, J. H. M. M., Cutispoto, G., & Dennerl, K. 1997, *A&A*, 320, 831
- Lalitha, S., Fuhrmeister, B., Wolter, U., et al. 2013, *A&A*, submitted
- Lim, J., Nelson, G. J., Castro, C., Kilkenny, D., & van Wyk, F. 1992, *ApJ*, 388, L27
- Lockwood, G. W., Radick, R. R., Henry, G. W., & Baliunas, S. L. 2004, in *Bulletin of the American Astronomical Society*, Vol. 36, *American Astronomical Society Meeting Abstracts #204*, 671
- Lockwood, G. W., Skiff, B. A., Henry, G. W., et al. 2007, *ApJS*, 171, 260
- Maggio, A., Pallavicini, R., Reale, F., & Tagliaferri, G. 2000, *A&A*, 356, 627
- Mewe, R., Kaastra, J. S., White, S. M., & Pallavicini, R. 1996, *A&A*, 315, 170
- Orlando, S., Peres, G., & Reale, F. 2000, *ApJ*, 528, 524
- Pakull, M. W. 1981, *A&A*, 104, 33
- Peres, G., Orlando, S., Reale, F., Rosner, R., & Hudson, H. 2000, *ApJ*, 528, 537
- Pojmanski, G. 1997, *Acta Astron.*, 47, 467
- Pojmanski, G., Pilecki, B., & Szczygiel, D. 2005, *Acta Astron.*, 55, 275
- Poppenhaeger, K., Günther, H. M., & Schmitt, J. H. M. M. 2012, *Astronomische Nachrichten*, 333, 26
- Press, W. 1992, *Numerical recipes in C: the art of scientific computing* (Cambridge Cambridge University Press)
- Robrade, J., Schmitt, J. H. M. M., & Favata, F. 2012, *A&A*, 543, A84
- Robrade, J., Schmitt, J. H. M. M., & Hempelmann, A. 2007, *Mem. Soc. Astron. Italiana*, 78, 311
- Rucinski, S. M. 1983, *A&AS*, 52, 281
- Sanz-Forcada, J., Maggio, A., & Micela, G. 2003, *A&A*, 408, 1087
- Schwabe, M. 1844, *Astronomische Nachrichten*, 21, 233
- Stern, R. A. 1998, in *Astronomical Society of the Pacific Conference Series*, Vol. 154, *Cool Stars, Stellar Systems, and the Sun*, ed. R. A. Donahue & J. A. Bookbinder, 223
- Stern, R. A., Alexander, D., & Acton, L. W. 2003, in *The Future of Cool-Star Astrophysics: 12th Cambridge Workshop on Cool Stars, Stellar Systems, and the Sun*, ed. A. Brown, G. M. Harper, & T. R. Ayres, Vol. 12, 906-911
- Tobiska, W. K. 1994, *Sol. Phys.*, 152, 207
- Unruh, Y. C., Collier Cameron, A., & Cutispoto, G. 1995, *MNRAS*, 277, 1145
- Vaughan, A. H., Preston, G. W., & Wilson, O. C. 1978, *PASP*, 90, 267
- Vilhu, O., Ambruster, C. W., Neff, J. E., et al. 1989, *A&A*, 222, 179
- Vilhu, O., & Linsky, J. L. 1987, *PASP*, 99, 1071
- Vilhu, O., Tsuru, T., Collier Cameron, A., et al. 1993, *A&A*, 278, 467
- Wilson, O. C. 1978, *ApJ*, 226, 379
- Wright, N. J., Drake, J. J., & Civano, F. 2010, *ApJ*, 725, 480
- Zechmeister, M. & Kürster, M. 2009, *A&A*, 496, 577

Part III

Conclusions

Chapter 8

Concluding remarks

In this chapter, I summarise the scientific results of my thesis and comment on the future research possibilities.

8.1 Summary and concluding remarks

In this thesis, different aspects of stellar activity were investigated, making use of different observational techniques both ground based as well as space borne facilities. In the first part, I characterised the coronal properties of potential planet host stars in the solar neighbourhood with an emphasis on the M dwarfs.

CARMENES

CARMENES is a low-mass planet search survey to be carried out on a sample composed of moderately active M dwarfs. Magnetic activity plays an important role for planet finding surveys, especially for low-mass stars. To optimize the scientific return from CARMENES, a careful analysis prior to selection has to be carried out. The pre-CARMENES list currently consists of ~ 1400 stars of which ~ 450 most suitable targets for CARMENES survey are to be selected. At X-ray wavelength no systematic studies of planet host stars have been published, however, comprehensive studies of coronal activity properties of late-type stars in solar neighbourhood have been carried out for several decades now. I revisited ROSAT observations to characterise the coronal properties of potential planet hosts.

Nearly 40% of the stars from the pre-CARMENES target list were detected as X-

ray sources. I estimated an upper-limit coronal flux for those stars which were not detected by ROSAT observations. During this characterisation I noticed that none of the stars in the pre-CARMENES target list are super-saturated M dwarfs and they are not X-ray dark as our Sun.

Furthermore, most of the detected X-ray sources were intrinsically active, therefore are not suitable for CARMENES survey and can be definitely excluded from pre-CARMENES target list. However, the non-detection do not rule out substantial activity. Those non-detected stars will be characterised further based on the most relevant chromospheric activity indicator $H\alpha$ emission and eliminated if not suitable for the CARMENES survey.

Flares in low mass stars

Low mass stars are capable of producing strong flares of short as well as longer durations. Even if an M Earth is detected in its habitable zone by the CARMENES survey, M dwarfs show flares that are of concern for the continuity of habitability on the surface of these planets. In the second step, I studied the properties of stellar flares on low mass stars. For this we chose two of the well-studied X-ray sources Proxima Centauri and AB Dor A. I studied the magnetic activity of Proxima Centauri and AB Dor A as manifested in its X-ray emission in quiescent and in flaring states.

Proxima Centauri is a magnetically active star of spectral type dM5.5 and is the star closest to the Sun with a distance of only 1.3 pc. We observed Proxima Centauri simultaneously using *XMM-Newton* and VLT/UVES. We tried to build an overall picture of the atmosphere

from the chromosphere to the corona. From the X-ray data I determined coronal densities, abundances, emission-measure and temperatures. We also noticed that the flare light curve is similar to the mega-flare on the same star described by Güdel et al. (2004) and exhibiting two bumps during the decay phase. The secondary flares have similar loop length as the main flare, show chromospheric line asymmetries, and chromospheric flare modelling shows that the first one exhibits similar chromospheric parameters as the main one. All this indicates, that the events are not independent of each other, but result from the same loop or at least an arcade with several arcade loops igniting consecutively.

In similar lines we investigated the coronal activity on the highly active K-dwarf star AB Dor A, the closest and brightest ultra-fast rotator. We notice that the Proxima Centauri and AB Dor A light curves are very similar with a large primary flare followed by secondary flares. This suggested that the flares originate in the same loop or arcade similar to Proxima Centauri. However, the high cadence optical spectra of AB Dor A clearly suggests that these events originate in different active regions. Furthermore, we notice that for one of the event the OM shows no counterpart, while the chromospheric lines do show some reaction, although it is hard to discern, if it is physically connected to the X-ray emission.

To build an overall picture of the atmosphere from the chromosphere to the corona, we compared the X-ray and optical/UV light curves of Proxima Centauri and AB Dor A during the flare onset. The optical/UV peak precede the X-ray peak in both targets suggesting Neupert effect is in action. However, during the large flare on AB Dor A, the chromospheric lines do not react strongly to the flare in amplitude, but X-ray and optical/UV light curves exhibit stronger emission before and after the flare events. Though the chromospheric lines react weakly to the flare, the stronger lines like Ca II, Balmer lines, He I D₃, etc. show turbulent broadening and the Balmer lines Stark Broadening. All these evidence suggests that for this large flare, the picture of a flare affect-

ing different atmospheric layers is consistent.

During the flare, the temperature and the emission measures are enhanced by more than an order of magnitude compared to the quiescent corona. We notice that the flare plasma shows a different composition, which can be considered to consist mostly of material evaporated from the chromosphere or the photosphere. In addition, we find that the coronal abundances of both Proxima Centauri and AB Dor A follow a trend of increasing abundance with increasing first ionisation potential (FIP) a behaviour which is called the inverse FIP effect. In other words, the high-FIP elements like oxygen, neon, and carbon are higher in abundance than that of the low-FIP elements like iron and silicon. An inverse-FIP effect is a reverse pattern of the FIP effect which is common among stars with high activity levels $\log(\frac{L_X}{L_{bol}}) > -4$, while inactive stars like Sun show a FIP effect.

In addition, to the overall abundance variation during the flare we also studied the temporal evolution of few elements individually. We infer from our data that the iron abundance increases from a level of quiescence directly before the onset of the flare to a maximum value, when the flare peak is reached in each of our target. This indicates that fresh plasma material is evaporated from the photosphere and chromosphere that has a different composition with a higher iron abundance than the quiescent coronal plasma. Oxygen is another element that produces very strong emission lines in our X-ray spectra, we also investigate possible oxygen abundance changes during the flare in the same fashion, but found no evidence of a similar behaviour.

Characteristics of AB Dor A flares

AB Dor A being a calibration source for the reflection grating spectrometer (RGS) on board *XMM-Newton*, has been repeatedly observed over the last decade. Making use of this unique opportunity, I characterised all the flares observed on AB Dor A ever since *XMM-Newton* been operational. Resulting in over 17 flares from XMM's PN and 27 flares from the RGS. This study provided a general comparison of

AB Dor A flare characteristics with those of other active X-ray stars and the Sun.

With this analysis, I emerge with the largest data set of AB Dor A flares, with peak luminosities in the range $26 < \log L_X < 28$ erg/s, several orders of magnitude more powerful than a solar flare. An important empirical result is that peak plasma temperatures measured by *XMM-Newton* are often between 20 and 30 MK. Further, I compared the flare properties of AB Dor A with the solar-stellar scaling laws derived by Aschwanden et al. (2008). All flares observed on AB Dor A seem to follow the solar-stellar trend between plasma peak emission measure and temperature, $EM_f \propto T_f^{4.7 \pm 0.1}$. The trend between flare duration and peak temperature is also consistent with previous findings. Further I derive the flare loop parameters using the well-established flare plasma model of Reale et al. (1997). The inferred sizes of AB Dor A's flaring structures are not remarkably large.

These observations of AB Dor A's corona over a decade provides an unique opportunity in fundamental understanding of short-term energy releases and their role in heating the atmospheres of highly active stars. As a next step, I estimated the energy radiated at X-ray wavelength above quiescent level for both PN and RGS separately and studied their distribution. The power-law indices obtained for the flare energy distribution cluster around a value of 2. Thus broadly equivalent to solar distributions, which suggests that the cause of flare initiation in magnetically very active stars may be similar to the Sun. A noticeable feature about AB Dor A's flare energy distributions is that the trend continues up to energies at least 2 orders of magnitude higher than observed on the Sun.

AB Dor A's activity cycle

AB Dor A, an active ultra-fast rotator shows modulation in its X-ray activity correlated with the photospheric brightness with a period of ≈ 17 years. The star exhibits an increasing activity during XMM-RGS observations between 2000 and 2005; in X-ray data from 2005-2011 exhibits a decline in the activity level. However,

the variation determined have a variability amplitude of a factor > 2.5 variation in the X-ray emission in 0.3-2.5 keV range. AB Dor A's X-ray brightness variation is about a factor of three smaller than the Sun, however, his amplitude of variation is very similar to the cycle amplitude seen in other K stars 61 Cyg A and B.

Further, I chose few subsets of XMM-RGS data covering more than stellar rotation and studied the short-term variability induced due to stellar rotation. An analysis of rotational modulation in XMM-RGS data is hampered by the fact that much of it is highly influenced by flares. The variability seen in individual light curves outside the large flare are quite irregular which attributes to low energy and short time scale flares. These strong episodic events/flares contribute substantially to the observed modulation, and do not follow a periodic behaviour as any purely rotation induced modulation. Thus I conclude that there is no evidence for any significant rotational modulation during XMM-RGS observations.

8.2 Outlook

In this section, I outline the questions which can arise from this thesis and describe the projects which are already pursued to be answered in the future. A major part of the outlook focuses on the influence of stellar activity on the planets orbiting low mass stars in their respective habitable zone and the influence of stellar activity on high-precision radial velocity measurement.

M dwarfs are faint stars, emitting the maximum of their radiation in the infrared, and most of them are highly active. Furthermore, small M-dwarf stars with masses around $0.3 M_{\odot}$ make up the majority of stars in the Galaxy and, consequently, the bulk of potential planet hosts. These factors seemingly conspire to make M dwarfs as excellent targets for RV surveys. Since, the amplitude of the planet-induced stellar motion—sometimes referred to as the RV-wobble—is larger for smaller stars, around which small planets are, therefore, more easily detected. For planet search programs using the RV method, the effects of stellar activity on spectral lines complicate the detection of

planets.

Stellar activity is the result of dynamically evolving magnetic fields, which are produced in the stellar interior. These magnetic fields are responsible, e.g., for the presence of starspots, chromospheric heating, and stellar flares. In the spectrum, the strength of chromospheric heating can be inferred from the presence of chromospheric emission lines such as the Ca II H&K lines, $H\alpha$, the Na I doublets, and the He I lines. The strength and variability of the emission in these lines is a measure of the activity level of the star. We successfully proposed to use the Vainu Bappu Telescope, and observations were carried out using echelle spectrograph for 10 consecutive nights to carry out a systematic investigation of stellar activity in a set of bright M dwarf stars extracted from the CARMENES sample. We plan to use the observed spectra to study the spectral variability and the stellar activity in the sample stars both on the one-night and the night-to-night scale. In particular, we will analyse the temporal evolution of the following chromospheric activity indicators: the hydrogen Balmer lines, the He D₃ and Na D₁ and D₂ lines, and the Ca infrared triplet lines. Based on the temporal analysis, we will derive the time scales and amplitudes of spectral variability. Further, we will test whether the activity indicators are correlated as has been observed in many active stars (see, e.g., Gomes da Silva et al. 2011). The results of this study will be important to understand stellar activity in M dwarf stars and how it affects radial velocity measurements. We will be able to determine to what extent our sample stars and similar objects are well suited for an extensive radial velocity monitoring by planet search campaigns like CARMENES and how stellar activity can be accounted.

For close-in super-Earth planets it is speculated, that they are formed due to the evaporation of outer atmospheres of Jovian planets. If we know the evolution of the emission in the X-ray/UV flux we should be able to trace the planet evolution, given an accurate knowledge of the density of the planet. Understanding the age-activity relations for the highest energy activity tracers (e.g. X-ray and EUV) is vital to

determine the incident radiation on planets in an orbit around low-mass dwarfs. Hence non-optical studies in the X-ray and UV observations would help assess the total coronal radiative losses for super-Earth host stars, and would inform models of planetary atmospheric evolution for the attendant planet. Additionally, these studies also provide an ideal opportunity to compare high-energy environment of super-Earth systems.

We successfully proposed an *XMM-Newton* observation of the transiting super-Earth system GJ 1214 at X-ray and UV wavelengths. Charbonneau et al. (2009) reported the discovery of the second *transiting* super-Earth — namely, GJ 1214b. This planet orbits a nearby (13 pc) M4.5-dwarf at a distance of no more than 0.014 AU once every 1.58 d. It has a radius of 2.68 Earth radii and only ≈ 6.55 times the Earth's mass. GJ 1214 stands out for being exceptionally close (13 pc) and showing the by far deepest transit of all close super-Earths. Recent studies have shown that high-energy emission can have a crucial influence on the evolution of planets. An important ingredient in atmospheric modeling is the strength of the surrounding high-energy radiation field, which is the major driver of planetary mass loss. Intense high-energy radiation can heat the exospheres of close-in planets to chromospheric temperatures of around 10 000 K (e.g., Lammer et al. 2003), which leads to planetary mass loss. In the case of an active host star such as CoRoT-2A, the planetary mass-loss rate can be as high as $4.5 \times 10^{12} \text{ g s}^{-1}$ (Schröter et al. 2011), but even for HD 209458b, which orbits an inactive star ($L_X < 1.3 \times 10^{26} \text{ erg s}^{-1}$, Sanz-Forcada et al. 2011), the mass-loss rate reaches $\approx 10^{11} \text{ g s}^{-1}$ (e.g., Lecavelier des Etangs et al. 2004). With our proposed observations, we will be able to characterize the high-energy environment of GJ 1214, compute the mass-loss rate and constrain models of GJ 1214b's atmosphere.

The activity of the host star obviously controls the evaporation of a planetary atmosphere and thus the fate of the planet itself. In the case of highly eccentric orbits the irradiation level is expected to strongly vary along the orbit.

We may in these cases expect temporal changes also in the ensuing evaporation. Therefore we composed a sample of nearby exoplanets with orbital eccentricities in excess of 0.1 and proposed *Chandra* observations to characterise the the high-energy environment of planet-bearing host stars. This study would provide a significant input into the study of extrasolar planets. If any of our proposed targets turns out to be an X-ray source, they could become a favourable target for a detailed follow-up study of star-planet interactions.

These observations will reveal new features that will contribute to additional understanding of the magnetic activity in planet host stars.

List of Figures

1.1	Giant spot on the surface of the Sun showing numerous granules, the dark umbral region and the light penumbral region. Image credit: SST, Royal Swedish Academy of Sciences.	4
1.2	Top panel : Butterfly diagram of sunspots. This plot shows that the spots migrate towards the equator during a given cycle. Bottom panel: The total area of sunspots as a percent of the visible hemisphere which follows a 11-year cycle. Image credit: David Hathaway, NASA/MSFC.	5
1.3	The solar chromosphere glowing in red around the edge of the moon. This image also shows the presence of prominence like structures around the limb of the Sun. Image credit: National Solar observatory.	7
1.4	The spectrum of AB Dor A in the range of 3910-4000 Å around the Ca II H and K lines. Note the strong but very narrow emission in the cores of Ca II K (3933.7 Å) and Ca II H (3968.5 Å) lines.	7
1.5	The elusive solar corona observed with Large Angle and Spectrometric COronagraph (LASCO) C2, showing the complex magnetic structure associated with it. Image credit: SOHO/EIT and SOHO/LASCO (ESA & NASA).	8
1.6	Temperature and density profile of the solar atmosphere as a function of height above the visible photosphere. Image credit: Eugene Avrett.	8
1.7	Colour-magnitude diagram of X-ray detected bright source catalog stars from Huensch et al. (1998); Hünsch et al. (1999). Depicted as yellow star is our Sun.	9
1.8	A schematic diagram of the general scenario of flares assuming energy release as a result of magnetic reconnection.	11
1.9	Left: A high energetic solar flare illustrating the abrupt increase in the flux to the peak followed by a gradual decrease in the flux (Kopp et al. 2005). Right: An X-ray flare observed on a low mass star AB Dor A (Lalitha et al. 2013).	12
2.1	Predicted location of the habitable zone around stars of different spectral class calculated based on stellar luminosity. Image credit: ESO.	13
2.2	Logarithmic scatter plot of mass of planet versus the semi-major axis of known planets. Plotted in blue are exoplanet detections using transit method and in red are the detections using radial velocity method. The horizontal line indicate the mass of Earth in Jupiter masses.	14
4.1	Evolution of mass loss for the detected super-Earths as a function of time. Plotted as thick point is the current age of the super-Earth systems.	24
4.2	Schematic representation of Earth's magnetosphere. The shape of the magnetosphere is highly influenced by the solar activity. Image credit: Lalitha Sairam	25

4.3	Simulated stellar radial velocity curve for a 2 Earth mass planet orbiting a M dwarf host (in red). Plotted in black is the radial velocity curve with added jitter due to starspots. Image credit: Barnes et al. (2011)	26
4.4	The X-ray luminosity of detected sources (red) and upper limits (blue) estimates for non-detections of the pre-CARMENES target sample plotted as a function of distance. Plotted as orange thick line is the mean limiting sensitivity achieved with ROSAT and as brown dashed line is the predicted detection limit of eROSITA.	28
4.5	Plot of the X-ray luminosity vs absolute magnitude (M_v) for pre-CARMENES sample stars; red dots denote detections and blue dots represents upper limit estimates for non-detection.	28
4.6	The distribution of $\log(L_X/L_{bol})$ for the X-ray detections (red) and the upper limits for non-detections (beige). The black thick line at -4.0 divides our sample into active and moderately active stars.	29
4.7	To understand the relation between chromospheric and coronal activity, $\log(L_X/L_{bol})$ and the $H\alpha$ equivalent width are plotted. The red circles indicates the detections in X-rays and the blue upside-down triangles indicates the upper-limit sample.	30
6.1	Distribution of flare peak emission measure plotted as a function of flare peak temperature for PN (left panel) and RGS (right panel) data.	70
6.2	Evolution of Fe abundance for a subset of flares observed on AB Dor by XMM-PN. Plotted as thick black line is a simple exponential fit showing the expected evolution.	71
6.3	The distribution of loop lengths for the flares observed by PN only in black and the flares observed by the RGS in grey.	72
6.4	Plot of flare peak emission measure vs. flare peak temperature for the flares observed by <i>XMM-Newton</i> . Also depicted are the AB Dor A flares observed with pn (red square) and RGS (green squares). Plotted as beige circles are COUP flares compiled by Getman et al. (2008). Flares observed in other stars compiled by Güdel (2004) are depicted as blue triangles. The linear regression obtained by Aschwanden et al. (2008) is plotted as blue thick line with 1σ range (blue dashed line). AB Dor A flares, other stellar flares and solar flares fit a similar correlation $EM_f \propto T_f^{4.7}$. Plotted as yellow thick line is the linear regression, I obtained considering only stellar flares. The error bar indicate the 1σ range obtained from our analysis.	74
6.5	Plot of flare duration vs. flare peak temperature for the flares observed by <i>XMM-Newton</i> . Symbols and lines are as in Fig. 6.4. AB Dor A flares, other stellar flares and solar flares fit a similar correlation $\tau_f \propto T_f^{0.91}$	74
6.6	Plot of flare loop lengths vs. flare peak temperature for all the flares observed by <i>XMM-Newton</i> . Symbols and lines are as in Fig. 6.4.	75
6.7	Frequency distribution of XMM-pn flares (left panel) and XMM-RGS flares (right panel) in AB Dor A as a function of total irradiated X-ray energy during the flare lifetime over spectral band 0.2-10 keV and 0.3-2.7 keV respectively. The straight line (in brown) is power-law fit to the distribution.	76

Bibliography

- Acton, L., Tsuneta, S., Ogawara, Y., Bentley, R., Bruner, M., Canfield, R., Culhane, L., Doschek, G., Hiei, E. & Hirayama, T. (1992), ‘The YOHKOH mission for high-energy solar physics’, *Science* **258**, 618–625.
- Amado, P. J., Quirrenbach, A., Ribas, I., Caballero, J. A., Sánchez-Carrasco, M. A., Reiners, A., Seifert, W., Mundt, R., Mandel, H. & CARMENES Consortium, t. (2012), ‘CARMENES. I. A radial-velocity survey for terrestrial planets in the habitable zones of M dwarfs. A historical overview’, *ArXiv e-prints*.
- Arnaud, K. A. (1996), XSPEC: The First Ten Years, in G. H. Jacoby & J. Barnes, eds, ‘ASP Conf. Ser. 101: Astronomical Data Analysis Software and Systems V’, pp. 17–+.
- Aschwanden, M. J. & Nightingale, R. W. (2005), ‘Elementary Loop Structures in the Solar Corona Analyzed from TRACE Triple-Filter Images’, *ApJ* **633**, 499–517.
- Aschwanden, M. J., Stern, R. A. & Güdel, M. (2008), ‘Scaling Laws of Solar and Stellar Flares’, *ApJ* **672**, 659–673.
- Audard, M., Güdel, M. & Guinan, E. F. (1999), ‘Implications from Extreme-Ultraviolet Observations for Coronal Heating of Active Stars’, *ApJ* **513**, L53–L56.
- Auvergne, M., Bodin, P., Boissard, L., Buey, J.-T., Chaintreuil, S., Epstein, G., Jouret, M., Lam-Trong, T., Levacher, P., Magnan, A., Perez, R., Plasson, P., Plessier, J., Peter, G., Steller, M., Tiphène, D., Baglin, A., Agogué, P., Appourchaux, T., Barbet, D., Beaufort, T., Bellenger, R., Berlin, R., Bernardi, P., Blouin, D., Boumier, P., Bonneau, F., Briet, R., Butler, B., Cautain, R., Chiavassa, F., Costes, V., Cuvillo, J., Cunha-Parro, V., de Oliveira Fialho, F., Decaudin, M., Defise, J.-M., Djalal, S., Docclo, A., Drummond, R., Dupuis, O., Exil, G., Fauré, C., Gaboriaud, A., Gamet, P., Gavalda, P., Grolleau, E., Gueguen, L., Guivarc’h, V., Guterman, P., Hasiba, J., Huntzinger, G., Hustaix, H., Imbert, C., Jeanville, G., Johlander, B., Jorda, L., Journoud, P., Karioty, F., Kerjean, L., Lafond, L., Lapeyrere, V., Landiech, P., Larqué, T., Laudet, P., Le Merrer, J., Leporati, L., Leruyet, B., Levieuge, B., Llebaria, A., Martin, L., Mazy, E., Mesnager, J.-M., Michel, J.-P., Moalic, J.-P., Monjoin, W., Naudet, D., Neukirchner, S., Nguyen-Kim, K., Ollivier, M., Orcesi, J.-L., Ottacher, H., Oulali, A., Parisot, J., Perruchot, S., Piacentino, A., Pinheiro da Silva, L., Platzer, J., Pontet, B., Pradines, A., Quentin, C., Rohbeck, U., Rolland, G., Rollenhagen, F., Romagnan, R., Russ, N., Samadi, R., Schmidt, R., Schwartz, N., Sebbag, I., Smit, H., Sunter, W., Tello, M., Toulouse, P., Ulmer, B., Vandermarcq, O., Vergnault, E., Wallner, R., Waultier, G. & Zanatta, P. (2009), ‘The CoRoT satellite in flight: description and performance’, *A&A* **506**, 411–424.
- Babcock, H. W. (1961), ‘The Topology of the Sun’s Magnetic Field and the 22-YEAR Cycle.’, *ApJ* **133**, 572.
- Baliunas, S. L. & Vaughan, A. H. (1985), ‘Stellar activity cycles’, *ARA&A* **23**, 379–412.
- Baliunas, S. L., Donahue, R. A., Soon, W. H., Horne, J. H., Frazer, J., Woodard-Eklund, L., Bradford, M., Rao, L. M., Wilson, O. C.,

- Zhang, Q., Bennett, W., Briggs, J., Carroll, S. M., Duncan, D. K., Figueroa, D., Lanning, H. H., Misch, T., Mueller, J., Noyes, R. W., Poppe, D., Porter, A. C., Robinson, C. R., Russell, J., Shelton, J. C., Soyumer, T., Vaughan, A. H. & Whitney, J. H. (1995), ‘Chromospheric variations in main-sequence stars’, *ApJ* **438**, 269–287.
- Barnes, J. R., Jeffers, S. V. & Jones, H. R. A. (2011), ‘The effect of M dwarf starspot activity on low-mass planet detection thresholds’, *MNRAS* **412**, 1599–1610.
- Bauer, S. J. & Lammer, H. (2004), *Planetary aeronomy : atmosphere environments in planetary systems*.
- Benz, A. O. (2008), ‘Flare Observations’, *Living Reviews in Solar Physics* **5**, 1.
- Berghoefer, T. W., Schmitt, J. H. M. M., Danner, R. & Cassinelli, J. P. (1997), ‘X-ray properties of bright OB-type stars detected in the ROSAT all-sky survey.’, *A&A* **322**, 167–174.
- Boella, G., Butler, R. C., Perola, G. C., Piro, L., Scarsi, L. & Bleeker, J. A. M. (1997), ‘BeppoSAX, the wide band mission for X-ray astronomy’, *A&AS* **122**, 299–307.
- Bonfils, X., Delfosse, X., Udry, S., Forveille, T., Mayor, M., Perrier, C., Bouchy, F., Gillon, M., Lovis, C., Pepe, F., Queloz, D., Santos, N. C., Ségransan, D. & Bertaux, J.-L. (2013), ‘The HARPS search for southern extra-solar planets. XXXI. The M-dwarf sample’, *A&A* **549**, A109.
- Borucki, W. J., Koch, D. G., Batalha, N., Bryson, S. T., Rowe, J., Fressin, F., Torres, G., Caldwell, D. A., Christensen-Dalsgaard, J., Cochran, W. D., DeVore, E., Gautier, T. N., Geary, J. C., Gilliland, R., Gould, A., Howell, S. B., Jenkins, J. M., Latham, D. W., Lissauer, J. J., Marcy, G. W., Sasselov, D., Boss, A., Charbonneau, D., Ciardi, D., Kaltenegger, L., Doyle, L., Dupree, A. K., Ford, E. B., Fortney, J., Holman, M. J., Steffen, J. H., Mullally, F., Still, M., Tarter, J., Ballard, S., Buchhave, L. A., Carter, J., Christiansen, J. L., Demory, B.-O., Désert, J.-M., Dressing, C., Endl, M., Fabrycky, D., Fischer, D., Haas, M. R., Henze, C., Horch, E., Howard, A. W., Isaacson, H., Kjeldsen, H., Johnson, J. A., Klaus, T., Kolodziejczak, J., Barclay, T., Li, J., Meibom, S., Prsa, A., Quinn, S. N., Quintana, E. V., Robertson, P., Sherry, W., Shporer, A., Tenenbaum, P., Thompson, S. E., Twicken, J. D., Van Cleve, J., Welsh, W. F., Basu, S., Chaplin, W., Miglio, A., Kawaler, S. D., Arentoft, T., Stello, D., Metcalfe, T. S., Verner, G. A., Karoff, C., Lundkvist, M., Lund, M. N., Handberg, R., Elsworth, Y., Hekker, S., Huber, D., Bedding, T. R. & Rapin, W. (2012), ‘Kepler-22b: A 2.4 Earth-radius Planet in the Habitable Zone of a Sun-like Star’, *ApJ* **745**, 120.
- Bray, R. J. & Loughhead, R. E. (1964), *Sunspots*.
- Cassinelli, J. P., Cohen, D. H., Macfarlane, J. J., Sanders, W. T. & Welsh, B. Y. (1994), ‘X-ray emission from near-main-sequence B stars’, *ApJ* **421**, 705–717.
- Charbonneau, D., Berta, Z. K., Irwin, J., Burke, C. J., Nutzman, P., Buchhave, L. A., Lovis, C., Bonfils, X., Latham, D. W., Udry, S., Murray-Clay, R. A., Holman, M. J., Falco, E. E., Winn, J. N., Queloz, D., Pepe, F., Mayor, M., Delfosse, X. & Forveille, T. (2009), ‘A super-Earth transiting a nearby low-mass star’, *Nature* **462**, 891–894.
- Collura, A., Pasquini, L. & Schmitt, J. H. M. M. (1988), ‘Time variability in the X-ray emission of dM stars observed by EXOSAT’, *A&A* **205**, 197–206.
- Courtillot, V. (2002), *Evolutionary Catastrophes*.
- Crosby, N. B., Aschwanden, M. J. & Dennis, B. R. (1993), ‘Frequency distributions and correlations of solar X-ray flare parameters’, *Sol. Phys.* **143**, 275–299.
- Desort, M., Lagrange, A.-M., Galland, F., Udry, S. & Mayor, M. (2007), ‘Search for exoplanets with the radial-velocity technique:

- quantitative diagnostics of stellar activity’, *A&A* **473**, 983–993.
- Domingo, V., Fleck, B. & Poland, A. I. (1995), ‘The SOHO Mission: an Overview’, *Sol. Phys.* **162**, 1–37.
- Dunstone, N. J., Collier Cameron, A., Barnes, J. R. & Jardine, M. (2006), ‘The coronal structure of Speedy Mic - II. Prominence masses and off-disc emission’, *MNRAS* **373**, 1308–1320.
- Feldman, U., Doschek, G. A., Mariska, J. T. & Brown, C. M. (1995), ‘Relationships between Temperature and Emission Measure in Solar Flares Determined from Highly Ionized Iron Spectra and from Broadband X-Ray Detectors’, *ApJ* **450**, 441.
- Fletcher, L., Dennis, B. R., Hudson, H. S., Krucker, S., Phillips, K., Veronig, A., Battaglia, M., Bone, L., Caspi, A., Chen, Q., Gallagher, P., Grigis, P. T., Ji, H., Liu, W., Milligan, R. O. & Temmer, M. (2011), ‘An Observational Overview of Solar Flares’, *Space Sci. Rev.* **159**, 19–106.
- Fressin, F., Torres, G., Rowe, J. F., Charbonneau, D., Rogers, L. A., Ballard, S., Batalha, N. M., Borucki, W. J., Bryson, S. T., Buchhave, L. A., Ciardi, D. R., Désert, J.-M., Dressing, C. D., Fabrycky, D. C., Ford, E. B., Gautier, III, T. N., Henze, C. E., Holman, M. J., Howard, A., Howell, S. B., Jenkins, J. M., Koch, D. G., Latham, D. W., Lissauer, J. J., Marcy, G. W., Quinn, S. N., Ragozzine, D., Sasselov, D. D., Seager, S., Barclay, T., Mullally, F., Seader, S. E., Still, M., Twicken, J. D., Thompson, S. E. & Uddin, K. (2012), ‘Two Earth-sized planets orbiting Kepler-20’, *Nature* **482**, 195–198.
- Fuhrmeister, B., Lalitha, S., Poppenhaeger, K., Rudolf, N., Liefke, C., Reiners, A., Schmitt, J. H. M. M. & Ness, J.-U. (2011), ‘Multi-wavelength observations of Proxima Centauri’, *A&A* **534**, A133.
- Futó, P. (2013), ‘Kepler 36B: A Transiting Super-Earth with an Earth-like Interior Structure’, *LPI Contributions* **1719**, 1552.
- Garrett, D. L. & Tousey, R. (1977), ‘Solar XUV grazing incidence spectrograph on SKYLAB’, *Appl. Opt.* **16**, 898–903.
- Gershberg, R. E. (1989), ‘Time scales and energy of flares on red dwarf stars - A review’, *Mem. Soc. Astron. Italiana* **60**, 263–287.
- Getman, K. V., Feigelson, E. D., Broos, P. S., Micela, G. & Garmire, G. P. (2008), ‘X-Ray Flares in Orion Young Stars. I. Flare Characteristics’, *ApJ* **688**, 418–436.
- Gomes da Silva, J., Santos, N. C., Bonfils, X., Delfosse, X., Forveille, T. & Udry, S. (2011), ‘Long-term magnetic activity of a sample of M-dwarf stars from the HARPS program. I. Comparison of activity indices’, *A&A* **534**, A30.
- Gray, D. F. (2005), *The Observation and Analysis of Stellar Photospheres*.
- Grevesse, N. & Sauval, A. J. (1998), ‘Standard Solar Composition’, *Space Sci. Rev.* **85**, 161–174.
- Güdel, M. (2004), ‘X-ray astronomy of stellar coronae’, *A&A Rev.* **12**, 71–237.
- Güdel, M., Audard, M., Reale, F., Skinner, S. L. & Linsky, J. L. (2004), ‘Flares from small to large: X-ray spectroscopy of Proxima Centauri with XMM-Newton’, *A&A* **416**, 713–732.
- Guirado, J. C., Marcaide, J. M., Martí-Vidal, I., Le Bouquin, J.-B., Close, L. M., Cotton, W. D. & Montalbán, J. (2011), ‘The size of AB Doradus A from VLTI/AMBER interferometry’, *A&A* **533**, A106.
- Haisch, B. M., Linsky, J. L., Slee, O. B., Hearn, D. R., Walker, A. R., Rydgren, A. E. & Nicolson, G. D. (1978), ‘A coordinated X-ray, optical, and microwave study of the flare star Proxima Centauri’, *ApJ* **225**, L35–L37.
- Hall, J. C. (2008), ‘Stellar Chromospheric Activity’, *Living Reviews in Solar Physics* **5**, 2.
- Haswell, C. A. (2010), *Transiting Exoplanets*.

- Hatzes, A. P., Fridlund, M., Nachmani, G., Mazeh, T., Valencia, D., Hébrard, G., Carone, L., Pätzold, M., Udry, S., Bouchy, F., Deleuil, M., Moutou, C., Barge, P., Bordé, P., Deeg, H., Tingley, B., Dvorak, R., Gandolfi, D., Ferraz-Mello, S., Wuchterl, G., Guenther, E., Guillot, T., Rauer, H., Erikson, A., Cabrera, J., Csizmadia, S., Léger, A., Lammer, H., Weingrill, J., Queloz, D., Alonso, R., Rouan, D. & Schneider, J. (2011), ‘The Mass of CoRoT-7b’, *ApJ* **743**, 75.
- Hawley, S. L., Gizis, J. E. & Reid, I. N. (1996), ‘The Palomar/MSU Nearby Star Spectroscopic Survey.II.The Southern M Dwarfs and Investigation of Magnetic Activity’, *AJ* **112**, 2799.
- Henry, T. J., Subasavage, J. P., Brown, M. A., Beaulieu, T. D., Jao, W.-C. & Hambly, N. C. (2004), ‘The Solar Neighborhood. X. New Nearby Stars in the Southern Sky and Accurate Photometric Distance Estimates for Red Dwarfs’, *AJ* **128**, 2460–2473.
- Hirayama, T. (1985), ‘Modern observations of solar prominences’, *Sol. Phys.* **100**, 415–434.
- Huang, S.-S. (1959), ‘Occurrence of life in the universe’, *American Scientist* **47**(3), pp. 397–402.
- Hudson, H. S. (1991), ‘Solar flares, microflares, nanoflares, and coronal heating’, *Sol. Phys.* **133**, 357–369.
- Huensch, M., Schmitt, J. H. M. M. & Voges, W. (1998), ‘The ROSAT all-sky survey catalogue of optically bright main-sequence stars and subgiant stars’, *A&AS* **132**, 155–171.
- Hünsch, M., Schmitt, J. H. M. M., Sterzik, M. F. & Voges, W. (1999), ‘The ROSAT all-sky survey catalogue of the nearby stars’, *A&AS* **135**, 319–338.
- Jansen, F., Lumb, D., Altieri, B., Clavel, J., Ehle, M., Erd, C., Gabriel, C., Guainazzi, M., Gondoin, P., Much, R., Munoz, R., Santos, M., Schartel, N., Texier, D. & Vacanti, G. (2001), ‘XMM-Newton observatory. I. The spacecraft and operations’, *A&A* **365**, L1–L6.
- Järvinen, S. P., Berdyugina, S. V., Tuominen, I., Cutispoto, G. & Bos, M. (2005), ‘Magnetic activity in the young solar analog AB Dor. Active longitudes and cycles from long-term photometry.’, *A&A* **432**, 657–664.
- Joy, A. H. & Humason, M. L. (1949), ‘Observations of the Faint Dwarf Star L 726-8’, *PASP* **61**, 133–134.
- Kaltenegger, L. & Sasselov, D. (2011), ‘Exploring the Habitable Zone for Kepler Planetary Candidates’, *ApJ* **736**, L25.
- Kasting, J. F., Whitmire, D. P. & Reynolds, R. T. (1993), ‘Habitable Zones around Main Sequence Stars’, **101**, 108–128.
- Kelch, W. L. & Linsky, J. L. (1978), ‘Physical properties of solar chromospheric plages. III - Models based on CA II and MG II observations’, *Sol. Phys.* **58**, 37–45.
- Kopp, G., Lawrence, G. & Rottman, G. (2005), ‘The Total Irradiance Monitor (TIM): Science Results’, *Sol. Phys.* **230**, 129–139.
- Kopp, R. A. & Pneuman, G. W. (1976), ‘Magnetic reconnection in the corona and the loop prominence phenomenon’, *Sol. Phys.* **50**, 85–98.
- Korhonen, H., Wittkowski, M., Kovári, Z., Granzer, T., Hackman, T. & Strassmeier, K. G. (2010), ‘Ellipsoidal primary of the RS CVn binary ζ Andromedae. Investigation using high-resolution spectroscopy and optical interferometry’, *A&A* **515**, A14.
- Kowalski, A. F., Hawley, S. L., Hilton, E. J., Becker, A. C., West, A. A., Bochanski, J. J. & Sesar, B. (2009), ‘M Dwarfs in Sloan Digital Sky Survey Stripe 82: Photometric Light Curves and Flare Rate Analysis’, *AJ* **138**, 633–648.
- Krucker, S. & Benz, A. O. (1998), ‘Energy Distribution of Heating Processes in the Quiet Solar Corona’, *ApJ* **501**, L213.

- Kuerster, M., Schmitt, J. H. M. M. & Cutispoto, G. (1994), ‘Doppler imaging with a CLEAN – like approach. 2: A photospheric image of AB Doradus (=HD 36705)’, *A&A* **289**, 899–921.
- Kürster, M., Endl, M., Rouesnel, F., Els, S., Kaufer, A., Brilliant, S., Hatzes, A. P., Saar, S. H. & Cochran, W. D. (2003), ‘The low-level radial velocity variability in Barnard’s star (= GJ 699). Secular acceleration, indications for convective redshift, and planet mass limits’, *A&A* **403**, 1077–1087.
- Lalitha, S., Fuhrmeister, B., Wolter, U., Schmitt, J. H. M. M., Engels, D. & Wieringa, M. (2013), ‘A multiwavelength view of AB Dor’s outer atmosphere - simultaneous X-ray and optical spectroscopy at high cadence’, *A&A* p. submitted.
- Lammer, H., Selsis, F., Ribas, I., Guinan, E. F., Bauer, S. J. & Weiss, W. W. (2003), ‘Atmospheric Loss of Exoplanets Resulting from Stellar X-Ray and Extreme-Ultraviolet Heating’, *ApJ* **598**, L121–L124.
- Lecavelier des Etangs, A., Vidal-Madjar, A., McConnell, J. C. & Hébrard, G. (2004), ‘Atmospheric escape from hot Jupiters’, *A&A* **418**, L1–L4.
- Léger, A., Rouan, D., Schneider, J., Barge, P., Fridlund, M., Samuel, B., Ollivier, M., Guenther, E., Deleuil, M., Deeg, H. J., Auvergne, M., Alonso, R., Aigrain, S., Alapini, A., Almenara, J. M., Baglin, A., Barbieri, M., Bruntt, H., Bordé, P., Bouchy, F., Cabrera, J., Catala, C., Carone, L., Carpano, S., Csizmadia, S., Dvorak, R., Erikson, A., Ferraz-Mello, S., Foing, B., Fressin, F., Gandolfi, D., Gillon, M., Gondoin, P., Grasset, O., Guillot, T., Hatzes, A., Hébrard, G., Jorda, L., Lammer, H., Llebaria, A., Loeillet, B., Mayor, M., Mazeh, T., Moutou, C., Pätzold, M., Pont, F., Queloz, D., Rauer, H., Renner, S., Samadi, R., Shporer, A., Sotin, C., Tingley, B., Wuchterl, G., Adda, M., Agogu, P., Appourchaux, T., Ballans, H., Baron, P., Beaufort, T., Bellenger, R., Berlin, R., Bernardi, P., Blouin, D., Baudin, F., Bodin, P., Boissard, L., Boit, L., Bonneau, F., Borzeix, S., Briet, R., Buey, J.-T., Butler, B., Cailleau, D., Cautain, R., Chabaud, P.-Y., Chaintreuil, S., Chiavassa, F., Costes, V., Cuna Parrho, V., de Oliveira Fialho, F., Decaudin, M., Defise, J.-M., Djalal, S., Epstein, G., Exil, G.-E., Fauré, C., Fenouillet, T., Gaboriaud, A., Gallic, A., Gamet, P., Gavalda, P., Grolleau, E., Gruneisen, R., Gueguen, L., Guis, V., Guivarc’h, V., Guterman, P., Hallouard, D., Hasiba, J., Heuripeau, F., Huntzinger, G., Hustaix, H., Imad, C., Imbert, C., Johlander, B., Jouret, M., Journoud, P., Karioty, F., Kerjean, L., Lafaille, V., Lafond, L., Lam-Trong, T., Landiech, P., Lapeyrere, V., Larqué, T., Laudet, P., Lautier, N., Lecann, H., Lefevre, L., Leruyet, B., Levacher, P., Magnan, A., Mazy, E., Mertens, F., Mesnager, J.-M., Meunier, J.-C., Michel, J.-P., Monjoin, W., Naudet, D., Nguyen-Kim, K., Orcesi, J.-L., Ottacher, H., Perez, R., Peter, G., Plasson, P., Plessieria, J.-Y., Pontet, B., Pradines, A., Quentin, C., Reynaud, J.-L., Rolland, G., Rollenhagen, F., Romagnan, R., Russ, N., Schmidt, R., Schwartz, N., Sebbag, I., Sedes, G., Smit, H., Steller, M. B., Sunter, W., Surace, C., Tello, M., Tiphène, D., Toulouse, P., Ulmer, B., Vandermarcq, O., Vergnault, E., Vuillemin, A. & Zanatta, P. (2009), ‘Transiting exoplanets from the CoRoT space mission. VIII. CoRoT-7b: the first super-Earth with measured radius’, *A&A* **506**, 287–302.
- Leighton, R. B. (1969), ‘A Magneto-Kinematic Model of the Solar Cycle’, *ApJ* **156**, 1.
- Levine, A. M., Bradt, H., Cui, W., Jernigan, J. G., Morgan, E. H., Remillard, R., Shirey, R. E. & Smith, D. A. (1996), ‘First Results from the All-Sky Monitor on the Rossi X-Ray Timing Explorer’, *ApJ* **469**, L33.
- Lin, R. P., Dennis, B. R., Hurford, G. J., Smith, D. M., Zehnder, A., Harvey, P. R., Curtis, D. W., Pankow, D., Turin, P., Bester, M., Csillaghy, A., Lewis, M., Madden, N., van Beek, H. F., Appleby, M., Raudorf, T., McTiernan, J., Ramaty, R., Schmahl,

- E., Schwartz, R., Krucker, S., Abiad, R., Quinn, T., Berg, P., Hashii, M., Sterling, R., Jackson, R., Pratt, R., Campbell, R. D., Malone, D., Landis, D., Barrington-Leigh, C. P., Slassi-Sennou, S., Cork, C., Clark, D., Amato, D., Orwig, L., Boyle, R., Banks, I. S., Shirey, K., Tolbert, A. K., Zarro, D., Snow, F., Thomsen, K., Henneck, R., McHedlishvili, A., Ming, P., Fivian, M., Jordan, J., Wanner, R., Crubb, J., Preble, J., Matrangola, M., Benz, A., Hudson, H., Canfield, R. C., Holman, G. D., Crannell, C., Kosugi, T., Emslie, A. G., Vilmer, N., Brown, J. C., Johns-Krull, C., Aschwanden, M., Metcalf, T. & Conway, A. (2002), ‘The Reuven Ramaty High-Energy Solar Spectroscopic Imager (RHESSI)’, *Sol. Phys.* **210**, 3–32.
- Lin, R. P., Schwartz, R. A., Kane, S. R., Pelling, R. M. & Hurley, K. C. (1984), ‘Solar hard X-ray microflares’, *ApJ* **283**, 421–425.
- Livingston, W., Wallace, L., White, O. R. & Giampapa, M. S. (2007), ‘Sun-as-a-Star Spectrum Variations 1974-2006’, *ApJ* **657**, 1137–1149.
- Lockwood, G. W., Radick, R. R., Henry, G. W. & Baliunas, S. L. (2004), A Comparison of Solar Irradiance Variations with those of Similar Stars, in ‘American Astronomical Society Meeting Abstracts #204’, Vol. 36 of *Bulletin of the American Astronomical Society*, p. 671.
- Lockwood, G. W., Skiff, B. A., Henry, G. W., Henry, S., Radick, R. R., Baliunas, S. L., Donahue, R. A. & Soon, W. (2007), ‘Patterns of Photometric and Chromospheric Variation among Sun-like Stars: A 20 Year Perspective’, *ApJS* **171**, 260–303.
- Martinez Pillet, V. (1997), Polarimetric Measurements of Sunspots, in B. Schmieder, J. C. del Toro Iniesta & M. Vazquez, eds, ‘1st Advances in Solar Physics Euroconference. Advances in Physics of Sunspots’, Vol. 118 of *Astronomical Society of the Pacific Conference Series*, p. 212.
- Mayor, M. & Queloz, D. (1995), ‘A Jupiter-mass companion to a solar-type star’, *Nature* **378**, 355–359.
- Mayor, M., Bonfils, X., Forveille, T., Delfosse, X., Udry, S., Bertaux, J.-L., Beust, H., Bouchy, F., Lovis, C., Pepe, F., Perrier, C., Queloz, D. & Santos, N. C. (2009a), ‘The HARPS search for southern extra-solar planets. XVIII. An Earth-mass planet in the GJ 581 planetary system’, *A&A* **507**, 487–494.
- Mayor, M., Marmier, M., Lovis, C., Udry, S., Ségransan, D., Pepe, F., Benz, W., Bertaux, J. ., Bouchy, F., Dumusque, X., Lo Curto, G., Mordasini, C., Queloz, D. & Santos, N. C. (2011), ‘The HARPS search for southern extra-solar planets XXXIV. Occurrence, mass distribution and orbital properties of super-Earths and Neptune-mass planets’, *ArXiv e-prints*.
- Mayor, M., Pepe, F., Queloz, D., Bouchy, F., Rupprecht, G., Lo Curto, G., Avila, G., Benz, W., Bertaux, J.-L., Bonfils, X., Dall, T., Dekker, H., Delabre, B., Eckert, W., Fleury, M., Gilliotte, A., Gojak, D., Guzman, J. C., Kohler, D., Lizon, J.-L., Longinotti, A., Lovis, C., Megevand, D., Pasquini, L., Reyes, J., Sivan, J.-P., Sosnowska, D., Soto, R., Udry, S., van Kesteren, A., Weber, L. & Weilenmann, U. (2003), ‘Setting New Standards with HARPS’, *The Messenger* **114**, 20–24.
- Mayor, M., Udry, S., Lovis, C., Pepe, F., Queloz, D., Benz, W., Bertaux, J.-L., Bouchy, F., Mordasini, C. & Ségransan, D. (2009b), ‘The HARPS search for southern extra-solar planets. XIII. A planetary system with 3 super-Earths (4.2, 6.9, and 9.2 M)’, *A&A* **493**, 639–644.
- Messina, S. & Guinan, E. F. (2002), ‘Magnetic activity of six young solar analogues I. Starspot cycles from long-term photometry’, *A&A* **393**, 225–237.
- Nordon, R. & Behar, E. (2008), ‘Abundance variations and first ionization potential trends during large stellar flares’, *A&A* **482**, 639–651.

- Nutzman, P. & Charbonneau, D. (2008), ‘Design Considerations for a Ground-Based Transit Search for Habitable Planets Orbiting M Dwarfs’, *PASP* **120**, 317–327.
- Pallavicini, R., Golub, L., Rosner, R., Vaiana, G. S., Ayres, T. & Linsky, J. L. (1981), ‘Relations among stellar X-ray emission observed from Einstein, stellar rotation and bolometric luminosity’, *ApJ* **248**, 279–290.
- Parker, E. N. (1955), ‘Hydromagnetic Dynamo Models.’, *ApJ* **122**, 293.
- Parker, E. N. (1988), ‘Nanoflares and the solar X-ray corona’, *ApJ* **330**, 474–479.
- Parnell, C. E. & Jupp, P. E. (2000), ‘Statistical Analysis of the Energy Distribution of Nanoflares in the Quiet Sun’, *ApJ* **529**, 554–569.
- Parsons, S. G., Marsh, T. R., Gänsicke, B. T. & Tappert, C. (2011), ‘A stellar prominence in the white dwarf/red dwarf binary QS Vir: evidence for a detached system’, *MNRAS* **412**, 2563–2570.
- Patsourakos, S. & Klimchuk, J. A. (2005), ‘Coronal Loop Heating by Nanoflares: The Impact of the Field-aligned Distribution of the Heating on Loop Observations’, *ApJ* **628**, 1023–1030.
- Phillips, M. J. & Hartmann, L. (1978), ‘Long-term variability of dMe stars’, *ApJ* **224**, 182–184.
- Quirrenbach, A., Amado, P. J., Seifert, W., Sánchez Carrasco, M. A., Mandel, H., Caballero, J. A., Mundt, R., Ribas, I., Reiners, A., Abril, M., Aceituno, J., Alonso-Floriano, J., Ammler-von Eiff, M., Anglada-Escude, G., Antona Jiménez, R., Anwand-Heerwart, H., Barrado y Navascués, D., Becerril, S., Bejar, V., Benitez, D., Cardenas, C., Claret, A., Colome, J., Cortés-Contreras, M., Czesla, S., del Burgo, C., Doellinger, M., Dorda, R., Dreizler, S., Feiz, C., Fernandez, M., Galadi, D., Garrido, R., González Hernández, J., Guardia, J., Guenther, E., de Guindos, E., Gutiérrez-Soto, J., Hagen, H. J., Hatzes, A., Hauschildt, P., Helmling, J., Henning, T., Herrero, E., Huber, A., Huber, K., Jeffers, S., Joergens, V., de Juan, E., Kehr, M., Klutsch, A., Kürster, M., Lalitha, S., Laun, W., Lemke, U., Lenzen, R., Lizon, J.-L., López del Fresno, M., López-Morales, M., López-Santiago, J., Mall, U., Martin, E., Martín-Ruiz, S., Mirabet, E., Montes, D., Morales, J. C., Morales Muñoz, R., Moya, A., Naranjo, V., Oreiro, R., Pérez Medialdea, D., Pluto, M., Rabaza, O., Ramon, A., Rebolo, R., Reffert, S., Rhode, P., Rix, H.-W., Rodler, F., Rodríguez, E., Rodríguez López, C., Rodríguez Pérez, E., Rodríguez Trinidad, A., Rohloff, R.-R., Sánchez-Blanco, E., Sanz-Forcada, J., Schäfer, S., Schiller, J., Schmidt, C., Schmitt, J., Solano, E., Stahl, O., Storz, C., Stürmer, J., Suarez, J. C., Thiele, U., Ulbrich, R., Vidal-Dasilva, M., Wagner, K., Winkler, J., Xu, W., Zapatero Osorio, M. R. & Zechmeister, M. (2012), CARMENES. I: instrument and survey overview, in ‘Society of Photo-Optical Instrumentation Engineers (SPIE) Conference Series’, Vol. 8446 of *Society of Photo-Optical Instrumentation Engineers (SPIE) Conference Series*.
- Reale, F. (2010), ‘Coronal Loops: Observations and Modeling of Confined Plasma’, *Living Reviews in Solar Physics*.
- Reale, F., Betta, R., Peres, G., Serio, S. & McTiernan, J. (1997), ‘Determination of the length of coronal loops from the decay of X-ray flares I. Solar flares observed with YOHKOH SXT.’, *A&A* **325**, 782–790.
- Reid, I. N., Hawley, S. L. & Gizis, J. E. (1995), ‘The Palomar/MSU Nearby-Star Spectroscopic Survey. I. The Northern M Dwarfs -Bandstrengths and Kinematics’, *AJ* **110**, 1838.
- Reiners, A. (2007), ‘Ultra-cool and extra-vigorous: Rotation and activity in M and L dwarfs’, *Astronomische Nachrichten* **328**, 1040.
- Reiners, A. (2009), ‘Activity-induced radial velocity jitter in a flaring M dwarf’, *A&A* **498**, 853–861.

- Reiners, A. & Basri, G. (2008), ‘Chromospheric Activity, Rotation, and Rotational Braking in M and L Dwarfs’, *ApJ* **684**, 1390–1403.
- Reiners, A. & Basri, G. (2010), ‘A Volume-Limited Sample of 63 M7-M9.5 Dwarfs. II. Activity, Magnetism, and the Fade of the Rotation-Dominated Dynamo’, *ApJ* **710**, 924–935.
- Ribas, I., Guinan, E. F., Güdel, M. & Audard, M. (2005), ‘Evolution of the Solar Activity over Time and Effects on Planetary Atmospheres. I. High-Energy Irradiances (1–1700 Å)’, *ApJ* **622**, 680–694.
- Robrade, J. & Schmitt, J. H. M. M. (2005), ‘X-ray properties of active M dwarfs as observed by XMM-Newton’, *A&A* **435**, 1073–1085.
- Rosner, R., Golub, L. & Vaiana, G. S. (1985), ‘On stellar X-ray emission’, *ARA&A* **23**, 413–452.
- Rosner, R., Tucker, W. H. & Vaiana, G. S. (1978), ‘Dynamics of the quiescent solar corona’, *ApJ* **220**, 643–645.
- Sanz-Forcada, J., Micela, G., Ribas, I., Pollock, A. M. T., Eiroa, C., Velasco, A., Solano, E. & García-Álvarez, D. (2011), ‘Estimation of the XUV radiation onto close planets and their evaporation’, *A&A* **532**, A6.
- Sanz-Forcada, J., Ribas, I., Micela, G., Pollock, A. M. T., García-Álvarez, D., Solano, E. & Eiroa, C. (2010), ‘A scenario of planet erosion by coronal radiation’, *A&A* **511**, L8.
- Schäfer, S. & Reiners, A. (2012), Two Fabry-Perot interferometers for high precision wavelength calibration in the near-infrared, *in* ‘Society of Photo-Optical Instrumentation Engineers (SPIE) Conference Series’, Vol. 8446 of *Society of Photo-Optical Instrumentation Engineers (SPIE) Conference Series*.
- Schmitt, J. H. M. M. (1997), ‘Coronae on solar-like stars.’, *A&A* **318**, 215–230.
- Schmitt, J. H. M. M. & Liefke, C. (2004), ‘NEXXUS: A comprehensive ROSAT survey of coronal X-ray emission among nearby solar-like stars’, *A&A* **417**, 651–665.
- Schmitt, J. H. M. M., Fleming, T. A. & Giampapa, M. S. (1995), ‘The X-Ray View of the Low-Mass Stars in the Solar Neighborhood’, *ApJ* **450**, 392.
- Schneider, J., Dedieu, C., Le Sidaner, P., Savalle, R. & Zolotukhin, I. (2011), ‘Defining and cataloging exoplanets: the exoplanet.eu database’, *A&A* **532**, A79.
- Schrijver, C. J. & Siscoe, G. L. (2009), *Heliophysics: Plasma Physics of the Local Cosmos*, Cambridge University Press.
- Schrijver, C. J. & Zwaan, C. (2000), *Solar and Stellar Magnetic Activity*.
- Schrijver, C. J., Title, A. M., Berger, T. E., Fletcher, L., Hurlburt, N. E., Nightingale, R. W., Shine, R. A., Tarbell, T. D., Wolfson, J., Golub, L., Bookbinder, J. A., Deluca, E. E., McMullen, R. A., Warren, H. P., Kankelborg, C. C., Handy, B. N. & de Pontieu, B. (1999), ‘A new view of the solar outer atmosphere by the Transition Region and Coronal Explorer’, *Sol. Phys.* **187**, 261–302.
- Schröter, S., Czesla, S., Wolter, U., Müller, H. M., Huber, K. F. & Schmitt, J. H. M. M. (2011), ‘The corona and companion of CoRoT-2a. Insights from X-rays and optical spectroscopy’, *A&A* **532**, A3.
- Schwabe, M. (1844), ‘Sonnenbeobachtungen im Jahre 1843. Von Herrn Hofrath Schwabe in Dessau’, *Astronomische Nachrichten* **21**, 233.
- Sciortino, S., Harnden, Jr., F. R., Maggio, A., Micela, G., Vaiana, G. S., Schmitt, J. & Rosner, R. (1988), The Einstein Observatory Stellar X-ray Database: an overview., *in* F. Murtagh, A. Heck & P. Benvenuti, eds, ‘European Southern Observatory Conference and Workshop Proceedings’, Vol. 28 of *European Southern Observatory Conference and Workshop Proceedings*, pp. 483–487.

- Selsis, F., Kasting, J. F., Levrard, B., Paillet, J., Ribas, I. & Delfosse, X. (2007), ‘Habitable planets around the star Gliese 581?’, *A&A* **476**, 1373–1387.
- Shibata, K. & Yokoyama, T. (1999), ‘Origin of the Universal Correlation between the Flare Temperature and the Emission Measure for Solar and Stellar Flares’, *ApJ* **526**, L49–L52.
- Shimizu, T. (1995), ‘Energetics and Occurrence Rate of Active-Region Transient Brightenings and Implications for the Heating of the Active-Region Corona’, *PASJ* **47**, 251–263.
- Singh, J., Banerjee, D., Venkatakrisnan, P., Kasiviswanathan, S. & Prasad B, R. (2012), Indian Solar mission to study inner solar corona: Aditya 1, in ‘39th COSPAR Scientific Assembly’, Vol. 39 of *COSPAR Meeting*, p. 1824.
- Skumanich, A., Smythe, C. & Frazier, E. N. (1975), ‘On the statistical description of inhomogeneities in the quiet solar atmosphere. I - Linear regression analysis and absolute calibration of multichannel observations of the Ca+/+ emission network’, *ApJ* **200**, 747–764.
- Solanki, S. K. (1997), Empirical Modelling and Thermal Structure of Sunspots, in B. Schmieder, J. C. del Toro Iniesta & M. Vazquez, eds, ‘1st Advances in Solar Physics Euroconference. Advances in Physics of Sunspots’, Vol. 118 of *Astronomical Society of the Pacific Conference Series*, p. 178.
- Solanki, S. K. (2002), ‘The magnetic structure of sunspots and starspots’, *Astronomische Nachrichten* **323**, 165–177.
- Solanki, S. K. (2003), ‘Sunspots: An overview’, *A&A Rev.* **11**, 153–286.
- Solanki, S. K., Livingston, W. & Ayres, T. (1994), ‘New Light on the Heart of Darkness of the Solar Chromosphere’, *Science* **263**, 64–66.
- Stern, R. A., Uchida, Y., Tsuneta, S. & Nagase, F. (1992), ‘GINGA observations of X-ray flares on Algol’, *ApJ* **400**, 321–329.
- Strassmeier, K. G. (2009), ‘Starspots’, *A&A Rev.* **17**, 251–308.
- Tandberg-Hanssen, E. & Emslie, A. G. (1988), *The physics of solar flares*.
- Truemper, J. (1992), ‘ROSAT - A new look at the X-ray sky (The 1991 Grubb-Parsons Lecture)’, *QJRAS* **33**, 165–174.
- Udry, S., Bonfils, X., Delfosse, X., Forveille, T., Mayor, M., Perrier, C., Bouchy, F., Lovis, C., Pepe, F., Queloz, D. & Bertaux, J.-L. (2007a), ‘The HARPS search for southern extra-solar planets. XI. Super-Earths (5 and 8 M \oplus)*ina3* - *planetsystem*’, *A&A* **469**, L43 – –L47.
- Udry, S., Bonfils, X., Delfosse, X., Forveille, T., Mayor, M., Perrier, C., Bouchy, F., Lovis, C., Pepe, F., Queloz, D. & Bertaux, J.-L. (2007b), ‘The HARPS search for southern extra-solar planets. XI. Super-Earths (5 and 8 M \oplus)*ina3* - *planetsystem*’, *A&A* **469**, L43 – –L47.
- Vaiana, G. S., Cassinelli, J. P., Fabbiano, G., Giacconi, R., Golub, L., Gorenstein, P., Haisch, B. M., Harnden, Jr., F. R., Johnson, H. M., Linsky, J. L., Maxson, C. W., Mewe, R., Rosner, R., Seward, F., Topka, K. & Zwaan, C. (1981), ‘Results from an extensive Einstein stellar survey’, *ApJ* **245**, 163–182.
- Valencia, D., Ikoma, M., Guillot, T. & Nettelmann, N. (2010), ‘Composition and fate of short-period super-Earths. The case of CoRoT-7b’, *A&A* **516**, A20.
- van Ballegooijen, A. A. & Martens, P. C. H. (1989), ‘Formation and eruption of solar prominences’, *ApJ* **343**, 971–984.
- Vernazza, J. E., Avrett, E. H. & Loeser, R. (1981), ‘Structure of the solar chromosphere. III - Models of the EUV brightness components of the quiet-sun’, *ApJS* **45**, 635–725.

- Voges, W., Aschenbach, B., Boller, T., Bräuninger, H., Briel, U., Burkert, W., Dennerl, K., Englhauser, J., Gruber, R., Haberl, F., Hartner, G., Hasinger, G., Kürster, M., Pfeffermann, E., Pietsch, W., Predehl, P., Rosso, C., Schmitt, J. H. M. M., Trümper, J. & Zimmermann, H. U. (1999), ‘The ROSAT all-sky survey bright source catalogue’, *A&A* **349**, 389–405.
- Vogt, S. S. (1981), ‘A method for unambiguous determination of starspot temperatures and areas - Application to II Pegasi, BY Draconis, and HD 209813’, *ApJ* **250**, 327–340.
- von Paris, P., Gebauer, S., Godolt, M., Grenfell, J. L., Hedelt, P., Kitzmann, D., Patzer, A. B. C., Rauer, H. & Stracke, B. (2010), ‘The extrasolar planet Gliese 581d: a potentially habitable planet?’, *A&A* **522**, A23.
- Weisskopf, M. C., Tananbaum, H. D., Van Speybroeck, L. P. & O’Dell, S. L. (2000), Chandra X-ray Observatory (CXO): overview, *in* J. E. Truemper & B. Aschenbach, eds, ‘Society of Photo-Optical Instrumentation Engineers (SPIE) Conference Series’, Vol. 4012 of *Society of Photo-Optical Instrumentation Engineers (SPIE) Conference Series*, pp. 2–16.
- White, O. R. & Livingston, W. (1978), ‘Solar luminosity variation. II - Behavior of calcium H and K at solar minimum and the onset of cycle 21’, *ApJ* **226**, 679–686.
- Wiedemann, G., Ayres, T. R., Jennings, D. E. & Saar, S. H. (1994), ‘Carbon Monoxide Fundamental Bands in Late-Type Stars. III. Chromosphere or CO-mosphere?’, *ApJ* **423**, 806.
- Wilson, O. C. (1978), ‘Chromospheric variations in main-sequence stars’, *ApJ* **226**, 379–396.
- Wittmann, A. D. & Xu, Z. T. (1987), ‘A catalogue of sunspot observations from 165 BC to AD 1684’, *A&AS* **70**, 83–94.
- Worthey, G. & Lee, H.-c. (2011), ‘An Empirical UBV RI JHK Color-Temperature Calibration for Stars’, *ApJS* **193**, 1.
- Wright, J. T. & Gaudi, B. S. (2013), *Exoplanet Detection Methods*, p. 489.
- Yuda, S., Hiei, E., Takahashi, M. & Watanabe, T. (1997), ‘Electron Temperature of Solar Flares Derived from Helium-Like Sulphur Lines’, *PASJ* **49**, 115–121.

Acknowledgements

When my family, friends and students from my past asked me about astronomy and my topic of research, I always told them I study about stars like our Sun with planets like the Earth. Then the first question would be if I have discovered any planet or is there a planet or a star named after me. Though I have no star/planet named after me yet, I am proud to have contributed a tiny drop to the vast ocean called the field of ‘Astronomy and Astrophysics’.

Firstly, I would like to express the deepest appreciation to my advisor Prof. Jürgen Schmitt for his advice, his encouragement and all his support. I would like to thank him for bringing a huge change in my attitude towards research and getting me out of my nut shell.

Further, thanks to my ex-/current office mates: Katja for making my initial stay in an unknown country easier, Birgit for proof reading my thesis and Micheal for helping me in translating the abstract to German, which would have been virtually impossible without him.

I am grateful to have found amazing friends at the observatory: Caro for always being there for me, for supporting me, for cheering me, travelling with me to all creapy places and for discovering the word ‘bestest’; Anna for answering all naive questions and making me do a lot of physical work; Vero for all the support. And special thanks to all my friends back home Sharon, Jo, Dulip, Deepa, Aru, Athray, Ravi, Manju, Rakhee and the list is never ending.

This journey would have been impossible without the support of my mom, dad, Karthik (my loving brother) and Aachu. I thank them for their constant encouragement through every walk of my life.

I acknowledge the support by the administrative staff at Hamburger Sternwarte and the DFG in the frame work of RTG 1351.

